University of Glasgow

Taylor, Gregor G. (2021) *Mid-infrared photon counting with superconducting nanowires.* PhD thesis.

https://theses.gla.ac.uk/82501/

Copyright and moral rights for this work are retained by the author

A copy can be downloaded for personal non-commercial research or study, without prior permission or charge

This work cannot be reproduced or quoted extensively from without first obtaining permission in writing from the author

The content must not be changed in any way or sold commercially in any format or medium without the formal permission of the author

When referring to this work, full bibliographic details including the author, title, awarding institution and date of the thesis must be given

Enlighten: Theses
https://theses.gla.ac.uk/
research-enlighten@glasgow.ac.uk

Mid-Infrared Photon Counting with Superconducting Nanowires

Gregor G. Taylor

Submitted in fulfilment of the requirements for the
Degree of Doctor of Philosophy

James Watt School of Engineering
College of Science and Engineering
University of Glasgow

July 2021

Abstract

Superconducting nanowire single photon detectors (SNSPDs) set the gold-standard in infrared single-photon detection. The detection metrics offered by these detectors - timing resolution, dark count rate, detection efficiency and wavelength sensitivity - are continuing topics of research as we strive towards the ultimate detector. In this work, efforts to explore and expand the wavelength sensitivity of SNSPDs are shown, where there is still much progress to be made. Expanding the wavelength range of SNSPDs to the mid-infrared will bring great benefits to a wide variety of fields especially in the domain of remote sensing and LIDAR.

The optimisation, fabrication and deployment of such SNSPDs into applications in the mid-infrared is presented. Investigations into atomic layer deposition as a novel technique for superconducting material growth for SNSPDs in the mid-infrared is shown, with characterisation of devices up to 2 μm. Tailored SNSPDs with enhanced absorption in the mid-infrared are fully characterised at a wavelength of 2.3 μm and presented. The viability of such devices for remote sensing applications in the mid-infrared is then demonstrated with a proof-of-principle SNSPD photon-counting LIDAR experiment at 2.3 μm. Additionally, a 1.55 μm wavelength scanning LIDAR field trial is shown with a novel differential readout tapered SNSPD providing ultra-fast timing resolution. The resulting depth images exhibit sub-mm depth resolution. It is hoped that this work will enable the advancement and deployment of SNSPDs for a wide-variety of near and mid-infrared applications where their unrivalled performance benefits can be leveraged.

Contents

List of Tables

List of Figures

Acknowledgements

It has always been my belief that attempting to list every single person who deserves my thanks would be a somewhat pointless endeavour as it is often the case that we are not always aware just how much someone has helped us. The risk that someone who has helped you feels undervalued because they didn't make it into an acknowledgements section of a thesis is also ever-present and, at least in my case, undesirable. So I'll preface this section with a heartfelt thanks to anyone who has ever helped me - no matter how small they may feel that contribution was. It is quite likely that you helped more than you will ever know. Science is an entirely collaborative endeavour, despite some people's best efforts, and I will do my best in my future career to always offer help and assistance to any who ask for it.

All that said, I would like to thank some people who directly made this work possible. Firstly, my supervisor, Professor Robert Hadfield who from the start has provided the ideal environment for me to complete my work, as well as always being available when problems inevitably arose. I am well aware that many PhD researchers were not so fortunate in their supervisors and I don't take it for granted. I would also extend my thanks to the rest of the research group for all of their assistance and especially to Dr Dmitry Morozov for his key role in most of the projects we have undertaken in the last 4 years. Dr Nathan Gemmell, Dr Kleanthis Erotokritou and Dr Shashi Prabhakar also deserve my thanks for their help and involvement in the work presented here. I would also extend my thanks to all of the technical staff at the University of Glasgow whose services make the research possible.

As mentioned, science is collaborative and I would like to thank all of our collaborators for their assistance and expertise whilst this work was carried out - Dr Shigehito Miki and colleagues at NICT Japan, Professor Gerald Buller and Dr Aongus McCarthy at Heriot-Watt University, Dr Boris Korzh and Dr Matthew Shaw at JPL, Dr Matteo Clerici's and his team here at the University of Glasgow, Dr Peter Barry and colleagues at the University of Chicago and all of the others across the world who were indirectly involved. I would also like to thank my examiners Professor Karl Berggren (MIT USA) and Dr Ashley Lyons (University of Glasgow) for the discussion and constructive feedback on the work presented in this thesis.

And lastly, to Emma, my parents, my brothers and Claire. For generally putting up with my shit for many years.

Declaration

With the exception of chapters 1 and 2, which contain introductory material, all work in this thesis was carried out by the author unless otherwise explicitly stated. Film growth and device nanofabrication was performed by colleagues at the University of Glasgow in the James Watt Nanofabrication Centre or by collaborators at their respective institutions - this has been made clear in the relevant sections of the text. No direct fabrication work was undertaken by the author and details of the processes are included for completeness and clarity. Device design input was provided by the author.

Acronyms and Symbols

Commonly Used Acronyms

ALD	Atomic Layer Deposition
BCS	Bardeen Cooper Schrieffer (theory)
CFD	Constant Fraction Discriminator
CPW	Coplanar Waveguide
DAQ	Data Acquisition Module
DBR	Distributed Bragg Reflector
DCR	Dark Count Rate
EMG	Exponentially Modified Gaussian
FWHM	Full Width Half Maximum
GM	Gifford-McMahon
IRF	Instrument Response Function
JWNC	James Watt Nanofabrication Centre
MIR	Mid Infrared
MLE	Maximum Likelihood Estimate
ND	Neutral Density (filter)
NF	Noise Figure
NIR	Near Infrared
LIDAR	Light Detection and Ranging
LNA	Low Noise Amplifier
OAP	Off-Axis Parabolic
OPO	Optical Parametric Oscillator

PBS	Polarising Beam Splitter
PCR	Photon Count Rate
PMT	Photomultiplier Tube
PPLN	Periodically Poled Lithium Niobate
QE	Quantum Efficiency
QKD	Quantum Key Distribution
RF	Radio Frequency
RJMCMC	Reversible-Jump Markov Chain Monte Carlo
RMS	Root Mean Square
RR	Repetition Rate
SDE	System Detection Efficiency
SEM	Scanning Electron Microscopy
SNR	Signal-to-noise Ratio
SNSPD	Superconducting Nanowire Single Photon Detector
SPAD	Single Photon Avalanche Diode
SWIR	Short-wave Infrared
TAC	Time to Amplitude Converter
TCSPC	Time Correlated Single Photon Counting
TEM	Transmission Electron Microscopy
TOF	Time of Flight
VAP	Vortex Antivortex Pair
VOA	Variable Optical Attenuator

Commonly Used Symbols

T_c	Critical Temperature
I_{sw}	Switching Current
I_c	Critical Current
I_{dep}	Depairing Current
J_c	Critical Current Density

H_c	Critical Magnetic Field
Δ	Superconducting Energy Gap
L_k	Kinetic Inductance
Z_{load}	Load Impedance

Physical Constants

h	Planck's constant (6.62×10^{-34} J·Hz^{-1}
$\hbar$	Planck's constant divided by 2π (1.054×10^{-34} J·Hz^{-1})
c	Speed of light in a vacuum (2.99×10^{8} m·s^{-1})
k	Boltzmann constant (1.380×10^{-23} m^2·kg·s^{-2}·K^{-1})

Chapter 1

Introduction

The ability to detect single photons is an essential part of the tool kit for quantum optics and underpins many emerging optical quantum technology applications. Superconducting nanowire single photon detectors (SNSPDs) have demonstrated unrivalled performance when compared to semiconductor technologies but much of the development focus has been on 1550 nm wavelength, the main telecom band. Indeed, we are now at a stage where, at the time of writing, commercial SNSPDs for visible and near-IR wavelengths are available with excellent detection metrics from a variety of companies across the world [1–5]. To date, extending the working wavelength of these detectors to the mid-infrared has not been the primary research goal. However, superconducting materials have an energy gap in the meV range and, in principle, a cut-off wavelength far into the mid-infrared. This thesis presents work towards an efficient and fast detector in the mid-infrared, as well as demonstrating some proof-of-principle remote sensing applications. The advantages of operating at mid-infrared wavelengths for free-space applications are also explored. The thesis is presented in the following manner:

Chapter two presents the background information behind photon-detection with superconducting materials as well as the competing technologies and key-performance parameters that are crucial to understand. It also presents the background and working theory behind time-correlated single photon counting (TCSPC) and single-photon light detection and ranging (LIDAR). Essential theoretical background is provided for context and understanding of the novel work throughout the rest of the thesis. Comprehensive and up-to-date references are provided for further reading.

Chapter three then details the experimental methods used throughout the thesis to gather data. Fabrication methods are explained such that the optimisation of these techniques can be better understood. It is explained how SNSPDs are mounted, coupled optically and electrically and then characterised.

Chapter four explains our work exploring atomic layer deposition (ALD) of NbN as an alternative to sputter-coating for SNSPDs. Fabricated devices are shown and then electrical and optical characterisation results up to 2006 nm wavelength are presented. This serves as a first investigation into the mid-infrared sensitivity of the material as a prelude to fabricating optimised devices.

Chapter five details our first-generation of SNSPDs for the mid-infrared. Devices are fabricated in optical cavities to enhance detection in the mid-infrared. These devices are then fully characterised utilising a mid-infrared test bench. Future and ongoing work is highlighted for the creation of our next-generation detectors.

Chapter six then shows experiments in single-photon LIDAR with SNSPDs. The work is split into two distinct sections - the first is a proof-of-concept tabletop LIDAR at 2.3 μm wavelength demonstrating the first single-photon LIDAR work at mid-infrared wavelengths. The second utilises ultra-low jitter SNSPDs and deploys them in a scanning optics field trial at 1.55 μm wavelength where their timing properties can be exploited.

There are three appendices provided to detail work carried out that does not fit into the context of the larger chapters. The first details the design and construction of a sub 1 Kelvin cryostat for use in the LIDAR field trials. It details the novel improvements made to existing cryostats to allow portable and easy operation. Appendix B then details all of the Python code used throughout the thesis. Throughout the PhD it has often been more sensible to write custom applications for data gathering and processing rather than rely on off-the-shelf products/libraries that do not quite fit the requirements. All of the code is available online and is fully referenced. The final appendix outlines the publications and presentations that have resulted from this thesis work. The work in Ch.4 on ALD deposited NbN SNSPDs was published in the paper 'Infrared single-photon sensitivity in atomic layer deposited superconducting nanowires' in 2021 [6]. The work on 2.3 μm wavelength LIDAR in Ch.6 was published in the paper 'Photon counting LIDAR at 2.3 μm wavelength with superconducting nanowires' in 2019 [7].

Chapter 2

Background

2.1 Single Photon Detection

2.1.1 Photon Detection

Photons are single quanta of electromagnetic radiation. The current photon concept was first introduced in the early 20th century when Albert Einstein, building on Max Planck's earlier work regarding blackbody radiation [8], published his pioneering work on the photoelectric effect - the observation that electrons are emitted when light is incident on a material. In terms of classical electromagnetic theory this emission was expected to be intensity-dependent when in fact it was clear that it was frequency dependent. To make sense of this Einstein proposed that light was quantised into discrete wave packets of finite frequency-dependent energy [9]. The term photon was not coined until 1926 by G.N. Lewis and was originally proposed as a real particle which carried energy from atom to atom - Lewis even specifically refuted that this particle was the light quantum [10]. In recent years however photon has become the accepted term for the quanta of electromagnetic radiation. This explanation of photons as point-like particles means that they do not spread out as they propagate and, crucially for single photon counting applications, are absorbed as a whole. Photons are massless, charge-less and have a frequency dependent energy given by the equation $E = h\nu$. They are emitted in a variety of naturally occurring processes which makes their detection and counting a valuable tool in understanding many natural phenomenon.

A single photon detector is a radiation detector that, when a single photon of electromagnetic radiation is incident on it, will emit a measurable signal that can be recorded in some way. In effect a single photon detector is a radiation detector that has achieved ultimate sensitivity. An ideal detector would be one that has a unity probability of incident radiation resulting in an output pulse, zero chance of an output pulse being generated when no radiation is incident (a dark count rate of zero), an infinitely small reset time following an output pulse being generated and should be sensitive over a wide range of energies.

2.1.2 Superconductivity

Superconductivity was first discovered in 1911 by Heike Kamerlingh Onnes when he observed that the resistance of mercury abruptly became zero when cooled in liquid helium to 4.19 K [11]. He described this phenomenon of zero electrical resistance when a material is cooled to a sufficiently low temperature in the following years and was awarded the Nobel prize in physics for the work in 1913. Later on in 1933 Walther Meissner and Robert Ochsenfeld subsequently discovered that superconductors also expelled applied magnetic fields - later to be called the Meissner effect [12]. Superconducting materials have a critical temperature (T_c), which varies from material to material, below which the state of superconductivity is achieved. Once below T_c a current in a loop of superconducting material, provided it is below the switching current (I_{sw}) above which the superconductivity breaks down, can persist indefinitely. Several theories were proposed following this discovery eventually resulting in a microscopic theory proposed by Bardeen, Cooper and Schrieffer (BCS theory) in 1957 [13]. This theory proposed that a weak attractive potential can overcome the Coulomb repulsion and cause electrons to pair up into Cooper pairs. This attractive potential is usually thought of as the electron-phonon interactions caused by the attraction between the positively charged ionic lattice and the electrons in conventional superconductors, though the origin of the attraction does not matter in the theory. These Cooper pairs then condense into a large Bose-Einstein condensate at low temperatures and give rise to a superconductivity. These bound electron condensates show an energy gap - called the superconducting energy gap - which is defined as the difference between the ground state and the energy required to create a quasiparticle excitation [14]. In order to break a Cooper pair it is necessary to add enough energy to create two quasiparticle excitations: $E > 2\Delta$ where Δ is the energy gap.

As stated above, superconductors require to be cooled to a temperature below the critical temperature, T_c, in order for them to exist in the superconducting state. It is also stated above that superconductors will expel applied magnetic fields. This occurs up to a critical field, H_c, above which the superconductor will revert back to its normal state. The final critical field is the critical current, I_c. It is dependent on the dimensions of the superconductor and is linked to the H_c. For a conductor of circular cross section it is given by:

$$I_c = 2\pi a H_c \tag{2.1}$$

Where a is the radius. The critical current density, J_c, is then given by:

$$J_c = \frac{2H_c}{a} \tag{2.2}$$

This is intuitive as an applied current induces a magnetic field and the J_c is reached when H_c is

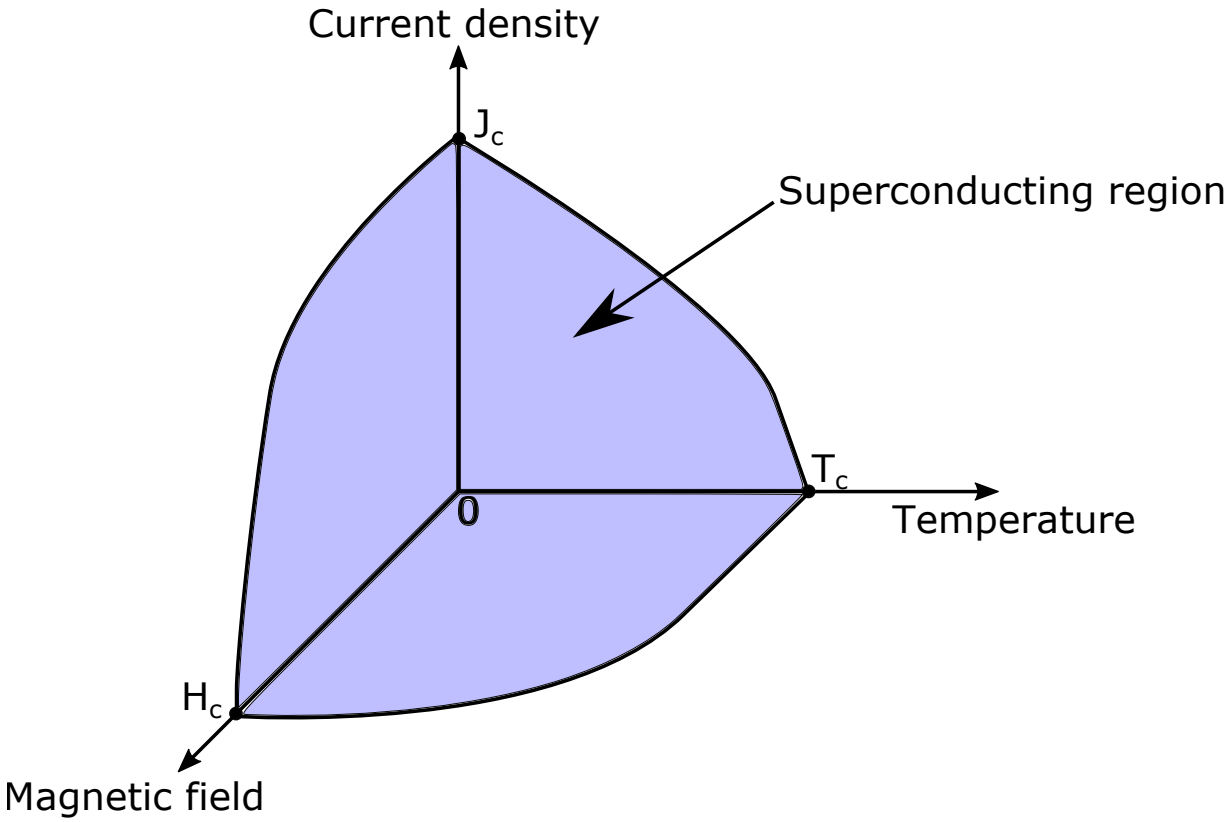

Figure 2.1: Phase diagram for general superconductor. The critical values of H_c, J_c and T_c are all inter-dependent and the shaded region in the middle represents the superconducting region.

exceeded [15]. Both of these critical values are also linked to temperature [16, 17]. For J_c it is given by:

$$J_c(T) = J_c(0)\frac{(T_c - T)}{T_c} \tag{2.3}$$

and the H_c dependence on T is given by:

$$H_c(T) = H_c(0)[1 - \left(\frac{T}{T_c}\right)^2] \tag{2.4}$$

This relationship between H_c, J_c and T_c is visualised in Fig. 2.1.

The diagram in Fig. 2.1 provides a helpful insight into the superconducting state but a further distinction between conventional low-temperature superconductors should be made by dividing them into type-I and type-II [18]. Type-I superconductors exhibit a phase diagram similar to Fig. 2.1, with a critical field H_c that is temperature dependent. Below this field they are in a perfect Meissner state and all magnetic flux is expelled from the material. In contrast type-II superconductors exhibit a lower critical field, H_{c1}, below which magnetic flux is expelled however there is also an upper critical field, H_{c2}. Between H_{c1} and H_{c2} the material exists in a mixed state where flux partially penetrates the material in units of the magnetic flux quantum.

Above H_{c2} the material is fully in its normal state. This trapping of magnetic flux as vortices is important for photo-detection as shall be discussed later in this section. Type-I superconductors tend to be pure metals such as Pb or Hg and type-II are generally alloys such as NbN or NbTi. For superconducting nanowire single photon detectors, type-II materials are generally utilised as these 'refractory' materials are rugged enough to survive device patterning and thermal cycling.

2.1.3 Superconducting Nanowire Single Photon Detectors

Superconducting nanowire single photon detectors (SNSPDs [19]), first demonstrated by Gol'tsman *et al* in 2001 [20], utilise the fact that the Cooper pairs are extremely weakly bound and the small energy of an incident photon can break them. In order to exploit this a thin superconducting film of a few nanometres thickness is deposited onto a substrate and patterned into a nanowire via lithography and reactive ion etching. The SNSPD device is cooled below the critical temperature and biased just below the switching current. An incident photon results in the disruption of the superconductive state locally to the photon absorption site. Current redistribution also contributes to this effect as parts of the nanowire turn resistive. This results in a measurable voltage pulse. The energy is then scattered away into the substrate of the detector, the superconductivity is restored and the detector is once again ready to detect incident radiation. A basic diagram of this process is shown in Fig. 2.2.

Fig. 2.2 and the explanation presented above presents a rather simplistic description of the photodetection process in SNSPDs and although useful for a general audience it is worth exploring the current thinking on the underlying mechanism here. First it is necessary to define the currents referred to throughout this thesis and to define a vortex. Superconducting vortices (or Abrikosov vortices [21]) are supercurrents that circulate around a vortex core that is in the normal state in type-II superconductors. They are trapped vortices of magnetic flux with each core equal to the single flux quantum. Vortices exist in SNSPDs either as vortex-antivortex pairs (VAPs) which can be decoupled with the addition of energy or as single vortices that enter via the edge of the nanowire. If the nanowire is biased with a current then the vortices will experience Lorentz force if they are unbound.

Generally in SNSPD literature the term I_c will appear and is defined as the current above which the device ceases to superconduct. It is more intuitive to describe this current where the device switches from superconducting state to normal state as the switching current, I_{sw} which is device dependent. The critical current is more helpfully defined as the current at which the energy barrier for vortex entry becomes 0, as in [22] (and indeed, analogous to the point defined in Fig. 2.1). A further current definition is the depairing current, I_{dep}, which can be defined as the fundamental maximum current that can be applied before the kinetic energy of the Cooper pairs

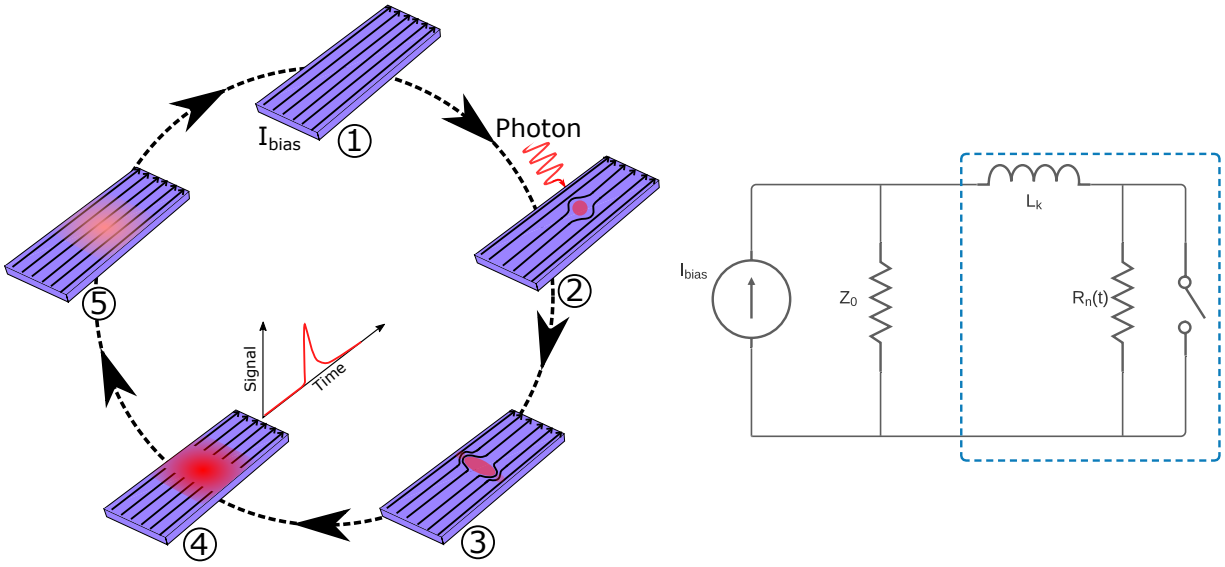

Figure 2.2: Left: Hotspot formation cycle in a superconducting nanowire. ① The nanowire is biased with a current, I_{bias}, below the switching current, I_{sw}. ② A photon is incident on the nanowire and is absorbed, disrupting the superconducting state. ③ The disruption continues. Current crowding occurs as as the current redistributes around the normal region. ④ The nanowire is now in the normal state, a measurable voltage pulse is observed. ⑤ The energy is scattered away through the substrate and the superconductivity returns, the nanowire is ready to detect another photon. Right: An equivalent circuit of the SNSPD. L_k is the kinetic inductance of the nanowire and R_n is the resistance of the nanowire in the normal state. The switch opening is the equivalent of a photon being absorbed and a pulse is measurable across Z_0. Figure adapted from [19].

exceeds their binding energy and they become unbound [17].

The vortex-assisted detection mechanisms can be split into two broad categories [23]: vortices overcoming the edge barrier due to the suppressed barrier height caused by the absorbed photon or VAPs becoming nucleated around normal regions (caused by incident photon) and then subsequently being unbound and moving in opposite directions due to the bias current. The photon-triggered vortex-entry model (or 'hotbelt model') [24] and the diffusion based vortex-entry model [25] both fall into the first category and provide a model for photo-detection that relies upon the entry or vortices from the edge of the nanowire. The normal core vortex model [26] is a more hybrid approach where both side-entry of vortices and nucleation and subsequent unbinding of VAPs is considered. Although no model yet exists that can adequately describe all observed experimental data across all SNSPD geometries and material systems, it is now generally accepted with a high degree of confidence that the detection mechanism in SNSPDs is vortex-assisted [23]. There is ongoing work to develop a universal model that better fits all of the data.

2.1.4 Key Performance Parameters

Detection Efficiency

When comparing SNSPDs to other methods of photon detection and counting it is necessary to define key parameters that characterise the effectiveness of a detector. The first is that of efficiency - the probability that a photon will trigger an output pulse from the detector - which is defined for a specified photon energy or wavelength. This broad efficiency is termed the system detection efficiency and can be decoupled into [27]:

$$\eta_{sde} = \eta_{coupling} \times \eta_{absorption} \times \eta_{registering} \tag{2.5}$$

The coupling efficiency, $\eta_{coupling}$, is determined by the optical coupling from the photon source to the active area of the detector. Whether coupled by fibre or freespace it is necessary to precisely align the active area of the detector with the incoming radiation in order that the energy is not absorbed, scattered or reflected by the environment. This leaves the remaining terms $\eta_{absorption}$(the probability that an incident photon will be absorbed by the nanowire) and $\eta_{registering}$(the probability that that absorbed radiation will result in an output pulse - also called the internal detection efficiency) which make up the *intrinsic efficiency* of the detector. These two parameters are affected by the detector geometry and material choice and are a key consideration when designing detectors. To date SNSPDs have achieved system detection efficiencies (η_{sde}) of up to 98% in the 1520-1610 nm range [28, 29].

Count Rate

The next parameter that must be optimised for single photon detectors is that of count rate - the maximum count rate the detector can achieve. This count rate is derived from the reset time of the detector, characterised by the rise time τ_{rise} and fall time τ_{fall}. These times are related to the kinetic inductance of the material which can be thought of as the time it takes to accelerate the finite-mass charge carriers within a material - all objects with mass have an associated rate of change of velocity, similar to the finite rate of change of magnetic flux within an inductor [30]. This inductance is related to the rise and fall times by the relationships [31]:

$$\tau_{rise} = \frac{L_k}{R_s + R_n} \tag{2.6}$$

$$\tau_{fall} = \frac{L_k}{R_s} \tag{2.7}$$

Where L_k is the kinetic inductance and R_s and R_n are the resistances of the shunt and nanowire in its resistive state. It is clear from these relationships that the reset time and hence maximum count rate is strongly related to the kinetic inductance of the nanowire, which is defined as [30]:

$$L_k = \frac{m}{ne^2} \times \frac{l}{wt} \tag{2.8}$$

The geometric element of this equation, l/wt where l is the length, w the width and t the film thickness is the variable controlled during fabrication. Various methods have been tried to reduce the kinetic inductance including an n-SNAP configuration based on n parallel nanowires where the nanowires are shorter (and therefore L_k is smaller) which operates via an avalanche based mechanism where an incident photon on one section of nanowire will result in all parallel wires being driven resistive and the current shunted to the readout electronics [32]. Other methods would include reducing the active area of the device or increasing wire width or thickness but this comes with a trade-off in detection efficiency [33] and spectral range.

Dark Count Rate

Dark count rate (DCR) is defined as the average number of counts that a detector registers in the absence of any incident radiation. In SNSPDs the DCR can be decoupled into two values; the intrinsic DCR, DCR_{int} and the background DCR, DCR_{back}. The background DCR is the DCR caused by stray photons incident on the device that are unwanted in terms of the experiment, these include photons coupled into the detector from the external environment or blackbody radiation from experimental components at ambient temperature. Blackbody radiation is the temperature dependent radiation emitted from a source - this radiation causes an issue if it is coupled into the optical fibre to the device as it will trigger a response from the detector. It is characterised by the

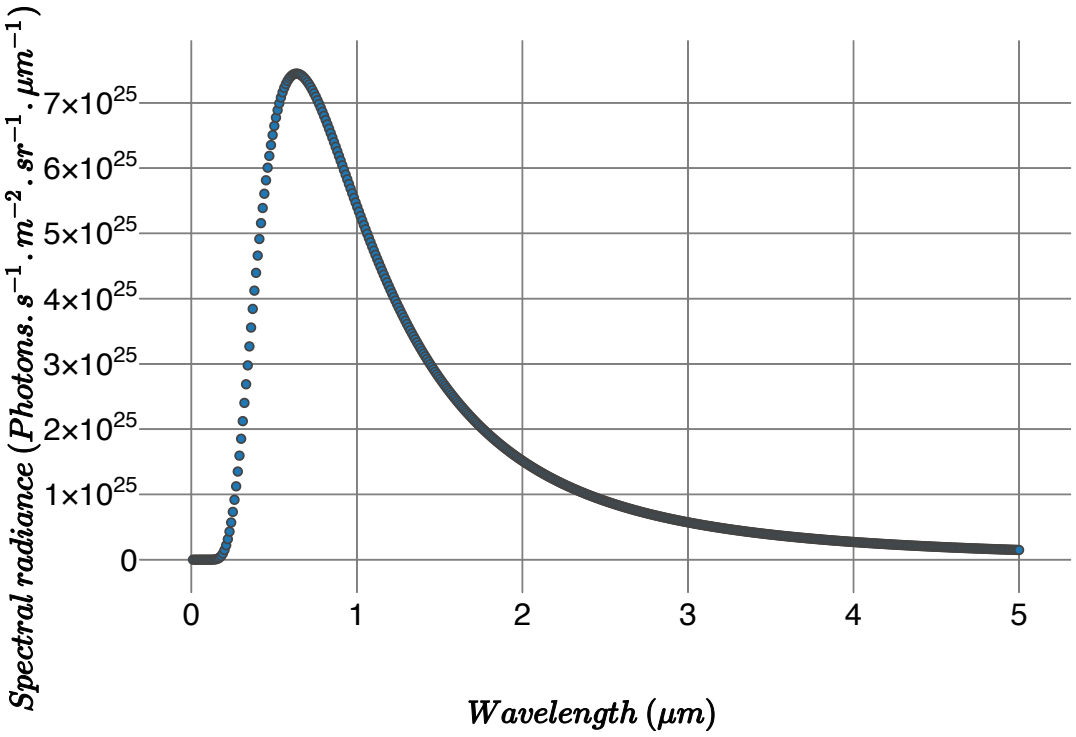

Figure 2.3: An example blackbody spectrum, here shown for a temperature of 5777 K, the approximate temperature of the sun. The peak emission is at 0.64 µm, for lower temperatures the radiation peak moves into the infrared spectrum.

formula:

$$B_v(T) = \frac{2hv^3}{c^2} \times \frac{1}{(e^{\frac{hv}{kT}} - 1)} \tag{2.9}$$

where $B_v(T)$ is the spectral radiance, h is Planck's constant, c is the speed of light in a vacuum, k is Boltzmann's constant, v is the frequency of the radiation emitted and T is the temperature. As can be seen from the above formula, it is possible to compute a spectrum of the emitted radiation for a given temperature - an example is shown in Fig. 2.3. At lower temperatures (such as room temperature, 300K) most of the emitted radiation is in the infrared which presents difficulties for extending detectors into the infrared. DCR_{back} can be improved with careful experimental design, implementation of cold filters before the detector [34, 35] or use of time gating if the experiment allows [36]. The intrinsic DCR, DCR_{int}, is the DCR that registers in a completely shielded detector. A few possible mechanisms have been brought forward including current-assisted thermal unbinding of vortex-antivortex pairs(VAPs), edge barrier vortex hopping and thermally activated phase slip events. [22, 37, 38]. There is current evidence to suggest that single vortex entry is likely the dominant mechanism [23].

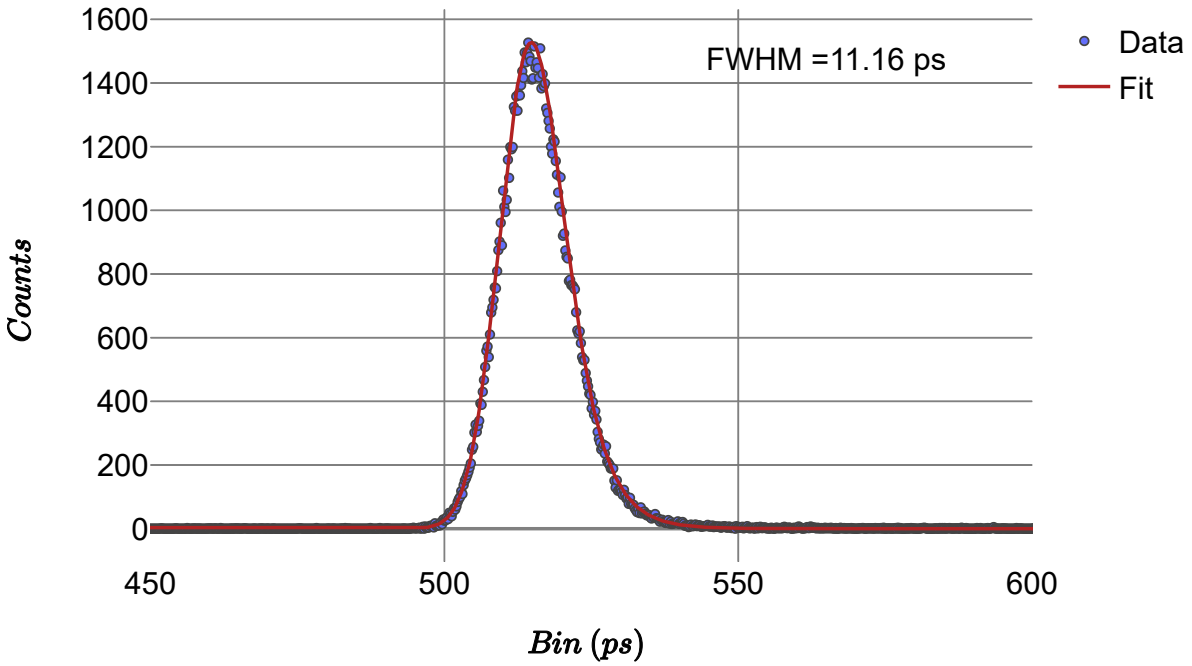

Figure 2.4: Typical timing histogram of an SNSPD jitter measurement. The data is fitted with an exponentially-modified Gaussian distribution to account for the tail in the distribution.

Timing Jitter

The timing jitter of a detector is the deviation of the response signal from an ideal periodic photon source. In any experiment there are contributions to the overall jitter from all of the components - typically the photon source, optical components such as optical fibres and any readout electronic circuits - which can also be minimised. It is typically quantified as the FWHM of the instrument response function (IRF) of the detector. Recent work has shown SNSPDs with working timing jitter of as low as 2.6 ps [39]. A timing histogram of a typical SNSPD timing jitter measurement is shown in Fig. 2.4. The distribution is characterised as an exponentially-modified Gaussian to account for the non-Gaussian tail at the end of the distribution, of the form:

$$f(x) = \frac{\lambda}{2} e^{\frac{\lambda}{2}(2\mu+\lambda\sigma^2-2x)} erfc(\frac{\mu+\lambda\sigma^2-x}{\sqrt{2\sigma}}) \tag{2.10}$$

where $erfc$ is the complementary error function, μ and σ are the mean and standard deviation of the Gaussian component and λ is the rate of the exponential component. The overall system jitter can be split into 3 component parts:

$$\Delta t_{system} = \Delta t_{experimental} + \Delta t_{geometric} + \Delta t_{intrinsic} \tag{2.11}$$

Experimental contributions to jitter, $\Delta t_{experimental}$ arise from electrical contributions such as amplifier noise and timing electronics jitter and optical noise arising from finite pulse-width optical pulses from the source as well as optical effects at the device-scale. The electrical contributions can be improved with cryogenic amplifiers and the latest time correlated single photon (TCSPC) cards as in [39]. The optical contributions from the laser source can be minimised when short fs-scale pulse length lasers are used. Due to the optical structures used to enhance the absorption of specific wavelengths in SNSPD devices (see §3.1.1) there is an optical component of the jitter due to the reflections of photons from various material boundaries within the device stack. For a nanowire positioned 500 μm above the bottom of the substrate this could account for 3.3 ps of variation and would increase in multiple reflection scenarios. The origin of the exponential tail observed in timing jitter histograms (as shown in Fig. 2.4 and discussed above) is currently not well understood and this effect could potentially account for some of it. Another possibility is the transverse position of the photon absorption (across the width of the nanowire) as discussed in [40].

The geometric component of the timing jitter, $\Delta t_{geometric}$ is due to the large kinetic inductance of superconducting nanowires. This means that the RF pulse generated from an incident photon propagates along the nanowire at a small fraction of the speed of light and brings a position-dependent time delay to the output pulse. This can be compensated for by using differential readout schemes [41] as will be explored more in Ch. 6. This leaves the intrinsic jitter of the device, $\Delta t_{intrinsic}$. This intrinsic jitter is the fundamental limit of the temporal resolution of an SNSPD and assuming perfectly uniform fabrication of nanowires is governed by Fano fluctuations [42].

Wavelength Dependence

It is desirable for single photon detectors to have the ability to operate at a wide range of photon energies. Some applications such as infrared spectroscopy [43] and remote gas sensing [44] require detectors that stretch far into the infrared spectrum. SNSPDs have shown saturated internal efficiencies far into the infrared [45, 46] which surpasses the currently available semiconductor technology [47, 48], see section 2.1.4. As SNSPDs have shown good internal efficiencies it now remains a challenge to increase the absorption efficiency using novel solutions such as integrated optical cavities at longer wavelengths, discussed in more detail in Ch.5.

Photon Number Resolution

A single photon detector that can distinguish the number of photons incident on it in a given time period is described as a photon number resolving detector. Although SNSPDs were initially

incapable of distinguishing between single and multi-photon events much progress has been made in recent years. Various schemes exist including exploiting the rise time variation between different n-photon events [49] or connecting multiple nanowires in series [50, 51].

Polarisation Dependence

SNSPDs can be sensitive to the polarisation of the incident light due to the nanowire structure [52]. Light polarised parallel to the nanowires will exhibit a greater detection efficiency compared to that polarised perpendicularly. This effect is both geometry and wavelength dependent, exhibiting a greater disparity between parallel and perpendicularly polarised light at longer wavelengths [53]. Depending on the application, this characteristic could be desirable and work has been performed to enhance the polarisation sensitivity of SNSPDs [54] for imaging applications [55, 56]. Equally, in some applications this characteristic is unwanted and designs such as stacking two nanowires [57] as well as novel nanowire patterns such as spirals [58] and fractals [59] that reduce the polarisation sensitivity due to their geometry have been demonstrated.

2.1.5 Alternative Photon Counting Technologies

Selection of a suitable single-photon detector will strongly depend on the application - cost, footprint and desired detection metrics will all have to be considered. Here, the two main competitors in the single-photon counting world - single photon avalanche diodes (SPADs) and photomultiplier tubes (PMTs) will be explained so that their reference in the text later on has context.

Single Photon Avalanche Diodes

SPADs are semiconductor devices that have the ability to detect single photons. A p-n junction is reverse-biased to a large value, well above the breakdown voltage, and an incident photon excites a carrier. This carrier is accelerated swiftly and leads to a self-sustaining avalanche, causing the current to rise to a steady level which can be detected. By sensing the leading edge of the current rise, a single photon detection event can be determined. As the avalanche is self sustaining the avalanche must be quenched which involves lowering the bias voltage below breakdown to stop the avalanche and then returning it so that further photons can be detected. A variety of passive and active quenching circuits have been proposed and demonstrated [60]. Silicon SPADs are a mature technology, offering excellent detection characteristics up to wavelengths of up to 900 nm [61]. They benefit from refined fabrication procedures and CMOS technology allowing device integration and fabrication of SPAD arrays [62] - although much progress has been made on SNSPD arrays recently [63] it still remains a challenge to scale the readout circuitry and SPADs are currently the leading technology here. Extending SPAD spectral sensitivity requires use of a smaller bandgap material such as InGaAs, allowing detection of single photons up to 1700

nm [64] but loses the ease of fabrication enjoyed by silicon technologies. For mid-infrared single-photon detection, very small bandgap materials are required such as InSb [65] or HgCdTe [66] are required. HgCdTe is the most developed with single-photon sensitivity demonstrated up to 4.3 μm at 77 K [67]. However these devices suffer from high dark count rates.

Photomultiplier Tubes

PMTs, which pre-date SPADs by some years, also operate by the photoelectric effect. A photon strikes a cathode which is encased in a vacuum tube and emits an electron. This electron is then accelerated into a series of dynodes which causes multiplication by secondary emission. Eventually the multiplied electrons arrive at the anode where they cause a measurable current. Thus a single incident photon can be detected. Various photocathode materials can be used depending on the target wavelength including Bialkali for the visible, Alkali-halide for the UV and InGaAs for the near-infrared [68]. In general, unless working at short wavelengths a SPAD will give superior detection characteristics when compared to a PMT, particularly in the near-infrared [69]. However, PMTs are still prized in photon counting applications which require a large detector area as PMTs are readily available with >10 cm diameter active area.

When compared to other photon counting devices such PMTs and SPADs [70], use of SNSPDs can give higher detection efficiencies [29], faster count rates [71], lower dark count rates [72] and smaller timing jitters [39]. When designing these detectors it is important to ascertain the desired characteristics of the final detector so that design decisions can be made to optimise the performance parameters for the application.

Due to the last decade of research interest in SNSPDs, commercial options with high detection efficiency (> 80 %) and low timing jitter (< 50 ps) in the near-infrared are available from several companies worldwide [1–5].

2.2 Mid-Infrared Photon Detection

As shown above, SNSPDs have exhibited photon sensitivity up to wavelengths of 10 μm [73], timing jitter as low as 3 ps [39], dark count rates as low as 10^{-4} Hz [35] and detection efficiencies as high as 98% at 1.55 μm [28]. These metrics, if examined in comparison, are far superior to alternative photon counting technologies available today. In this thesis, the spectral sensitivity of SNSPDs is exploited and work is performed to extend their usable efficiency into the mid-infrared at wavelengths greater than 2 μm. In this section alternative photon counting technologies at these long wavelengths are outlined and some of the motivation behind working at such long wavelengths is shown.

Before discussion of mid-infrared photon detection it is beneficial to describe the wavelength regions used throughout this thesis. Somewhat confusingly, these are typically ill-defined throughout the literature - for example the region above the visible can be both described as the near-infrared (NIR) or short-wave infrared (SWIR) depending on the definition used. In this thesis the regions will be described as shown in Table 2.1 with the mid-infrared region extending from 2 μm out to 10 μm.

Region	**Start (nm)**	**End (nm)**
Ultraviolet (UV)	100	400
Visible	400	700
Near-Infrared (NIR)	700	2000
Telecom*	1260	1625
Mid-Infrared (MIR)	2000	10000

Table 2.1: Definition of spectral regions used throughout this thesis.
*The telecom region lies within the NIR region and is based on the low-loss region of silica fibre optics used for communications.

As the photon energy decreases as wavelength increases the underlying detection mechanism behind most semiconductor photon detectors begins to fail. InGaAs single photon avalanche diodes (SPADs), for example while offering good performance at higher operating temperatures for wavelengths up to around 1700 nm, cannot resolve photon detection events at longer wavelengths due to the band gap being on the order of eV [74]. Superconducting energy gaps (that is - the energy required to break a Cooper pair) in comparison are on the order of meV [75]. The main competing technologies for photon counting applications in the mid-IR are summarised in Table 2.2. HgCdTe is a compound semiconductor material with a tunable band gap down to 100meV [80], in principle allowing a spectral cut off of 12 μm. Detectors using this material suffer from afterpulsing effects - multiple pulses emitted after the detection pulse due to trapped charge carriers [81] - and large DCRs [82, 83] but can operate at 77K. Commercial InAsSb detectors are available for cut off wavelengths up to 11 μm but these devices are not single photon sensitive so for quantum applications are unsuitable. Other superconducting detectors such as microwave kinetic inductance detectors (MKIDs) [84] and transition edge sensors (TESs) [85] show good detection efficiency in the infrared but due to their mechanism are very slow, limiting count rates. They also typically operate at mK range, which requires even greater cooling requirements than SNSPDs, but do have other attractive properties such as energy resolving capability. The last method outlined in Table 2.2 is the use of frequency up conversion to convert incoming mid-infrared photons in a non-linear medium to the near-IR range and then detecting them using commercial detectors, typically a Si SPAD. This has advantages as

Detector	Mid IR single photon sensitive?	NEP ($W\sqrt{Hz}$)	Time Constant	Efficiency (1.55 µm)	References
HgCdTe	Yes	~10^{-16}	~100 ns	70%	[67]
TES	Yes	~10^{-19}	~1 µs	95%	[76]
MKID	Yes	~10^{-18}	~100 µs	-	[77]
Mid IR up-conversion*	Yes	-	-	20%	[78]
InAsSb	Not shown	~10^{-11}	~10 µs	-	[79]
SNSPD	Yes	~10^{-19}	~10 ns	98%	[28, 72]

Table 2.2: Comparison table of detectors suitable for use in the mid-infrared. TES is transition edge sensor. MKID is microwave kinetic inductance detector. Figures given for noise equivalent power (NEP) and time constant are on the order of the figure given.
*Metrics depend on the detector used post up conversion. The efficiency for this technique is the conversion efficiency.

high temperature low cost detectors can be deployed but conversion efficiencies are generally poor [86,87] and detection metrics depend on the detector used to detect the up-converted photons.

It is evident that although many types of detector offer the energy sensitivity to allow single-photon detection in the mid-infrared it comes at the cost of temporal resolution, count rate or sensitivity. It is evident that, similar to operation at shorter wavelengths, SNSPDs can potentially offer unrivalled performance characteristics such as jitter, count rate and DCR deep into the mid-infrared.

2.2.1 Why Mid-Infrared?

It is worth considering here the merit of pursuing the extension of SNSPDs into the mid-infrared. In a similar way to 1.55 µm being selected for telecommunications applications due to its low-loss propagation in single mode fibre, mid-infrared light is far better suited to free-space applications such as free-space quantum key distribution (QKD) or space to ground communication. Fig. 2.5 shows a plot of the solar irradiance and atmospheric absorption as a function of wavelength. As can be seen, the atmospheric absorption in the 2-2.5 µm highlighted region is at a minimum and the background solar flux is greatly reduced, three times as low as at 1.55 µm, which results in a reduced background DCR for the detectors - a crucial quality for high quality QKD [90] [91]. Although particularly suited to free-space applications, longer wavelengths are being investigated for use in classical guided communications to avoid the 'capacity crunch' [92]. Low-loss fibres [93] and wide band Thulium based amplifiers and sources [94] have been investigated and it is necessary that detector technology keeps up with these developments. For on chip applications, SiGe waveguides have been shown to achieve 10Gbit/s at 2 µm [95] [96].

Moving away from telecommunications the properties of low absorption and low DCR can

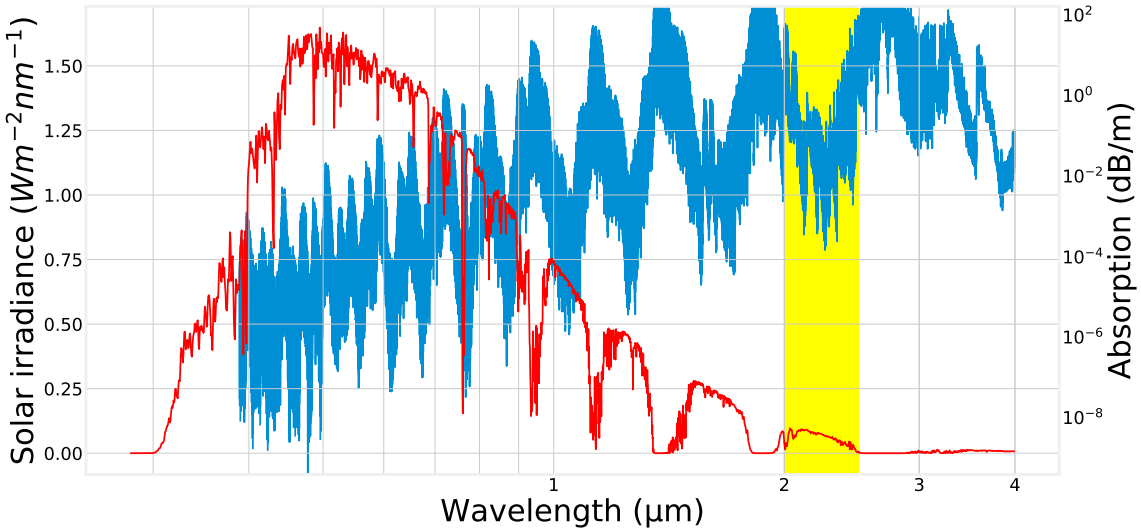

Figure 2.5: Solar irradiance and atmospheric absorption. The solar irradiance is shown in red and corresponds to the left y-axis. The absorption is shown in blue and corresponds to the right y-axis. Solar data from ASTM [88], absorption data from HITRAN [89].

also be exploited for sensing applications such as light detection and ranging (LIDAR), increasing SNR and allowing quick acquisition of target data. The spectral region from 2-5 μm highlighted in is important for remote sensing of pollutants and chemicals with absorption lines within this region. A typical differential absorption LIDAR (DIAL) scheme involves tuning the source on and off the absorption band and the ratios can then be compared and a gas concentration extracted. This necessitates high efficiency detectors for fast acquisition and fast timing jitter for spatial resolution of the gas molecules [97] [98]. Single photon LIDAR in the mid-infrared will be explored in more detail in Ch. 6.

It is clear that the mid-infrared already offers many opportunities in sensing and communications and that there is progress towards optical components to meet these opportunities. Development of MIR SNSPDs will be crucial in many of these applications where their superior detection properties can be utilised.

2.2.2 Challenges of Working in the Mid-Infrared

Although spectral sensitivity into the mid-infrared has been demonstrated [45], it remains an engineering challenge to fabricate detectors that rival the best detection characteristics of detectors at 1.55 μm. This is not overly surprising - as wavelength increases each photon is depositing a lower amount of energy into the superconductor (from $E = hc/\lambda$), decreasing the chance of a detection being registered. The practicalities of testing and deploying mid-infrared detectors should also not be underestimated. Commercial optical components such as variable attenuators,

filters and fibre components are not easily available and expensive when compared to low-cost telecom equipment. The fibre itself also poses a problem. Standard silica fibre gets increasingly lossy above 2 μm and becomes unusable at around 2.3 μm [99]. Alternatives for optical fibre in the mid-infrared fall into one of three categories: fluoride based fibres, chalcogenide based fibres or photonic crystal fibres (PCFs). Fluoride fibres (heavy metal fluoride glasses, HMFG) are commercially available fibres that are commonly either zirconium fluoride (often referred to as ZBLAN) or indium fluoride based. Offering low-loss transmission out to around 5 μm, these fibres are somewhat fragile and are not as resilient to bends as conventional silica fibre [100]. Chalcogenide glasses are a class of glasses that contain one or more of the chalcogen elements (sulphur, selenium and tellurium [101]) that has been used for optical fibres since the 60s [102]. They offer transmission out to 12 μm [103] but similarly to fluoride options suffer from poor mechanical robustness. In recent years efforts have been made in multi-material chalcogenide fibres where the fibre is encased in a polymer jacket, thus increasing the mechanical robustness of the final fibre [104]. PCFs are fibres based on photonic crystals that have the ability to confine light in hollow cores. This means that silica can be used - meaning a more mechanically robust fibre - to guide mid-infrared light [105]. They can be designed for wavelengths in the mid-infrared with low bend-loss but require a more complex fabrication procedure [106] than all-glass fibres. It is clear that solutions exist to the fibre problem but they add a layer of complexity and expense when designing experiments.

With the problems working in the mid-infrared explored above, calibrated measurements of mid-infrared SNSPDs are scarce. Demonstration of sensitivity out to 10 μm wavelength has been shown in uncalibrated measurements very recently [73], building on previous work [45]. Divochiy *et al* reported efficiencies of 15% at 2.3 μm [107] and more recently Zhou *et al* [108] reported 60% at 2 μm. Here at Glasgow a characterisation setup has been developed that allows characterisation of detectors up to 4 μm, which will be explained in detail in Ch. 3.

Designing SNSPDs for the mid-infrared requires some thought. Certain materials offer a smaller superconducting energy gap meaning low-energy mid-infrared photons will create more excited quasiparticles upon absorption. - discussed more in Ch. 3. Beyond this, it is clear that minimising nanowire width increases the probability of the entire nanowire switching and registering a count. This is key for smaller energy mid-infrared photons when the effective hot-spot will be smaller as the deposited energy is smaller. Minimising wire width comes with problems, however, as narrower nanowires are more prone to fabrication imperfections, limiting the fraction of the depairing current that can be reached [109], which will in turn limit the timing jitter and detection efficiency. To avoid current-crowding effects in the bends of the nanowire it is also important to optimise the shape of the bends [110], ensuring rounded edges rather than abrupt corners. This again allows biasing of the nanowire to a high fraction of its

depairing current. To maximise the absorption in the nanowire it is also necessary to design an optical stack for the specific wavelength (or wavelengths) of interest. It is not possible to take a detector optimised for telecom wavelength and expect it to perform well in the mid-infrared.

A novel approach to increasing the efficiency of detectors in the mid-infrared may be to engineer the microstructure and defects in the superconducting film. Zhang *et al* [111] successfully increases the detection efficiency of a NbN SNSPD at 1.55 μm by a factor of 2 (49% to 92%) by irradiation with He ions. While this result was demonstrated in SNSPDs for telecom wavelengths, the results show that the superconducting energy gap in the films was effectively suppressed by the process which holds promise for detectors aimed at longer wavelengths where photon energies are lower.

2.3 Time Correlated Single Photon Counting and Applications

2.3.1 Time Correlated Single Photon Counting

Time correlated single photon counting (TCSPC) is a technique utilised in photon counting applications such as fluorescence lifetime measurements [112], time-of-flight imaging [113] and quantum optics demonstrations [114]. It is used extensively throughout this thesis for characterisation of timing jitter and single-photon LIDAR experiments so in this section I will set out the principles and practicalities of the technique.

Overview

TCSPC takes a periodic light source, such as a pulsed laser, and measures the time from the periodic source firing to the detection of photons by a detector. In this way the time between the initial pulse (commonly referred to as the excitation pulse due to TCSPC's roots in fluorescence lifetime measurements) and the photons being detected can be measured with sub-ps resolution. Over time a histogram of photon arrival times is built up and the characteristics of the distribution can provide information about the detector being used. For example, in this thesis, the timing histogram is often used to determine the timing jitter of devices presented. A diagram of the TCSPC process is shown in Fig. 2.6. As is seen in the figure a histogram is built up over many pulses and the precise arrival time of the photons in relation to the excitation pulse can be obtained. TCSPC covers a large dynamic range and is not limited by the detector linearity [115]. Time bin width can be as low as 203 fs with modern TCSPC cards and this is invaluable when probing the fundamental limits of SNSPD timing resolution.

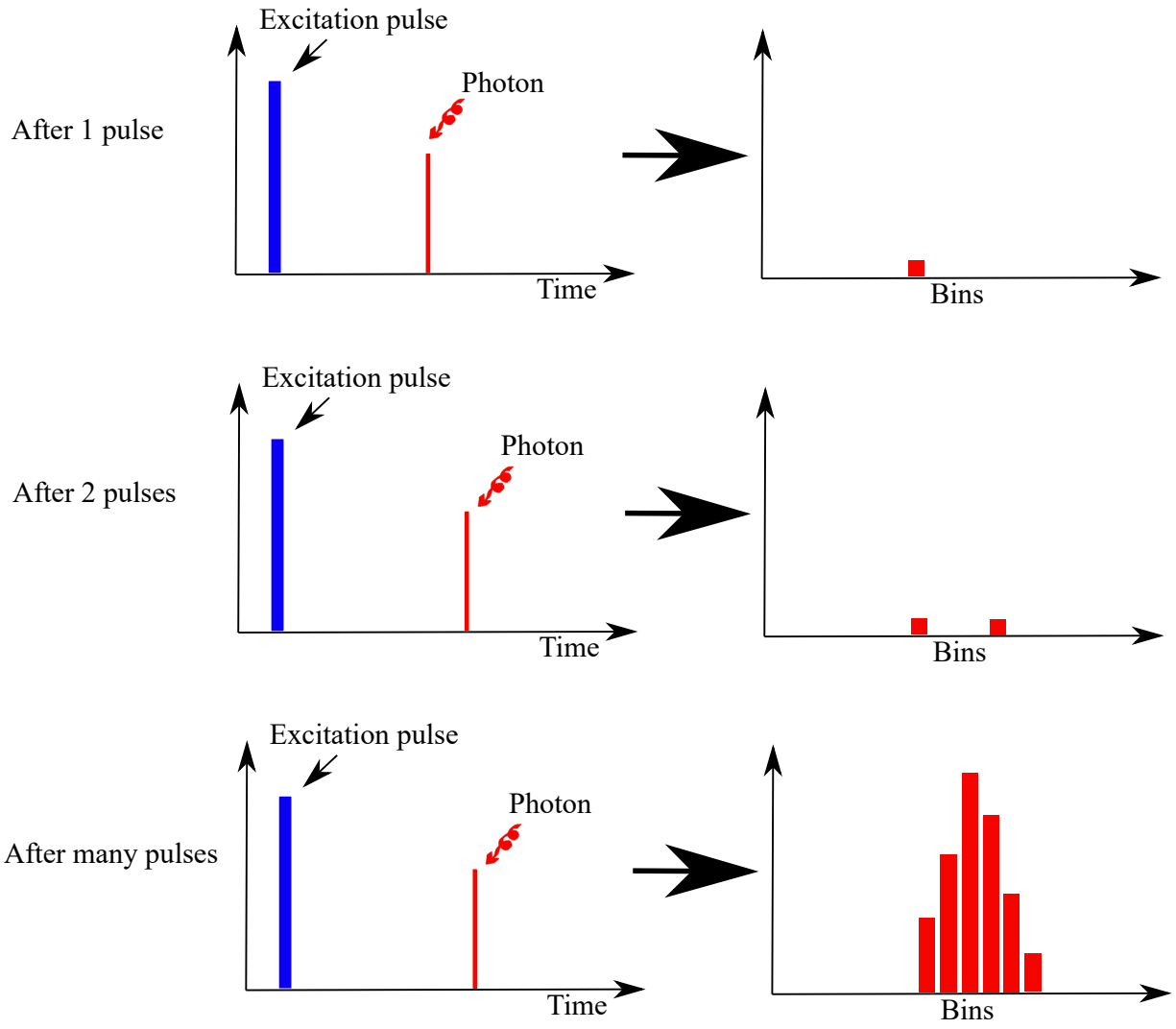

Figure 2.6: Overview of the TCSPC process. Starting at the top a photon is recorded some time, t, after the periodic excitation (or sync) pulse. This causes a count to be registered in the timing bin associated with t. A second pulse is then recorded in the next excitation pulse and a second count is registered in the timing histogram. As more photon events are recorded a histogram is built up as is shown in the bottom of the figure.

Implementation

To implement the TCSPC technique a suitable timing card must first be chosen. In the labs in Glasgow there are options from the PicoQuant HydraHarp [116] range which offer multiple channels (up to 4), an easy-to-use interface and a timing bin resolution down to 1 ps. There is also a high-end offering from Becker and Hickl [117] offering single-channel timing bin resolution down to 203 fs. Both ranges have their merits and it is application dependent which is chosen. A sync signal (excitation pulse) is required and this is typically provided by the laser either in the form of an electrical sync pulse or by splitting the laser optical output and sending a portion to a fast photodetector which then provides the electrical pulse. The signals are attenuated and inverted if required and sent to the timing cards. The signal is detected by the card using a constant fraction discriminator (CFD - note some TCSPC cards only use a CFD on the input channel not the sync channel where they employ a simple threshold detector instead). The CFD triggers on a constant fraction of the pulses height which removes the effects of amplitude jitter of the signal. The optical pulse is detected by the experiment detector (SNSPD in this case) and the output signal follows a similar signal path and is detected by a separate CFD. The outputs from the CFDs are then fed into a time-to-amplitude converter (TAC) which can be thought of as a voltage ramp that is started when the first pulse comes in and stopped when the second. As the ramp rate is known the time between the start and stop events can be determined from the voltage output. In low photon flux experiments there will often be times when there are no detected photons in a particular sync period (before another sync pulse is received) . To account for this a reverse-start-stop configuration is used. In this scheme the TAC is started when a photon is detected and then stopped when the next sync pulse is received. In this way the time can be determined without continuously starting the TAC for every sync pulse (often high repetition rates) and only when a photon is actually detected. The one caveat of this technique is that the sync signal must be periodic and free of its own jitter in order to accurately determine the arrival time of the photon relative to its own sync pulse. Amplifiers may then be employed to select a portion of the TACs range and improve the resolution at the expense of the total time range.

2.3.2 Single Photon Light Detection and Ranging

In recent years, light detection and ranging (LIDAR) has matured as a powerful technique in imaging and sensing applications. Through this technique high resolution depth images can be reconstructed at ranges of many tens of kilometres. In this section, the concept of single-photon LIDAR experiments and how SNSPDs can be utilised in such experiments to leverage their excellent detection characteristics is outlined.

Time-of-flight LIDAR

Time-of-flight LIDAR is an elegant technique where a pulsed laser source is used to send light pulses to be reflected from the target. A start signal (or sync) is triggered when the laser pulse leaves the laser and a stop signal is recoded when the returns trigger the detector. With basic calculation the range of the target can be determined:

$$d = \frac{c\Delta t}{2} \tag{2.12}$$

where d is the distance, c is the speed of light and Δt is the time difference between the sync and return pulse. Depending on the repetition rate (RR) of the laser, the absolute range may be difficult to determine due to the laser emitting a second (or more) output pulse before the returns have been collected. This range ambiguity can be solved by a variety of methods including reducing the repetition rate of the laser, determining the approximate distance of the target in a different way, transmitting a non-periodic pulse train [118] or encoding the output pulses with micropulses [119]. However, if a depth image is desired without an unambiguous total range then the laser RR governs the largest separation between targets - or the maximum depth resolution - that can be obtained unambiguously. A plot of laser RR against maximum depth resolution is shown in Fig. 2.7. As can be seen in the figure, a good spread of targets can be profiled in depth with a reasonably fast RR (20 MHz giving 8 metres). By scanning the optical beam over the target high resolution three dimensional images or depth profiles [120] can be easily built up . A diagram of the process is shown in Fig. 2.8 As is shown, this is a fairly basic process however steps can be taken to optimise the system for long-range depth measurements. As can be seen in Fig. 2.8 there are two main parts of a LIDAR setup; the optical system (scanning or otherwise) and the detector system. The optical system must focus the beam on to the target and collect returns from it. The system can be monostatic [121] which is advantageous for building compact systems or bistatic [122] which is popular in LIDAR design for atmospheric measurement [123]. Scanning can be controlled mechanically such as the galvanometer mirrors shown in [121] or, more recently, electronically with phased arrays [124]. The desirable characteristics of the optical system are fast scan rate and low-loss transmission of the transmit and receive beam.

The detector system is the second main part of a LIDAR setup. The distinction must be made here between standard LIDAR and single-photon LIDAR. As the name implies, single-photon LIDAR systems must be sensitive to single photons of light which offers some advantages to LIDAR systems. For mapping and imaging applications, the use of single-photon LIDAR affords much better sensitivity and the ability to create images from photon-sparse returns [125]. For a given laser output power, the range of the system is effectively maximised by using single-photon detectors as the optical power in the returned pulse will diminish as $1/R^2$, R being the distance. The ability to detect such small returns also allow for detection of targets obscured

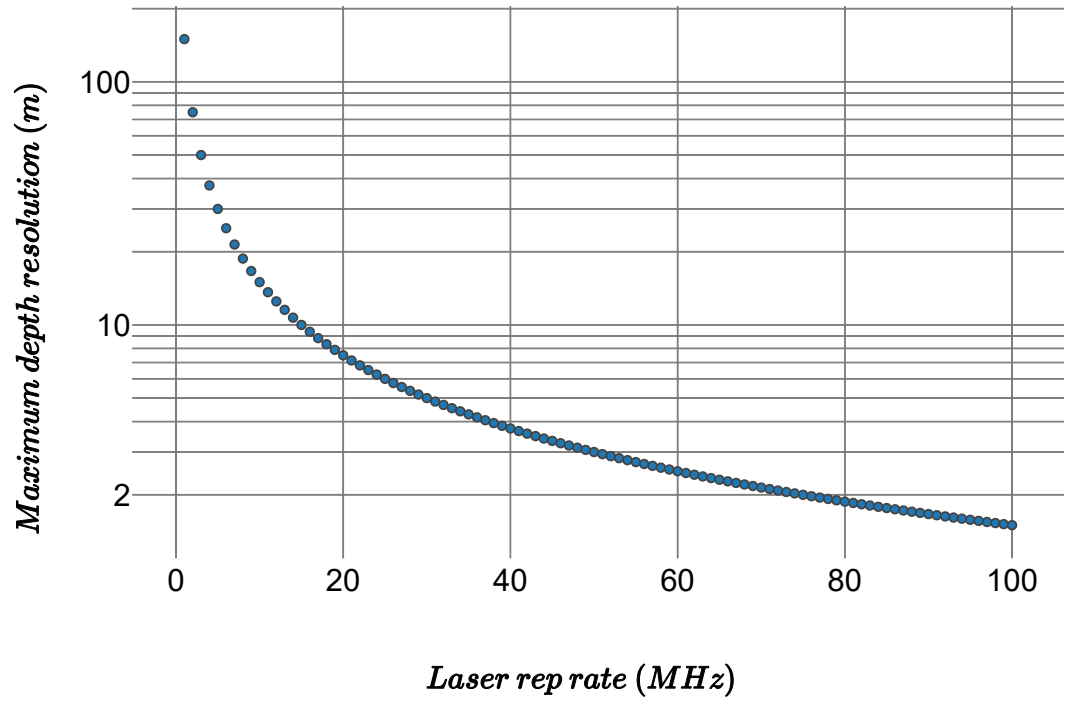

Figure 2.7: Maximum depth resolution against laser repetition rate

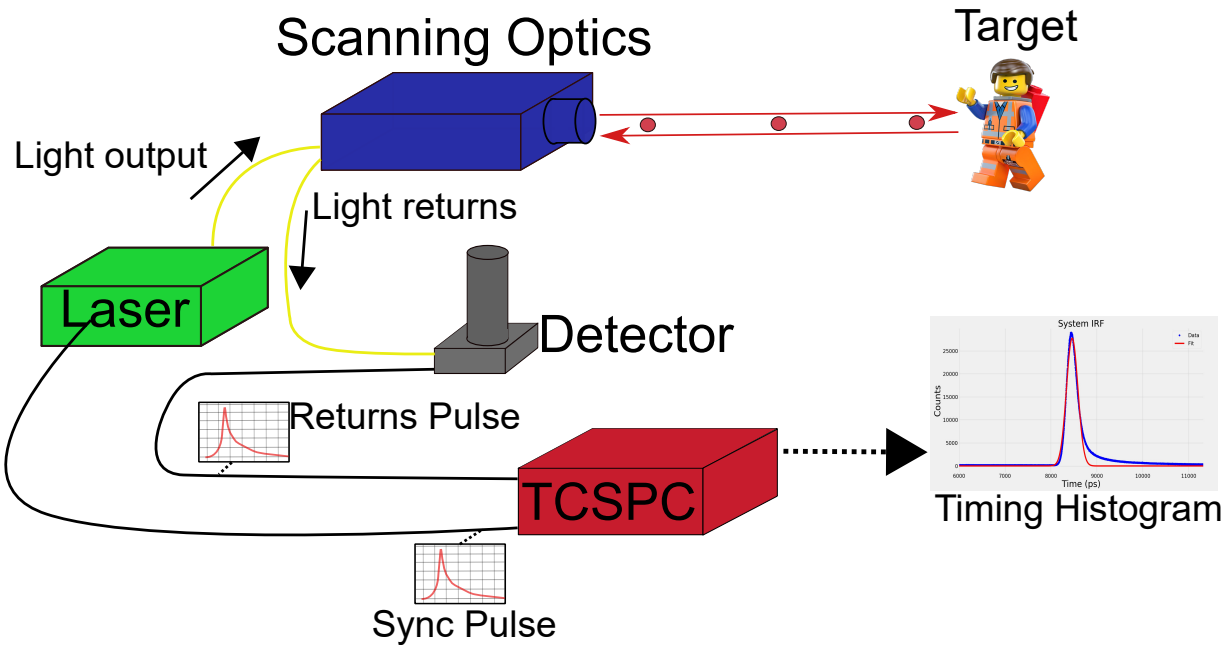

Figure 2.8: An example of a time-of-flight LIDAR setup. Fibre connections are shown in yellow, RF connections in black. TCSPC is the time correlated single photon counter.

by clutter [126] or in challenging environments such as underwater imaging [127]. Due to their sensitivity, single-photon LIDAR systems can also be operated at eye-safe and covert power levels. Herein any discussion on LIDAR will be about single-photon LIDAR unless specifically stated. LIDAR requires fast timing electronics to resolve small ($\sim$ ps) differences in returns - time correlated single photon counting modules (TCSPC) offer ps resolution time stamping of photon counts and are ideal for LIDAR applications. The variety of single-photon detectors available has been discussed earlier in this chapter so here the characteristics that are advantageous to LIDAR applications will be explored in more depth.

Signal-to-noise ratio (SNR) is a key parameter when considering detectors for LIDAR [128]. The SNR can be written in terms of the number of photon counts in the returns peak, η_p and the mean number of background counts, η_b as:

$$SNR = \frac{\eta_p}{\sqrt{\eta_p + \eta_b}} \tag{2.13}$$

which implies that a reduction in background counts, η_b will result in an improvement in the SNR as will an increase in the number of counts in the peak, η_p. As shown earlier in this thesis, SNSPDs exhibit extremely low intrinsic dark counts making them suitable for use here. The other term that contributes to background counts is ambient light photons coupling to the detector. One obvious solution is to operate these LIDAR systems at night where the background flux is much lower and improved images can be obtained [129]. Another approach is to carefully select the working wavelength of the system to minimise solar background flux - the solar flux can be modelled as a blackbody at 5778 K, see Fig. 2.3, so exhibits a peak emission at around 500 nm wavelength then tails off. This will be explored more in Ch. 6. An obvious approach in order to maximise the SNR is also to have a high detection efficiency detector so that the maximum number of returned photons can be converted into counts, η_p, and increase the SNR.

The uncertainty in the timing bin of a returned photon, σ_p , follows Poisson statistics as:

$$\sigma_p = \frac{\Delta t}{\sqrt{N}} \tag{2.14}$$

Where Δt is the timing jitter of the system and N is the number of counts. In real terms the number of counts for a fixed laser power is proportional to the integration time, t_{int} so it is possible to say that:

$$\sigma_p \propto \frac{\Delta t}{\sqrt{t_{int}}} \tag{2.15}$$

Hence, a reduction in timing jitter of the system will result in a quadratic reduction in integration time for a given time bin error. This means that selecting low jitter detectors is an important consideration for fast scanning LIDAR where reduction in integration time means faster image

acquisition.

Building a Depth Image

Typically in photon counting LIDAR based on TCSPC the data is a histogram of photon returns which shows the spread in time of the photon returns relative to the sync signal in one integration period. The width of this histogram is dictated by the timing jitter of the detector system. Although often it is possible to reconstruct an image using the return intensity of each pixel, if a depth image is desired it is necessary to accurately determine the peak position of each histogram so an image can be reconstructed based on the differences in peak position. Some basic techniques will now be examined as well as outlining some more advanced algorithms.

As shown in Ch. 2 the instrument response function of a typical SNSPD is an exponentially modified Gaussian (EMG). A simple approach to peak finding would be to fit each returned histogram with an EMG function and then determine the peak position from the resulting fit parameters. This technique is shown to good effect in [39, 130] and provides a good estimation of the depth if the SNR is fairly high and the fitting can be easily obtained through a least squares method or similar. For large images, however, this is a slow process on a moderately powered PC and in noisy data the fitting parameters may be difficult to obtain accurately. An alternative technique is cross-correlation of the returns histogram with the IRF of the detector. Cross-correlation measures the similarity of two functions as a function of the movement of one of them. It can be thought of as taking the ideal response of the detector system - the IRF - which has been taken over a long integration period in clean conditions to maximise the SNR and sliding it along the x-axis (time) of the return histogram giving a measure of the similarity of the signals as a function of the slide. Mathematically, for discrete functions f and g, it is:

$$(f \star g)(n) = \sum_{m=-\infty}^{\infty} \bar{f}(m) g(m+n) \tag{2.16}$$

where $\bar{f}$ is complex conjugate of the function f and n is the time shift applied. Computationally it is faster to utilise the correlation theorem and the above becomes:

$$(f \star g) = \mathscr{F}^{-1}[\mathscr{F}\{f(m)\}(\mathscr{F}\{g(m)\})^*] \tag{2.17}$$

where $\mathscr{F}$ denotes the Fourier transform and $\mathscr{F}^*$ is the complex conjugate of the Fourier transform. Once the cross-correlation has been computed its maximum value is ascertained and used as the peak position. As the peak moves around for each pixel the maximum of the cross-correlation will be at a different time shift and so the depth image can be reconstructed. This technique is robust and fast and has been used in numerous LIDAR demonstrations in various forms [131] [132] [125].

Advanced Algorithms

Cross-correlation is a useful tool when looking to build fast and high quality images but it typically returns a single peak per pixel and is unsuitable if there are multiple peaks in the return. It will also fail in high-noise situations when the SNR is poor. Two more complex methods that address one or both of these issues are maximum likelihood estimation (MLE) techniques and reversible jump Markov chain Monte Carlo (RJMCMC) techniques. MLE [133] is a parameter estimation method that can be used in LIDAR to detect multiple returns peaks in a single histogram. The basis of the technique is to fit a model to the data and compute the parameters that maximise the likelihood that those parameters give rise to the observed data. Wallace *et al* [134] demonstrated a TCSPC LIDAR system which utilised a 'bump-hunting' process to determine approximate peak locations and then applied MLE to determine the parameters that best explained those peaks (BH-MLE). Once the maximum likelihoods are calculated the probable number, position and amplitude of the peaks can be determined. This technique gave good results but was prone to failure when the background noise obscured the returns peaks. Hernandez-Marin *et al* [135] developed a technique based on RJMCMC that addressed these issues. RJMCMC [136] is a Bayesian technique that sequentially generates random samples of a proposed distribution (or model) to explore the distribution space and approximate the parameters of the distribution in question. The reversible-jump component indicates that this is performed over a set of sub-spaces of different dimensions where space-jumping is permitted. In [135], the RJMCMC methods are applied to LIDAR returns to estimate the return peaks by altering the positions, amplitudes and background level as well as allowing the random birth/death and splitting/merging of peaks. A comparison to the BH-MLE technique is demonstrated in the paper where the RJMCMC method obtains far better peak detection in noisy data than the BH-MLE.

Algorithm development for LIDAR is an active field with incremental gains and novel techniques being reported every year [137] [138]. From a detector perspective, clean data - large SNR and narrow IRF - lessens the workload by the algorithm and will allow faster image processing.

Chapter 3

Experimental Methods

In this chapter I outline the methods used throughout this thesis to fabricate SNSPDs and perform experiments. Devices in this thesis were fabricated in the James Watt Nanofabrication Centre (JWNC) here at the University of Glasgow by members of the research group - Dr Dmitry Morozov and Dr Kleanthis Erotokritou - with support from our collaborators at the National Institute of Communciations Technology, Japan and Argonne National Laboratory, USA. For the ultra-low jitter LIDAR experiments at 1550 nm outlined in Ch. 6 the devices were fabricated at the Jet Propulsion Lab, USA, by our collaborators with additional support from colleagues at the Massachusetts Institute of Technology, USA. Although devices were not fabricated personally by the author it is helpful to explain the basic methods used for the fabrication here.

3.1 Fabrication

Fabrication of SNSPDs is a multi-stage nanoscale process that requires precise control of fabrication parameters. In this section the fabrication procedure will be shown and some of the design considerations that must be tailored to the application will be explored.

3.1.1 Design

When fabricating an SNSPD device it is necessary to consider the key parameters of efficiency, count rate, dark count rate, temporal jitter and wavelength of interest. Depending on the application it might be necessary to trade off certain performance aspects for improvements elsewhere in order to meet application-specific goals. The first step in SNSPD fabrication is device design and material selection.

Selection of an appropriate superconducting material plays a large part in the characteristics of the final device. If a comparison of various materials with promising superconducting properties is looked at, stark differences are observed. This data is summarised in Table 3.1. If the most

Material	NbN	WSi	MoSi	MoGe	WRe
Bulk T_c(K)	16	5	7.5	7.36	8.5
Thin-film T_c(K)	8.6 (3 nm)	3.7 (4.5 nm)	4.5 (6 nm)	4.5 (6.2 nm)	4.1 (5 nm)
Bulk energy gap (meV)	4.9	1.52	2.28	2.2	2.58

Table 3.1: Comparison of superconducting material properties. Data from [75]

frequently used crystalline material, niobium nitride (NbN), is examined and compared to the amorphous material tungsten silicide (WSi), which has been successfully used to fabricate some of the most efficient detectors seen to date at 1550nm [29], then it is evident that the T_c of WSi is far smaller than NbN both in bulk and thin film form which will place more stringent cooling requirements on the experimental setup. On the other hand the energy gap is significantly smaller for WSi which has implications for operating detectors at longer wavelengths where photons have less energy. Other materials presented are good candidate materials for SNSPDs as they exhibit higher critical temperatures than WSi but an energy gap lower than NbN. Critical current density is an important parameter in device design - leading to higher amplitude output pulses and improved SNR. Although affected by many other factors including nanowire width and operating temperature it is clear that in comparably measured devices MoSi and MoGe show higher critical current densities than the other amorphous materials explored here and as such show good promise as detector materials. [75]. An interesting recent study by Banerjee *et al* [139] compares a host of refractory metal based thin films and results indicate that MoSi and TiN show increased absorption at longer wavelengths when compared to NbN, adding further evidence that these materials may make good candidates for mid-infrared single photon detectors.

Once a suitable material has been selected the next item to be addressed is the geometry of the active area of the device - the nanowire. A basic meander detector is shown in Fig. 3.1 - the extended and rounded corners are to minimise current crowding effects. A basic meander increases overall device active area to make precise optical coupling easier but it is important to optimise the geometry of the nanowire. By manipulating the film thickness, wire width and fill factor it is possible to influence the critical temperature, current density and absorption as desired [140] [52]. As mentioned earlier there have been various attempts at novel nanowire geometries including n-SNAP geometries [141] [142] and novel micron wide NbN bridges [143] which often improve certain parameters of the device at the expense of others.

In order to increase absorption of specific wavelengths in the device it is possible to fabricate on chip waveguides [144] [145], optical antenna [146] and optical cavities [147]. All of the best results in terms of overall system detection efficiency have been achieved with integrated optical cavities or distributed Bragg reflector (see Ch. 5) type designs, including the benchmark 98% at 1550 nm [28]. The method to fabricate such devices varies depending on the exact optical

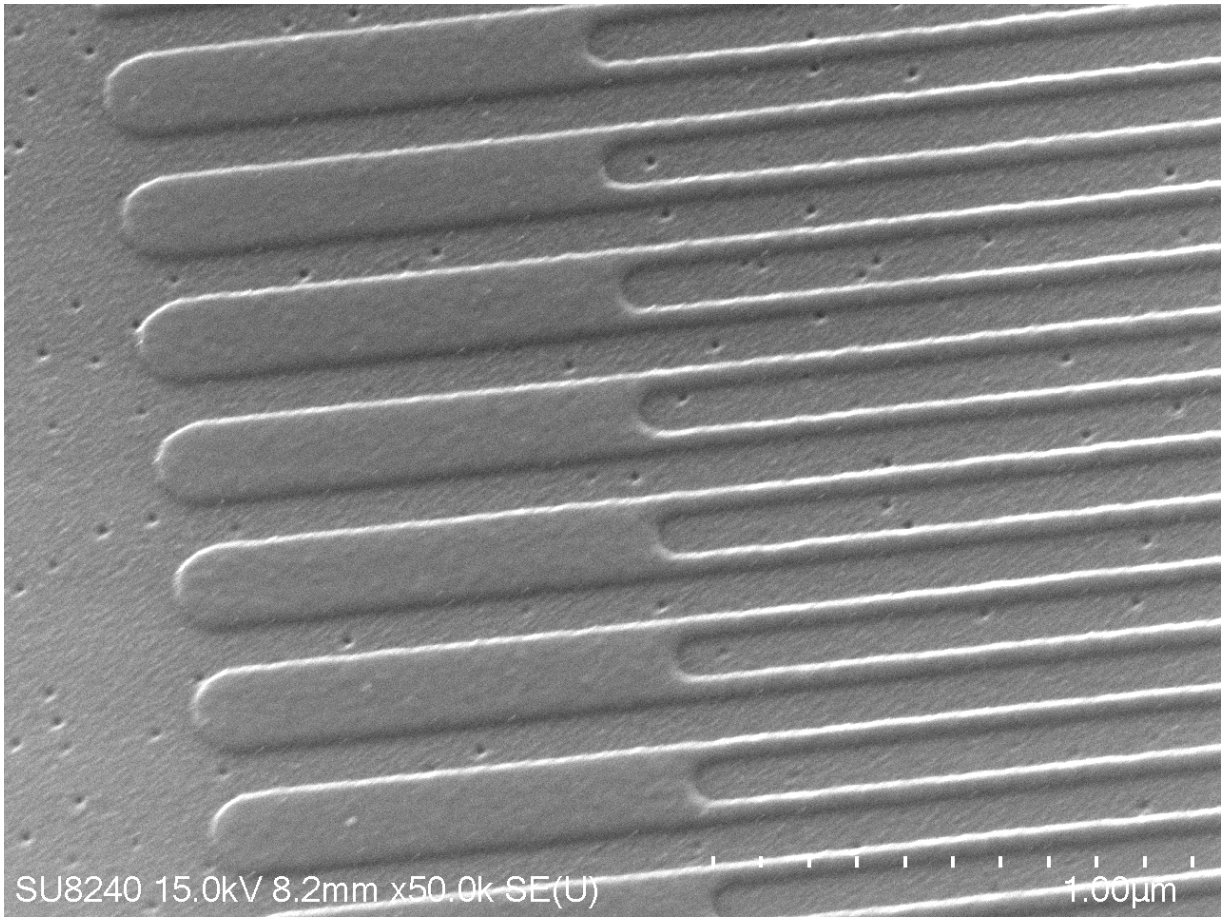

Figure 3.1: SEM image of an example meandering nanowire. Courtesy of Dr Dmitry Morozov, University of Glasgow.

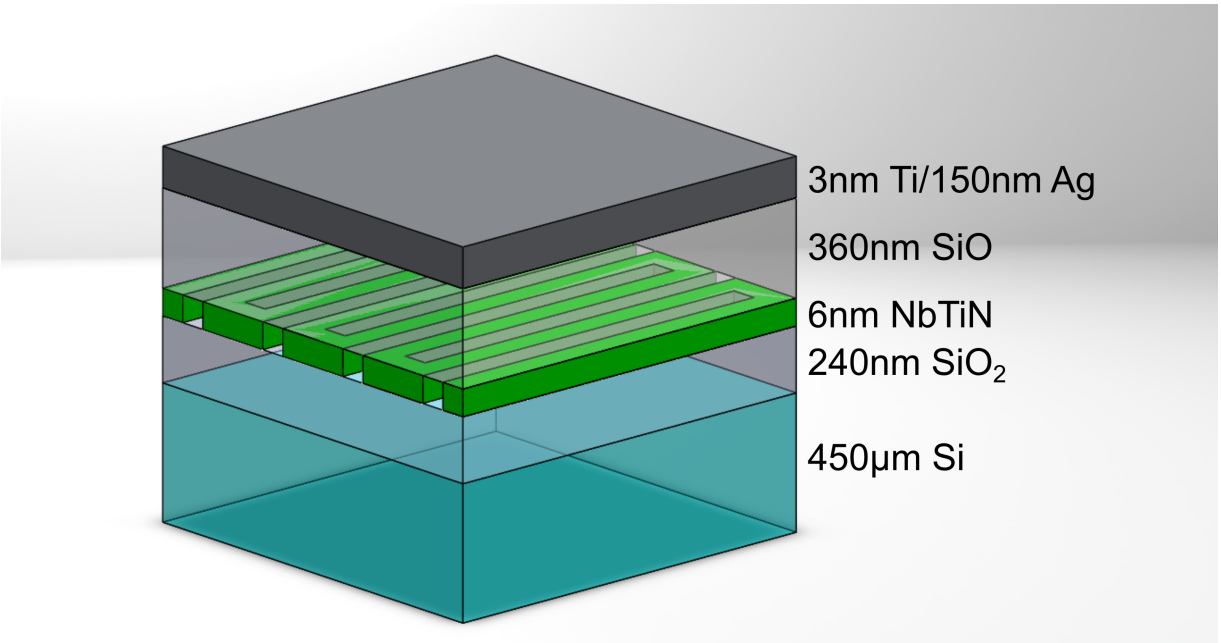

Figure 3.2: Example of a cavity structure. The photons are incident from the bottom of the figure through the substrate (blue). The nanowire (green) is embedded in a dielectric stack and capped with a mirror on top (dark grey). An alternative is to embed the mirror in the stack on top of the substrate and illuminate from the top, effectively reversing the stack shown here.

enhancement chosen but for an integrated optical cavity, an optical stack is fabricated from dielectric materials with the nanowire sandwiched in between. This is capped with a mirror. An anti reflection coating can be applied to the illumination side of the device also. An example of an optical cavity type SNSPD is shown in Fig. 3.2. Experimental results have shown almost 100% absorptance measurements with integration of such optical cavities. [148]

3.1.2 Film growth

Superconducting thin films are grown on substrate materials here at the University of Glasgow James Watt Nanofabrication Centre (JWNC), using either an ultra-high vacuum sputter system (Plassys Bestek) or an atomic layer deposition (ALD) system (Oxford Instruments Plasma Technology). DC magnetron sputter deposition is the most common method and involves bombarding a target material with gas ions in order to eject particles from that target material. Ejected particles are accelerated towards a substrate where they are deposited. Thin films can be sputtered from an alloy target or co-sputtered using two metallic targets. A diagram of the sputtering procedure is shown in Fig. 3.3. During sputtering it is important to optimise the process parameters to achieve the desired properties from the film. Several studies have been done into optimisation of the sputtering parameters to achieve films suitable for SNSPD fabrication [149, 150].

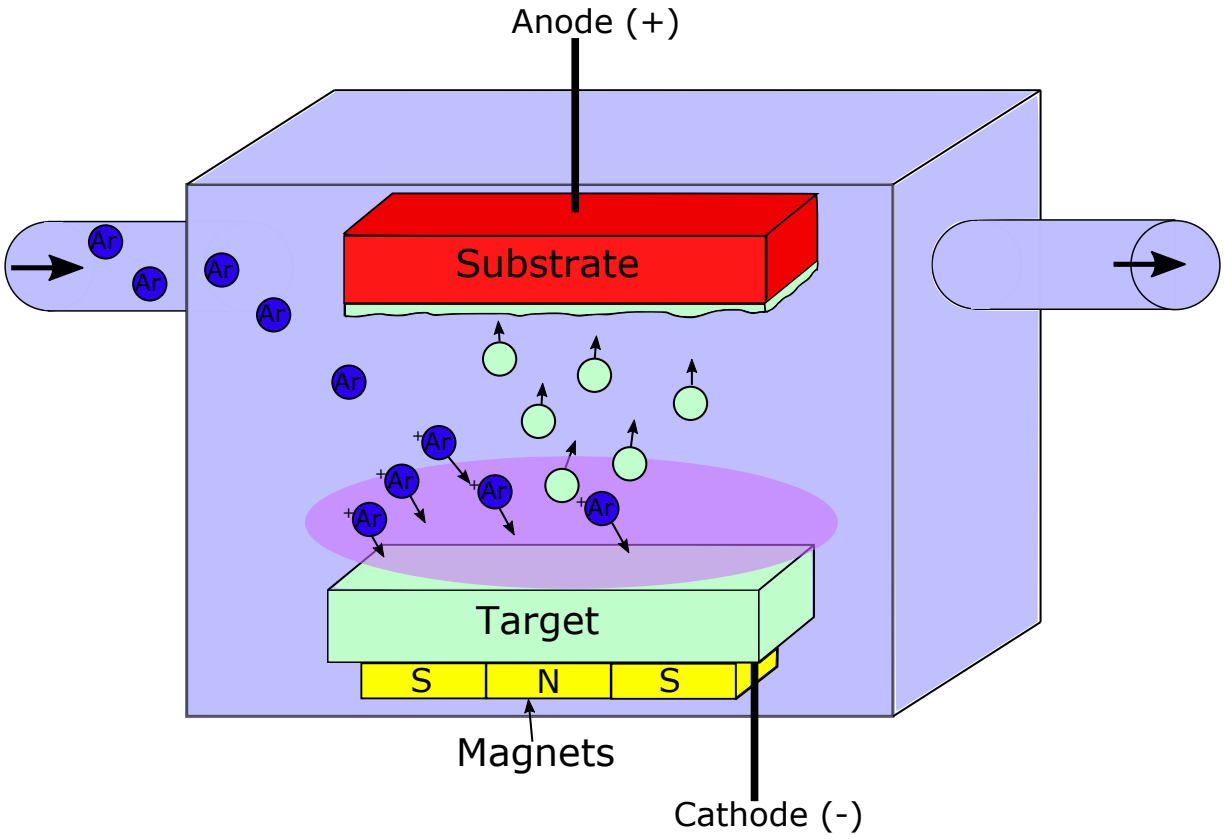

Figure 3.3: The DC magnetron sputtering setup is shown here. The magnets confine the plasma (purple) on the target. Gas enters from the left and is ionised in the centre. Ions are accelerated towards the cathode and target atoms are ejected. These are then redeposited on the substrate. The gas used to sputter can be inert such as the Ar in the diagram if no reaction is desired or mixed with a reactive species if a reaction is required, for example nitrogen gas, N_2, to achieve nitride.

An emerging technique for thin film growth of superconducting materials is atomic layer deposition (ALD) [151]. The basic process of this technique is a substrate is sequentially exposed to two chemicals (or precursors). The reaction is set up in such a way that the first precursor is introduced and will react until all of the reactant sites on the substrate have been used up - i.e it is self-limited. This precursor is then removed from the system and the second precursor introduced. After one cycle (two precursor introductions and flushes) a thin film one layer thick is left. The process can then be repeated until the desired film thickness is achieved. Through this technique precise thickness control and films that are very smooth and conformal [152] can be achieved. Recent work on superconducting thin films for detectors made from NbN [153] and TiN [79] show promise but more work is needed to assess their detection properties when compared to the sputter-deposited equivalents. Ch. 4 of this thesis explores this technique in more detail.

3.1.3 Electron Beam Lithography

Electron Beam Lithography (EBL) is the process used, once a suitable film has been found, to define the features of the device. This usually involves several stages which must be optimised and kept consistent to allow repeatable device characteristics to remain over several fabrication runs. The first stage is to spin a polymer 'resist' onto the bare film. This resist is a electron-sensitive polymer that is applied onto the film using a spinner. Split into two categories, positive resists where the areas of exposure will be removed during development and negative resist where the exposed areas will remain after development. There are many different types of resists including hydrogen silsesquioxane (HSQ), polymethylmethacrylate (PMMA) and ZEP which must be selected based on many factors including desired feature size, line edge roughness and required etch resistance [154]. Once a suitable resist polymer has been chosen it is mixed with a solvent to the desired solution strength and then spun onto the substrate to a specific thickness - controlled by the spin speed and time as well as the dilution strength. It is then baked in an oven or hotplate to remove the solvent and leave a layer of resist on top of the superconducting film. This can then be sent to the Vistec VB6 electron beam lithography machine housed in the JWNC (Note: this machine was upgraded to a Raith EPG system in 2019) to write the designated pattern. This unit works by accelerating a beam of electrons into the resist which causes cross-linked bonds within the polymer to form (for negative resists) or break (positive resists). Care must be taken when selecting EBL parameters to take account for the proximity effect - the effect of beam broadening due to unwanted electron scattering resulting in reduced pattern fidelity [155]. There are multiple approaches to proximity effect correction that have been developed [156, 157]. Following the EBL exposure, the sample is immersed in a developer solution specific to the resist polymer which will cause un-crosslinked bonds to dissolve, leaving the desired pattern.

Depending what the pattern is will determine what happens next. If the pattern is for metallised contact pads then a layer of the desired metal will be deposited onto the sample. Then by removing the resist using solvent in a 'lift off' process a layer of metal in the desired pattern that was written by the e-beam machine is left. A diagram of this process is shown for patterning and depositing metallic patterns in Fig. 3.4. If etching of a nanowire into the superconducting film is desired then a process known as Reactive Ion Etching (RIE) will be used which involves creating a plasma and then accelerating it towards the sample, etching away the superconducting film but not the areas covered with resist. A diagram of this process is shown in Fig. 3.5. RIE can be implemented with various gases depending on the target material [158]. Usually when fabricating a device it will be necessary to run the above process multiple times, depending on the complexity of the device. For clarity the steps of fabrication for a simple meander type device with gold electrical contact pads is outlined below.

- A electron beam resist polymer is spun onto the superconducting thin film and then baked. It is possible to implement a dual layer of resist for more sharply defined edges during the

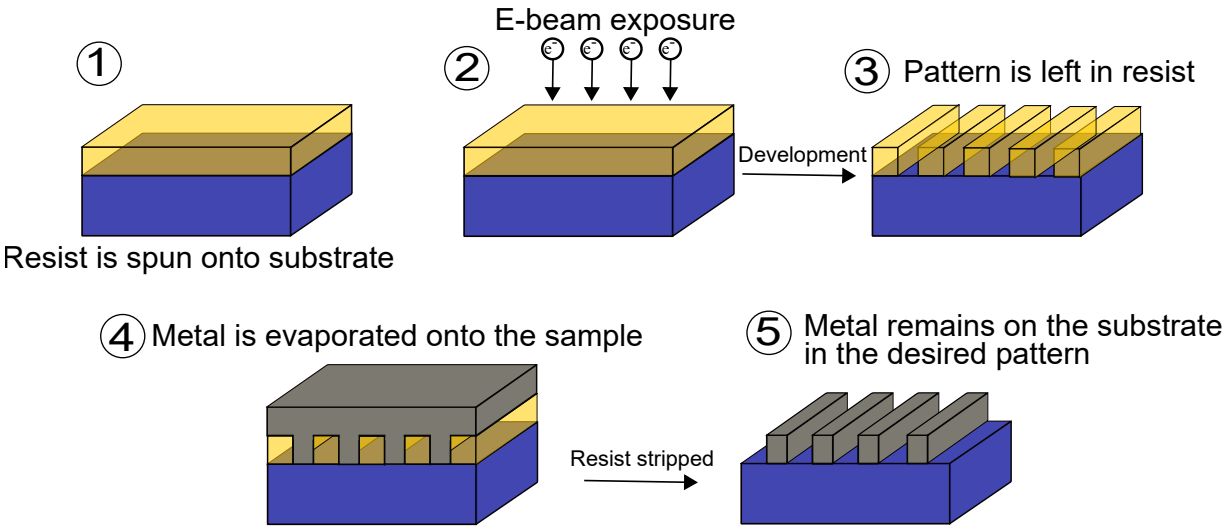

Figure 3.4: Process diagram showing the writing of a pattern using electron beam lithography. This shows deposition of metallic contacts in a desired pattern. This is the typical method for adding alignment markers and contact pads on a SNSPD device chip

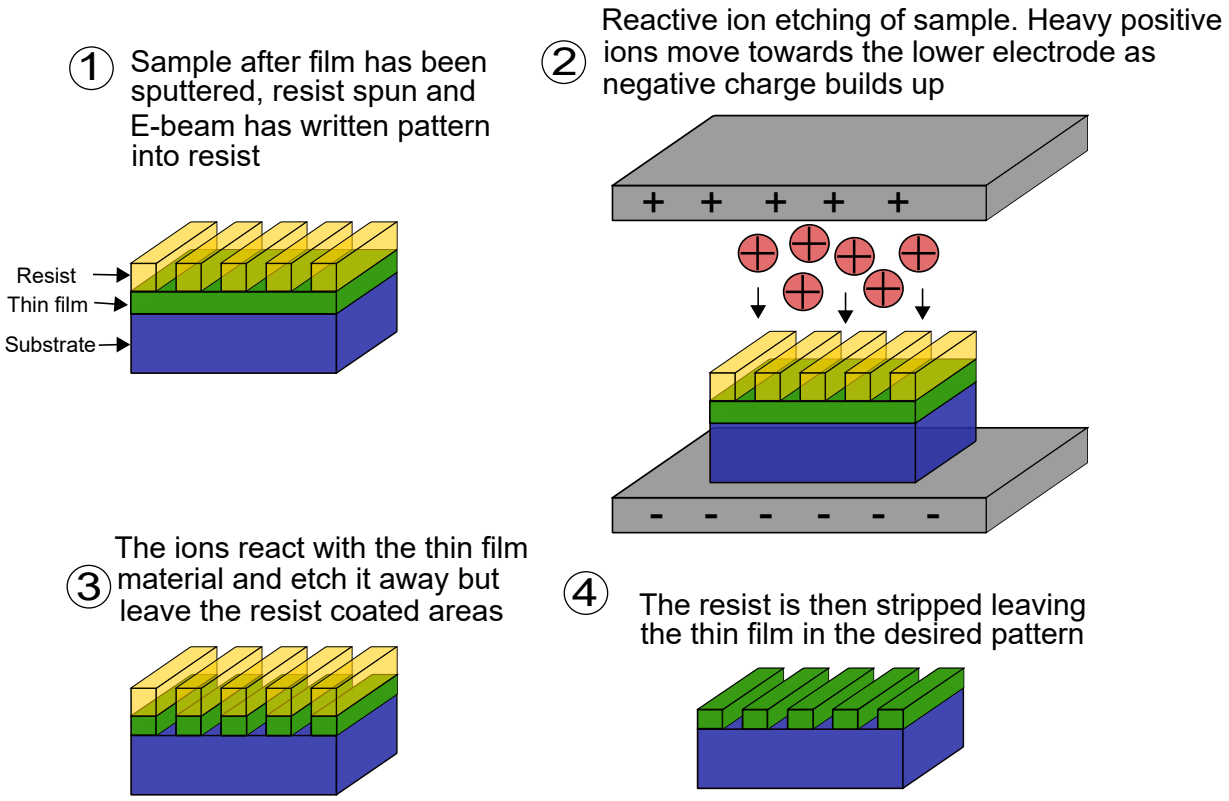

Figure 3.5: Process diagram showing the etching of a pattern into a thin film.This is the typical method for defining the meander nanowire for a SNSPD device

subsequent lift off process.

- The VB6 writes the pattern for the contact pads and alignment markers - these are important when aligning multiple stages of e-beam patterns.
- The resist is developed to remove exposed areas (for positive resist).
- A metallic layer of gold is evaporated onto the sample.
- The resist is then stripped, leaving a layer of gold in the appropriate places.
- A electron beam resist polymer is spun onto the superconducting thin film and then baked.
- The VB6 writes the pattern for the nanowire meander.
- The resist is again developed.
- RIE is used to etch away the nanowire.
- Remaining resist is stripped.

Of course, through all fabrication steps it is necessary to tune recipes to obtain desired parameters - resist thickness, etch rate, pattern resolution to name a few. It is imperative that once tuned these are kept as constant as possible to ensure even fabrication throughout runs. Fabrication imperfections - particularly in structures with nanometre dimensions - can have large effects on device performance.

3.1.4 Device Uniformity

As mentioned above, device uniformity is critical when fabricating high performance detectors. Variations along the length of the nanowire in all dimensions result in variation of the current density and detection characteristics are therefore spatially-dependent. If the theory in [42] is examined the authors show that the width of the transition of the photon counting behaviour against bias current differ from the ideal step function due to a combination of Fano fluctuations and spatial inhomogeneities. For a particular wavelength photon, λ, the detection current, I_{det}, can be defined as the current required to trigger a detection for the photon energy, $E = hc/\lambda$. This is a fraction of the depairing current, I_{dep}, defined as the current at which the kinetic energy of the charge carriers exceeds the binding energy of the Cooper pairs [17]. As the bias of the nanowire is increased it should get to a theoretical point where the bias current, $I_{\text{bias}} > I_{\text{det}}$ and the detection efficiency should jump from zero to its maximum instantaneously. This of course is ideal and as seen in the work by Kozorezov *et al* [42] there is a sigmoidal shape to the transition even in the absence of inhomogeneities. Nanowire imperfections introduce position-dependent bias currents which makes the transition broader and in some cases can suppress the ability to

bias the nanowire sufficiently enough to achieve saturated detection efficiency. Frasca *et al* [109] developed a method to determine the depairing current for each geometry and film used in each fabrication run and propose that the ratio of switching to depairing currents, $C = I_{sw}/I_{dep}$, is a more useful metric than critical current alone when determining device performance as it gives a measure of the quality of the nanowire. Maximising C will ensure good nanowire quality which will make it easier to bias at $>I_{det}$ across the entire nanowire ensuring saturated detection efficiency and minimimal timing jitter.

3.2 Optical Coupling of SNSPDs

Once fabrication has been completed the devices must be mounted and coupled both electrically and optically. The devices are first glued to a copper sample holder using low-temperature GE varnish - care is taken to ensure good thermal contact - and then wirebonded to an SMP connector. The device is then fibre coupled with a fibre appropriate for the working wavelength of the device. Devices are either illuminated from the top of the nanowire (frontside-coupled) or through the substrate (backside-coupled). Depending on which design is chosen the fibre is either offered up to the top or bottom of the device. A suitable fibre is either screwed or glued - depending on the fibre design - into a copper holding piece and aligned with the active area of the detector. This is achieved with a 1.55 μm laser illuminating the detector through the fibre. By using an InGaAs camera above the detector the position of the spot of light output from the fibre can be determined with respect to the active area. Using an X-Y micrometre stage the fibre ferrule is then moved until the spot lines up with the active area of the device. Shims can be added to the fibre holding piece to adjust the separation between the ferrule and the device to optimise the coupling. A diagram of this process is shown in Fig. 3.6 and an image of an example aligned device is shown in Fig. 3.7. Once aligned the fibre is fixed in place and the device is ready to be used. The above diagrams and explanation show a backside-coupled device being aligned. For a frontside-coupled device the process is very similar but the sample mount is inverted in the alignment setup so that the fibre is brought close to the top of the device and the spot is viewed from the bottom.

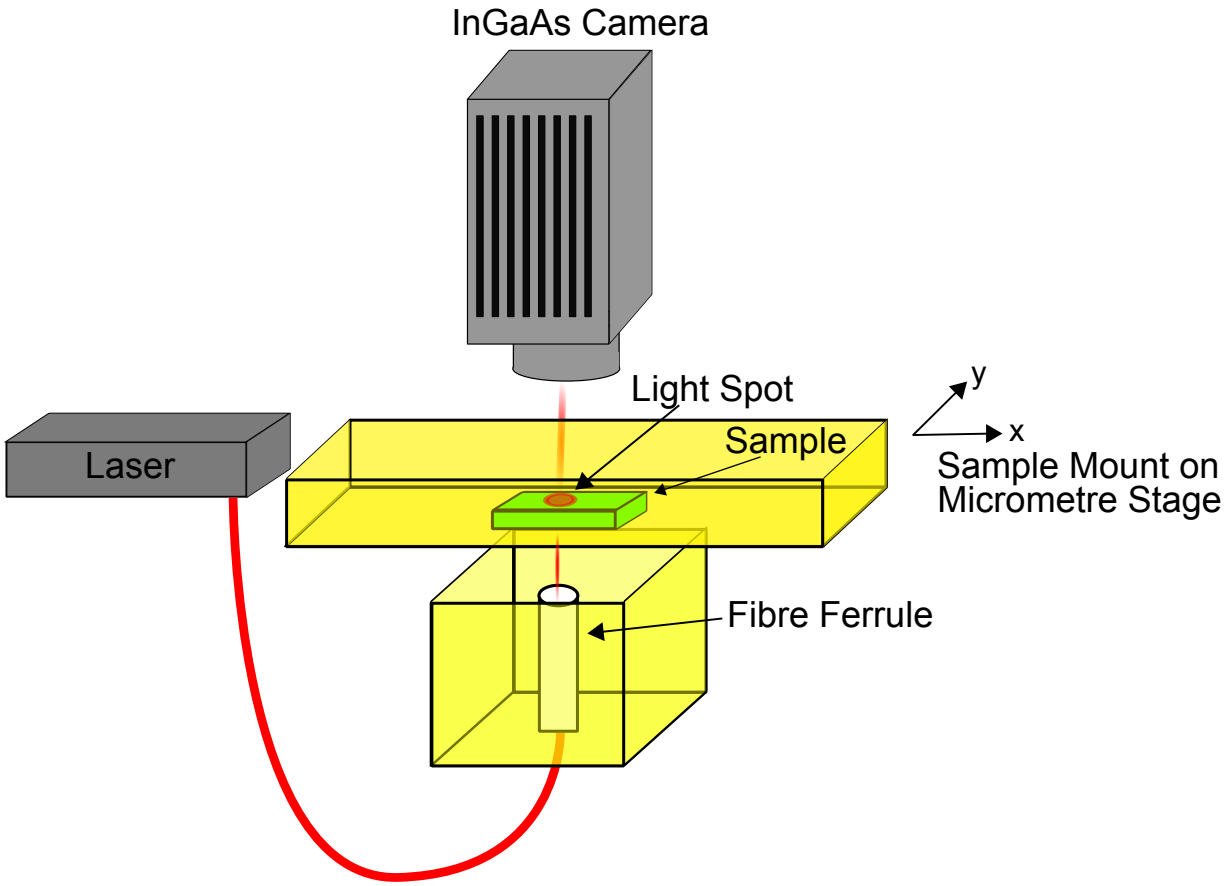

Figure 3.6: Alignment setup for aligning fibre optics with detectors. The device can be mounted so that the fibre is against the substrate (backside-coupled) or the nanowire (frontside-coupled).

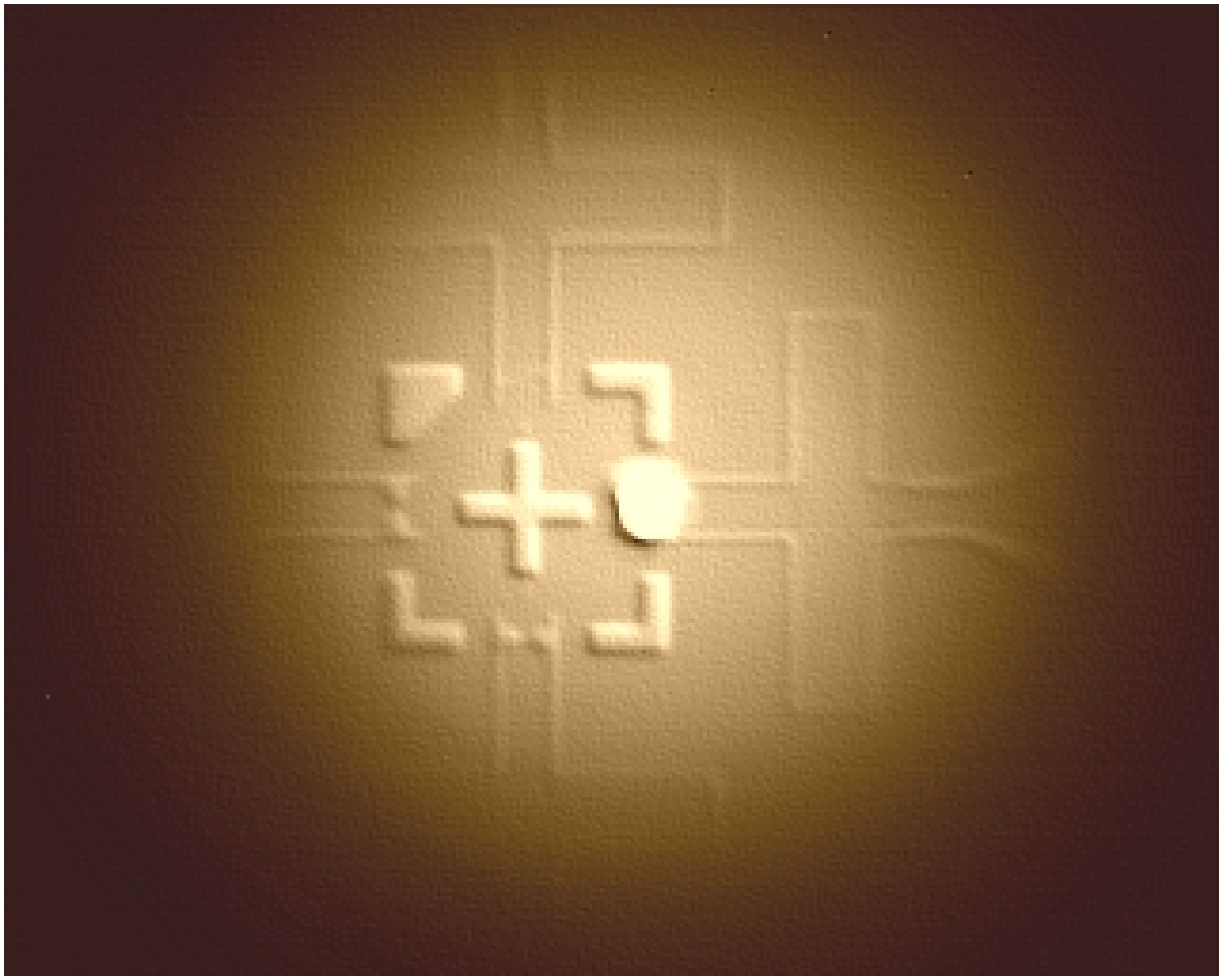

Figure 3.7: False colour image of an aligned device. The light spot is seen on the right over the active area between the two gold markers.

3.3 Cooling and Counting Pulses from SNSPDs

Throughout this thesis, I will regularly refer to cryostats and readout electronics used to count photons with SNSPDs. Therefore in this section I will briefly describe the experimental apparatus used later on for cooling and reading out detector pulses.

3.3.1 Cooling

Cooling of devices is achieved using closed-cycle cryostats. In the lab there are a variety of cryostats available with differing temperatures and hold times. In this work I will primarily refer to three types of cryostat. The first is a 2.5 K fridge design based on the RDK-101D cold head from Sumitomo Cryogenics. A schematic of such a fridge is shown in Fig. 3.8. There are three identical cryostats of this configuration and they are used interchangeably. They are Gifford-McMahon (GM) [159] type cryostats that can be connected to a compact CNA-11 compressor or a larger Zephyr compressor (both Sumitomo Cryogenics). The larger compressor offers additional cooling power (and a slight decrease of minimum temperature to around 2.3 K) at the expense of bulk. When a working temperature of 2.5 K or 2.3 K is referenced then one of these three cryostats is being employed. A cryogenic amplifier is sometimes mounted as discussed in the next section.

The second option used throughout this thesis is an RDK-101D coldhead and Zephyr compressor as above connected to a GL4 ^{4}He sorption fridge from Chase Research Cryogenics. A schematic of this is shown in Fig. 3.9. This setup utilises a liquid ^{4}He pump/heat switch arrangement and can maintain temperatures of 850 mK for over 24 hrs. This cryostat was designed and constructed by myself as part of this PhD to be portable and user-friendly. Drawing on my experience working with other fridges I added features such as touch-screen operation, remote operation and packaged the system in a portable small-footprint frame. A full description of the design and operation of this cryostat is given in Appendix A where the operation of sorption fridges and GM coldheads are discussed in more depth.

The final cryostat used is based on a PT 405 pulse-tube cryocooler [160] from Cryomech and a GL7 ^{3}He sorption fridge from Chase Research Cryogenics. A schematic of this is shown in Fig. 3.10. This setup uses the pulse-tube to cool to 3 K and then a ^{3}He sorption stage (buffered by a ^{4}He sorption stage) to cool to 350 mK. The operation of the sorption stage is similar to the process outlined for the 1 K cryostat above (and described in detail in Appendix A) with the difference that two of these stages are used. The first stage is a ^{4}He sorption stage that pre-cools the system to below 2 K and then a second ^{3}He sorption stage is initiated which then cools the cold stage to 350 mK. The first ^{4}He stage also buffers the second stage which reduces the heat load on the 350 mK stage and prolongs runtime. This setup allowed temperatures of 350 mK for

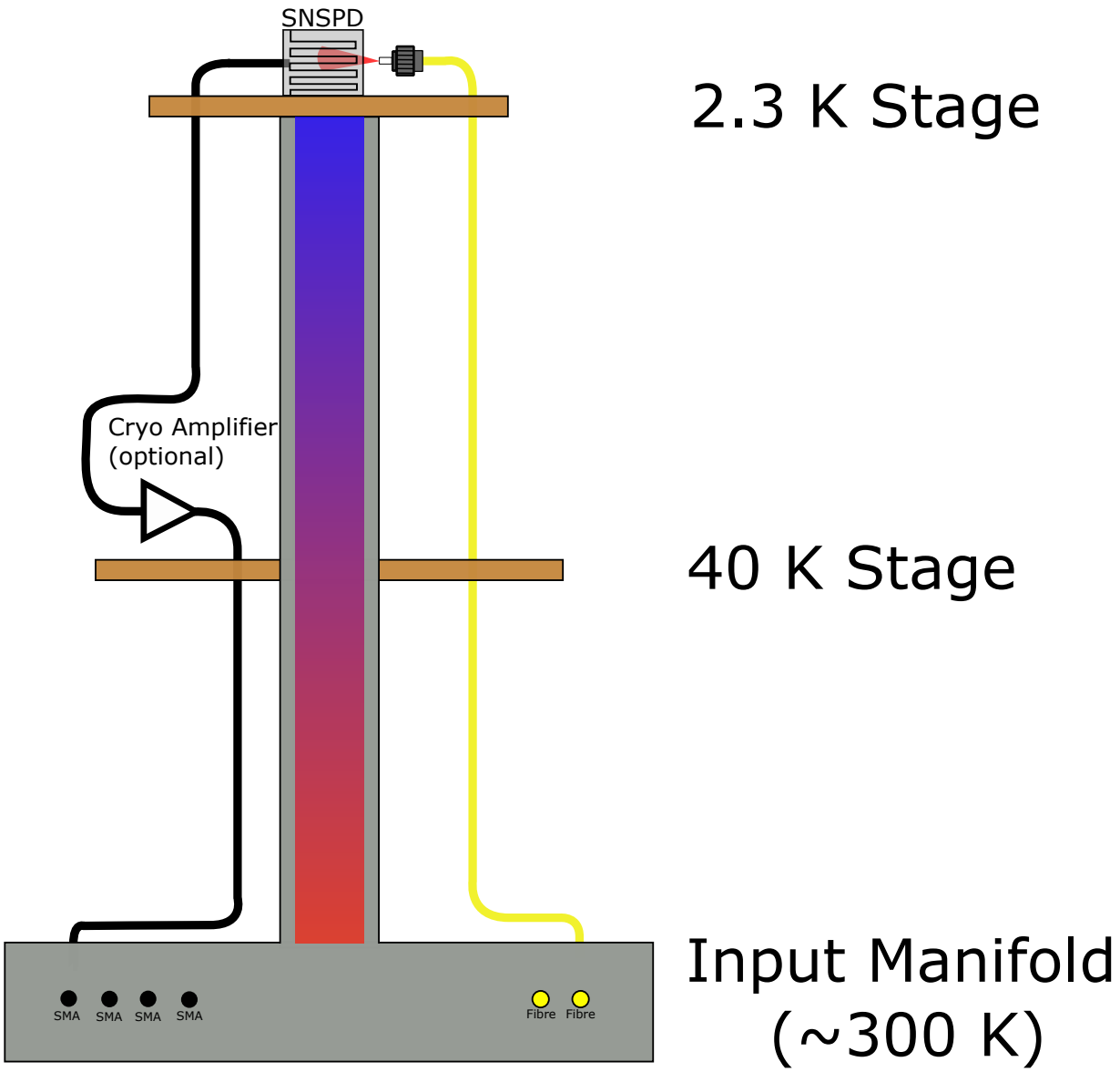

Figure 3.8: Schematic of 2 K cryostat. The heat bar indicates the temperature gradient in the RDK-101D coldhead. Black connections are electrical and yellow connections are fibre optics.

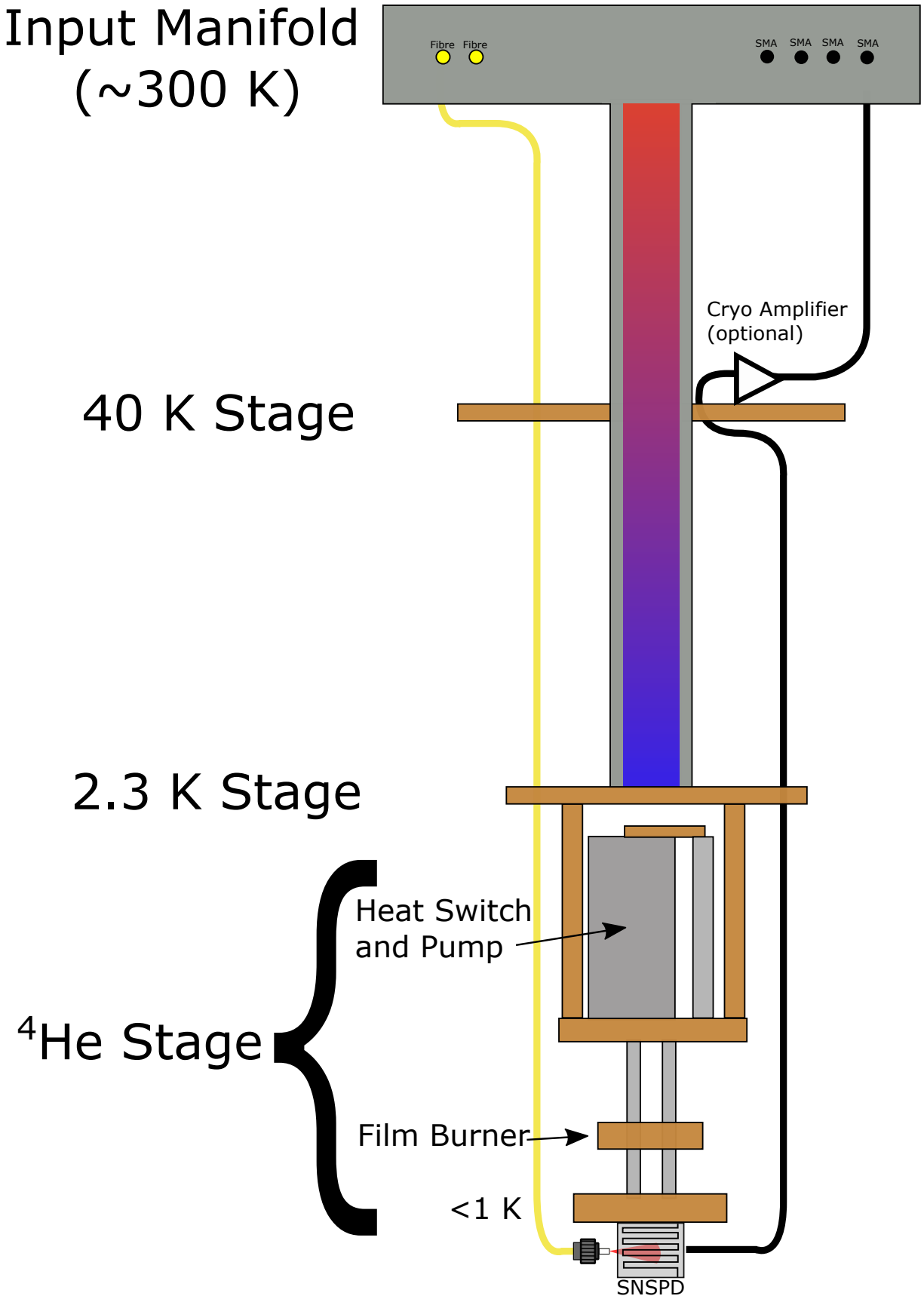

Figure 3.9: Schematic of 1 K cryostat. The heat bar indicates the temperature gradient in the RDK-101D coldhead. A Chase Croygenics GL4 ^{4}He sorption stage is mounted to the 2 K plate of the coldhead. Black connections are electrical and yellow connections are fibre optics.

up to 3 hours to be achieved.

3.3.2 Counting Output Pulses

When SNSPDs change to the normal state they emit a voltage pulse that travels through the electrical signal path and can be read out. The height of this output pulse is directly proportional to the switching current, I_{sw}, as for $V = I_{sw}Z_{load}$ where Z_{load} is the load impedance, typically 50 Ω. This pulse will then generally require amplification before it is suitable for the readout electronics. This is achieved with low noise amplifiers (LNAs) at room temperature although for devices with low I_{sw} it is desirable to employ cryogenic amplification to lower the noise floor and heighten the signal-to-noise ratio. A further method to improve signal height is use of a tapered readout [161] which will be discussed more in Ch. 6 in the context of minimising timing jitter.

The room temperature amplifier chain typically used in the lab consists of an LNA-580 (gain of 23 dB, 10 to 580 MHz, NF of 0.7 dB) followed by an LNA-1000 (gain of 33 dB, 0.01 to 1 GHz, NF of 2 dB) from RF BAY Inc. giving around 53 dB of gain with a noise figure of 0.71 dB. A bias tee is implemented to bias the detectors and readout the output pulses. A diagram of the setup is shown in Fig. 3.11. An example pulse where room temperature LNA's are employed is shown in Fig. 3.12. Note the pulse is inverted when using the room temperature amplifier setup due to the inverting nature of one of the LNAs.

If a cryogenic amplifier is required then a CITLF1 from Cosmic Microwave Technology is available. This offers 44 dB of gain with a noise figure of <0.11 dB at 20 K, improving at lower temperatures. It also houses an integrated resistive bias tee for biasing the device. A circuit diagram is shown in Fig. 3.13. An example output pulse after amplification with cryogenic amplification is shown in Fig. 3.14. The rise time for this pulse is 1.4 ns and the 1/e decay time is 32 ns. This would give a theoretical maximum count rate for this device of around 30 MHz. The reflections observed in the falling edge of the pulse are a result of the cryogenic amplifier used and are not resent in the pulse utilising the room temperature readout shown in Fig. 3.12.

The output pulses are then ready to be used. If a photon counting experiment such as efficiency characterisation is being performed then a Agilent 53131A universal counter is used. If a time based experiment is being performed (such as LIDAR or jitter characterisation) then the output pulses are fed directly into the TCSPC timing module.

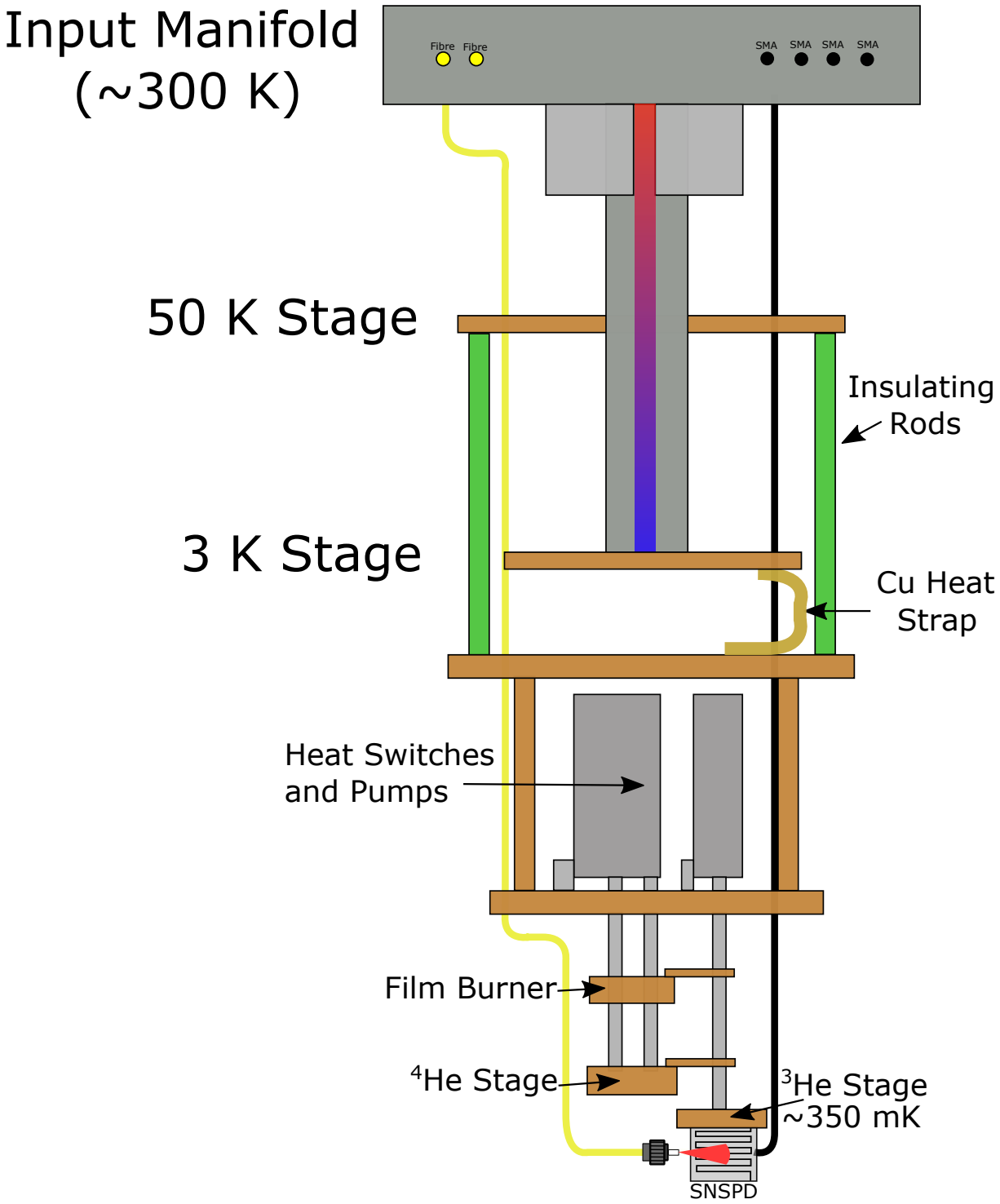

Figure 3.10: Schematic of 350 mK cryostat. The heat bar indicates the temperature gradient in the Cryomech PT405-RM pulse tube cooler. A Chase Cryogenics GL7 ^{4}He/^{3}He sorption stage is mounted to the 3 K stage. Black connections are electrical and yellow connections are fibre optics.

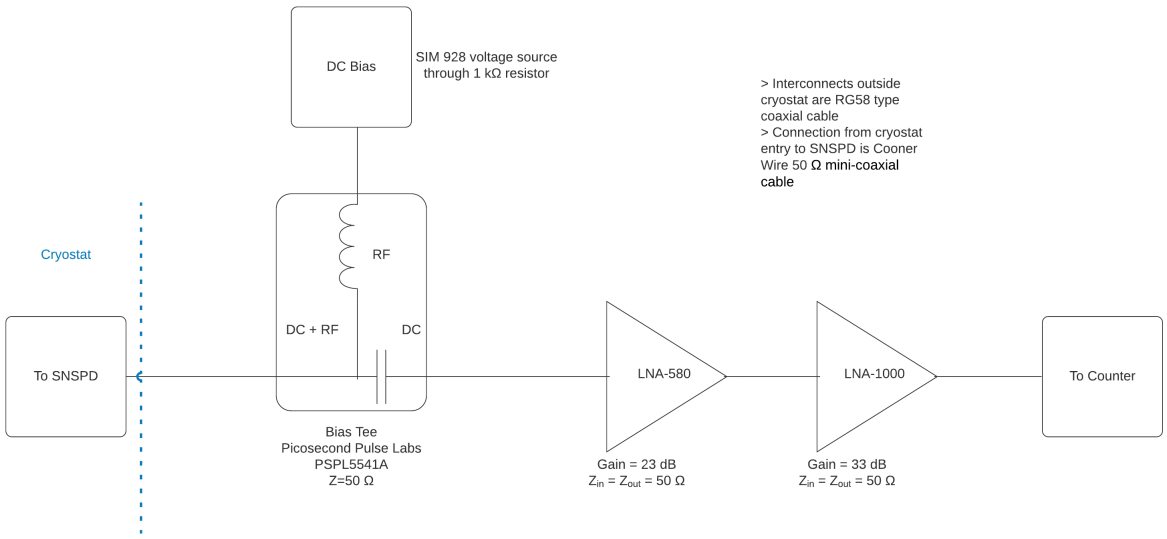

Figure 3.11: Circuit diagram of typical room temperature SNSPD readout.

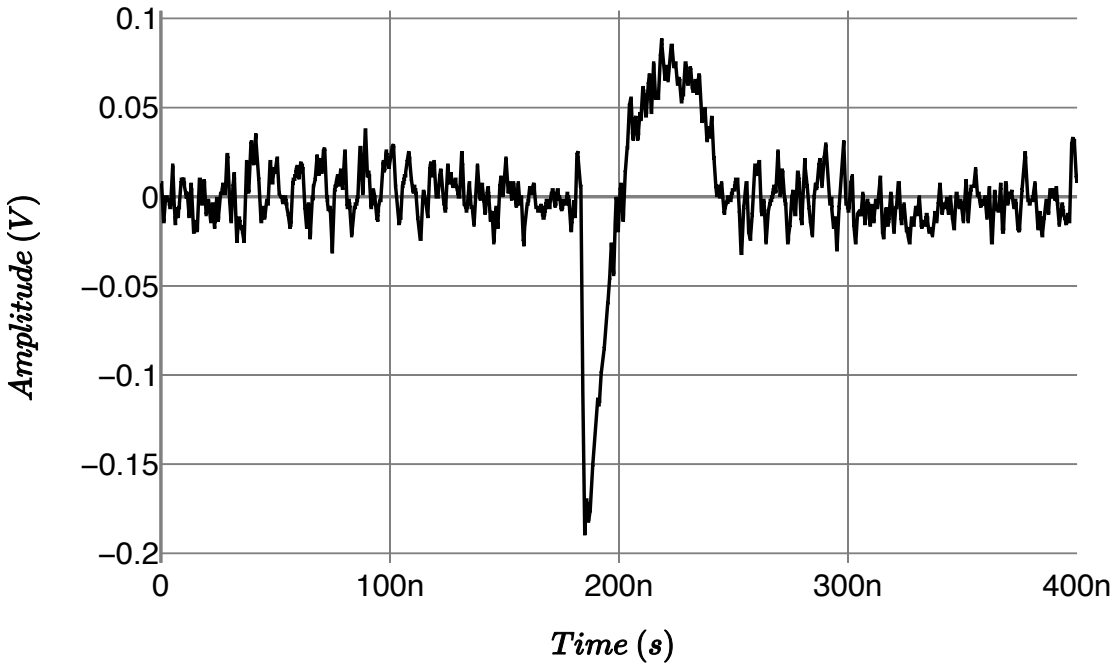

Figure 3.12: An example of an output pulse from an SNSPD, post amplification using the room temperature amplifier setup described in the text. Note the heightened noise floor compared to the pulse in Fig. 3.14. The pulse is inverted due to the amplifiers used.

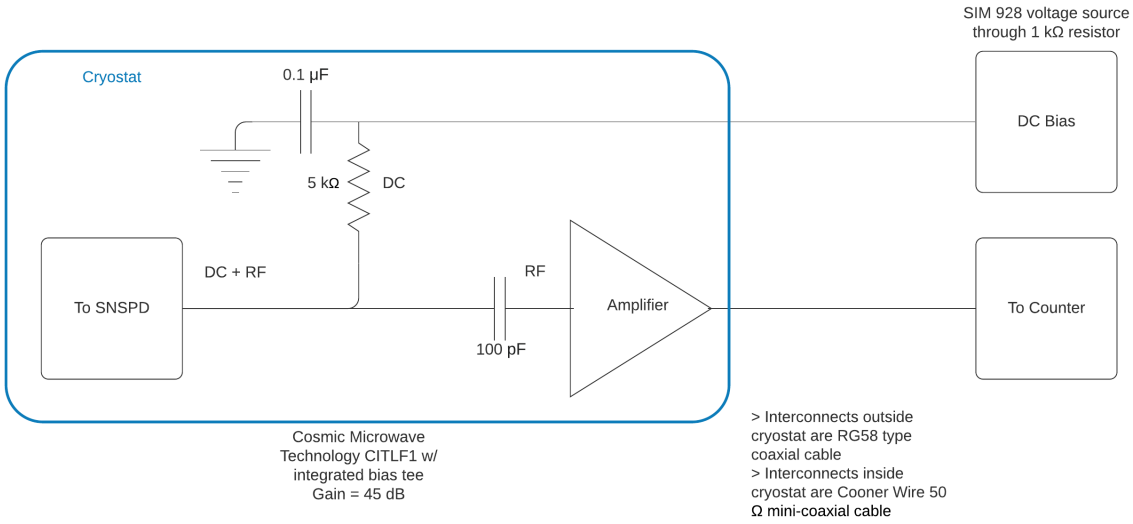

Figure 3.13: Circuit diagram of typical cryogenic SNSPD readout.

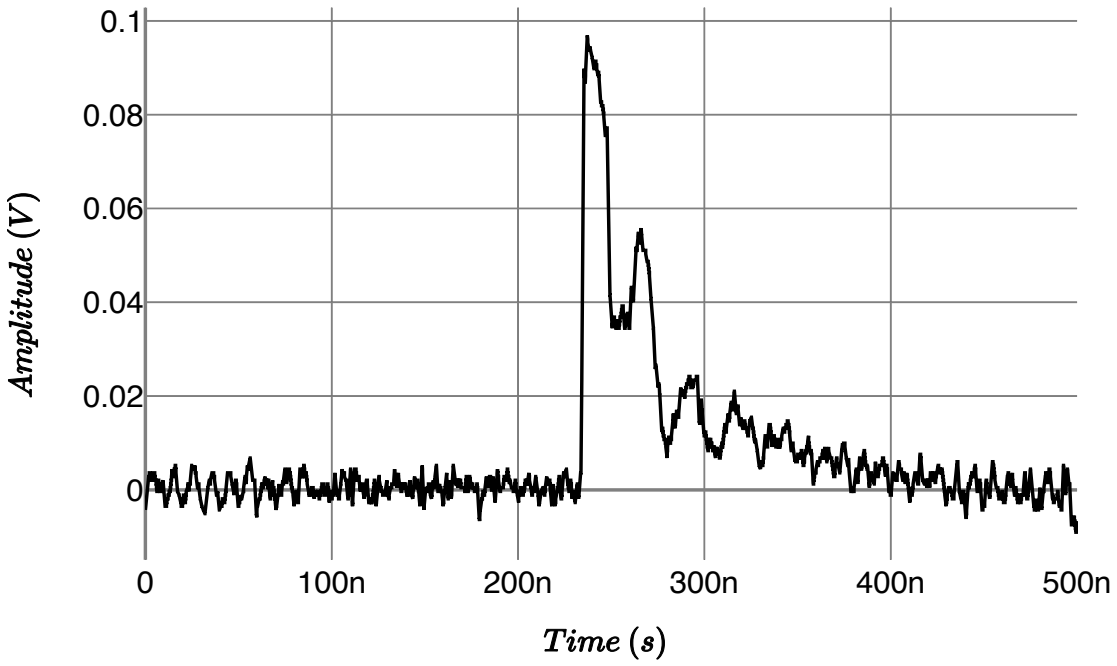

Figure 3.14: An example of an output pulse from an SNSPD, post amplification. In this case the cryogenic CITLF1 amplifier was used which causes the reflections in the output pulse.

3.4 Mid-infrared Characterisation

As discussed in Ch. 2, §2.2.2, characterisation at long wavelengths is not trivial. Here a test-setup to characterise and test devices has been built around an optical parametric oscillator (OPO, Chromacity Ltd) that delivers short ($\sim$ps) pulses, tunable in wavelength from 1.5 to 4.2 μm. This OPO pumps a periodically poled lithium niobate (PPLN) crystal at 1040 nm and delivers two outputs, signal and idler into ZBLAN mid-infrared fibre. The output is tunable, as mentioned, by varying the cavity length and grating periodicity. An example output spectrum is shown in Fig. 3.15. As can be seen in Fig. 3.15, the output of the idler (and signal) is broadband. Therefore for characterisation and test at specific wavelengths, bandpass filtering is necessary. The OPO output is collimated into a free-space filtering setup where a narrow bandpass filter of the desired wavelength can easily be changed. For single-photon characterisation it is also necessary to attenuate the output down to single-photon levels. This is achieved with a second fixed filtering setup utilising neutral-density (ND) filters that have a flat response across the infrared spectrum. With the output power of the OPO (10s of mWs), the flat response of the filters and an off-the-shelf power meter (Thorlabs S148C) up to 45dB of fixed attenuation per attenuator can be achieved. The attenuation can be tuned by misaligning the input and output couplers to the attenuating setup. A diagram of the complete filtering setup is shown in Fig. 3.16. Utilising the two filtering setups a short-pulse single-photon source is available that can be utilised to make calibrated efficiency measurements. Due to the short pulses the setup can also be used to make timing jitter measurements at mid-infrared wavelengths - the shorter wavelength sync pulse can be used as a start signal while the idler pulse is delayed and then delivered to the SNSPD. A timing histogram can be obtained and the jitter is given by the FWHM of the distribution. The system has been designed so that all optical components are designed to work over the whole wavelength range up to 4.2 μm so that any wavelength can be tested with a suitable bandpass filter. For shorter wavelength measurements, such as at 2 μm (as for the ALD devices presented in Ch. 4) it is possible to take the filtered output of the OPO and utilise MEMs based in-fibre (SM-2000) attenuators to achieve single-photon levels. These are not effective at longer wavelengths due to the fibre limitations.

It is worth noting here that typical efficiency measurements are given where the point of reference is the fibre input to the cryostat. For mid-infrared measurements without the use of specialist mid-infrared fibres, the lossy silica fibres within the cryostat can result in a lower value for the detection efficiency than may be expected as the 1-2 m of fibre within the cryostat contributes a large optical loss. Calibration of the fibre losses within the cryostat is necessary to remove this extra term, though in practical terms minimising the loss and quoting the efficiency inclusive of it is a more useful metric when deploying detectors in real-world applications.

Dark count rate in the mid-infrared is strongly affected by blackbody radiation. Fig. 3.17

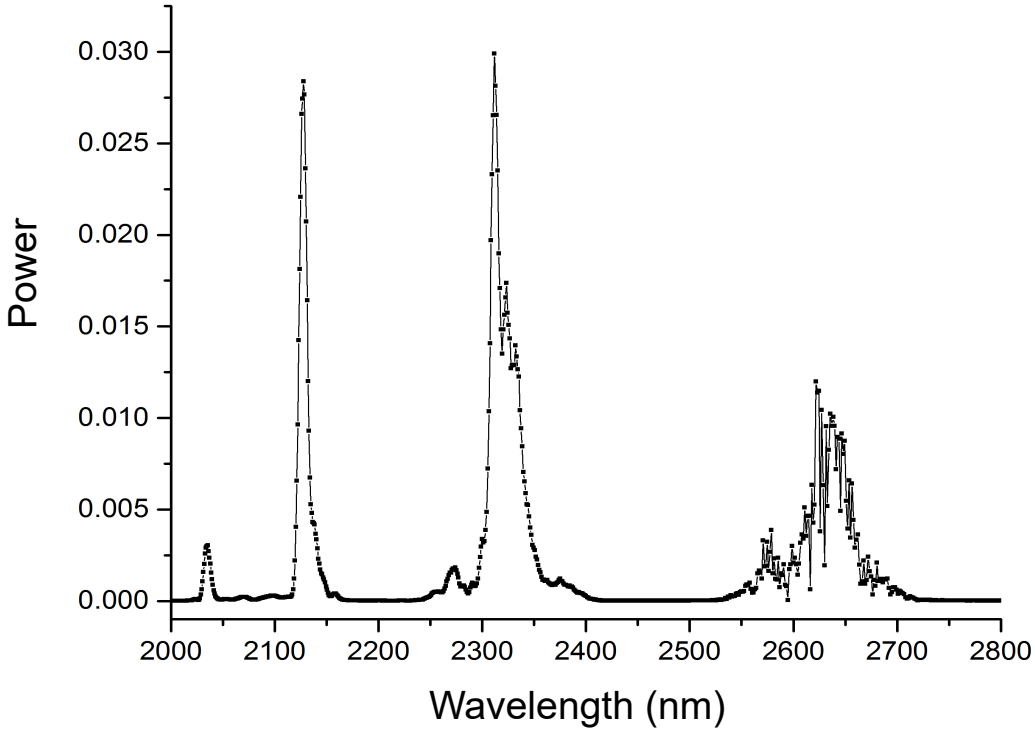

Figure 3.15: Example idler output from OPO [162].

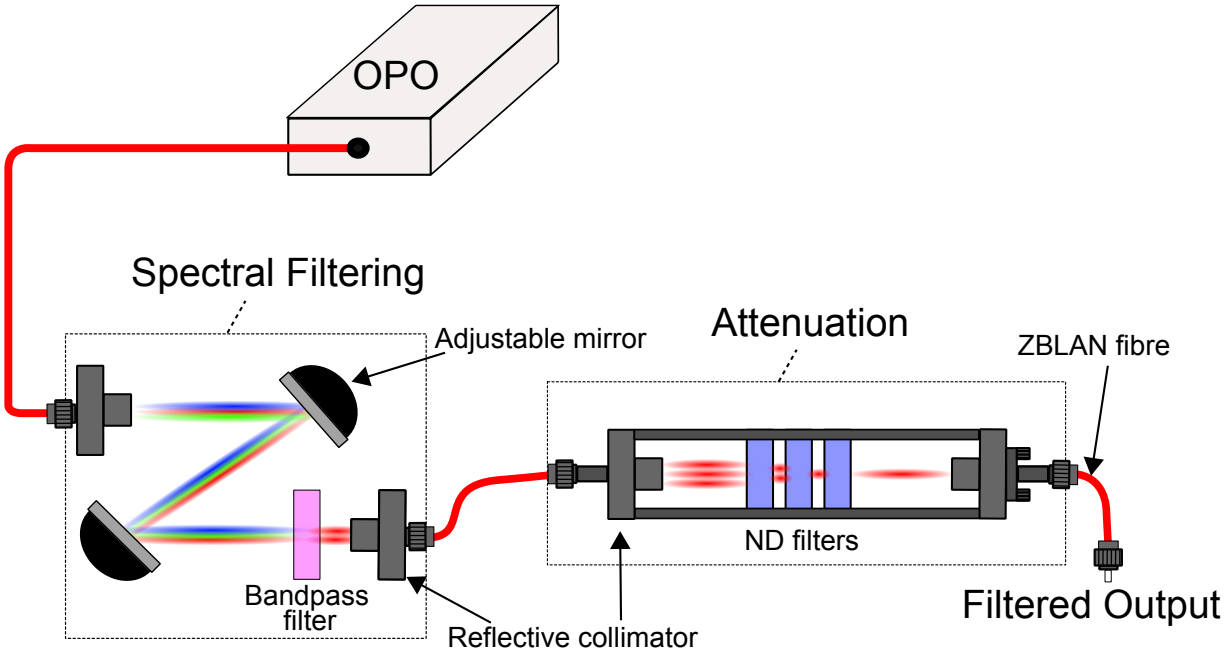

Figure 3.16: OPO filtering setup.

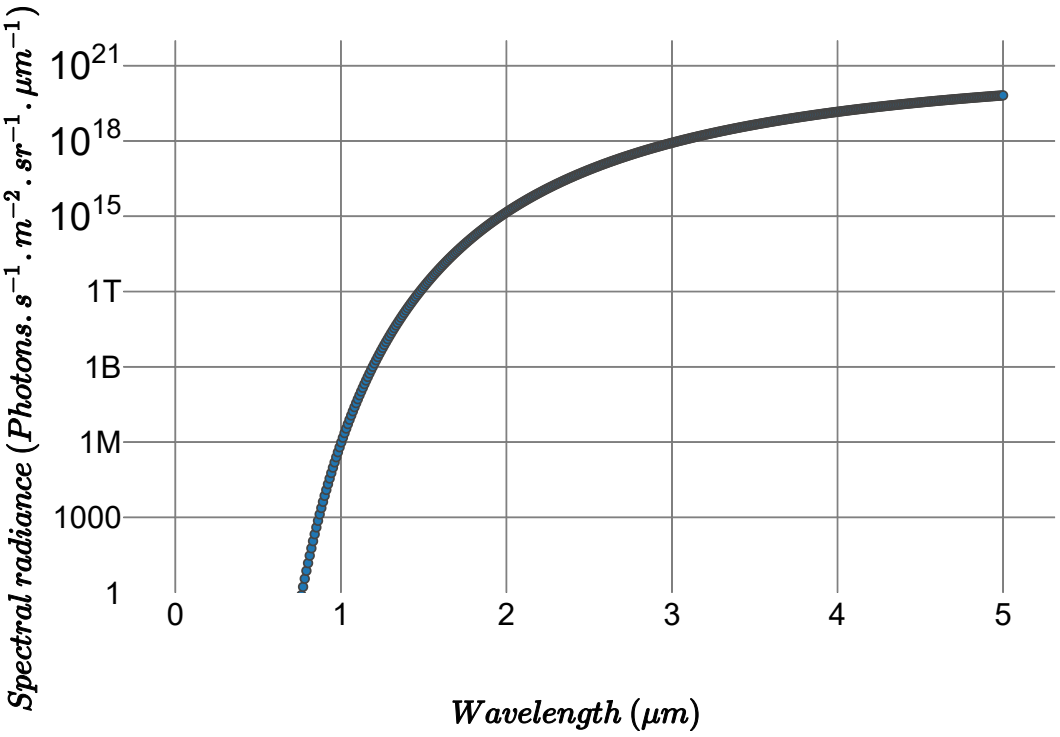

Figure 3.17: Blackbody spectrum at room temperature, 300 K.

shows a blackbody spectrum at room temperature (300 K). As is seen, below 2 μm the blackbody radiation is weak but as wavelength increases the photon flux increases dramatically. When using infrared optical fibres this radiation couples into the fibre and is evident in the dark count rate of the SNSPD. This typically shows itself in dark count rate plots of mid-infrared SNSPDs as a characteristic 'hump' in the plot at lower bias currents before the onset of an exponential increase close to the switching current. For shorter wavelength detectors as the bias is increased the dark count rate typically stays close to zero until the critical current is approached where it will rapidly increase. In mid-infrared SNSPDs the dark count rate increases at a much lower bias current and will slowly increase, mimicking the shape of the photon counts curve before rapidly increasing as the critical current is approached. An example of this is shown in Fig. 3.18. The red dots show the characteristic dark count plot for shorter wavelength detectors while the blue dots show a typical plot for a mid-infrared detector. The highlighted region shows the hump in the mid-infrared plot showing the result of blackbody radiation coupling into the mid-infrared fibre. This problem can be dealt with somewhat by introduction of cold-filtering at the wavelength of interest which will limit the blackbody radiation to in-band radiation. The dark count plot will retain the same shape but the blackbody photon flux will decrease.

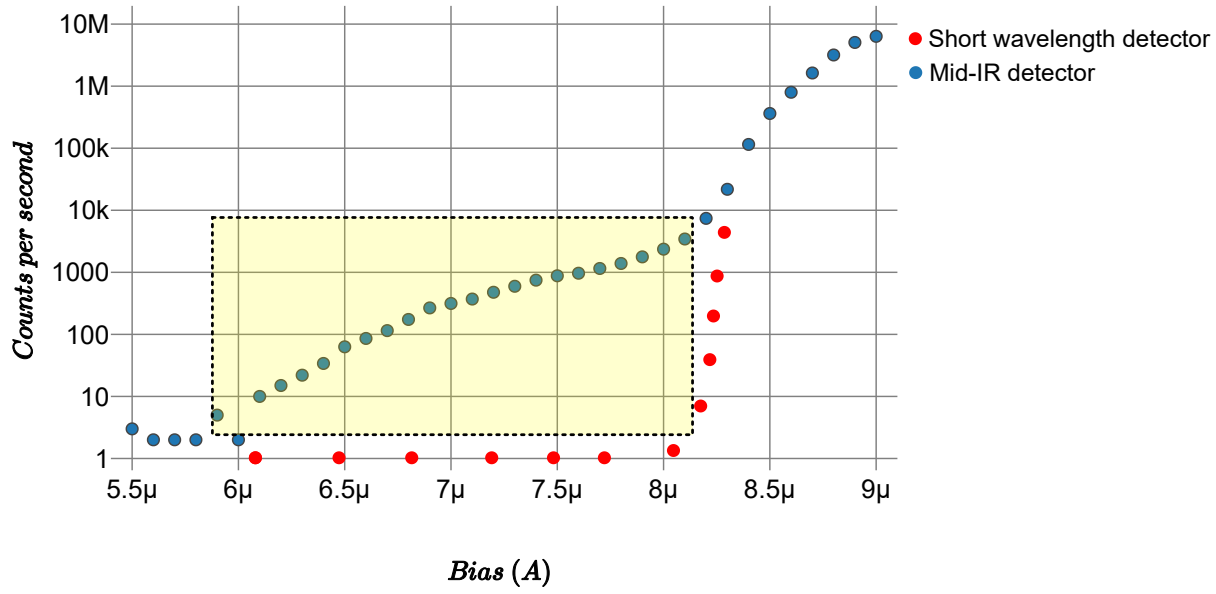

Figure 3.18: An example of the blackbody seen in dark count rate plots in the mid-infrared when compared to shorter-wavelength detectors. The highlighted region shows the characteristic hump.

Chapter 4

Material Development for Mid-Infrared SNSPDs

As outlined in Ch. 3, material selection can play a large part in the detection characteristics of SNSPDs. This is particularly true for longer wavelengths in the mid-infrared, where photon energy decreases. In this chapter I will outline the efforts to explore the atomic layer deposition (ALD) technique as an alternative to sputtering for SNSPD fabrication. The ALD films used in this work were grown by Dr Peter Barry and colleagues at the University of Chicago and then fabricated into devices by Dr Dmitry Morozov at the James Watt Nanofabrication Centre, University of Glasgow. The TEM images were acquired at the Kelvin Nanocharacterisation Centre by Mr Ciaran Lennon, University of Glasgow. Device characterisation and analysis was performed by the author.

4.1 Motivation

As well as simply selecting a material for SNSPD fabrication that exhibits the properties desirable for the application (Δ or T_c, see Ch. 3, table 3.1) there is also scope to tune the material properties to achieve the desired device characteristics. This can be achieved in a variety of ways. One approach is to alter the materials composition in order to reduce the free carrier density. This increases the resistance of the material and results in an incident photon's energy being distributed amongst less quasiparticles. This has been demonstrated in both NbN [163] and WSi [73] with the effect of lengthening the saturated plateau at longer wavelengths - therefore indicating that the internal efficiency was increased. Another consideration is the homogeneity of the film - as this reduces the chance of fabrication defects that could lead to constrictions or imperfections - see Ch.3, §3.1.4. To date, the majority of superconducting films for SNSPD fabrication are deposited using DC magnetron sputtering. ALD offers an alternative technique that may provide a pathway to tunable and homogeneous films for mid-infrared applications.

As mentioned in Ch. 3, §3.1.2, ALD is a subclass of chemical vapour deposition based on the sequential, self-limiting exposure of individual gas-phase precursor species, forming a single atomic layer of material. A single deposition step, known as an "ALD cycle", can then be repeated ad infinitum to form a film of desired thickness, with Ångstrom-level sensitivity [152]. In the specific case of plasma-enhanced ALD (PEALD), an additional plasma exposure step is added after precursor exposure to remove unreacted material byproducts [164]. The self-limiting nature of the ALD process removes the statistical aspect of conventional deposition techniques (such as sputtering), where localised areas of the surface often react first due to the randomness of precursor flux, creating rough and pinhole-laden films. Consequently, ALD films are highly uniform and conformal, as well as pinhole-free [165, 166]. ALD translates well to large area deposition, with the only limit being the size of the deposition chamber, as well as concurrent processing of multiple substrates. Recent developments in the use of ALD for deposition of high quality superconducting metal nitrides has consequently made it an attractive technique for the fabrication of superconducting technologies, with particular progress in the use of PEALD for the deposition of NbN and TiN thin films respectively [167–169]. These materials advances, coupled with the unparalleled uniformity and conformality of ALD, therefore makes this growth technique an ideal candidate for the fabrication of SNSPDs.

Some early results on ALD NbN SNSPDs have emerged in the last couple of years. Knehr et al [153] analysed the transport properties of bare films and analaysed single photon response in non-meander SNSPDs for wavelengths up to the near-infrared. They reported saturation of internal efficiency for shorter wavelengths (λ = 385 nm). A further exhaustive study by Cheng et al [170] conducted a statistical analysis of hundreds of ALD SNSPDs and confirmed the exceptional homogeneity of ALD deposited films with a device yield approaching unity. Both of these works were performed up to a maximum wavelength of 1550 nm. In addition to this work there has been ongoing development to utilise ALD TiN in kinetic inductance detectors (KIDs) for astronomical work [171]. In the following work the mid-infrared sensitivity of ALD SNSPDs is confirmed in order to assess the candidacy of such devices for experiments in the mid-infrared.

4.2 Device Fabrication

ALD films were grown at the University of Chicago by our collaborators with organic based precursors. Films were deposited on high resistivity Si <100> substrates with resistivity of > 10 kΩ·cm, which were cleaned with organic solvents before deposition. The chamber and substrate temperature was allowed to stabilise in vacuum for an hour before starting the process. TBTDEN precursor and N_2/H_2 plasma was used in each deposition cycle, while the substrate was heated to 300 °C. In the initial optimisation of the ALD NbN deposition process, a NbN thickness similar to that used by many leading groups employing reactive sputtered NbN for SNSPDs [31] was

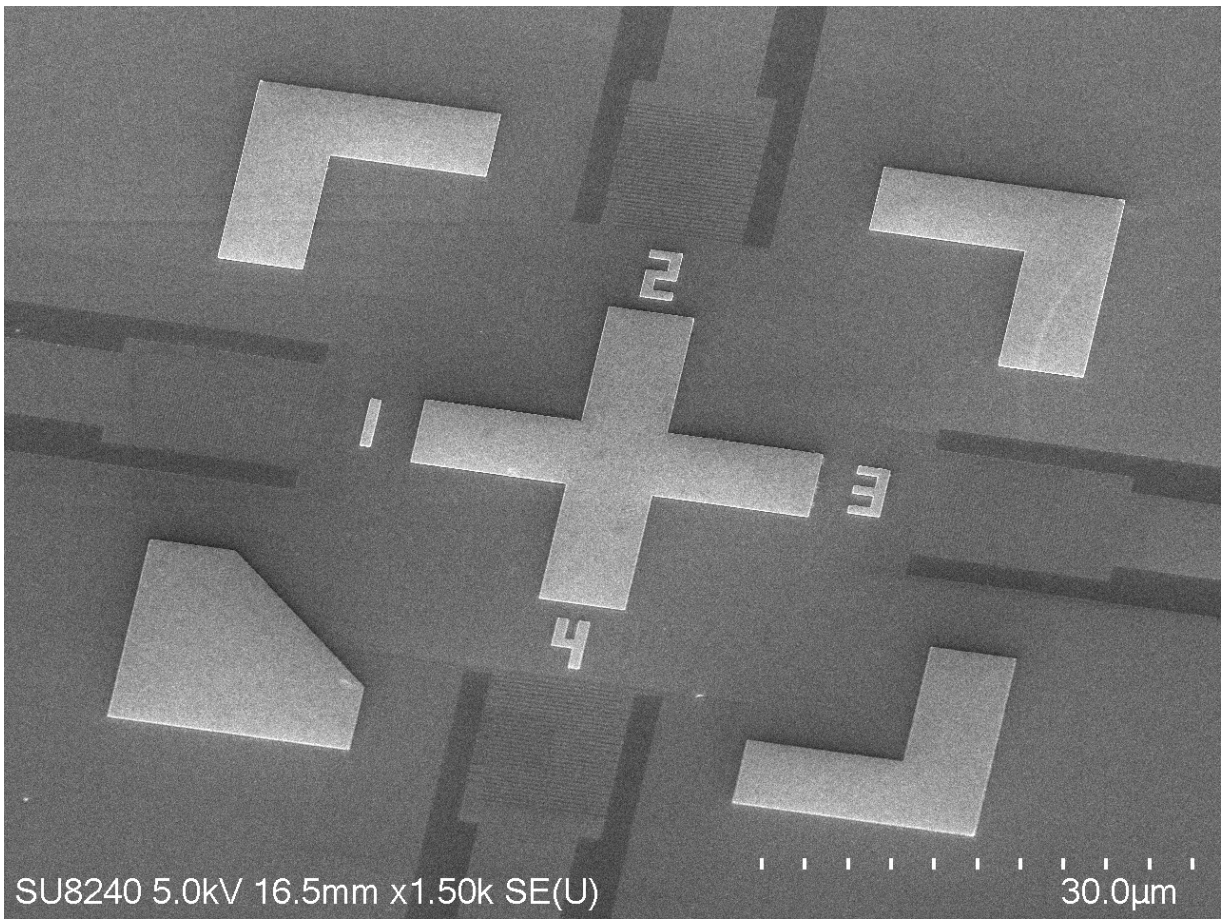

Figure 4.1: SEM image of ALD SNSPD chip showing the four devices on each chip. Courtesy of Dr Dmitry Morozov, University of Glasgow.

targeted and a film thickness of 4.65 nm was achieved with 75 ALD cycles at an approximate rate of 0.6 Å per cycle [169].

SNSPDs were then fabricated at the James Watt Nanofabrication Centre (Glasgow) with 100 kV electron-beam lithography and plasma etch. Firstly, Ti/Au alignment markers and contact pads were formed with a lift-off procedure. ZEP520 was then used as an etch mask followed by a SF_6/N_2 plasma etch to etch the meander structure. The SNSPD meander covers an active area of 10 µm x 9.6 µm. Four devices were fabricated on each chip - two with a line width of 100 nm and a fill factor of 0.5 and two with a line width of 200 nm, again with a fill factor of 0.5. An SEM image of the overall chip layout is shown in Fig. 4.1. For each pair of equally sized nanowires (100 nm and 200 nm) one of them was fabricated with square corners in the bends of the meander whereas one was fabricated with curved corners. This was to investigate the difference in the I_{sw} of the device as current crowding should be a more pronounced effect in the square cornered devices, as shown by other research groups [110]. A scanning electron microscope image of a nanowire of width 100 nm with rounded corners is shown in Fig. 4.2.

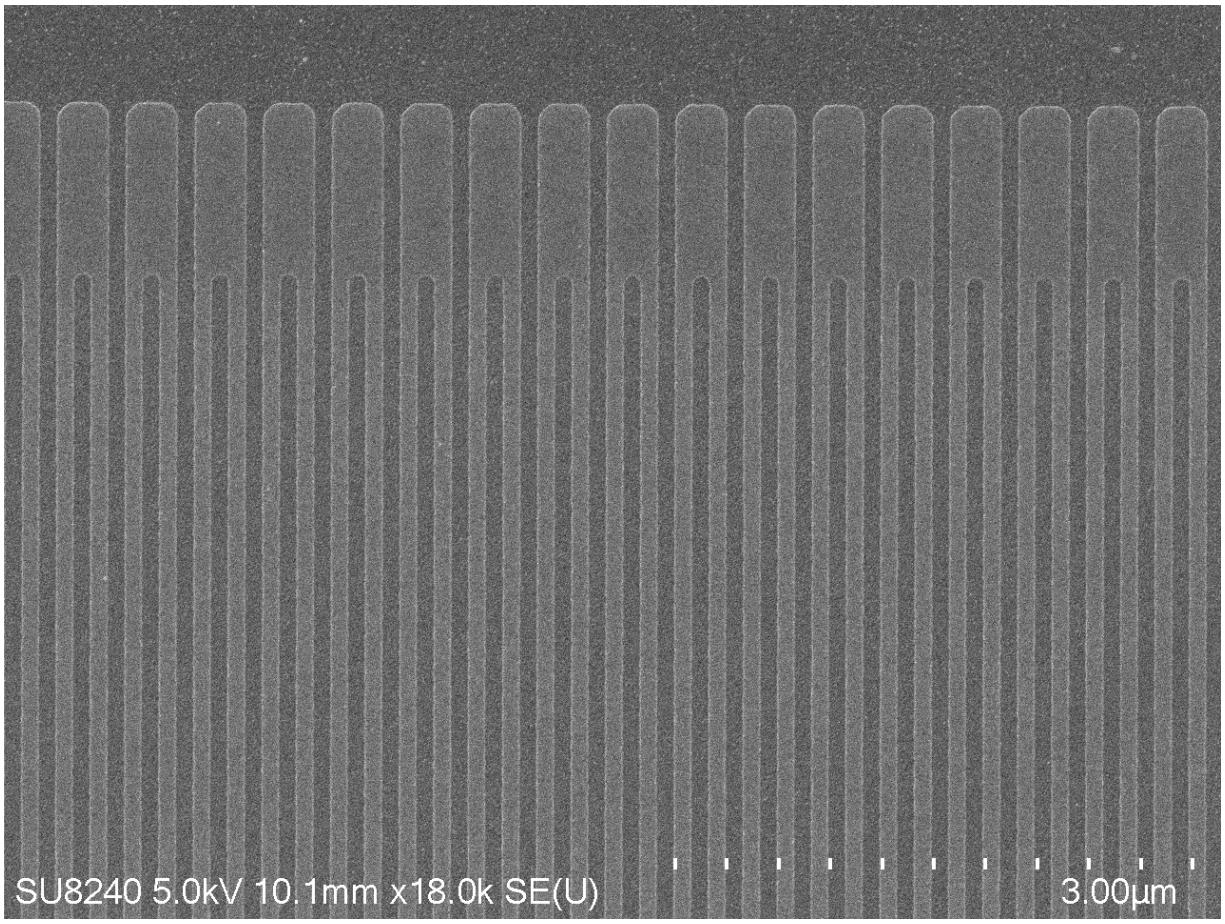

Figure 4.2: SEM image of ALD SNSPD nanowire. The nanowire is 100 nm width with a gap size of 100 nm and the corners have been rounded to reduce current crowding. Courtesy of Dr Dmitry Morozov, University of Glasgow.

Transmission electron microscopy (TEM) was then carried out in the Kelvin Nanocharacterisation Centre (University of Glasgow) using a FEI Technai T20 microscope. Samples were prepared using a conventional focused ion beam lift-out technique [172]. The TEM samples were prepared from a 200 nm width nanowire meander device. A TEM image of a section of the nanowire is shown in Fig. 4.3. TEM images were analysed and the NbN film thickness was estimated to be 4.53 nm - well aligned with the target of 4.65 nm. A native oxide was present on the film and was estimated to be 1.57 nm in thickness. Analysis of multiple nanowires in the meander showed good uniformity across the film. The edges of the nanowire can be seen to be trapezoidal in shape, with evidence of over-etching into the Si substrate. This is a concern for achieving high fractions of the depairing current, as discussed in Ch. 3, §3.1.4, and achieving high internal detection efficiency [173]. The width of the nanowire was designed at 200 nm but in the TEM it appears to be slightly wider at ~220 nm. This could be due to small errors in the lithography process. In the image the substrate appears in light grey to the left of the image and the material evident on top of the nanowire is Pt deposited during the TEM sample preparation.

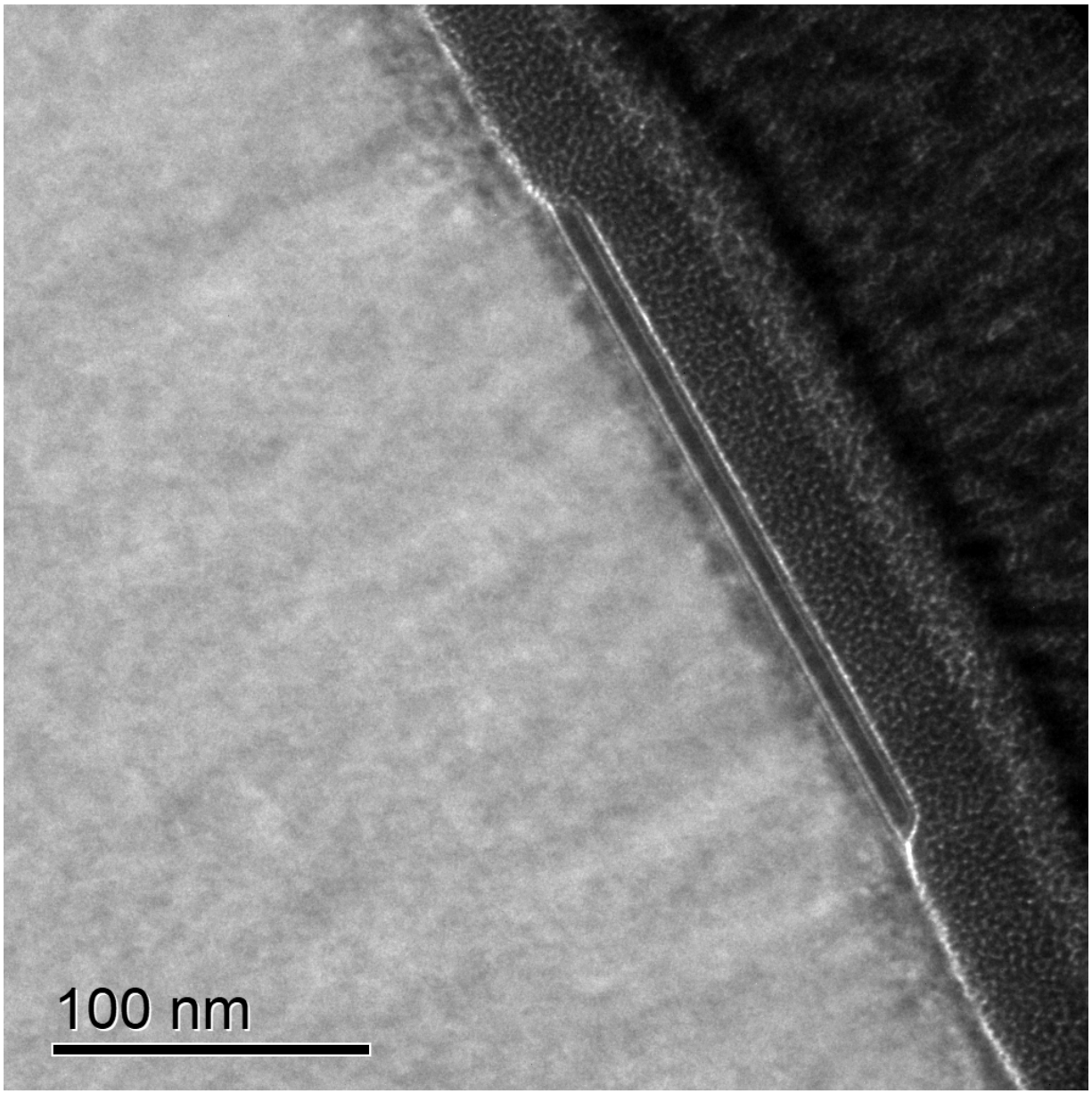

Figure 4.3: TEM image of ALD SNSPD nanowire. Analysis of the thickness gives a NbN thickness of 4.53 nm and a native oxide thickness of 1.57 nm. Courtesy of Mr Ciaran Lennon, University of Glasgow.

4.3 Results

4.3.1 Switching Current Variations

In order to assess the effect of rounding the corners of the nanowire on the switching current of the nanowire, eight devices were cooled and measured. The switching current was determined by performing a 2-point I-V measurement. This was done by increasing the bias current to the device and monitoring the voltage over the device. When the voltage increases due to the SNSPD turning resistive the bias point is taken as the I_{sw}. The bias current is swept both positive and negative to account for any DC offset. A diagram of the I-V setup is shown in Fig. 4.4. It should be noted that measuring I-V characteristics in this way has some drawbacks - mainly that the voltmeter used induces an offset in the I_{sw} due to the noise from the instrument. I_{sw}'s measured by increasing the bias to a shielded detector and noting where the dark count rate drops to zero are consistently 10-20 % larger than those measured for the same devices using the above I-V method. However as a comparison tool, I-V measurements as outlined are useful as they allow the determination of the I_{sw} for devices where counting pulses would not be possible due to the small pulses being lost in noise. A table of the devices tested is shown in Table. 4.1. For all devices the measurement was performed at 2.5 K.

Device	**Geometry**	I_{sw} **(µA)**
Chip2Dev1	100 nm rounded	4.09
Chip2Dev2	200 nm rounded	10.86
Chip2Dev3	100 nm square	4.4
Chip2Dev4	200 nm square	9.42
Chip3Dev1	100 nm rounded	1.2
Chip3Dev2	200 nm rounded	7.6
Chip3Dev3	100 nm square	1.83
Chip3Dev4	200 nm square	9.14

Table 4.1: Switching currents of ALD SNSPDs tested.

The data does not paint a particularly clear picture but there are some important points to note. Firstly, Chip3 clearly exhibits reduced switching currents for comparably sized nanowires from Chip2. Both 100 nm wide devices from Chip3 exhibit I_{sw}'s of less than 2 µA which makes them difficult to count pulses from. The wider devices also show lower switching currents than their Chip2 counterparts. Chip3Dev4 exhibited some strange behaviour when measuring the DCR - the switching to the normal state occurs at a very low count rate (around 2 kCPS) as opposed to all other 200 nm wide devices switching at a much higher rate (see Fig. 4.5). All of this indicates some sort of fabrication issues with Chip3, possibly constrictions in the nanowire or impurities in the thin film lowering the overall I_{sw} of each device and causing strange behaviour.

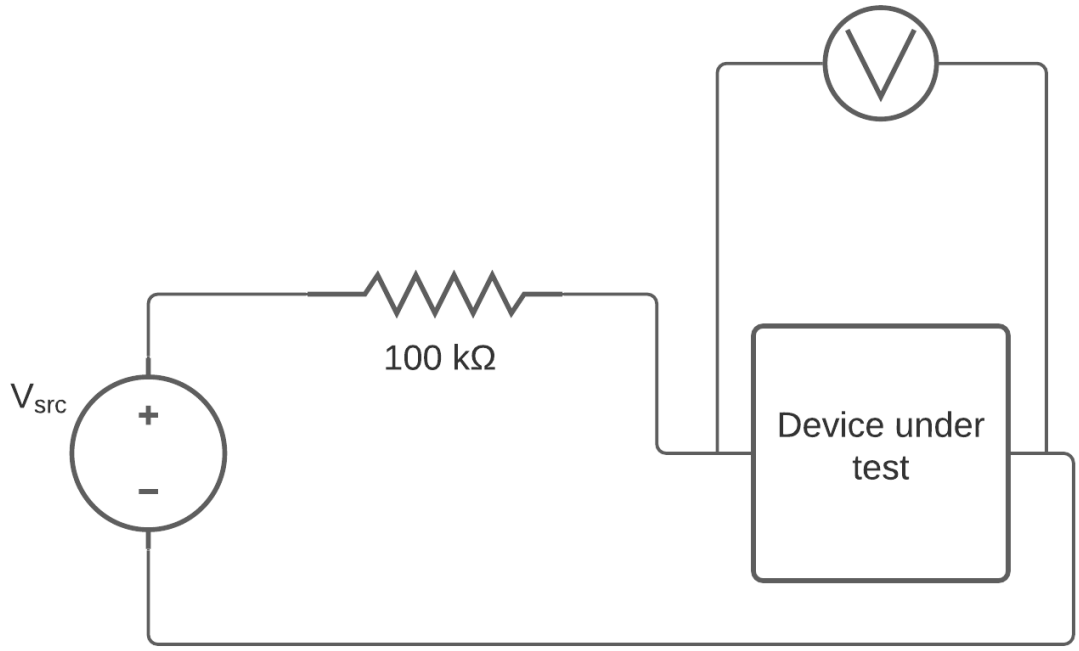

Figure 4.4: Circuit for I-V measurements. The DC voltage source is swept to change the bias current while the voltage over the device is monitored.

If Chip2 is then examined, there are some interesting features to note. It is expected that the 200 nm wires have a critical current double that of the 100 nm width wires, but actually closer to a 3 times increase is observed. This points to the 100 nm wires having some constrictions or imperfections which are not evident in the 200 nm wires. The difference in I_{sw} for the rounded and square turn wires is not particularly pronounced. Looking at the theoretical models in [110] it is possible to calculate the reduction factor, R, that the switching current of a straight section of nanowire is reduced by for a given geometry. Comparing the hairpin bends with rounded and square corners gives us remarkably similar values. For geometry comparable to our devices $R_{rounded} = 0.7$ and $R_{square} = 0.69$. This aligns well with our observed switching currents where not much variation is seen between the geometries for a given wire width and fill factor. It seems that local constrictions and imperfections may have more of an effect on the variation of switching currents between devices. The DCR curves for each of the devices when completely shielded is shown in Fig. 4.5. As can be seen in the plot the DCR curve is similar for each pair of similar devices and peaks at a similar value. There is an I_{sw} improvement in D4 from D3 evident which could indicate less constrictions in that particular device as well as a slight reduction in R due to the rounded corners of the meander.

Again examining the data from [110] it is evident that decreasing the fill factor of the devices

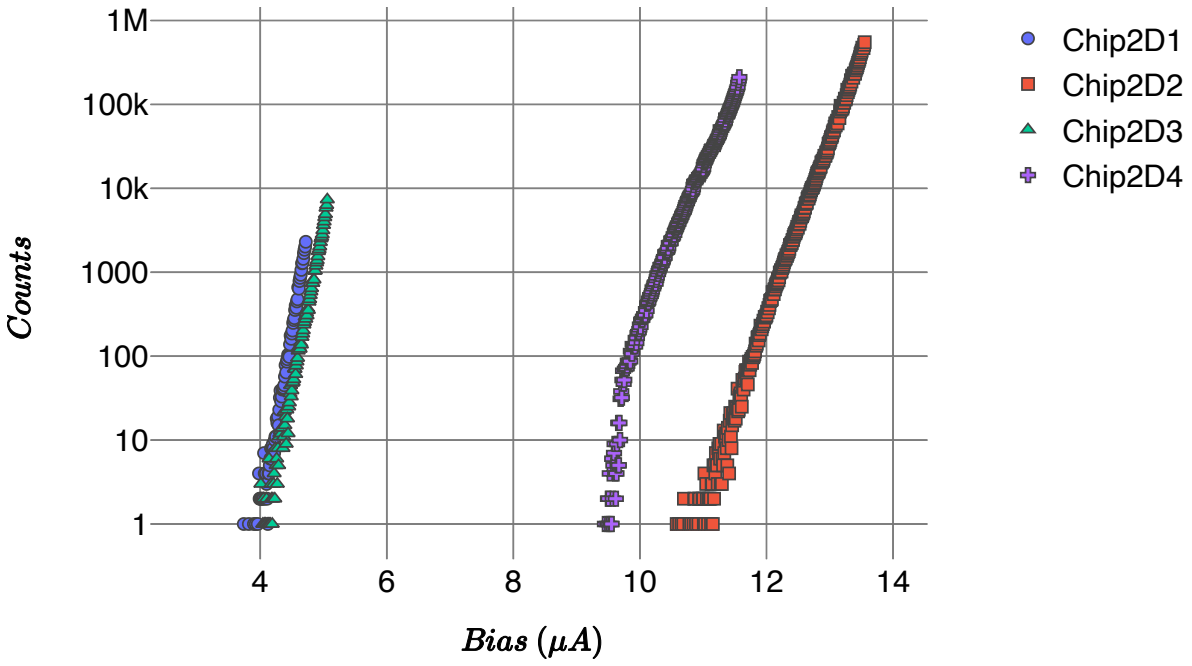

Figure 4.5: Comparison of DCR vs bias current for SNSPDs of various geometries. Measurement was performed at 2.5 K.

will have a much larger effect on the I_{sw} of the devices, at the expense of some detection efficiency. This could be a key parameter to optimise. The number of devices tested here was quite small especially if Chip3 is disregarded and it is difficult to form conclusions with a high degree of certainty. A more thorough study of the I_{sw} variation with variation of both fill factor and geometry would be a good avenue for future work. It will be interesting to fabricate nanowires with a 100 nm width but a 200 nm gap (fill factor of 33 %) to take advantage of the decreased current crowding whilst maintaining a narrow nanowire for effective detection of low energy photons.

4.3.2 Optical Response

Device Chip2D1 was chosen from chip 2 to fibre coupled to determine the optical response of the nanowire at a variety of wavelengths. This was a nanowire of 100 nm width with rounded corners chosen as it exhibited a good switching current. The device was coupled with SMF-28 fibre and alignment was performed manually as outlined in Ch.3, §3.2. An image of the aligned device is shown in Fig. 4.6. Good alignment was achieved, although manual alignment will typically exhibit more loss than a self-aligned scheme [174].

Once coupled, the detector was installed in a cryostat operating at 2.5 K. A diagram of the measurement setup is shown in Fig. 4.7. A cryogenic amplifier (Cosmic Microwave Technology CITLF1) was installed on the 40 K plate of the cryostat to amplify the detection pulses. The devices were tested at wavelengths of 1310 nm, 1550 nm and 2006 nm. Illumination was provided by CW laser diodes (Thorlabs) for the 1310 nm and 1550 nm measurements and an optical parametric oscillator (OPO) for the 2006 nm measurement. Variable optical attenuators (VOAs) were used to attenuate the photon flux to single-photon levels. For the two shorter wavelengths programmable optical attenuators from Agilent (8156A) were utilised and for the mid-infrared measurement MEMs based VOAs from Thorlabs were used.

The resistance-temperature (R-T) curve was taken to determine the T_c of the device. This was accomplished by a resistor heater located on the 2.5 K stage of the cryostat that was used to vary the temperature and record the resistance of the device against temperature. The resistance was recorded in 2-point measurement using a digital voltmeter with a device bias of 0.09 μA. The resulting R-T curve is shown in Fig.4.8. The T_c is defined as the midpoint in the transition and found to be 7.44 K. The transition width is defined between the points where the resistance is at 10 % and 90 % of its maximum and found to be 0.52 K. The temperature was varied up and then back down over a period of 4 hours to allow good thermalising of the device - there was no evidence of hysteresis in the measurement.

The output pulse of the SNSPD is shown in Fig.4.9. The rise time of the pulse is observed

Figure 4.6: Device 1 is aligned with the output from an SMF-28 optical fibre.

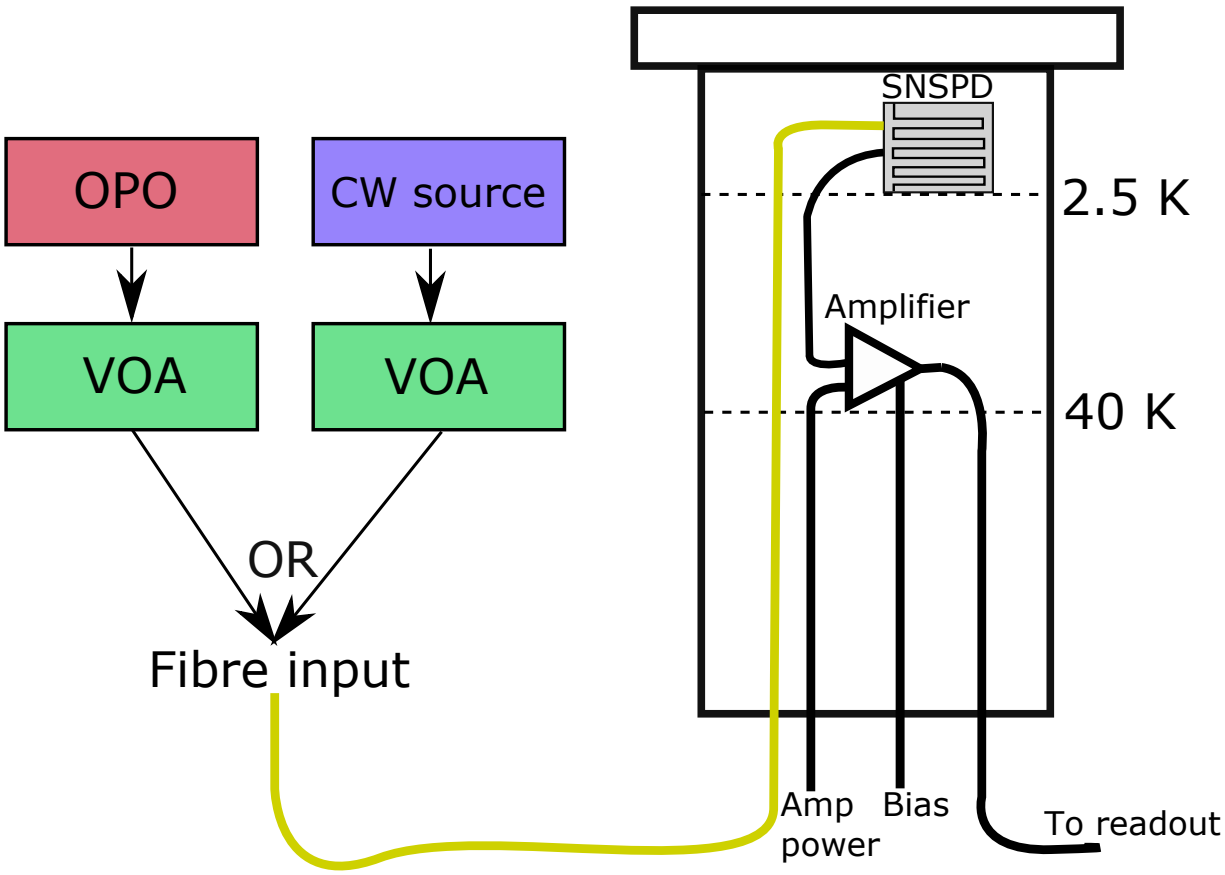

Figure 4.7: Experimental setup for ALD device testing. The CW source provided photons at 1310 nm and 1550 nm and the OPO provided 2006 nm photons. Photon flux was attenuated using the variable optical attenuators (VOAs) and sent to the SNSPD. Output pulses were amplified with a cryogenic amplifier mounted at 40 K. Yellow connections are fibre optic and black are electrical.

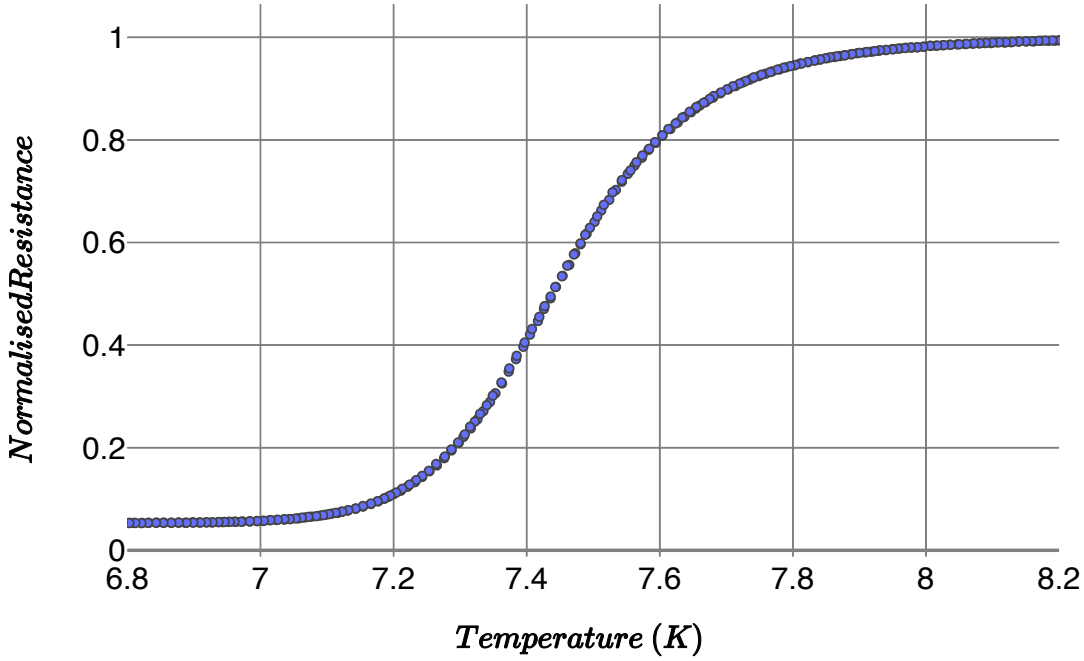

Figure 4.8: R-T curve for ALD device. The T_c is 7.44 K with a transition width of 0.52 K.

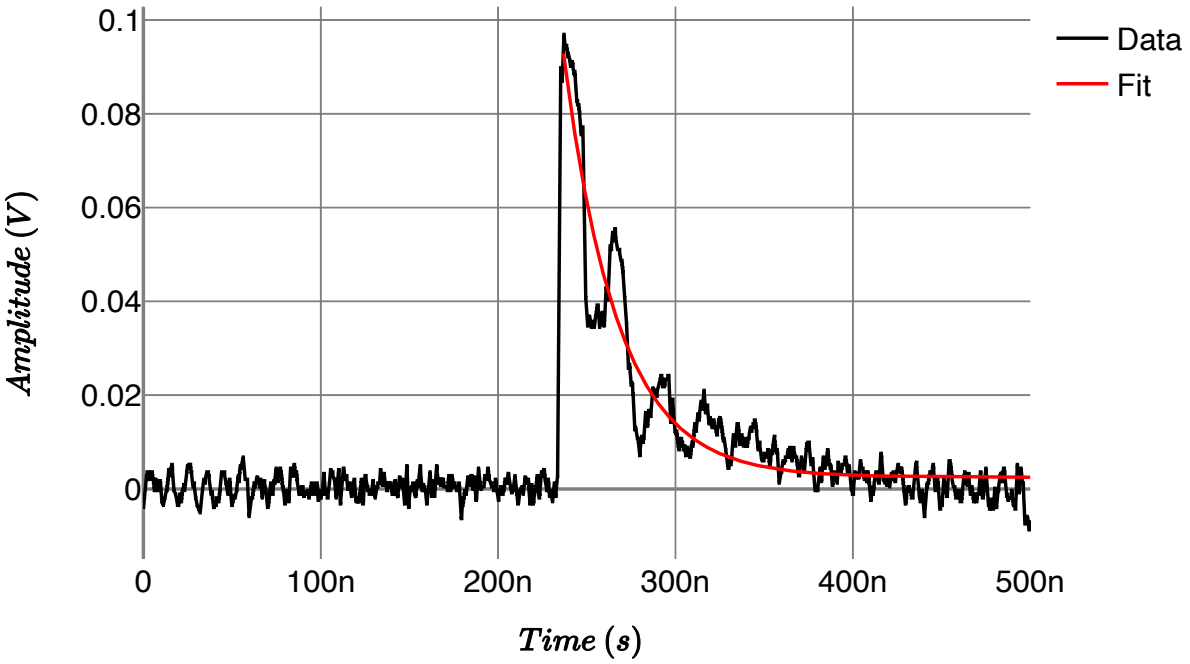

Figure 4.9: Pulse of ALD SNSPD. The rise time is 1.4 ns and the 1/e decay time is 32 ns. The reflections are an artefact of the cryogenic amplifier. Black line is the signal and the red line is the fitted function.

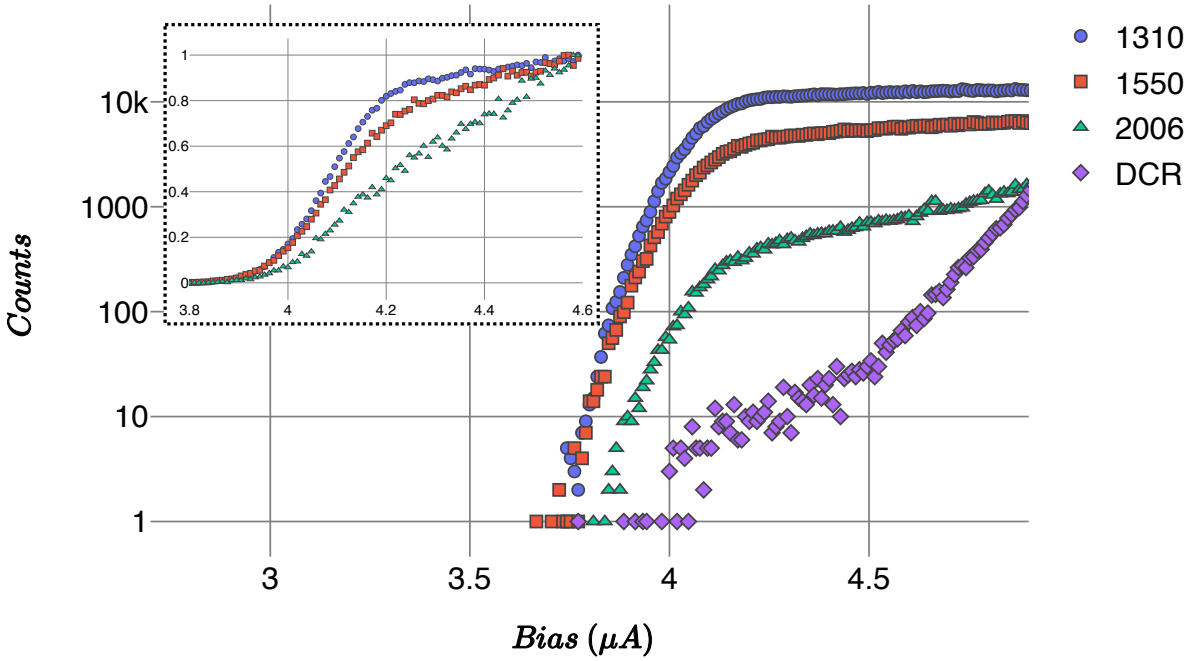

Figure 4.10: PCR and DCR curves for ALD device. The inset shows the same data on a linear scale and normalised for clarity.

to be 1.4 ns and then an exponential function is fitted to the decay to determine the decay time. From the fitting (shown in red in Fig.4.9) the 1/e decay time is determined to be 32 ns. From this the maximum count rate is estimated to be around 30 MHz.

For the photon response experiment the output photon flux was calibrated to 1 MHz for all wavelengths using the setup shown in Fig. 4.7 and connected to the fibre input at the input of the cryostat. The bias is then increased and a count reading taken for each point. The dark count rate (DCR) is measured with the source blocked and then each wavelength is measured to determine the photon count rate (PCR). Plots of PCR for each wavelength along with the DCR are shown in Fig. 4.10. A plateau region (that is where the PCR no longer increases with increasing bias current) is indication that the internal efficiency has saturated for the material for that particular wavelength. Essentially every photon that is absorbed results in a detector click. For wavelengths of 1310 nm and 1550 nm there is good evidence of such a plateau. For the 2006 nm measurement the effect is more subtle but there is still evidence of an inflection point in the data where the curve changes and flattens out. This inflection point is evidence that operation above the cut-off current, I_{co}, is being achieved. Above this operation in the deterministic single-photon detection regime is occurring, above the probabilistic detection regime [42]. The increasing of the count rate above

the saturated region is nevertheless present at all wavelengths and merits some discussion. It is hypothesised that this is caused by fabrication imperfections along the length or current-crowding in the bends of the nanowire that result in a non-uniform switching current across the length of the nanowire. This would result in sections of the nanowire achieving sufficient bias to operate above I_{co} whilst others were still operating in the probabilistic regime and therefore continue to increase in internal efficiency as the bias is further increased. The effect of increasing PCR above the saturated region is evident in many previous published works, particularly where ultra-narrow nanowires are used [45] (and hence chance of nanowire imperfections is increased). It is also in good agreement with previous work where long constrictions were deliberately fabricated into nanowires [175]. This hypothesis is also in agreement with the analysis of the switching currents presented earlier in this chapter where it was explained that the smaller than expected switching currents of the 100 nm nanowire could point to constrictions in the nanowire. This effect would become more pronounced as wavelength increases and photon energy decreases - which is in good agreement with the results.

As the input photon flux was calibrated to 1 MHz it is possible to compute some rough efficiency figures for each wavelength by subtracting the DCR from the PCR and dividing by the input photon flux. The values obtained are 1.2 % at 1310 nm, 0.6 % at 1550 nm and 0.1 % for 2006 nm. This value was taken at a bias current of 4.6 μA, 90 % of the I_{sw} for this device.

To measure the timing jitter, Δt, a pulsed fiber laser at 1550 nm was used giving fs pulses (<100 fs, KPhotonics CNT-1550) at 50 MHz. The output was split with a 90:10 optical splitter and a portion sent to a photodetector to act as a sync signal for a Becker and Hickl time correlated single photon counting card. The other portion of the split optical signal was attenuated to single photon levels and sent to the detector as per the PCR curve experiments. By integrating, a timing histogram of the variation of SNSPD pulse arrival times with respect to the sync signal was obtained. The full-width-half- maximum (FWHM) value of this is defined as Δt. Fig. 4.11 shows a Δt of 50.4 ps for the 1550 nm jitter test. For this test the detector was biased at $0.93I_{sw}$.

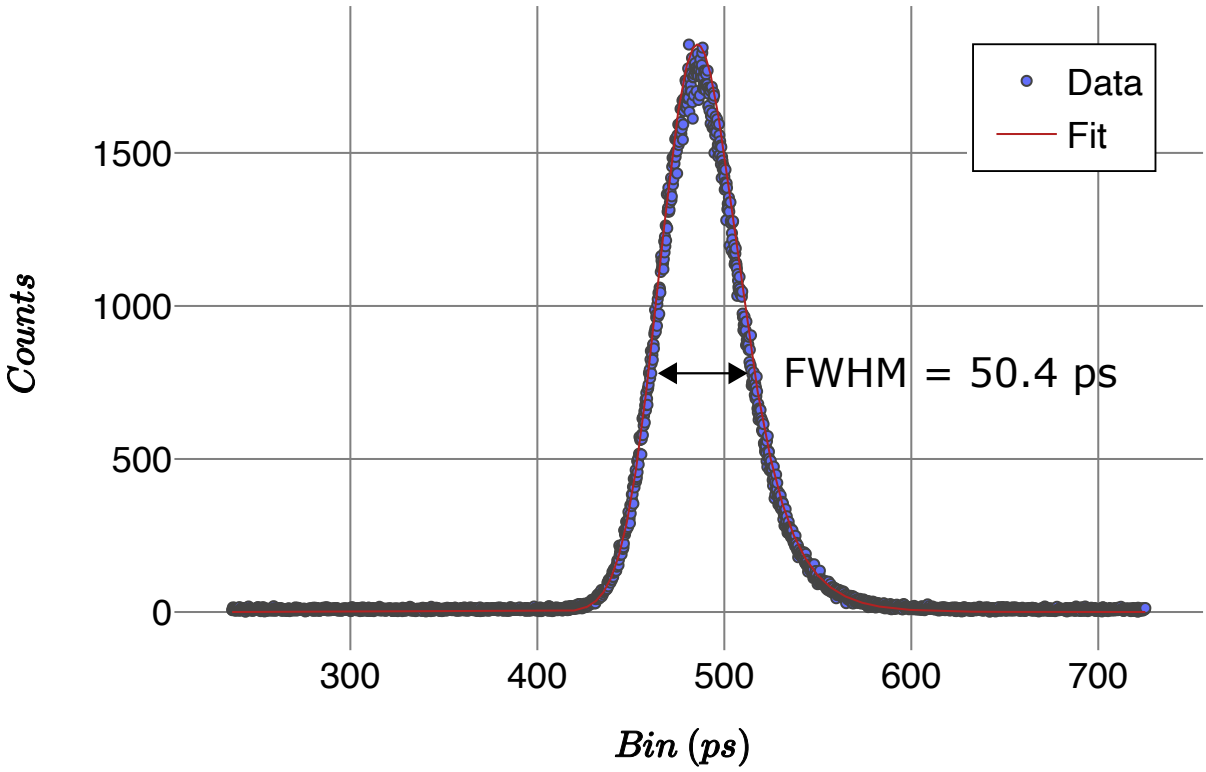

Figure 4.11: Jitter results for ALD device. A FWHM of 50.4 ps is determined after fitting the data with an exponentially-modified Gaussian.

4.4 Conclusions and Outlook

In this chapter the single-photon sensitivity of ALD NbN nanowires to infrared light up to a wavelength of 2006 nm was demonstrated. The timing jitter and single photon response was measured and found to be comparable to results for similar sputtered devices. The SDE's presented here are for bare superconducting nanowires - that is, a nanowire with no optical absorption enhancement. Embedding the nanowire into an optical cavity to enhance absorption at specific wavelengths [147, 176] would enhance the photon response greatly as per previously published work. It is also worth noting that for the 2006 nm measurement, the SMF-28 fiber was operating outside of it's specified wavelength regime and therefore additional loss in the cryostat was encountered. This will manifest itself as a reduction in the overall detection efficiency at longer wavelengths. Future work will include coupling with specialist mid-infrared fiber to combat this issue, discussed more in Ch. 5. The timing jitter is for a meander type device where no steps have been taken to mitigate the geometric component of the timing jitter associated with the meandering wire [41]. The evidence of saturated internal efficiency is a good indicator of the quality of the ALD film and shows the promise of this technology for SNSPDs. The next steps are to deposit NbN via ALD in an optical cavity type structure designed for use in the mid-infrared. Full optical characterisation of ALD NbN thin films in order to compare it more fully to sputtered NbN [177] will also be performed. Optimising film deposition is an ongoing

area of enquiry with the goal to deposit thin films of consistently high uniformity from which constriction-free nanowires can be fabricated.

In conclusion extended infrared single photon sensitivity in SNSPDs fabricated with ALD NbN was demonstrated with large area (10 μm x 10 μm) meander SNSPDs that are suitable for fibre optic coupling. Operation in the saturated internal detection efficiency regime of this material for wavelengths up to 2006 nm was shown. This demonstrates the viability of this growth technique, particularly for future work where reducing inhomogeneities in thin films in order to increase detector efficiency at long wavelengths will be the goal. This will also aid in the pursuit of scaling up devices to larger areas [178]. The next stage is to produce ALD NbN SNSPDs integrated in optical cavities for the mid-infrared to better investigate their detection characteristics at such wavelengths and enhance the system detection efficiency. Further optimisation of the ALD growth process in order to tune material composition and structure is also planned.

Chapter 5

SNSPDs for the Mid-Infrared

Development of mid-infrared SNSPDs currently lags far behind the work performed at telecom wavelengths. This is due to the underlying detection process not being fully understood at longer wavelengths as well as optical equipment for the mid-infrared being generally unavailable. SNSPDs, however, remain the only current realistic choice for single-photon detection in the mid-infrared (see Ch. 2, §2.2). In this chapter I will outline the fabrication and characterisation of SNSPDs for use in the mid-infrared. The devices presented here were fabricated by Dr Kleanthis Erotokritou whilst on an internship at the National Institute of Communication Technology (NICT) in Japan. We thank our collaborators at NICT for the opportunity and ongoing collaboration. The mid-infrared characterisation setup was designed and implemented by the author. All device characterisation and analysis was performed by the author. The DBR simulations and design was conducted by the author.

5.1 NbTiN Backside Coupled Detectors

5.1.1 Design

Our first attempt at SNSPDs for the mid-infrared was a backside-coupled cavity design using a NbTiN nanowire. A model of the design is shown in Fig 5.1. Backside-coupled refers to the fact that the optical fibre coupling the light to the detector is butted up against the bottom of the substrate and aligned so that the photons pass through the substrate onto the nanowire. The design was based on a NbTiN film of thickness 6 nm (T_c of 7 k) which was patterned into a nanowire of width 60 nm, meandering with an 80 nm gap over a 15 μm by 15 μm area. The nanowire was embedded in an optical cavity designed to enhance absorption in the mid-infrared and then capped with an Ag mirror. The absorption was simulated and the result is shown in Fig. 5.2. As can be seen in Fig. 5.2 the absorption peaks at 2.8 μm. These detectors were mounted onto copper sample mounts as in Ch. 3, §3.2. They were then fibre-coupled with SM-2000 fibre - an extended wavelength silica fibre option that offers transmission out to 2.3 μm, albeit with fairly

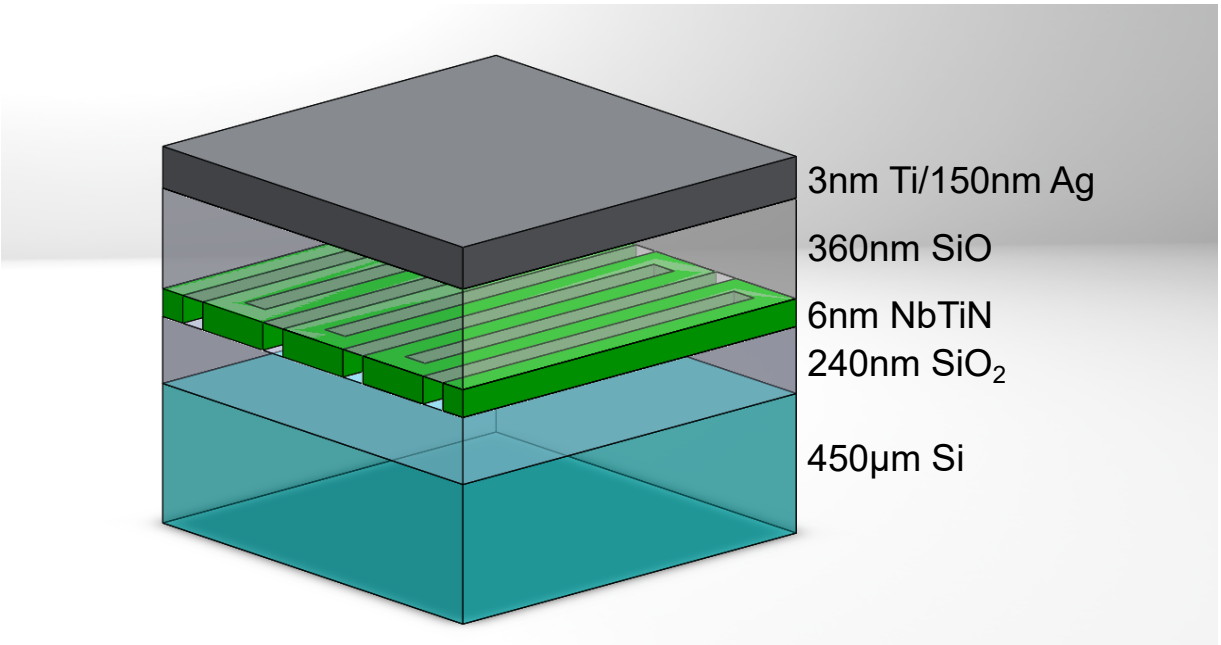

Figure 5.1: Model of NbTiN backside coupled mid-infrared SNSPDs. Not to scale.

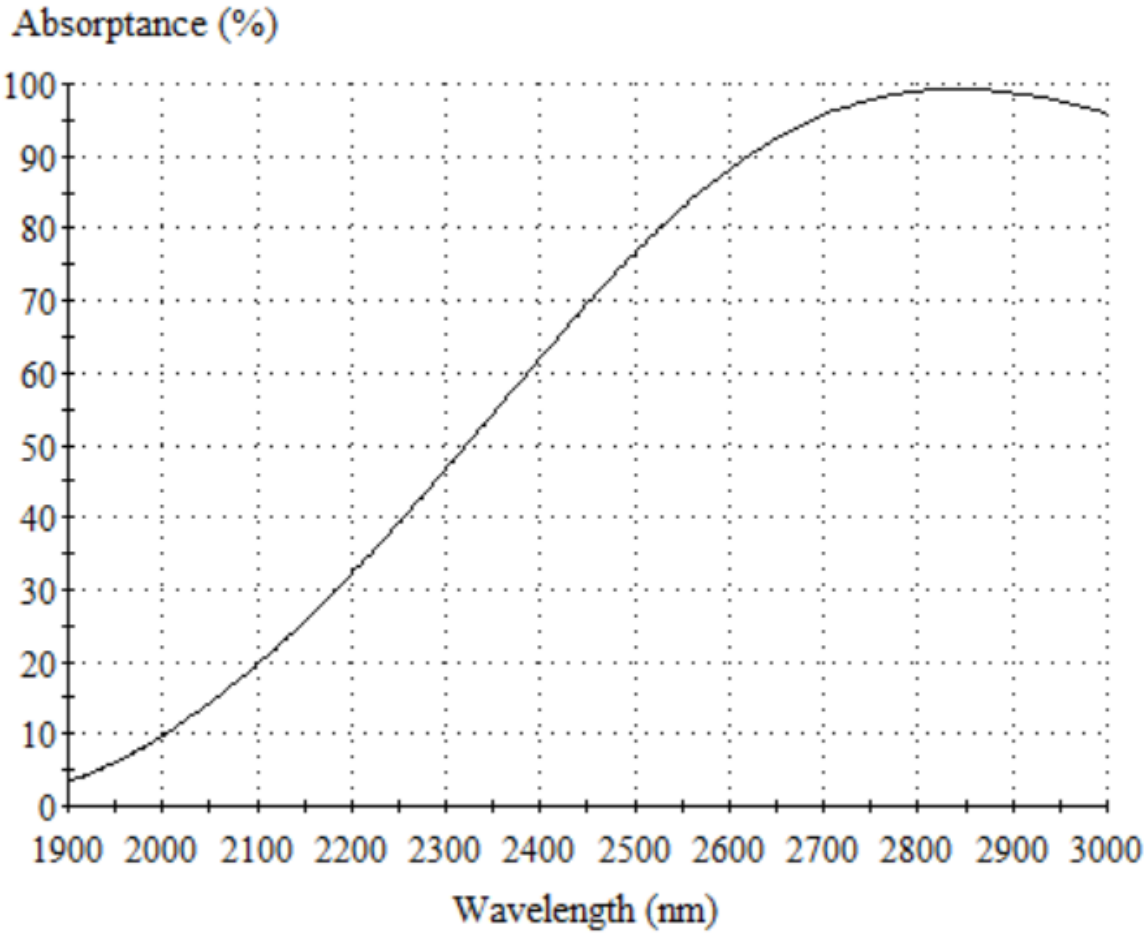

Figure 5.2: Simulation of absorption of the mid-infrared cavity design.

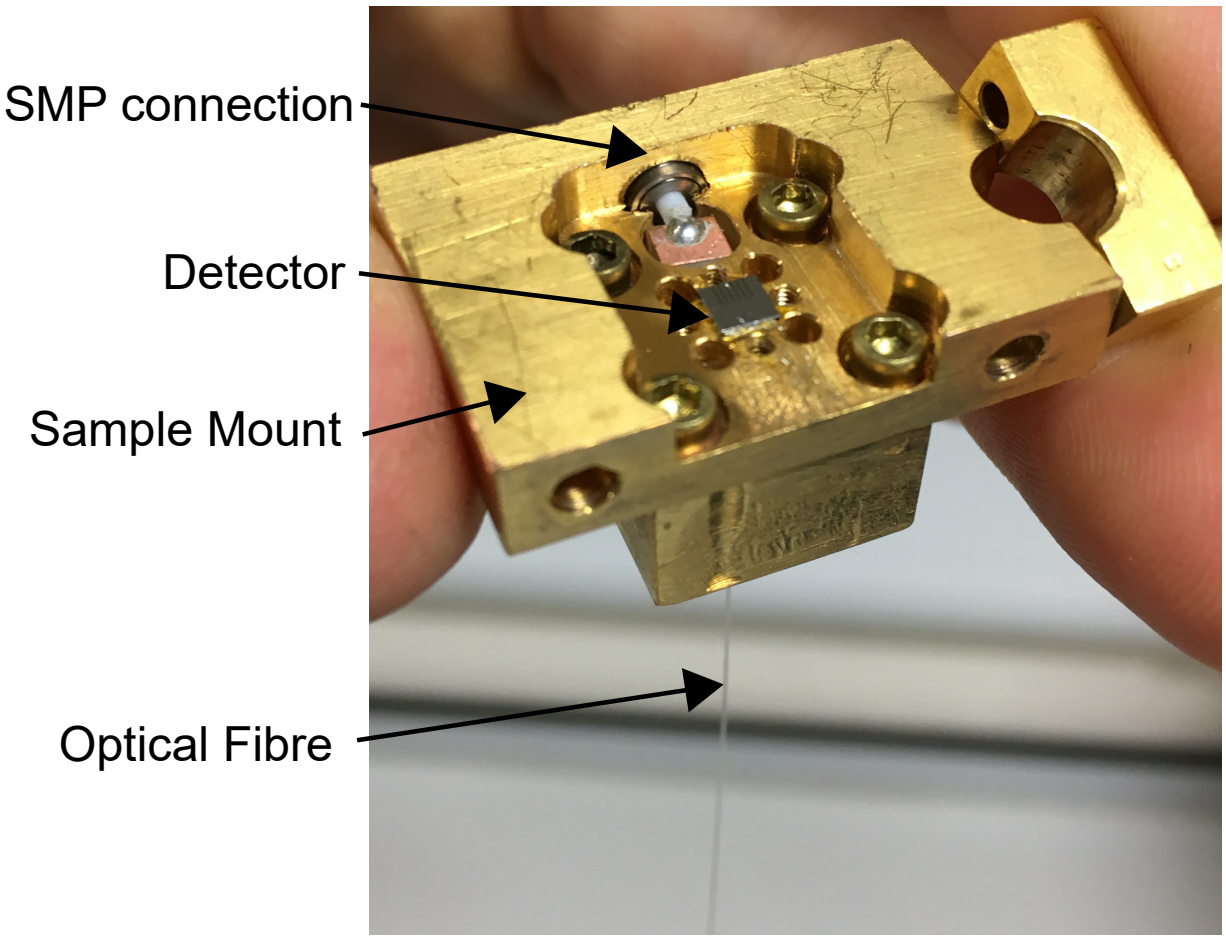

Figure 5.3: Mounted and fibre-coupled device.

large bend-induced loss (>5 dB for <10 mm bend radius). A photograph of a finished mounted device is shown in Fig. 5.3.

5.1.2 Detector Characterisation

The devices were characterised at 2.5 K utilising the OPO setup described in Ch. 3, §3.4. The critical current was experimentally determined to be 9 µA and served as the upper limit to the bias. The output of the OPO was set to 2.3 µm and attenuated down to 0.5 photons per pulse. The bias to the detector was then swept whilst the laser was off - to obtain the dark count rate (DCR) - and on - to measure the photon count rate (PCR). A plot of the DCR and PCR for the best measured device (device G1) is shown in Fig. 5.4. Fig. 5.4 shows the characteristic blackbody hump in the DCR as discussed earlier. The system detection efficiency of the detector is then calculated using the following:

$$SDE = \frac{PCR - DCR}{N} \tag{5.1}$$

where N is the number of photons per second, calculated from the photons per pulse and the repetition rate. This gives an efficiency vs bias plot shown in Fig. 5.5.

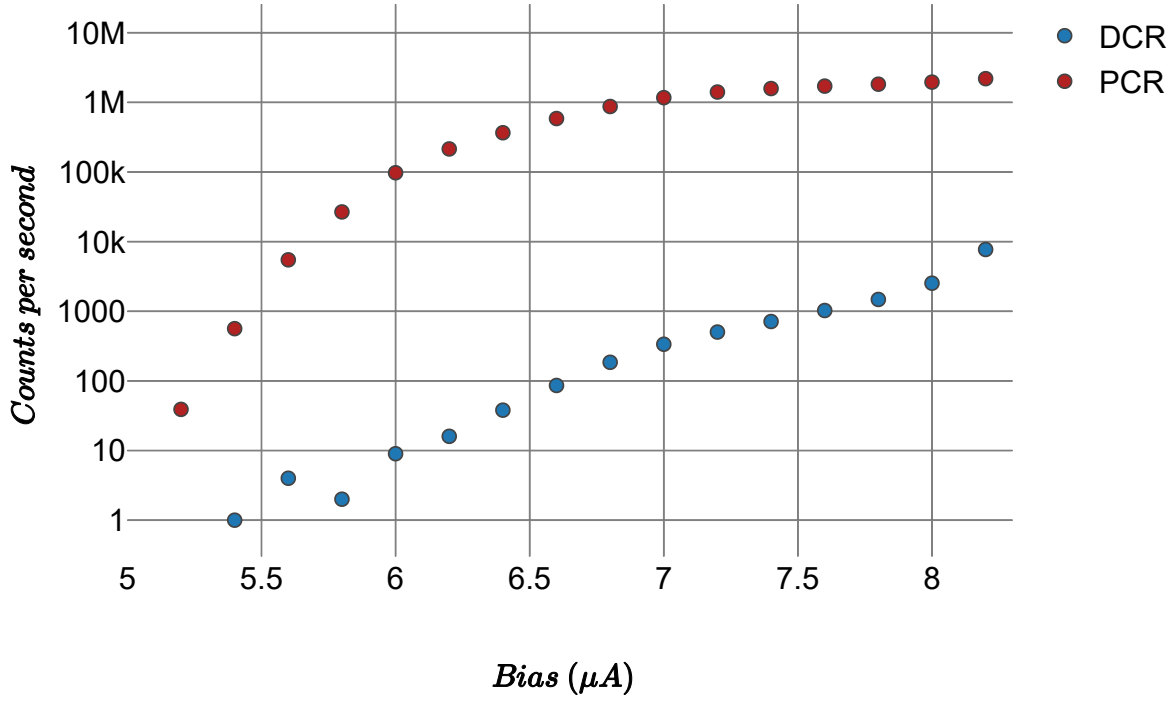

Figure 5.4: Photon count rate (PCR) and dark count rate (DCR) for device G1.

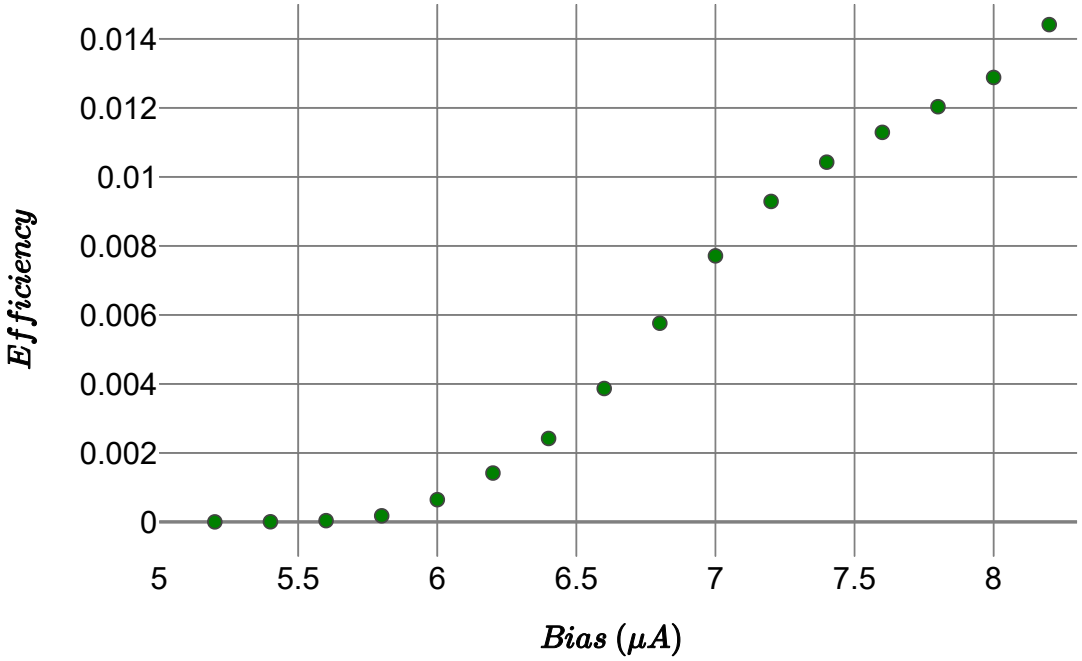

Figure 5.5: Efficiency against bias for device G1.

The efficiency of these devices exhibits a maximum of 1.5% at 2.3 μm. This is small in comparison to what would have been hoped but there can be some reasoning behind the observed low efficiency. As shown above, the absorption of this cavity shows a peak at 2.8 μm, but due to fibre restrictions the devices were operated on the edge of the SM-2000 operating window - 2.3 μm. If the absorption plot shown in Fig. 5.2 is examined it is evident that only 50% absorption at 2.3 μm is achieved. This can be taken as the absorption efficiency. A design issue with the backside-coupling of detectors in the mid-infrared has also become apparent. In prior backside-coupled detectors [179] at 1.55 μm, lensed SMF-28 fibre was used to focus the light through the substrate onto the active area of the device. Unfortunately at mid-infrared wavelengths lensed fibre is not commercially available - at time of writing - so standard flat ceramic ferrules were utilised. The divergence of the light from the end face of an SM-2000 fibre is given by [180]:

$$w(z) = w_0\sqrt{1+(\frac{z}{z_R(w_0)})^2} \tag{5.2}$$

where $w(z)$ is the beam radius, w_0 is the initial radius at the fibre end face, z is the distance and z_R is the Rayleigh range given by:

$$z_R(w_0) = \frac{n\pi}{\lambda_0}w_0^2 \tag{5.3}$$

where λ_0 is the wavelength and n is the refractive index of the medium (Si = 3.44). For 2.3 μm wavelength and the initial beam radius for SM-2000 of 6.5 μm, a beam radius of 15.7 μm is calculated. This gives a beam area of 774 μm^2. Given the active area of the device is 225 μm^2 then this means that only $\sim$29% of the light will fall onto the active area. This coupled with the 50% absorption at 2.3 μm wavelength gives an approximate absorption loss of 8.5 dB. As mentioned earlier in this chapter SM-2000 fibre exhibits fairly large bend-losses at 2.3 μm. A test with 1 m of SM-2000 fibre positioned in a cryostat gave a loss figure of 0.7 dB. If the 2 m of fibre utilised in the characterisation setup is taken and included with two FC/FC fibre connectors it is not unreasonable that the loss approaches 2 dB. Adding this fibre loss to the coupling and absorption losses would give a maximum system detection efficiency of around 9%, still somewhat larger than the maximum measurement. If Fig. 5.5 is examined we can observe that there is no evidence of a saturated efficiency plateau - it would be expected that the efficiency rises and then flattens out as the bias is increased. This indicates issues with the detectors, preventing the achievement of maximum detection efficiency, which will be discussed at the end of this section.

As mentioned, for these efficiency measurements, the output of the OPO was attenuated down to 0.5 photons per pulse. Following Poisson statistics, the probability of a detector click being

caused by a multi-photon absorption is given by:

$$P = \frac{\lambda^k e^{-\lambda}}{k!} \tag{5.4}$$

where λ is the actual absorbed photons per pulse and k is the number of absorbed photons per pulse that the probability is being assessed for. The most likely multi-photon event is for $k = 2$ so the probability of this event is assessed. The number of absorbed photons per pulse is given by the absorption efficiency outlined above, 0.145, given by the coupling efficiency multiplied by the absorption efficiency. This is multiplied by the number of photons per pulse from the source, 0.5, to get 7.25×10^{-2}. Plugging these numbers into Eq. 5.4 a probability, P, of absorbing 2 photons in a pulse of 2.4×10^{-3} is calculated. As progressive probabilities for higher order multi-photon events will continue to decrease it is therefore reasonable to conclude that the device is single-photon sensitive.

The timing jitter of this device was measured using a Hydraharp 400 time correlated single photon counting (TCSPC) module from Picoquant. TCSPC modules are sensitive timing instruments that can timestamp photon arrival times relative to a sync signal to, in the case of the Hydraharp 400, 1 ps intervals. To measure the jitter of the device the OPO sync output (lower wavelength) output was fed into a fast photodetector (Thorlabs DET08CFC) which served as the sync pulse (start) for the Hydraharp. The idler OPO output was delayed in a length of fibre and sent to the SNSPD input. The output pulse from the SNSPD was then sent to the Hydraharp as the stop signal. In this way after sufficient integration time a timing histogram is built up. This histogram can be fit with an EMG function as described in Ch. 2, §2.1.3, and a full-width-half-maximum (FWHM) value of the timing jitter obtained. The output from device G1 is shown in Fig. 5.6. Here a value of 280 ps FWHM is obtained for the device G1. To verify this two SNSPDs from the same batch - G1 and a second device E3 are used. Instead of using the DET08CFC as a sync the idler output from the OPO is split and the first half sent to E3. The pulses from E3 serve as the sync for the Hydraharp. The second half was delayed and sent to device G1 as before. This should yield a FWHM that is the addition of the two jitters as:

$$\Delta t_{total} = \sqrt{\Delta t_{E3}^2 + \Delta t_{G1}^2} \tag{5.5}$$

This yielded the result shown in Fig. 5.7 with a FWHM value of 400 ps. Assuming jitter is similar across devices from the same wafer this aligns well with the 280 ps measurement for a single device. The maximum count rate of the detector was estimated from the reset time of the detector - 100 ns - to be 10 MHz.

The characterisation results shown here at 2.5 K for 2.3 μm wavelength suggest that G1 is not achieving a sufficiently high bias current for saturated internal detection efficiency and low

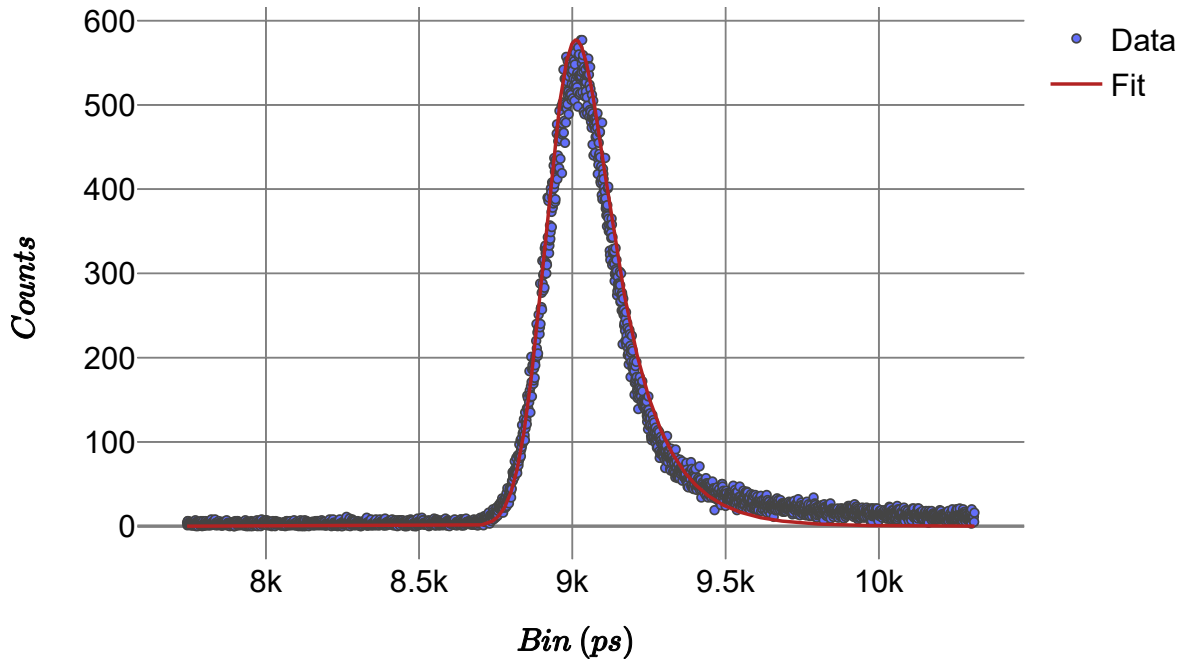

Figure 5.6: Jitter histogram for device G1 at 2.3 µm. A FWHM value of 280 ps is obtained. The data has been fitted with an exponentially modified Gaussian as discussed in Ch.2, §2.1.3

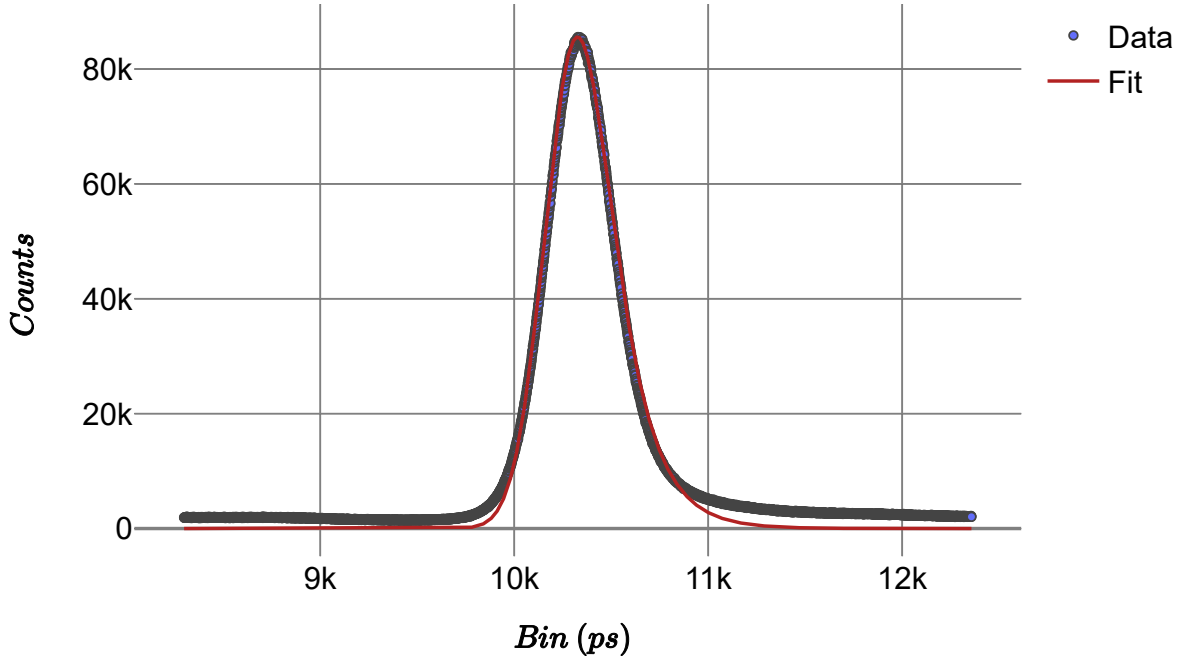

Figure 5.7: Combined jitter measurement for two SNSPDs (G1 and E3) at 2.3 µm wavelength. A FWHM of 400 ps is obtained.

timing jitter. As outlined in Ch. 3, §3.1.4, if it is not possible to bias to a sufficiently high fraction, C, of the depairing current then operation on the efficiency plateau will not be achieved. As can be seen in Fig. 5.5 the efficiency curve shows no plateau. This also ties in with the high timing jitter measured - it would be expected that a value of < 100 ps would be obtained for a similar NbTiN devices, as well as a critical current larger than the 9 μA measured here [181] [182]. This all points to an issue with uniformity of the film or nanowire preventing the achievement of a high C, limiting the internal detection efficiency and increasing the timing jitter.

5.1.3 Characterisation at 350 mK

To gain further insight into the characteristics of the detectors, detector G1 was cooled in a different cryostat to 350 mK (see Ch. 3, §3.3, for description of cryostats). The characterisation setup was kept as before except the output of the filtering and attenuation setup was sent through 10 m of SM2000 fibre to a neighbouring laboratory where the colder cryostat was housed. The loss in the long fibre was measured and added to the total attenuation therefore the efficiency figures shown here are from the optical input to the cryostat. Fig. 5.8 shows the DCR and PCR as well as the calculated efficiency for G1 at 350 mK for 2.3 μm wavelength.

Fig. 5.8 shows a few interesting features that are worthy of discussion. The first is that the efficiency of the device appears to have dropped from a maximum of around 1.5% at 2.5 K to around 0.5 % at 350 mK. This is quite the opposite of what might be expected from the literature [183] where it is expected that for homogeneous nanowires it would remain relatively constant or even increase if constrictions are evident. The shape of the efficiency curve is, however, similar to that shown in Fig. 5.5 which indicates that the efficiency degradation may be due to losses in the cryostat. The 350 mK cryostat has a smaller inner volume and less room to manoeuvre fibres without bending them. Another possibility is that, due to events outside of our control, the devices were left at room temperature and atmospheric pressure for several months between measurements which may have lead to degradation of the detectors. Although difficult to concretely measure due to the fibre at the detector end being permanently fixed it is hypothesized that these efficiency losses are mainly due to optical loss rather than detector degradation. The switching current, I_{sw} is slightly lower at 350 mK (7 μA) than at 2.5 K (8 μA) which may indicate degradation (and again is against what may be expected [184]) but the varying DC offsets in the neighbouring labs could also account for this small change. What is encouraging is that the device starts counting earlier in its bias range at 350 mK. This indicates a broadening of the detection range and although still not saturated at 2.3 μm was interesting to look at for shorter wavelengths. Fig. 5.9 shows the comparison of 1550 μm efficiency data for 2.5 K (top) and 350 mK (bottom). As is evident in the figure the lower temperature significantly extends the saturated plateau as per other results [185]. The improvement of the maximum detection efficiency also further indicates that device degradation is not responsible for the drop in 2.3 μm efficiency and

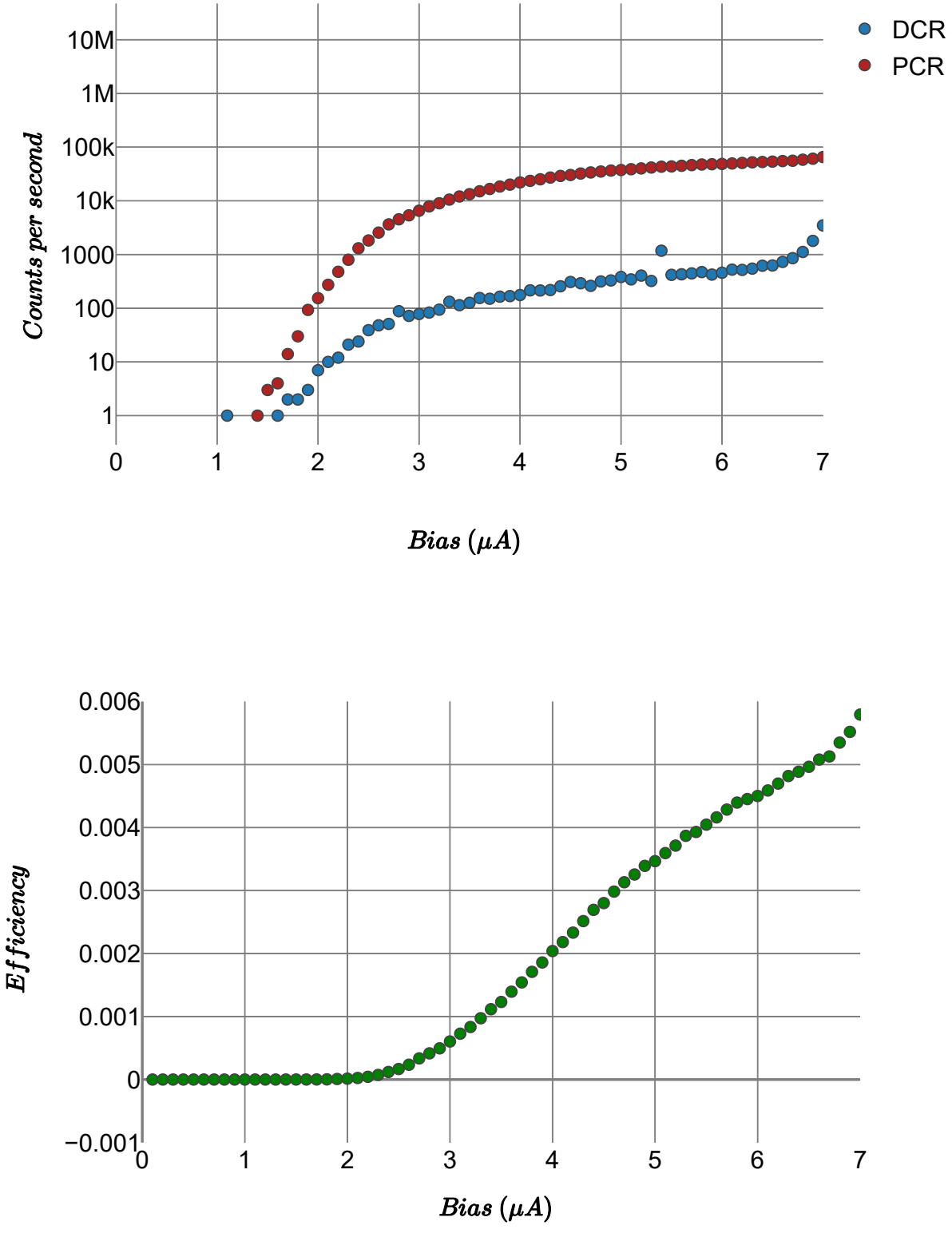

Figure 5.8: Top: DCR and PCR for 2.3 µm wavelength photons incident on device G1 at 350 mK. Bottom: Calculated efficiency for the same device.

further points to optical losses - as 1550 nm light will not be as significantly affected by bends in the optical fibre.

As shown in [39] and [109] the lower operating temperature should result in a higher fraction of the depairing current, C, being attained and therefore the timing jitter should decrease - as well as the lengthening of the saturated plateau observed above. Fig. 5.10 shows the timing histogram for device G1 at 350 mK when illuminated with 2.3 μm photons. A FWHM value of 179 ps is observed which is over 100 ps improved when compared to the same device and wavelength at a temperature of 2.5 K.

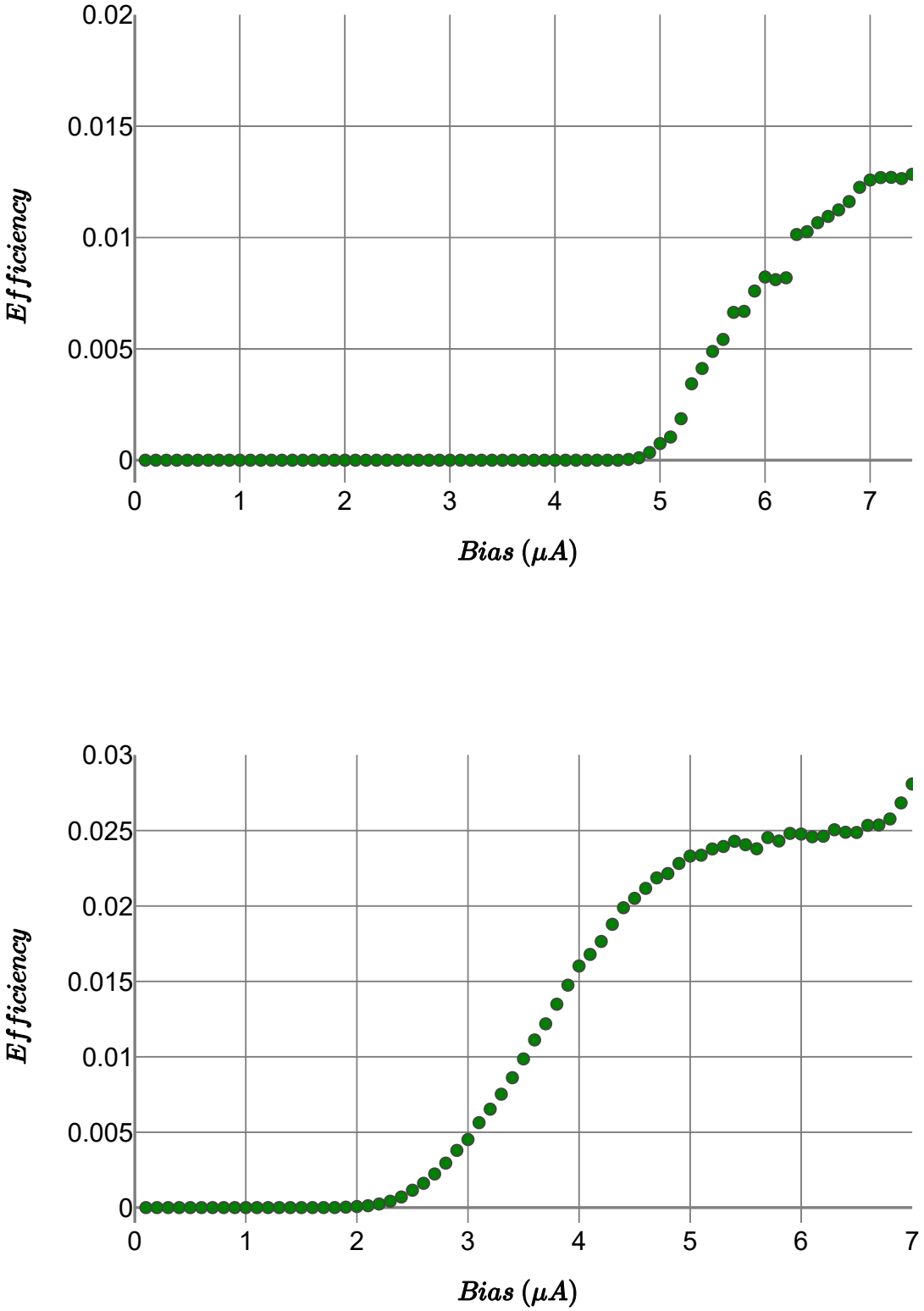

Figure 5.9: Top: Efficiency of G1 at 1550 µm at 2.5 K. Bottom: Efficiency of G1 at 1550 µm at 350 mK.

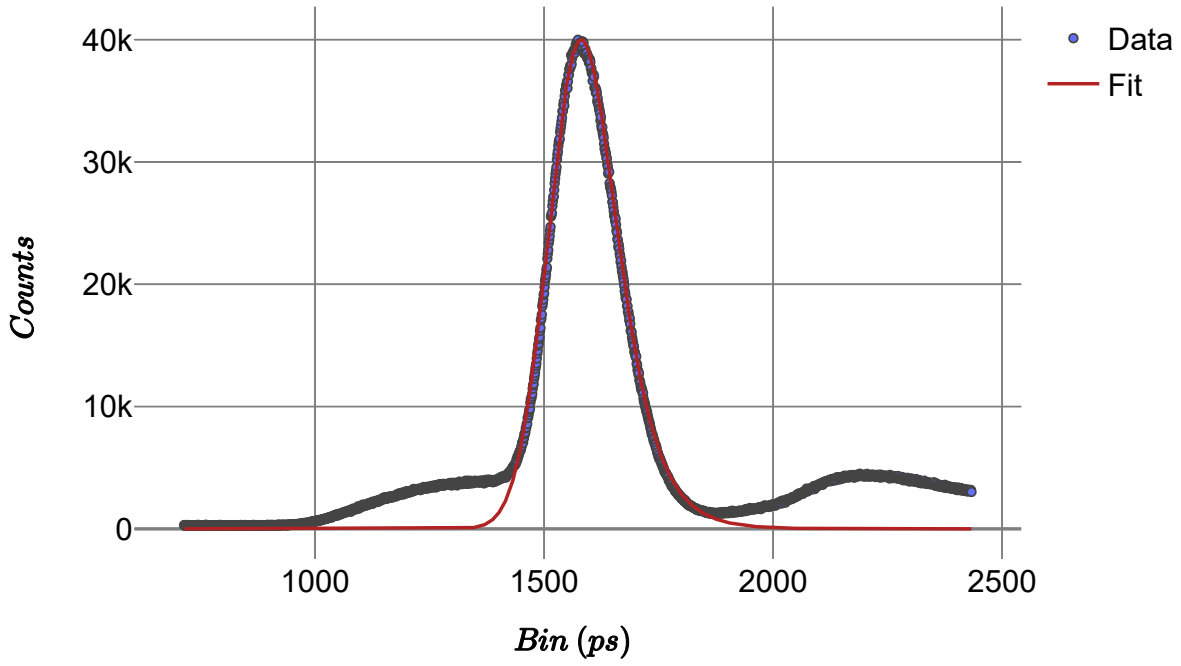

Figure 5.10: Timing jitter histogram of device G1 at 350 mK for 2.3 µm photons. A FWHM value of 179 ps is seen. The reflections observed in the histogram are likely due to optical reflections within the system such as fibre connections.

5.2 DBR Frontside Coupled Detectors

The first generation detectors helped the development and validated the test setup as well as providing some detectors to undertake initial proof-of-concept experiments (see Ch. 6). However there were some obvious design flaws which were addressed in the design of the next batch of detectors.

5.2.1 Design

The first clear issue to address was that of the backside-coupling. As shown in the previous section, backside-coupling without the introduction of lensed fibres results in less than 30% of incident light hitting the nanowire (for 450 μm Si substrate). The obvious solution is to switch to frontside-coupled devices where the fibre end-face is butted up against the nanowire, minimising the distance the light travels. Possible candidate designs would include a cavity type design similar to the previous backside-coupled work but with the layers reversed, such that the Ag mirror is grown on top of the substrate and then the dielectric-sandwiched nanowire. An alternative approach is to utilise distributed-Bragg-reflectors (DBRs) [186]. DBRs (also known as Bragg mirrors) are reflectors based on alternating layers of materials with a varying refractive index. Each boundary causes a reflection and with suitable design considerations, constructive interference between subsequent reflections can create a wavelength-selective high reflectivity mirror. Good results at shorter wavelengths have been previously achieved with a DBR type device [176] and indeed the record efficiency of 98 % at 1550 nm was achieved with a DBR device. A SiO_2/Ta_2O_5 DBR with 10 bilayer repeats (20 layers total) was chosen. A simulation of the reflectance of such a structure is shown in Fig. 5.11. A niobium nitride (NbN) film will then be deposited on top of the DBR and the nanowire will be patterned into that. A model of the design is shown in Fig. 5.12.

The DBR parameters to achieve the simulation response shown in Fig. 5.11 were a bilayer with 274 nm of Ta_2O_5 and 401 nm of SiO_2. This was then repeated 10 times giving a total thickness of 6.75 μm, on top of the Si substrate. Leading on from the ALD work shown in Ch. 4, ALD NbN has been chosen to be deposited on top of the DBRs for fabrication into SNSPDs. Unfortunately, due to pandemic restrictions across 2020 and 2021, fabrication has not been completed at the time of writing this thesis. Therefore it is not possible for me to present characterisation results for these devices. Nevertheless, the DBR substrates are with collaborators for ALD growth and it is hoped that these will be ready for fabrication in the coming months.

In parallel to the above the mid-infrared testing setup has undergone further development and now has the capability to couple from the OPO to the device entirely in ZBLAN mid-infrared fibre. This will afford the ability to characterise detectors further into the mid-infrared than is

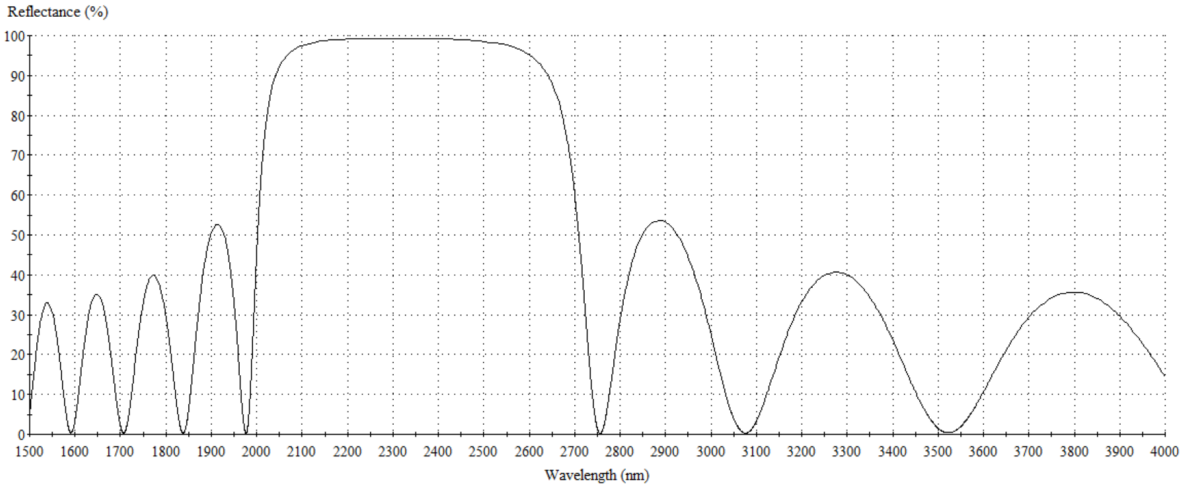

Figure 5.11: Simulated reflectance of a 10 bilayer DBR of SiO_2/Ta_2O_5.

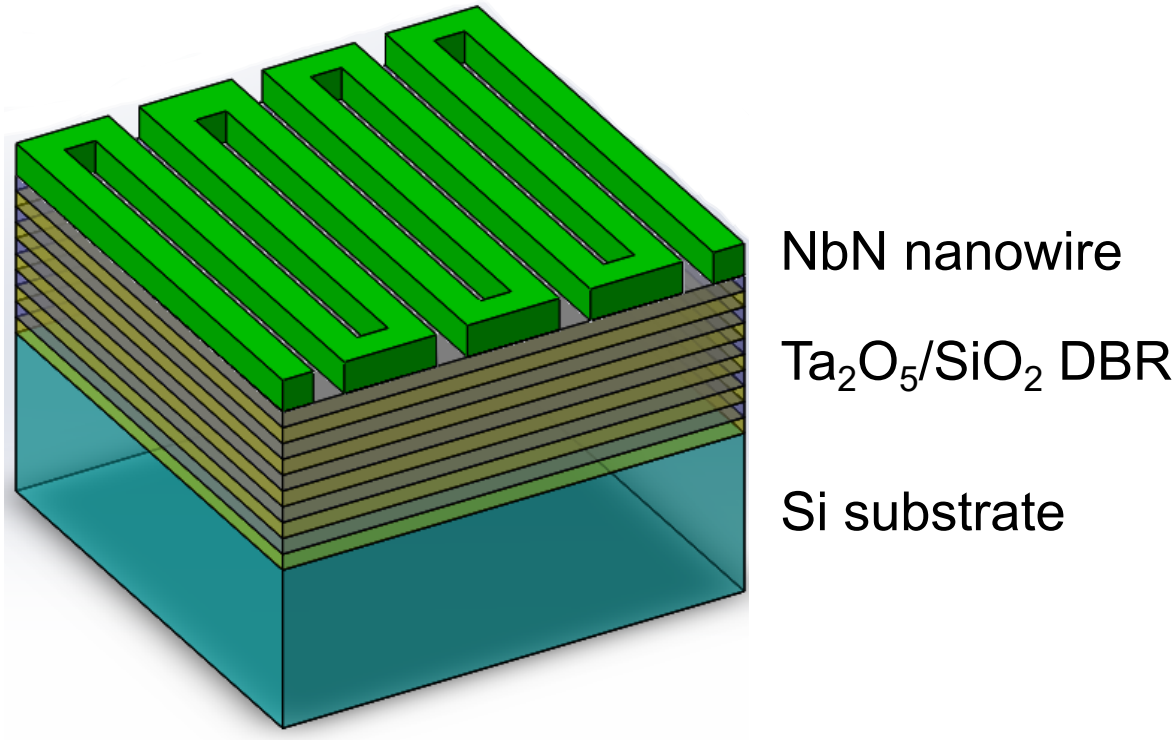

Figure 5.12: Model of planned DBR based frontside-coupled device. Not to scale.

currently possible - right out to 4 μm. A second <1 K cryostat of similar design to that shown in Appendix. A is under construction to allow characterisation at this lower temperature also.

5.3 Outlook

The first generation of mid-infrared cavity SNSPDs were by no means perfect but allowed the exploration of applications in the mid-infrared whilst informing the design decisions for the second-generation. As well as the proof-of-principle mid-infrared LIDAR experiments described in detail in Ch. 6, the detectors were also used in the first demonstration of quantum interference in the mid-infrared [114]. This involved pumping a custom periodically-poled lithium niobate (PPLN) crystal at 1040 nm and produce entangled photon pairs at 2.1 μm by spontaneous parametric down-conversion. Indistinguishably was verified through a Hong-Ou-Mandel (HOM) interferometer and polarisation entanglement demonstrated. This work was an encouraging first step into further quantum optics and quantum key distribution experiments in the mid-infrared where SNSPDs will be the only suitable detector.

As shown above, work is well under way to improving the detection metrics of the next generation of mid-infrared SNSPDs. With these improved detectors it is hoped to conduct further demonstrations of mid-infrared quantum optics such as free-space quantum distribution in the 2 to 2.5 μm window where the advantages outlined in Ch. 2, §2.2.1, can be realised.

Chapter 6

Experiments in Single Photon LIDAR with SNSPDs

As was explored in Ch. 2, §2.3.2, SNSPDs lend themselves well to single-photon LIDAR experiments due to their detection characteristics. In this chapter, two LIDAR experiments utilising SNSPDs are reported. The first is a proof-of-principle mid-IR scheme at 2.3 μm wavelength [7]. As shown in Ch. 2, §2.2.1, the mid-IR offers unique advantages for free-space applications such as LIDAR. The second experiment employs a novel design of SNSPD employing a differential tapered readout to allow a timing jitter of $\sim$13 ps. As described in Ch. 2, §2.3.2, the reduction of the timing jitter results in a narrow returns histogram that reduces the integration time quadratically for a given SNR. This experiment was conducted over long ranges at 1.55 μm.

The devices used for the mid-infrared LIDAR at 2.3 μm were fabricated by Dr Kleanthis Erotokritou whilst on an internship at the National Institute of Communications Technology (NICT) in Japan as characterised in Ch.5, §5.1. The LIDAR experiment was performed by the author building on previous work by Dr Nathan Gemmell. Nathan was also generous with his advice throughout the whole experiment and I am grateful. Data processing and analysis was performed by the author.

For the ultra-low jitter LIDAR, devices were fabricated jointly by collaborators at the Jet Propulsion Lab (JPL) in California, USA and the Massachusetts Institute of Technology (MIT) in Massachusetts, USA. The scanning transceiver was designed and built by Dr Aongus McCarthy from Heriot-Watt University, UK, who also provided invaluable LIDAR expertise. Cryostat design and construction was performed by the author (see Appendix A). Characterisation of devices in Glasgow was performed by the author. The field trials were conducted by the author with Dr Aongus McCarthy. Analysis of the data and image construction was performed by the author. I again would like to thank all of our collaborators for making this work possible.

6.1 Mid-Infrared LIDAR at 2.3 µm

6.1.1 Motivation

To date, most single photon LIDAR systems have been at the telecom wavelength of 1.55 µm [131] [132] [125]. As can be seen in Fig. 2.5 (Ch. 2) This wavelength shows an area of low atmospheric attenuation and less solar background radiation than shorter wavelengths as well as affording the use of low-cost, easily-available telecom components. If the area further up the wavelength scale in Fig. 2.5 is examined an area between 2 and 2.5 µm is evident which shows an equally low atmospheric attenuation as well as exhibiting an area of solar background over 3 times lower than at 1.55 µm. This is attractive for LIDAR as solar background is a large contributor to system dark count rate when operating in daylight conditions and minimising it will result in an increase in SNR. It is worth noting that if the spectral region further up the wavelength scale in Fig. 2.5 are investigated there are further windows of minimal solar irradiance - for example an area just below 4 µm. However as shown in Ch. 3, §2.2.2, the blackbody radiation from room-temperature components is an issue at mid-infrared wavelengths and the effective crossing point of RT blackbody and solar radiation is at ∼2.3 µm. Above this wavelength RT blackbody increases and swamps the detector unless some sort of mitigating experimental design is considered - for example cold filtering in the cryostat.

6.1.2 Experimental Setup

The detector used in this experiment was a 2.3 µm cavity backside-coupled device fabricated at NICT Japan and characterised in Ch. 5, §5.1.2. It was a NbTiN based device exhibiting detection efficiency of 1.5% at 2.3 µm, 1 kHz DCR and a temporal jitter of 280 ps FWHM. This device was mounted into a Gifford-McMahon cryocooler (Sumitomo RDK-101D) and cooled to 2.5 K. SM2000 silica fibre was used to interface the detector with the receive channel of the optical setup. The optical parametric oscillator (OPO) from Chromacity was tuned to give ∼ps pulses at 2.3 µm wavelength as a source and was passed through a bandpass filter (CW 2328 nm +/- 43 nm) and ND filters as required to attenuate the output to a suitable level. This was coupled into the transmit section of the optical setup. A full diagram of the system is shown in Fig. 6.1. The OPO provides an output pulse and sync pulse that is fed into a fast photodetector (Thorlabs DET08CFC) to act as the start signal for the TCSPC module (Hydraharp from Picoquant). The filtered output pulses from the OPO are input into the optical setup through a reflective collimation package and then passed through a variable aperture to control the beam size. Once through the aperture they are output through the central hole (3.2 mm) of an annular mirror (an off-axis parabolic (OAP) mirror with a central hole) and sent out towards the target. Once reflected from the target of interest the annular mirror collects the returns and they are focussed by a plano-convex lens and a further parabolic mirror into the fibre running to the SNSPD. The output pulse from the

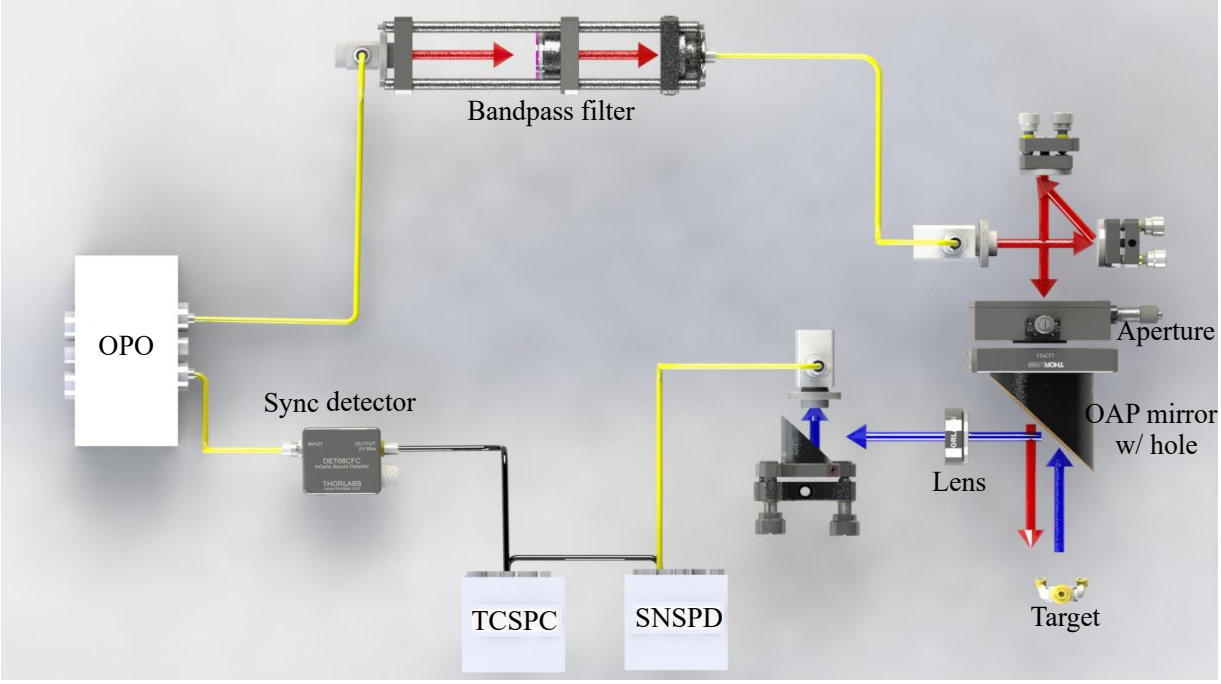

Figure 6.1: Experimental setup of 2.3 µm LIDAR demonstration. The outgoing light path is shown in red and the return shown in blue. Black connections indicate electrical connections while yellow indicates optical fibre.

SNSPD is then coupled to the TCSPC module to act as the stop signal.

6.1.3 Results

Instrument Response Function

In order to perform cross-correlation a clean IRF is required. To obtain this pulses are sent through the LIDAR setup described above and reflected from a flat metallic surface. A histogram is built up over a 30 second integration period and then fitted with a exponentially-modified Gaussian distribution to determine the timing jitter of the system - a plot of this is shown in Fig. 6.2. This reveals a timing jitter of ∼280 ps as measured in Ch.5, §5.1.2, for this detector.

Determination of Resolution

The initial test of the system was to determine the separation of two non-reflective white cardboard sheets that were co-illuminated by the output beam at 2.3 µm wavelength. A diagram of the setup is shown in Fig. 6.3. As is shown in the figure the separation between the two sheets, d, can be varied. The beam is incident on both sheets and photons are returned from them both. In this way a histogram is produced with two peaks, one corresponding to the first sheet of paper and one by the second. By fitting the data with a double Gaussian distribution the peak positions can be determined and hence the distance between the two peaks. The separation is reduced gradually until the two peaks can no longer be distinguished by the fitting. In Fig. 6.4 the distance between

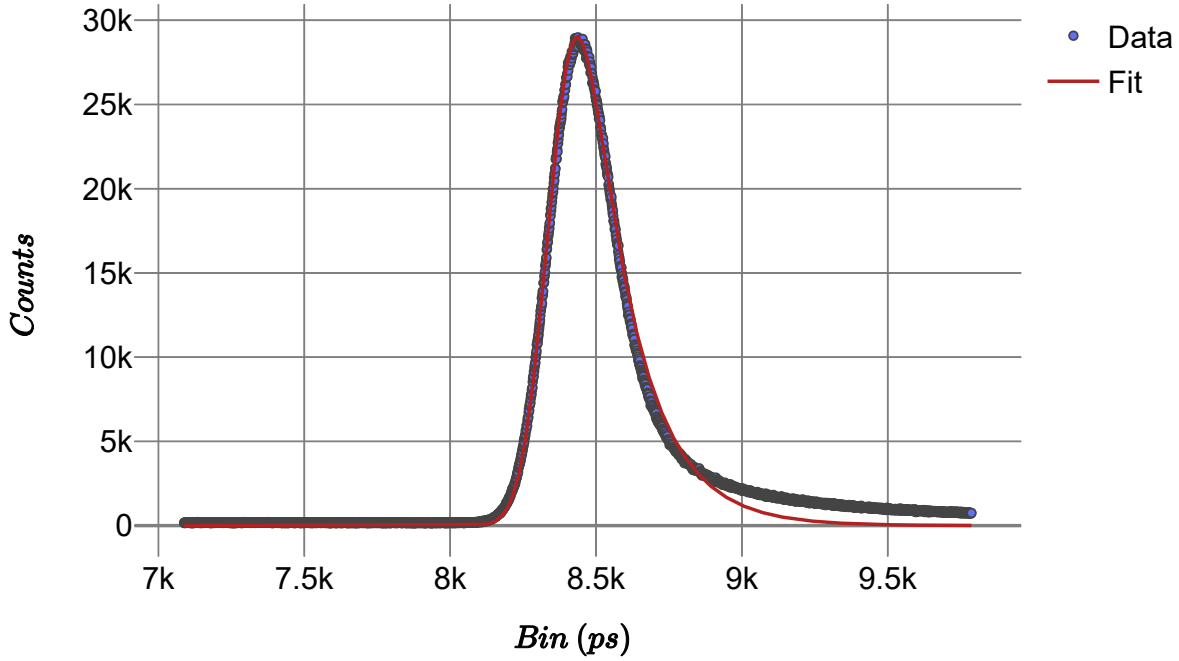

Figure 6.2: Instrument response function of the LIDAR setup. A FWHM of 280 ps is measured.

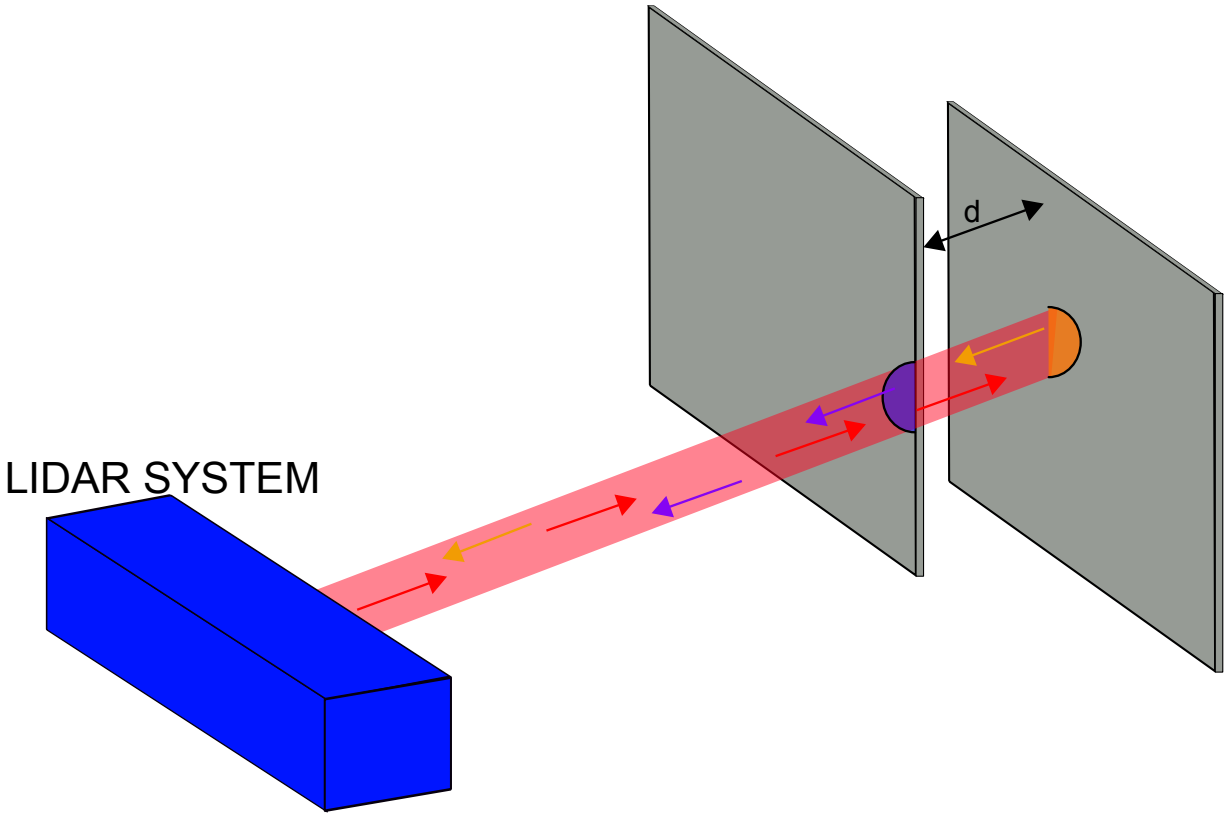

Figure 6.3: Diagram of the depth resolution test. The red shows the path of the optical pulses. Red arrows indicate outward pulses and reflections from surface one and two are shown in purple and orange respectively.

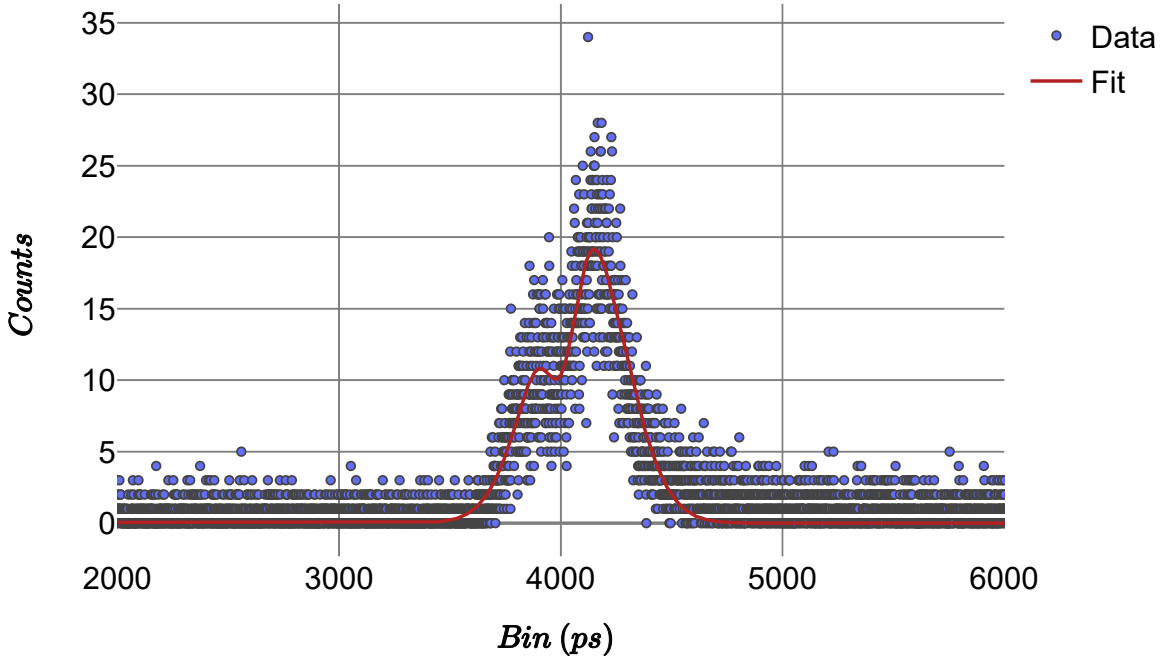

Figure 6.4: Fitted histogram of two surfaces separated by 4 cm. The integration time was 10 seconds.

the two sheets is 4 cm and the integration time was 10 seconds. Below this separation the fit struggles to distinguish the two peaks. A smaller timing jitter device would narrow the response peaks and allow a better distance resolution. The peak positions returned by the fitting procedure here are bins 3910 ps and 4153 ps, giving a Δt of 243 ps and a distance separation of 3.7 cm, well aligned with the ruler measurement of 4 cm.

Scanning Targets

Next, a stage mounted onto two motorised translation stages in an X-Y configuration was introduced at a range of 350 mm from the beam output. By placing targets onto the stage and scanning them through the beam a 50 mm by 50 mm scanned image could be produced. To begin with a cardboard cut-out of a smiley face was scanned. This gave two surfaces separated by a large distance (few cm) so they were easily distinguished. A photograph of the target and the subsequent image acquired with the system is shown in Fig. 6.5. The images are constructed using the cross-correlation method outlined in Ch. 2, §2.3.2. The IRF acquired in the previous experiment was cross-correlated with the each pixel in turn. Once the cross-correlation function was obtained the timing bin where this function was at a maximum was taken as the pixel position. By repeating for all of the pixels a depth image can be built up. Both the data gathering and post-processing was performed using Python.

A target with more complex edges and less defined depths was then selected. A LEGO model of the London landmark, Big Ben clock tower, was chosen as it had an easily recognisable shape with a good variety of curves and edges whilst being lightweight enough to mount on a motorized translation stage. A photograph of the target and corresponding depth image are shown in Fig. 6.6. Although the scan area was smaller than the total model, key features can easily be picked out in the depth image including the raised clock face (3 mm raised from next surface), edges of the tower and holes beneath the spire. This image was taken with an integration time of 1 s per pixel. For both of the above images, the average emitted power was < 12 μW.

This experimental demonstration shows the first demonstration of single-photon LIDAR in the mid-infrared. Although the detectors used were far from ideal, they showed that SNSPDs are a viable route to mid-infrared LIDAR and can provide the spectral sensitivity required. An obvious next step here will be to substitute the second-generation frontside-coupled DBR detectors into this setup to utilise their improved detection characteristics.

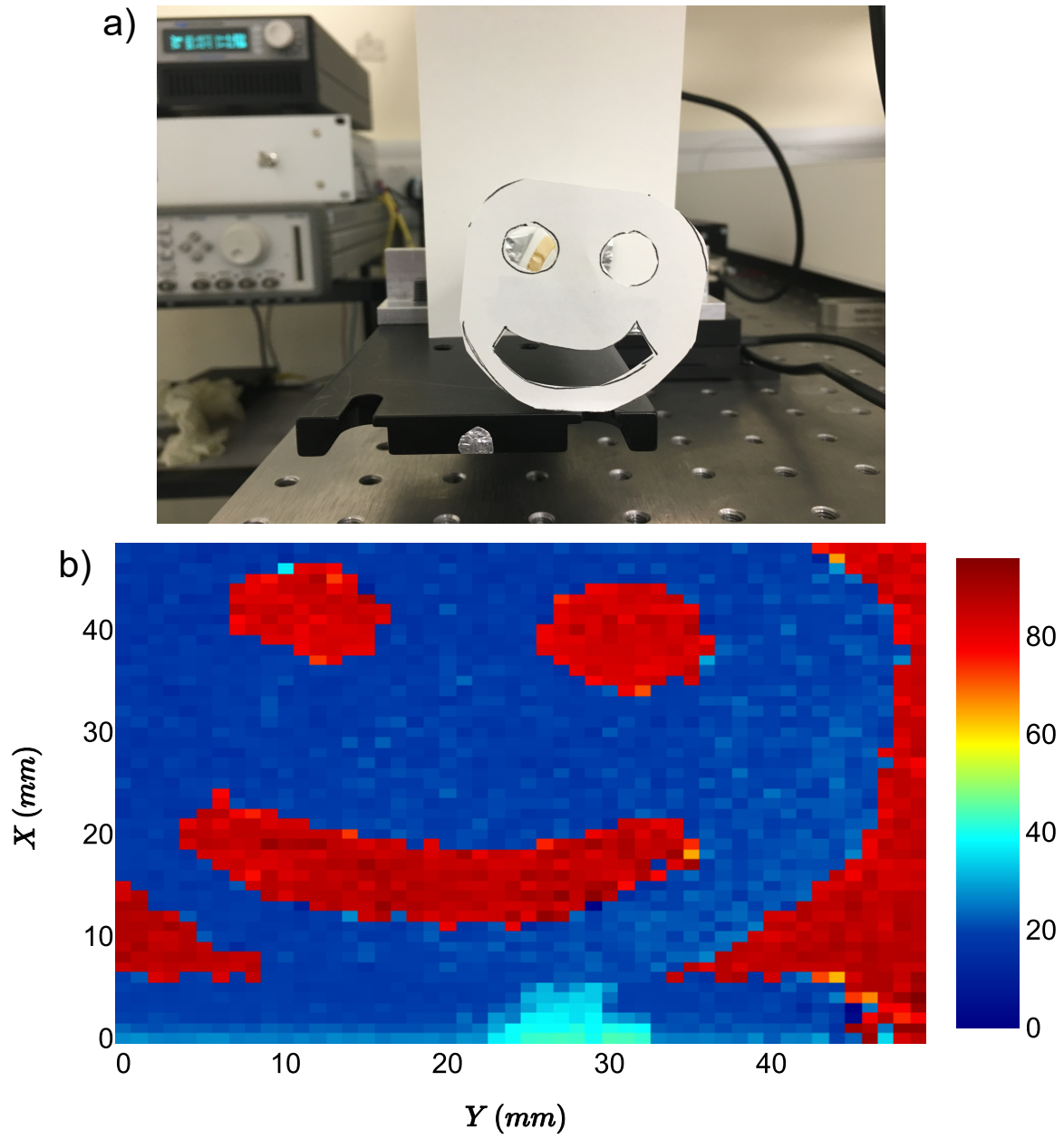

Figure 6.5: a) Photograph of smiley face cut-out. b) LIDAR depth image of the smiley face. The scale bar is in mm.

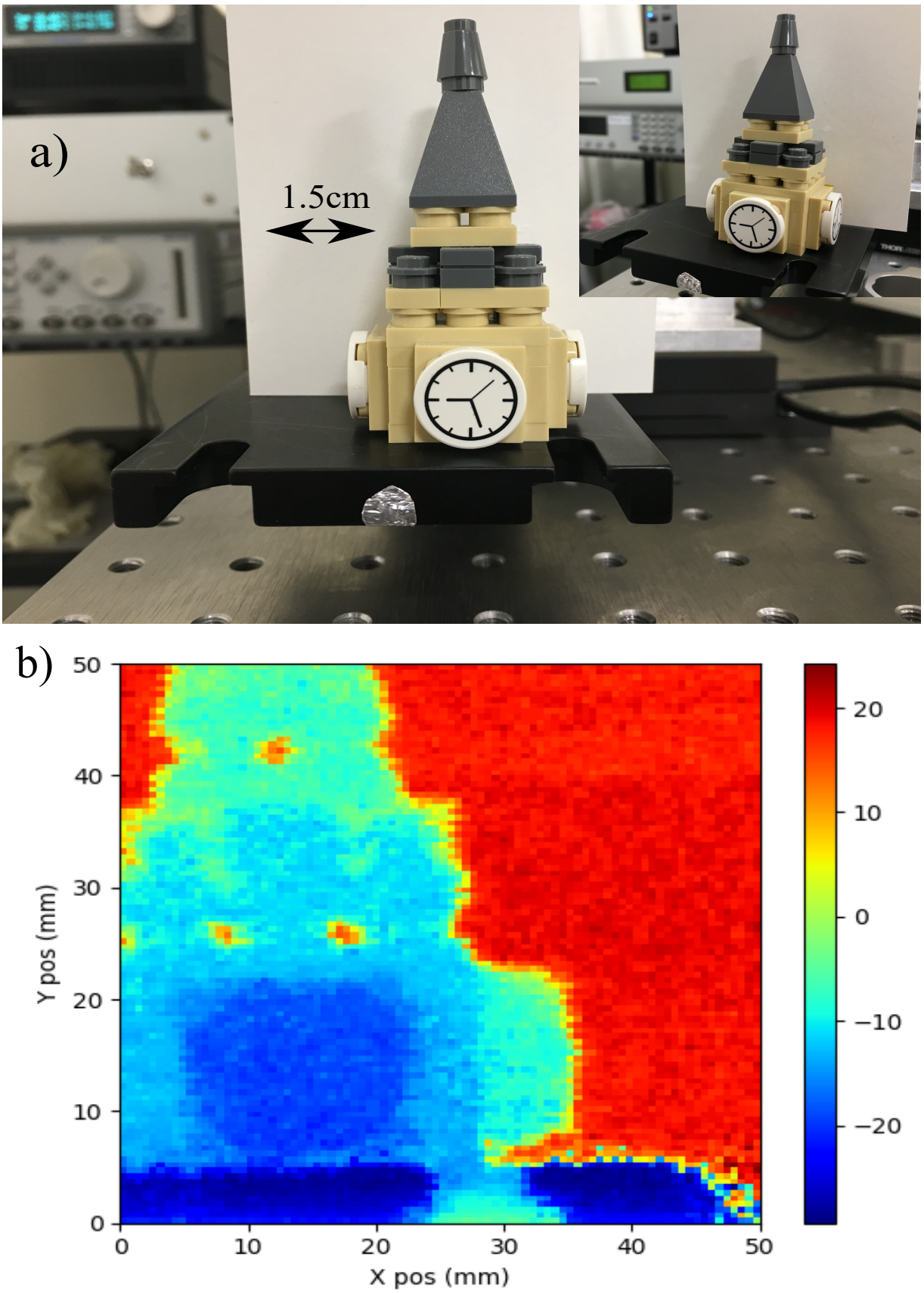

Figure 6.6: a) Photograph of Big Ben model. b) Image acquired with LIDAR system. The cardboard backboard has been scaled to allow the details to be easily picked out. The scale bar shows depth in mm.

6.2 Ultra-low Jitter LIDAR at 1.55 µm

6.2.1 Motivation

Recently, SNSPDs were developed with a FWHM timing jitter of < 3 ps [39]. This represents an exciting breakthrough in the technology as it was demonstrated that with careful engineering it was possible to mitigate the electrical and geometric components of timing jitter and utilise the extremely-low intrinsic timing jitter of SNSPDs in practical devices. Of course in this work the detection efficiency was incredibly low due to the small active area of the device and so not that useful for real world experiments. In the following work, together with collaborators at Jet Propulsion Lab (JPL), California USA, and Heriot-Watt University (HW), Edinburgh UK, practical low-jitter devices based on tapered differential readout SNSPDs are realised and deployed into a km-range field trial experiment to demonstrate the increased imaging performance of such low-jitter devices.

6.2.2 Experimental Setup

Tapered differential SNSPDs

As discussed in Ch. 2, §2.1.3, the timing jitter of SNSPDs can be decomposed into three terms: the electronic and optical jitter, Δt_{exp}, the intrinsic jitter, Δt_{int} and the geometric jitter, Δt_{geo}. It is the terms Δt_{geo} and Δt_{exp} that are minimised in this work. When a photon is incident on a meandering nanowire it creates a location-dependent resistive hotspot - as described in Ch. 2, §2.1.2. Due to the high kinetic inductance of superconducting nanowires the propagation velocity of the resulting signal is a small fraction of the speed of light along the nanowire. This, coupled with the fact that meandering nanowires are of significant length mean that the location of the photon absorption along the nanowire results in a timing variation. This timing variation is the geometric jitter, Δt_{geo}. In [39], the Δt_{geo} was compensated for by utilising a very short nanowire - however this resulted in a poor detection efficiency. In work at MIT [187] [188], the Δt_{geo} was shown to be removable if a differential readout architecture was used. When a photon is absorbed, it generates two electrical pulses of opposite polarity which propagate to opposite ends of the nanowire. If the length of the nanowire is taken to be L then the arrival times of the two photons, t_1 and t_2, can be written as a function of the position x, where they were absorbed, as:

$$t_1 = \frac{x}{v} \tag{6.1}$$

$$t_2 = \frac{(L-x)}{v} \tag{6.2}$$

where x is in the range 0 to L and v is the speed of the signal propagation. These arrival times can then be averaged:

$$t_{avg} = \frac{t_1 + t_2}{2} = \frac{L}{2v} \tag{6.3}$$

which shows that the timing variation (or jitter) of t_{avg} does not depend on the position, x, and is therefore independent of the geometric jitter, Δt_{geo}.

The second jitter contribution that can be suppressed with careful design is the experimental jitter, Δt_{exp}. This can further be broken down into two categories - optical jitter, Δt_{opt}, and electrical jitter, Δt_{elec}. As mentioned in Ch. 2, the optical jitter can largely be compensated for with fast ($\sim$fs) lasers and low-dispersion fibres. The electrical jitter is a combination of contributions from the low noise amplifier (LNA or LNAs for multiple amps) and the timing electronics (TCSPC modules) used to record photon events. The latest TCSPC modules can give a timing resolution of sub-3 ps so the contribution here can be minimised with appropriate experimental equipment. The amplifier noise contribution was fully analysed in [189]. Following linear small-signal perturbation theory [190] the jitter from the amplifier noise can be given as:

$$\Delta t_{amp} = \frac{\sigma_n}{k} 2.355 \tag{6.4}$$

where σ_n is the RMS of the circuit noise and k is the slope of the signal at the discriminator value. For long nanowires with high kinetic inductance, it can be shown that:

$$\Delta t_{amp} = \frac{NF \times \tau_{rise} \times N_i}{V_i} \times 2.355 \tag{6.5}$$

where NF is the amplifier noise figure, τ_{rise} is the rise time of the pulse, N_i is the noise level at the input and V_i is the signal level at the input. This equation shows there are three main routes to improving the amplifier timing jitter. The first is to lower the noise figure of the amplifier or the general noise at the input to the amplifier. This can be achieved through amplifier selection and careful experimental design. The second is to decrease the rise time of the output pulse and the third is to increase the signal level. These latter two can be combined as the slew rate, τ_{slew} equal to V_i/τ_{rise} and Eq. 6.5 rewritten as:

$$\Delta t_{amp} = \frac{NF \times N_i}{\tau_{slew}} \times 2.355 \tag{6.6}$$

The slew rate can be reduced and hence the amplifier induced jitter improved with the introduction of tapered readout SNSPDs.

Tapered readout SNSPDs [161] are a relatively recent development where a tapering co-planar waveguide (CPW) is fabricated at the output of the nanowire in order to deal with impedance-

matching issues. The output voltage from an SNSPD is limited by the bias current, I_b, and the the load impedance, Z_{load}. I_b is governed by nanowire geometry and material selection - as discussed previously, increasing the depairing current by changing the nanowire width or film thickness and increasing the fraction of this, C, that I_b can be set to to by ensuring good uniformity. Z_{load} is set by the coaxial cabling and readout electronics used in SNSPD readout - conventionally 50 Ω. The idea of the tapered readout geometry is to load the SNSPD with a kΩ impedance and then gradually transform this to 50 Ω to interface with standard coaxial cable and electronics. This tapered scheme amplifies the pulse while preserving its fast rising edge. This results in a much faster slew rate, τ_{slew}, which as shown in Eq. 6.6 reduces the electrical contribution to timing jitter.

In this work, the differential readout and tapered readout are combined into a differential tapered readout scheme that allows the removal of the geometric jitter component and a reduction of the electrical jitter component. The devices are based on a NbN (6 nm thick, T_c of 7.6 K) nanowire - 100 nm width with a pitch of 500 nm - meandered over a 25 μm by 10 μm active area and embedded in an optical cavity designed to enhance absorption at 1.55 μm. Both ends of the meander are interfaced to an impedance matching taper based on a Klopfenstein taper [191], 7.55 mm long with a cut-off frequency of 500 MHz. The detectors are frontside-coupled and are shaped to fit into an standard optical fibre sleeve. This self-alignment 'keyhole' shape allows the precise alignment of an optical fibre output with the active area with out the time-consuming alignment procedures shown in Ch. 3, §3.2. A photograph of the device is shown in Fig. 6.7. The SNSPD (JPL1) was mounted in a ^{4}He sorption fridge attached to a GM cryocooler capable of achieving 850 mK operation for > 24 hrs. The 50 Ω taper ends were connected to the centre conductors of two separate SMA connections and connected to a cryogenic bias tee mounted to the 40 K plate of the GM cooler. Separate coaxial cables from outside the cryostat connected to this bias tee to provide DC bias and read out SNSPD output pulses from both ends of the detector. Outside the cryostat, the output pulses were connected to separate LNA-650 low noise amplifiers followed by a differential amplifier. The outputs of the amplification section were then fed into an RF balun (Texas Instruments ADC-WB-BB/NOPB - modified to remove 100 Ω impedance matching resistors). The balun converts the differential signal into an unbalanced single ended one which can then be fed into standard counters and TCSPC cards. A circuit diagram of the setup is shown in Fig. 6.8. Throughout both signal paths until the balun, care was taken to ensure that the electrical path lengths were identical so that both signals arrive at the same time. The TCSPC card used was a SPC-150-NXX from Becker and Hickl. This gave a time channel width down to 203 fs with a resolution of less than 3 ps. Specially designed for the sub-3 ps work in [39], this card allows the low-jitter SNSPD design to be fully exploited by reducing the timing electronics contribution significantly.

The detectors were fabricated at JPL/MIT and characterised at 1.55 μm in a similar cryostat

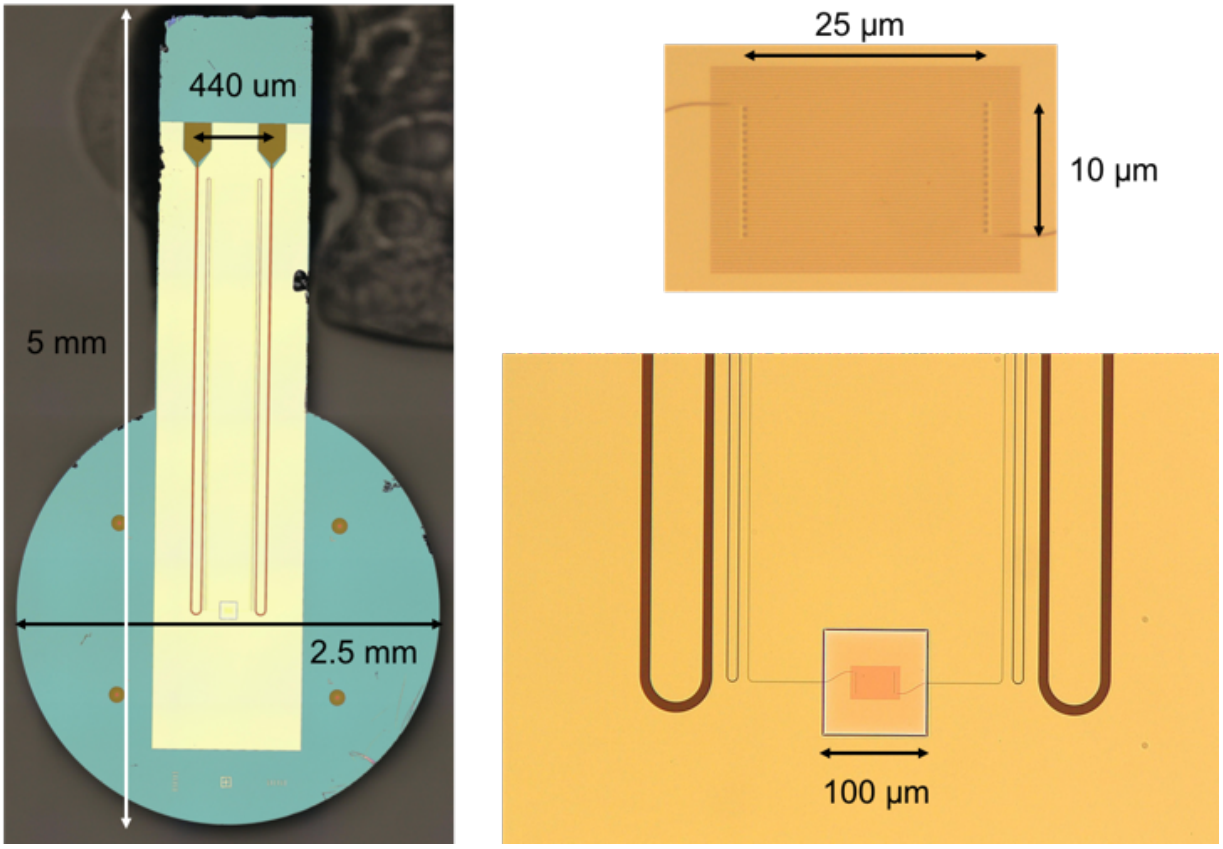

Figure 6.7: Image of JPL1 differential tapered SNSPD. The top right panel shows the nanowire, the bottom right shows a close up of the tapers interfacing to the nanowire and the left panel shows the full device with the tapers seen interfacing to the gold contact pads at the top of the device. Courtesy of Dr Boris Korzh, Jet Propulsion Lab.

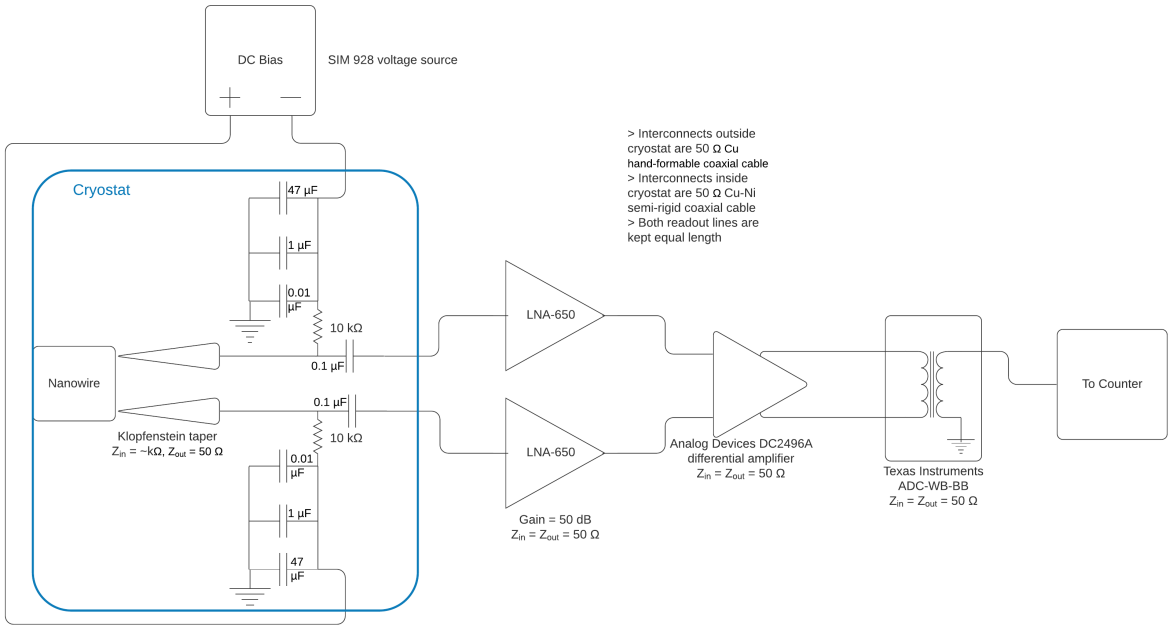

Figure 6.8: Circuit diagram of dual-taper differential SNSPD readout.

setup before being transferred to Glasgow for installation in the setup described above. Characterisation was performed as per the detectors in Ch. 5, §5.1.1, and gave saturated detection efficiency of over 60% and a FWHM timing jitter of 12.8 ps. These values were re-measured upon installation in Glasgow and confirmed to be in agreement - the jitter exhibited a marginal increase to 13 ps FWHM likely due to the variations in hardware - different TCSPC card, amplifiers and optical setup. Fig. 6.9 shows the efficiency against bias and a timing jitter histogram for the JPL1 device. Once the performance was confirmed the detector system was moved to HW University in Edinburgh and installed in their roof lab setup at the David Brewster building to allow field trials to commence.

Optical Setup

The optical setup for the LIDAR field trials is shown in Fig. 6.10. The laser source is a CNT-1550-TK from KPhotonics which has a centre wavelength at 1560 nm, a repetition rate of 20 MHz and a pulse width of <100 fs. All light outside of the transceiver box is delivered in SMF-28 fibre ensuring safe operation. The output from the laser is sent to a optical splitter where 1 % is coupled off and sent to a photodetector (InGaAs - Thorlabs) to provide the sync signal for the LIDAR experiments. The remaining 99 % is first filtered with three spectral filters - a 1500 nm long pass, 1600 nm short pass and narrow bandpass at 1560 nm - to ensure any unwanted spectral components are excluded. This is then sent to a variable attenuator and attenuated as necessary before being connected to the scanning transceiver setup. The transceiver setup is shown in Fig. 6.11. As can be seen, light arrives in fibre and is transformed into a free space beam with a reflective collimation package. A polarising beam splitter (PBS) serves to split the outgoing and returning photons. A linear polariser and half wave plate are inserted before the PBS in order to maximise the throughput of the PBS for the outgoing beam. After the PBS, the beam reflects through a scanning galvanometer mirror, two off-axis parabolic mirrors and a further scanning mirror before finally being sent through the objective lens and out to the target. The scanning galvanometer mirrors are controlled by the control PC to scan the beam across the target. The objective lens is changeable depending on the range of interest. For this work either a f/3.5 300 mm focal length SWIR lens or a f/8 2 m focal length Ritchey-Chrétien telescope was used. Once photons have returned from the target they return co-axially through the transceiver until the PBS where they are directed out through another reflective collimation package back into fibre. This fibre is connected to the input of the SNSPD.

The other blocks seen in Fig. 6.10 are the TCSPC acquisition module (Becker and Hickl SPC-150NX) and the control PC which is responsible for interfacing the data acquisition on the TCSPC card with the commands sent to the galvanometer mirrors to ensure each pixel in the image is acquired correctly. A USB data acquisition module (DAQ - National Instruments USB-6221) is used used to provide the voltages to the galvanometers as well as interface with the

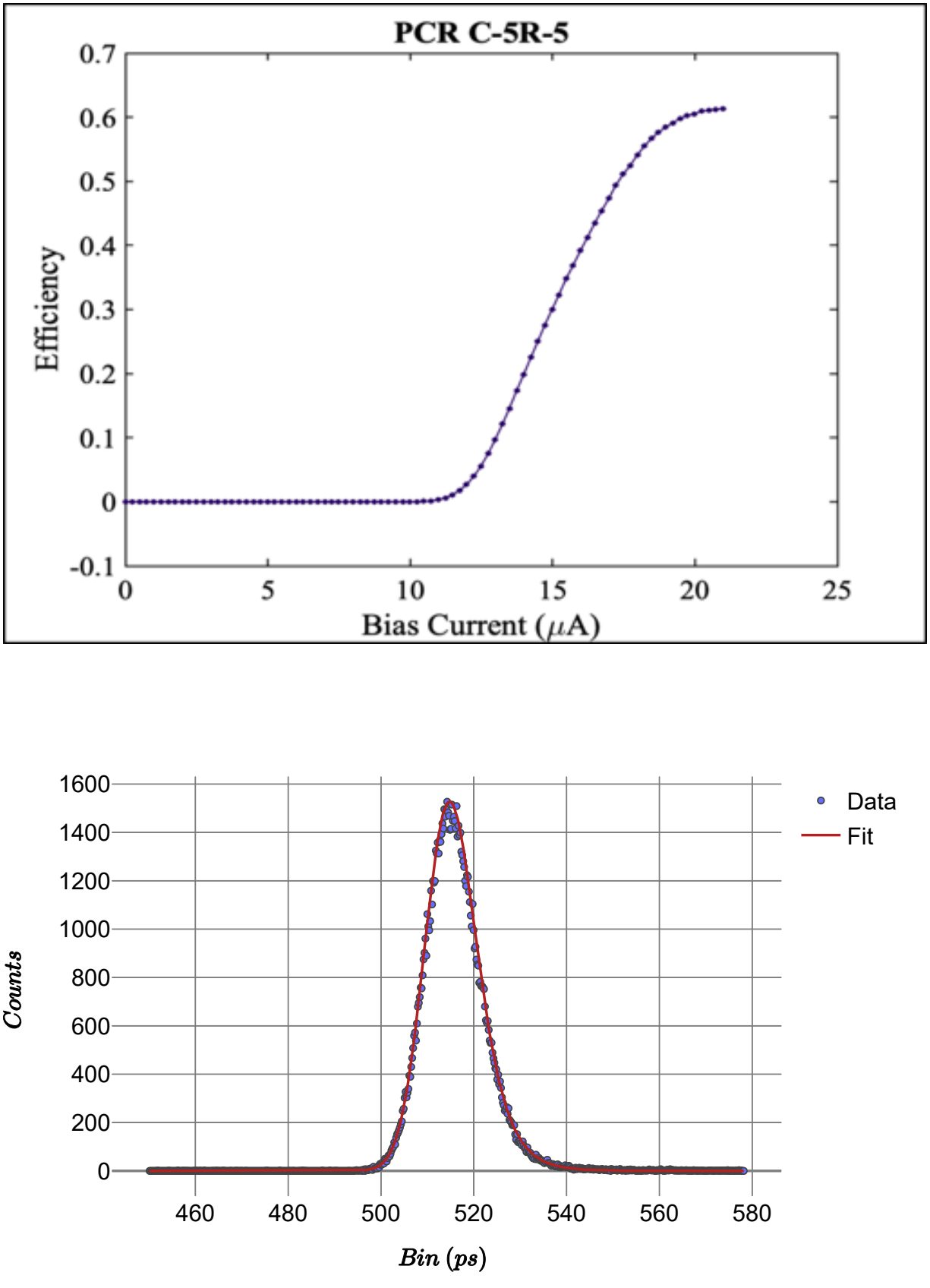

Figure 6.9: Top: Efficiency of JPL1 device - saturation at around 60% is observed. Bottom: Timing histogram of JPL1 device showing a FWHM of 13 ps.

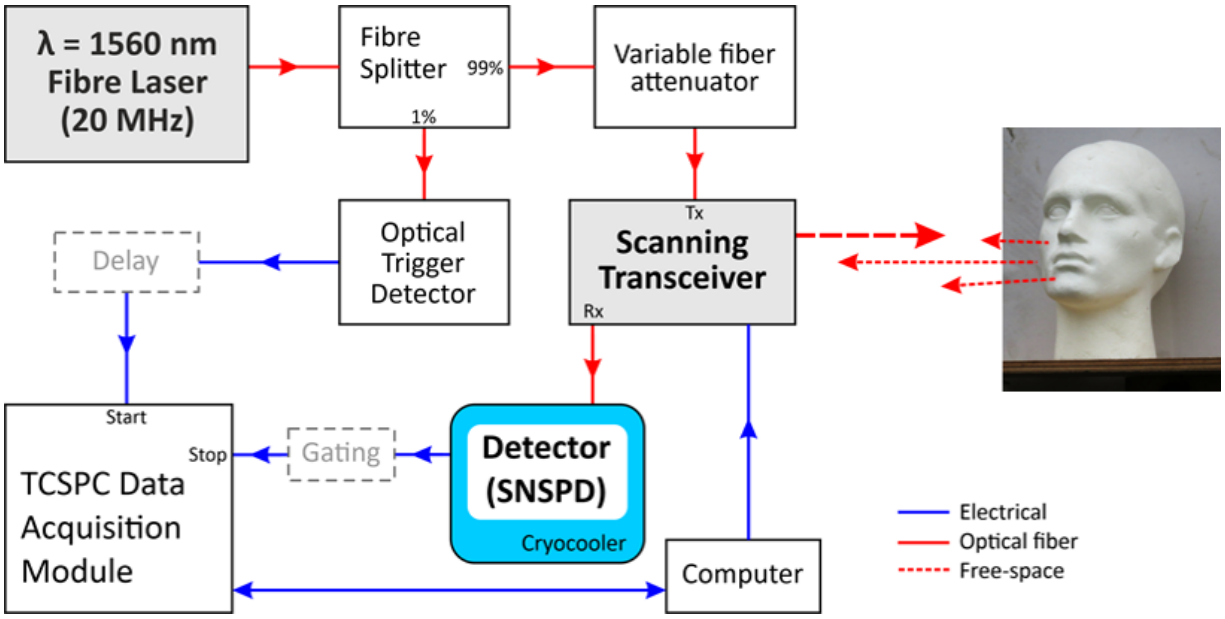

Figure 6.10: LIDAR scanning system. The output of the fs laser goes to a splitter with a small portion being coupled off as a sync signal. The rest is attenuated as necessary before being sent out through the transceiver. The returns are collected and coupled to the SNSPD for counting. The TCSPC system processes the return counts into histograms. Courtesy of Dr Aongus McCarthy, Heriot-Watt University.

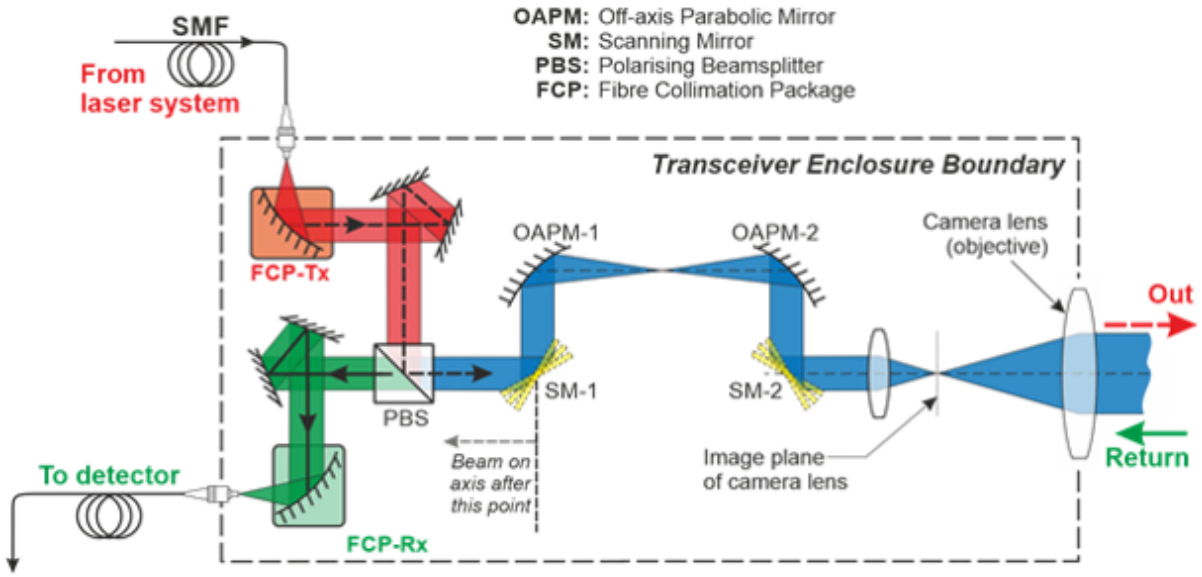

Figure 6.11: LIDAR transceiver system. Laser light is output from SMF-28 fibre and passes through a reflective collimation package to transform it to free-space. A polarising beam splitter splits the outgoing and returning photons and the two scanning mirrors can scan the beam across the scene. The objective lens is changeable depending on the range requirements. After returning photons have been split at the PBS they are recoupled into SMF-28 fibre with a reflective collimator and sent to the SNSPD. Courtesy of Dr Aongus McCarthy, Heriot-Watt University.

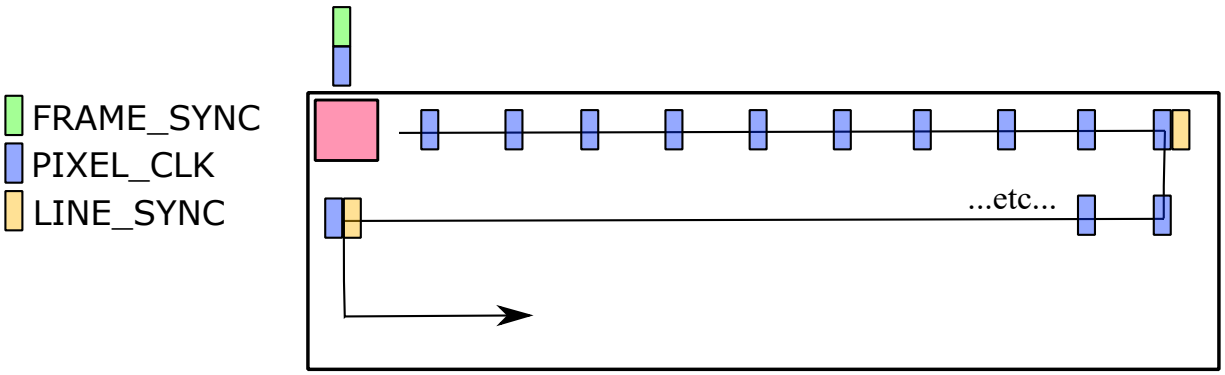

Figure 6.12: LIDAR scan signal sequence as described in the text.

TCSPC card. This has two analogue channels to provide control voltages to the mirror servos and digital output lines to provide signals to the TCSPC card. At the start of the image acquisition a FRAME_SYNC signal is sent to the TCSPC card to tell it that an image is going to be taken. The image size is also input into the TCSPC card. Then, the following sequence is performed:

- A PIXEL_CLK signal is sent to the TCSPC card from the DAQ. This tells the card to start taking data. The DAQ tells the galvanometers to move the beam to the corner of the image.
- Data is taken as that pixel is illuminated for the integration time (controlled by the PC).
- The DAQ sends a further PIXEL_CLK signal to instruct the TCSPC card to save the histogram for that pixel and start taking data for the next one. It also moves the galvanometers to the next pixel across by changing the voltages.
- The above is repeated as the scanning moves along the top line. At the end of the line a LINE_SYNC is also sent with the PIXEL_CLK to tell the TCSPC card that it needs to change lines. Depending on the setup this can either be bi-directional or include a flyback.
- Once the entire image has been taken a 2D array of histograms corresponding to the pixels in the image is available, ready for processing.

Fig. 6.12 shows a diagram of the sequence described above.

Data Processing

After the sequence in the previous section a 2D array of histograms is obtained, ready to be processed into an image. Initial processing involves cross correlation of each pixel histogram with the instrument response function as utilised in the previous experiments shown earlier in this chapter. For this work the processing was implemented in a custom GUI in Python designed to be user friendly and simple. More details of this can be found in Appendix B.

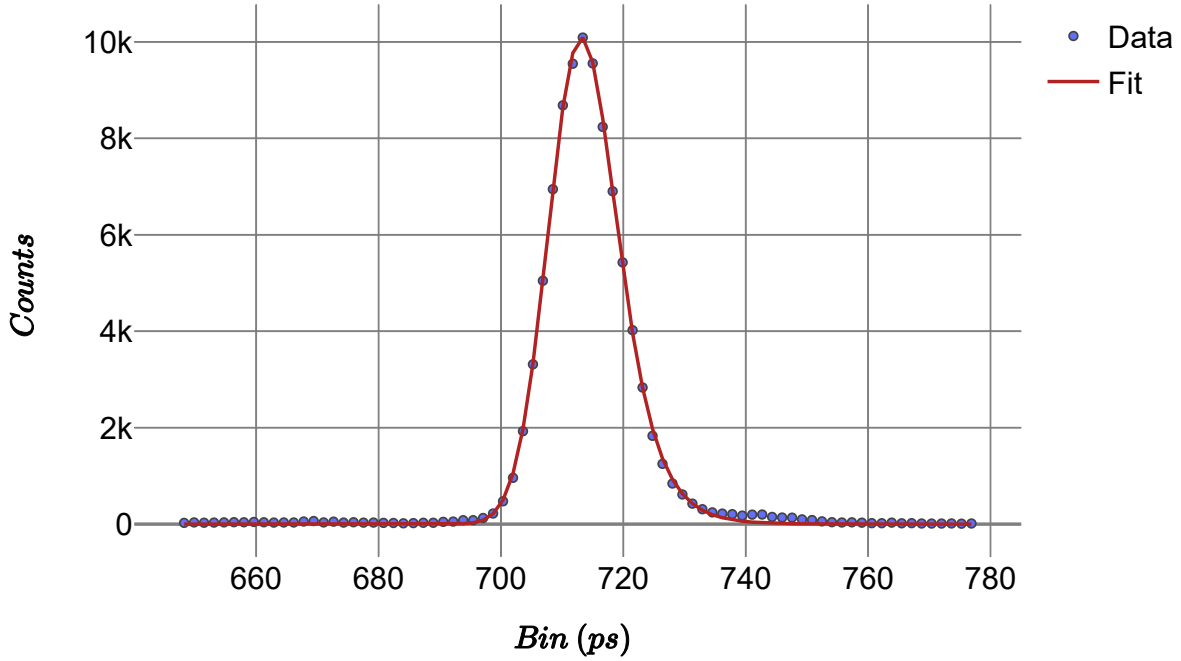

Figure 6.13: IRF of the LIDAR setup at a range of 30 m. A FWHM of 13 ps is obtained.

6.2.3 Depth Imaging at 1550 nm Wavelength

Instrument Response Function

The first data to be obtained was an instrument response function of the entire LIDAR scanning system. A piece of retro-reflective material was set up on an adjacent roof at a range of 30 m and a histogram was taken with an integration time of 30 s. The resulting histogram is shown in Fig. 6.13. A FWHM value of 13 ps was obtained which indicated that the addition of the optical components had negligibly affected the timing jitter of the device. Likely due to the use of short lengths of fibre optics with low-dispersion as well as the narrow linewidth of the filtered laser output.

Targets at 30 m Range

The first experiments were performed at a range of 30 m and a 3d-printed plastic pillar target was used to gauge the depth resolution abilities of the system. A photograph of the target is shown in Fig. 6.14a. The pillars in the target begin in the top left hand corner at 32 mm wide and 32 mm tall. The diameter then reduces by a factor of $\sqrt{2}$ going towards the top right hand corner and the height of the pillars reduces by a factor of 2 going towards the bottom right corner. The smallest

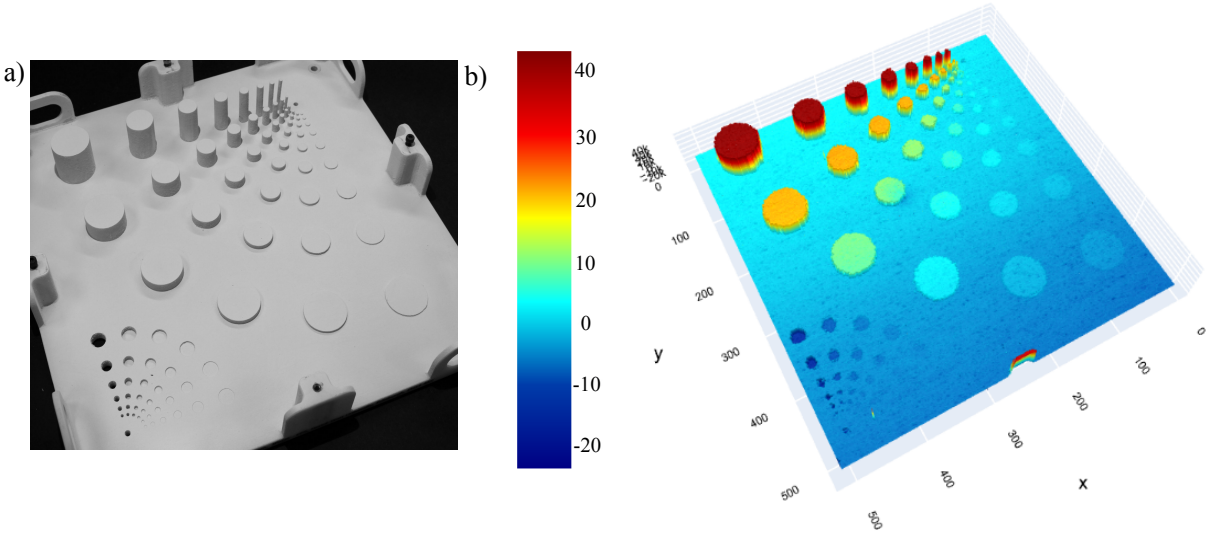

Figure 6.14: a) Plastic pillar target for gauging depth abilities of system, the dimensions are described in the text. b) 512 x 512 pixel depth image of the target at a range of 30 m. The scale bar is in mm.

height is 1 mm. In the bottom left hand corner there is a similar arrangement of holes ranging from a depth of 8 mm to 0.5 mm.

The target was then scanned at a range of 30 m, mounted on an adjacent rooftop. A 512 x 512 pixel image was obtained with an integration time per pixel of 5 ms. The scan area was 275 mm x 275 mm and the laser power was adjusted to set the count rate to the order of MHz. At this count rate and a laser repetition rate of 20 MHz, we are operating in the low-flux regime and probability of multiple photon detections per pulse is low. The depth image produced is shown in Fig. 6.14b and exhibits excellent detail - all of the pillar heights and holes can be distinguished from the back board and the subtle tilt in the target can be identified from the colour gradient in the back board.

Targets at 325 m Range

The pillar target was then moved to a range of 325 m to observe how the image was degraded with a smaller return signal and the effects of atmospheric turbulence. Image parameters were kept constant so again a 512 x 512 pixel image was scanned with an area of 275 mm^2 and a 5 ms integration time per pixel. Again the laser output power was adjusted to keep the detector's count rate at the MHz scale. The image is shown in Fig. 6.15. As can be seen in the image, the effects of atmospheric turbulence are clearly observable with the lateral edges of the pillars being blurred and ragged. The conditions on the day of testing were cool and sunny which is likely to create thermal fluctuations due to hotspots in the air. As detector count rate was kept comparable to the 30 m test, shot noise should be similar and the effects observed can be attributed to atmospheric

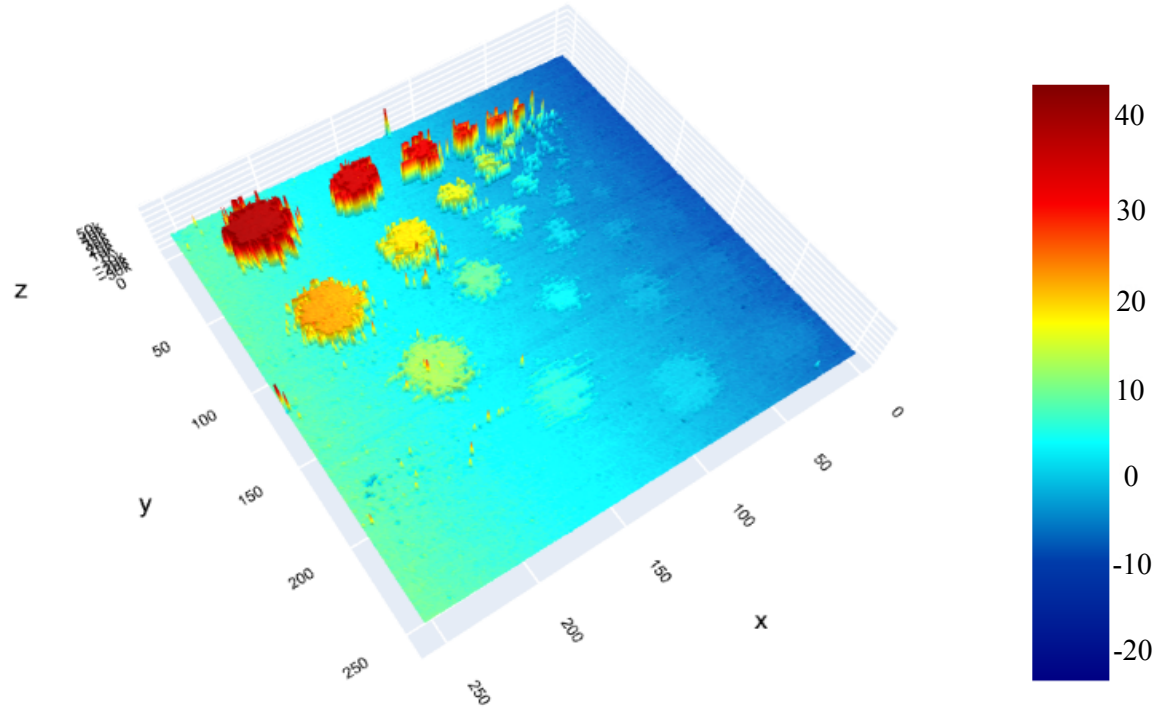

Figure 6.15: Scan of pillar target at 325 m. The effects of atmospheric turbulence can be observed in the image. The scale bar is in mm.

effects. The depth of the features is still well resolved with the pillars down to 1 mm height still being resolvable, despite the smaller diameter pillars and holes being degraded due to the decreased side-to-side resolution. All of the images presented in this chapter were taken in similar cold and sunny conditions.

After verifying that the depth information was well preserved at a range of 325 m a variety of targets with different shapes and reflectivity were scanned. The first was a gloved human hand against a back board. The image is a 256 x 256 pixel image of scan area 275 mm^2 with an integration time of 5 ms per pixel. Fig. 6.16a and Fig. 6.16b show the depth image and photograph of the target respectively. Fig. 6.16c also shows a photon counts map to illustrate the amount of photons counts required to construct an image. For the counts map the number in each pixel is the photon count in the highest-valued timing bin (the peak) and no integration was performed under the broader peak. For this image an average peak of 8.6 photons per pixel is registered. The variation across the image is caused by the atmospheric turbulence resulting in a reduction in the number of returned photons for some bins, similar to that observed in the pillar target above. The only post-processing performed here was a binning of the data into 3 ps timing bins to increase the SNR of the histogram and improve the final image. Details of this process are given in Appendix B. The tips of the fingers and cuff strap of the glove were coated in a rubber material which has low reflectivity at 1550 nm so these manifest themselves as areas of no returns in the image. These aside the image is as expected with the curves of the hand and

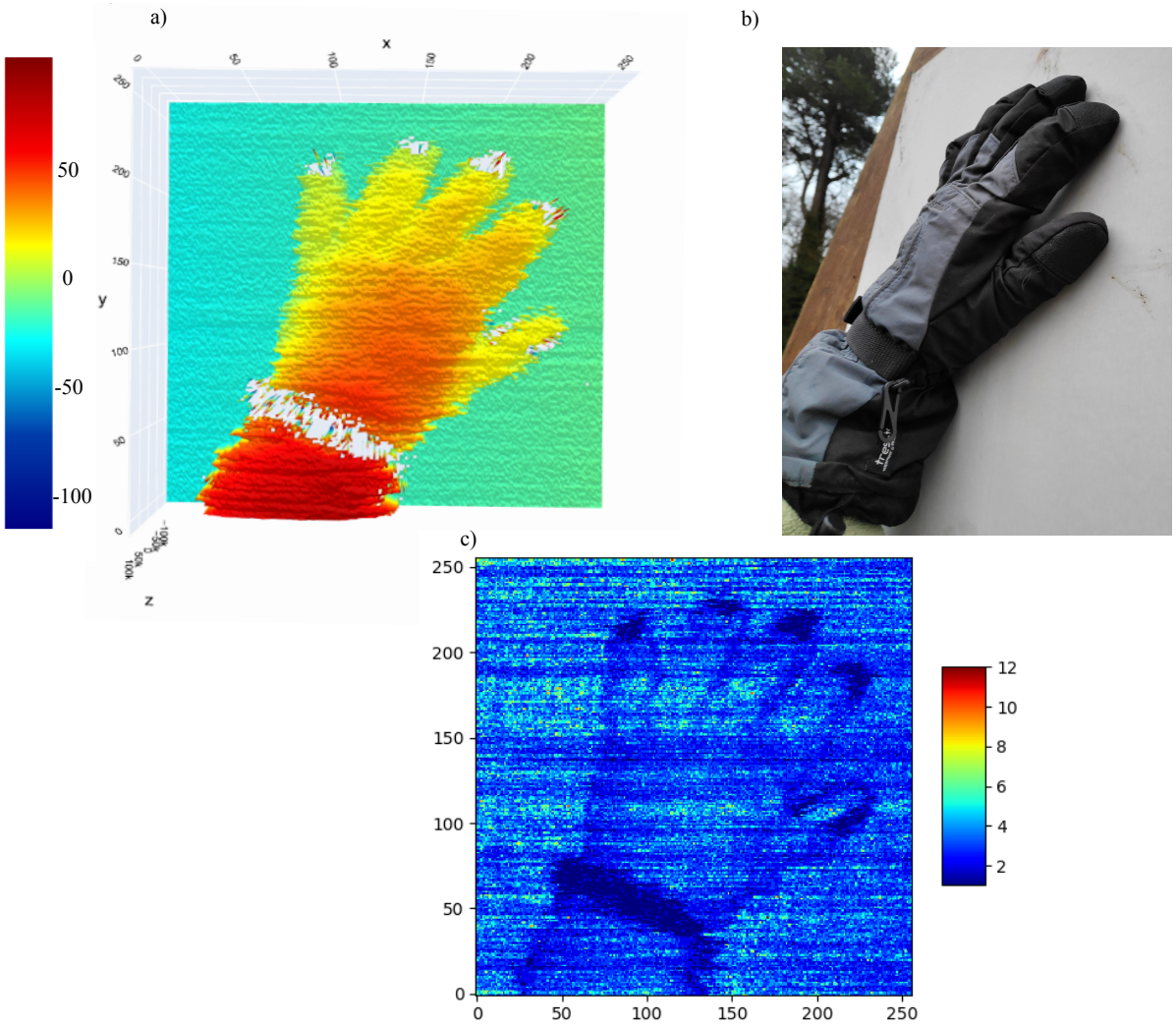

Figure 6.16: a) Scan of gloved human hand at 325 m. The scale bar is in mm. b) Photograph of the target. c) Counts map of the target showing an average peak of 8.6 photons per bin.

arm being obvious in the depth image.

To further test the system, two human-like objects were imaged at 325 m next. Firstly a 256 x 256 pixel scan of a polystyrene head at an integration time of 5 ms per pixel. The result is shown in Fig. 6.17 along with a photograph of the target. The image had an average peak photon count of just 3.5 photons and a total image acquisition time of 5 minutes. All features of the head are well recognisable.

Next a plastic mask was imaged. This was again a 256 x 256 pixel image but with a lengthened integration time of 10 ms per pixel giving an image with an average peak photon count of 4.7 photons - due to the lower reflectivity of the plastic target at 1550 nm compared to the polystyrene. Total image acquisition time was around 10 minutes. The image is shown in Fig. 6.18 along with a photograph of the target. In both of the above images the effects of atmospheric turbulence can

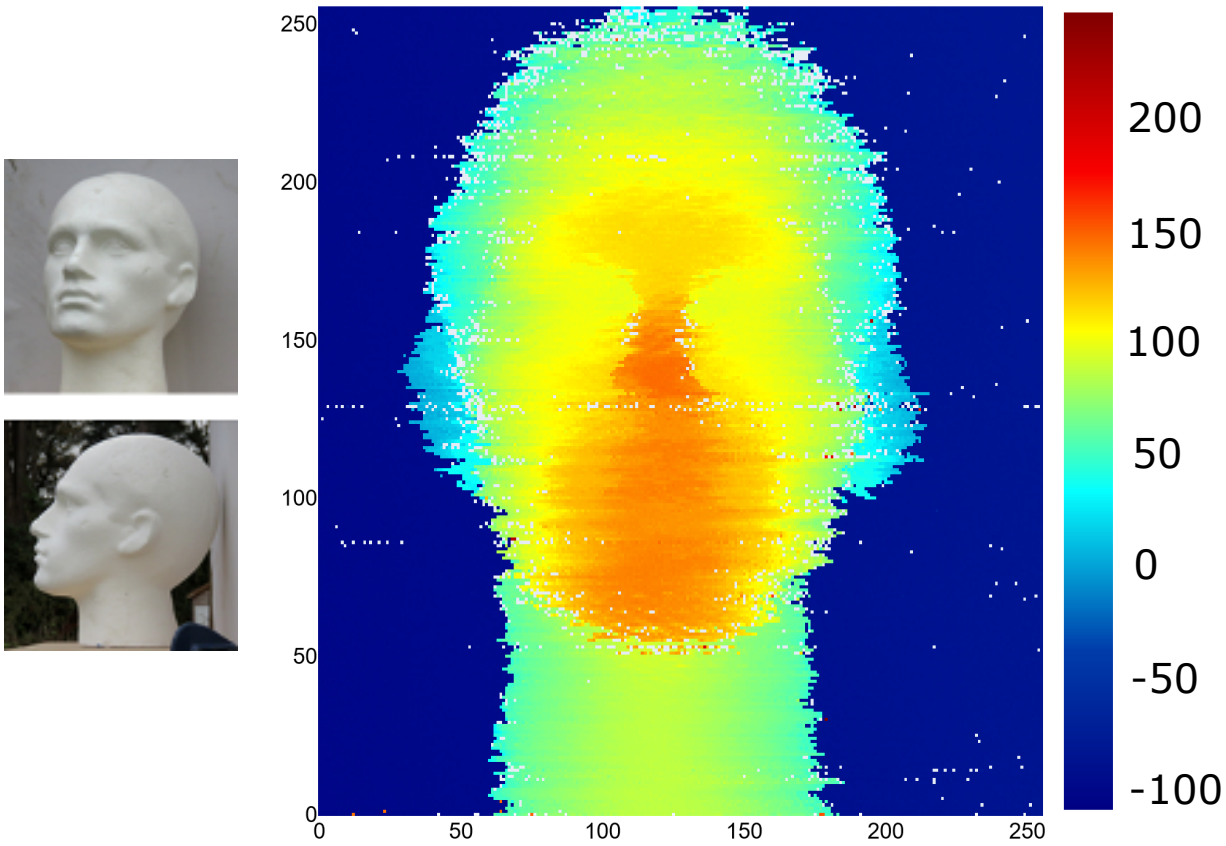

Figure 6.17: Scan of polystyrene head at 325 m with a photo of the target on the left. The scale bar is in mm.

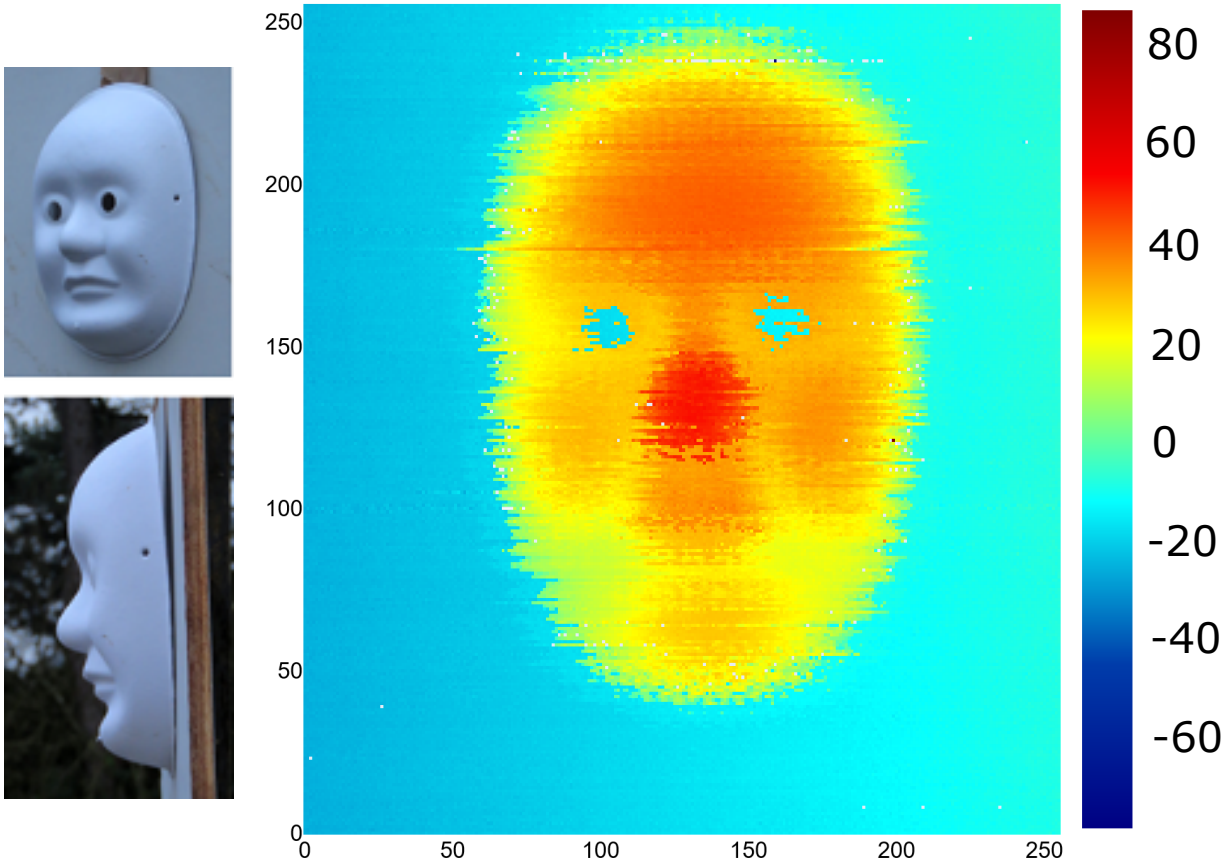

Figure 6.18: Scan of plastic mask at 325 m with a photo of the target on the left. The scale bar is in mm.

be observed with the horizontal streaking in the image. However, the details of the faces are well defined and easily recognisable even with this distortion present. For both scans the scan area was 275 mm^2 as before.

Human skin is a poor reflector in the short-wave infrared. [192]. However the ability to image human faces is an attractive prospect. A live target was set up wearing a hat and done-up collar at 325 m and then imaged with the system. As can be seen in Fig. 6.19 the returns on the face section are poor. It is still possible, however to pick out the nose and eye features as well as the shape of the face. Optimisation of the optical system as discussed in the next section may help to maximise returns and clean up the image.

All of the object scans at 325 m were performed with an output power (at the input to the transceiver) of around 1.5 mW. Even neglecting optical losses in the output path of the transceiver (see next section) this is well below the laser eye safety limit for 1550 nm lasers.

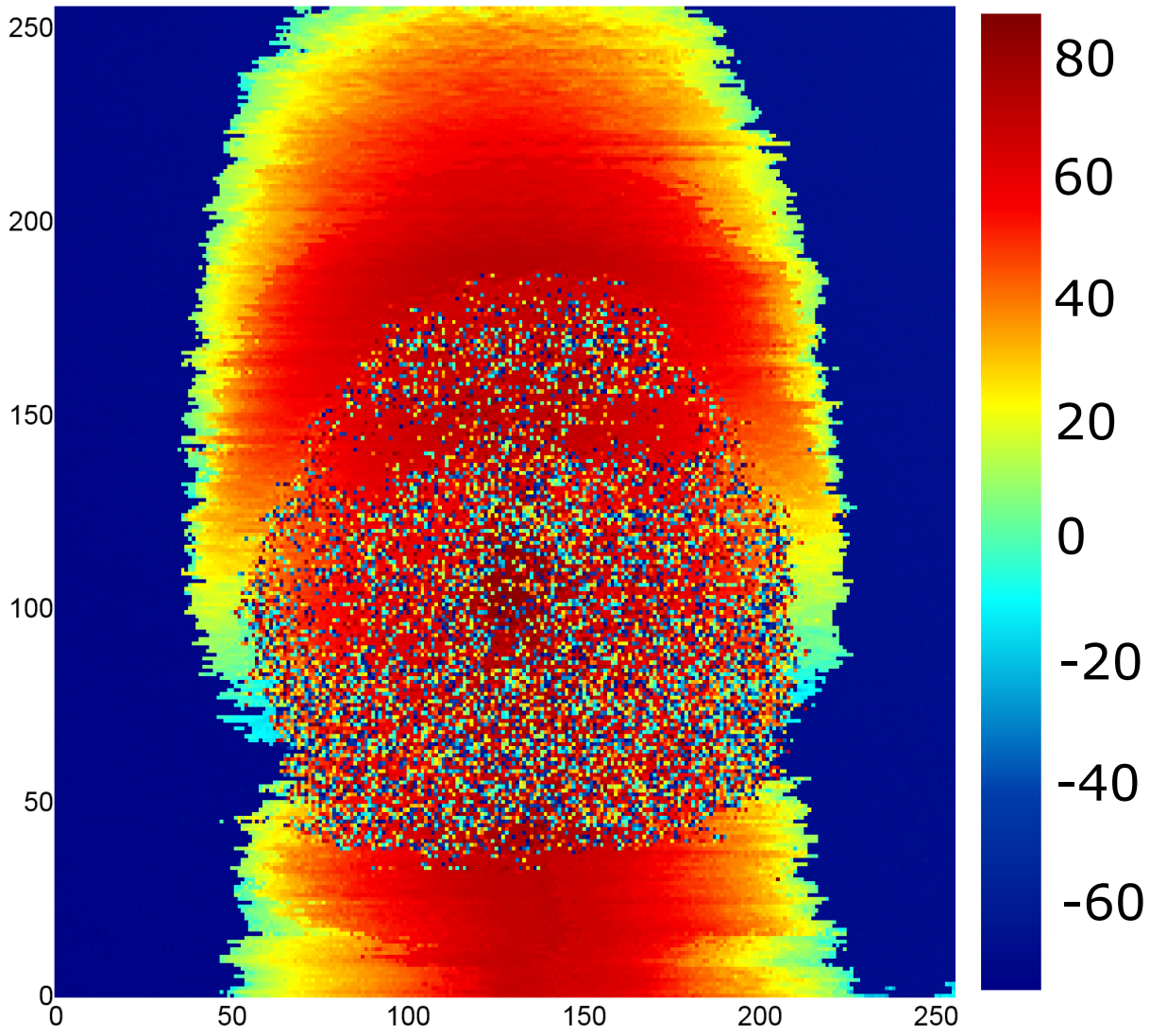

Figure 6.19: Scan of human head at 325 m. The scale bar is in mm.

6.3 Outlook

The above images show the current capabilities of the LIDAR imaging system with the differential tapered SNSPD. Throughout the course of the experiments it became clear that some deficiencies in the optical performance of the transceiver was limiting the capabilities of the system. There are two things to consider when optimising the system. In principle, the maximum range of the imaging system is only limited by the available laser output power, however, the transceiver has some back reflections present from the optical components (PBS/mirrors/etc) so if these are not minimised then turning up the optical power results in the SNSPD being swamped with back reflections and is effectively blinded to the actual returns. Careful positioning and tweaking of optical components leads to a reduction of the back reflections and mitigation of this issue.

The other major issue which became apparent during the initial trials and needed to be addressed was that of optical loss in the system. The losses were characterised on both the Tx and Rx paths as 3.36 dB and 16.6 dB respectively. The Tx path was at the expected level of attenuation but the Rx path seemed too high, given the insertion loss of the components used. Examining the reflective coating on the collimators revealed some manufacturing defects which were likely leading to large losses - new collimators have now been purchased. The losses of the system were characterised from the Tx-input to the combined-output of the transceiver and then reversed from the combined-output to the Rx-output. This did not take into account the losses that may arise from an improperly aligned system - if for instance the Tx-beam and Rx-beam were not co-incident on the same spot on the target. To get a feel for this problem the SNSPD was swapped for an InGaAs SPAD and the beam was reflected off of a known target that had been previously scanned with a different optical system. In this way the performance of the new optical setup could be determined and compared to a known benchmark. It was the expectation that the optical system would perform better than the previous generation which would allow full exploration of the low-jitter SNSPD system's capabilities. However it was found that the returns were lower than with the previous system, indicating some issues - possibly with alignment.

Current work is under way to realign and characterise the optical system. Some sources of loss have been identified and the next step is to benchmark the fixes with the InGaAs SPAD. Once this is confirmed to be as good (or better) than the previous generation scanner, the range of the trials can be increased past the 1 km mark and beyond. Maximising the returns will also aid in reconstruction of low-reflectivity targets such as the face shown in Fig. 6.19. A further avenue of research is the implementation of more advanced imaging algorithms as discussed in Ch. 2, §2.3.2.

An overarching goal of both the above work and the LIDAR experiments at 2.3 μm is to combine them into a low-jitter LIDAR demonstration in the field at mid-infrared wavelengths. This would allow full leverage of the unique timing metrics of SNSPDs as well as the reduced

background photon flux that comes with working in the mid-infrared.

Chapter 7

Conclusion

In this thesis, I have presented the work performed with the goal of developing SNSPDs for the mid-infrared. A mid-infrared test setup was constructed based on an optical parametric oscillator that allows characterisation of detectors out to 4.2 μm wavelength. ALD superconducting films were investigated as an alternative to sputter-coated films and determined to be a good candidate for mid-infrared detection [6] where their uniformity and homogeneity can be leveraged to achieve high fractions of the depairing current. First generation mid-infrared detectors were characterised and deployed in a proof-of-principle single-photon LIDAR experiment at 2.3 μm, a wavelength never previously demonstrated [7]. Ultra-low jitter SNSPDs in the near-infrared were utilised to demonstrate the advantages offered in imaging applications such as the LIDAR presented [193].

The work carried out and outlined in this thesis will open a pathway towards achieving our goal of efficient and fast single-photon detection in the mid-infrared. Our second-generation of mid-infrared detectors have been outlined in Ch.5 and this will bring together the research performed with optical cavities in Ch.5 and the material development performed in Ch. 4 by growing ALD NbN on DBR substrates to increase absorption. The work done characterising multiple detectors has lead to a better understanding of the parameters that require to be optimised for good detector performance - mainly optimising the switching currents such that we can achieve high fractions of the depairing currents [109]. Our fabrication can be tuned as a result of this research which will hopefully lead to improved fabrication yield and more uniform detectors.

It is hoped that this will lead to a more efficient and lower timing-jitter device operating in the 2 μm to 3 μm wavelength range. This will open up multiple avenues of exciting work on novel applications in mid-infrared single-photon sensing. A primary objective will be to combine the mid-infrared detectors with our scanning LIDAR setup to perform depth imaging at mid-infrared wavelengths over km ranges. This will allow the advantages of operating in daylight at mid-infrared wavelengths to be fully explored and will open the door to more demonstrations of free-space applications such as free-space mid-infrared quantum key distribution [114]. This may well

also have implications for astronomical applications or space-to-ground communication [194].

Looking further to the future, the implications of extending efficient detectors out to wavelengths as long as 10 μm is an exciting prospect [73]. The mid-infrared is home to many absorption signatures for molecules and this is interesting for imaging and sensing [195, 196] both here on our own planet and extra-terrestrially. Exoplanet spectroscopy [197, 198] and dark matter detection [199] are examples of fields that will benefit from such detectors.

Of course, such detectors present engineering challenges that must be overcome. Fabrication perfection will become more of a necessity for developing efficient mid-infrared SNSPDs and optimising line-edge roughness (LER) of the nanowire structure will be a key parameter. As discussed in Ch. 3, §3.1.4, LER of the nanowires can impede the achievable switching current for a device and limits the fraction of the depairing current that can be obtained. For electron beam lithography, optimising parameters such as dose and resist thickness can improve the LER [200]. Indeed, in recent work research groups have improved the switching current and photoresponse of SNSPDs by tailoring the resist thickness [201] or resist type [202]. Looking to the future, advancements in photolithography from the semiconductor industry such as extreme-UV lithography [203] or immersion lithography [204] could provide a new approach to SNSPD fabrication. This would be particularly advantageous when scaling up to imaging arrays where uniformity across the array is desirable.

The other requirement for mid-infrared single-photon experiments will be the availability of optical components. As a starter, fibre development has advanced in recent years such that there are now a variety of options to fibre-couple SNSPDs for use in the mid-infrared. Whilst specialist glass fibres such as ZBLAN [205] and Chalcogenide [101] have been available for some years and are beginning to become more affordable, new designs of hollow-core photonic crystal fibres (HC-PCFs) for use in the mid-infrared are a fairly recent development [206]. These fibres could alleviate some of the mechanical robustness concerns of the specialist glass fibres, particularly for use in space-constrained cryostats for SNSPD coupling. Other fibre components necessary for many optical experimental setups are beginning to emerge with a small variety of in-fibre splitters and attenuators now available at the shorter wavelength end of the mid-infrared spectrum.

Over the time whilst my PhD was undertaken, SNSPDs have advanced rapidly in many areas outwith the sphere of extending them to mid-infrared wavelengths. Novel detector designs continue to emerge, such as the differential tapered readout [161] SNSPDs discussed in Ch. 6, §6.2, which have allowed advancements in the fundamental limit of timing jitter [39] to be leveraged in efficient detectors. The maximum count rate of SNSPDs is another area that has been pushed in recent years. Designs such as interleaving multiple shorter nanowires to reduce

the kinetic inductance [207] and connecting multiple devices in parallel [208] have boosted the maximum count rate of the detectors to the GHz regime. Lastly, scaling devices up to large areas is an intense area of ongoing research. The advantages of an SNSPD array are clear to see and whilst highly uniform arrays up to a kilopixel have now been demonstrated [63], it remains a challenge to scale the readout circuitry up to larger arrays. Several schemes have been demonstrated including row-column readout [63], thermal row-column readout [209], single-flux quantum (SFQ) logic [210], delay-line readout [188] and frequency [211] and amplitude [212] based multiplexing schemes. There are advantages to each scheme and, at the time of writing, there is no obvious best candidate for large area arrays. Constructing an SNSPD array optimised for use in the mid-infrared would create a powerful tool for a wide variety of fields such as life-science and environmental applications that no other technology can currently provide. A different approach to large-area SNSPDs was recently demonstrated with the emergence of microwire SNSPDs [213]. These large wire-width detectors allow the use of photolithography [214] and have achieved saturated internal detection efficiency at 1.55 μm with an active area of 400 μm^2 [215].

With the rise of integrated photonics [216], integrating SNSPDs on-chip with waveguides has also been a topic of interest [217]. This has resulted in fully integrated photonic circuits being realised with waveguide integrated SNSPDs [218] for optical quantum computing or optical neuromorphic computing applications. This is still an ongoing area of research with SNSPDs recently used to validate mid-infrared integrated photonic circuits [219], exploiting their long wavelength sensitivity.

All of these novel results have cross-over with each other and advances in the understanding of the processes required to advance each individual detection metric feed into the goal of achieving the ultimate single-photon detector. In parallel to the experimental demonstrations, theoretical advances in the understanding of the underlying detection mechanism [23, 220, 221] continue to be investigated in pursuit of the goal of an all-encompassing model that fits all of the experimental data. This deeper understanding of the detection process will aid in the design and fabrication of high-quality detectors.

The final technological deficiency currently barring the way to widespread adoption of SNSPDs as the single-photon detector of choice is that of the cooling requirements. Although detection metrics of SNSPDs currently far outperform semiconductor alternatives, the requirement to cool the devices to sub-10 K temperatures is unsuitable for some applications. That said, advances in turn-key cryogenics solutions have made this easier than ever, removing the requirement for prior knowledge of the cryogenics. Miniaturisation of the cryogenics is also a goal and an SNSPD system with a miniaturised 4 K cryostat has been demonstrated [222]. This system was based on a demonstrator unit for the Planck space mission, and a functionally equivalent version

was successfully launched in 2009. Commercial companies are also actively developing smaller versions of their products in a bid to decrease the size, weight and power consumption of the cryostats and widen the potential customer base.

It is clear from the recent advances shown above that SNSPDs are an active and growing field of research, now entering their 20th year since the first demonstration. With a variety of research groups around the world now focussed on advancing these detectors to the best that they can be, it seems likely that new benchmark metrics and novel detector designs will continue to appear into the future. The work presented here is a further step along the road to efficient, fast and user-friendly single-photon detection in the mid-infrared and all of the exciting applications that will follow.

Appendix A

Design and Operation of sub-1K Cryostat

In this appendix I will explain my design and the subsequent construction of the sub-1K cryostat used for the single-photon LIDAR experiments in Ch. 6.

A.1 Design

The base of the design was an RDK-101D coldhead and Zephyr compressor, both from Sumitomo Heavy Industries (SHI). This combination gives an easy-to-operate two stage coldhead capable of reaching 2.3 K, with the Zephyr compressor offering more cooling power - 0.16 W @ 4.2 K - than the more compact CNA-11 - 0.1 W @ 4.2 K. This is a Gifford-McMahon (GM) [223] type mechanical cryocooler. Mechanical GM cryocoolers utilise rotary valves to control the cooling cycle which allows them to be used with relatively cheap commercial compressors [224]. The GM cycle is shown in Fig. A.1 and described here:

- The compressor provides a high pressure (send) line and a low pressure (return). The coldhead has a hot end, T_{h} and cold end, T_{c}. In section A the rotary valve allows the high pressure gas to enter the coldhead and then the regenerator/displacer (R/D - shown in red) moves to the left, moved by the coldhead motor.
- Arrive at section B where the gas has moved passed the R/D and cooled down to sit in the cold end of the coldhead.
- Then the rotary valve moves and the coldhead is now connected to the low pressure side, section C.
- Gas moves past the R/D and into the low pressure outflow. The gas expands and heat is removed. Now the R/D moves and gas is forced past it, cooling the R/D as it passes. Now at section D.
- The rotary valve moves again and the system arrives back at section A to begin the cycle again.

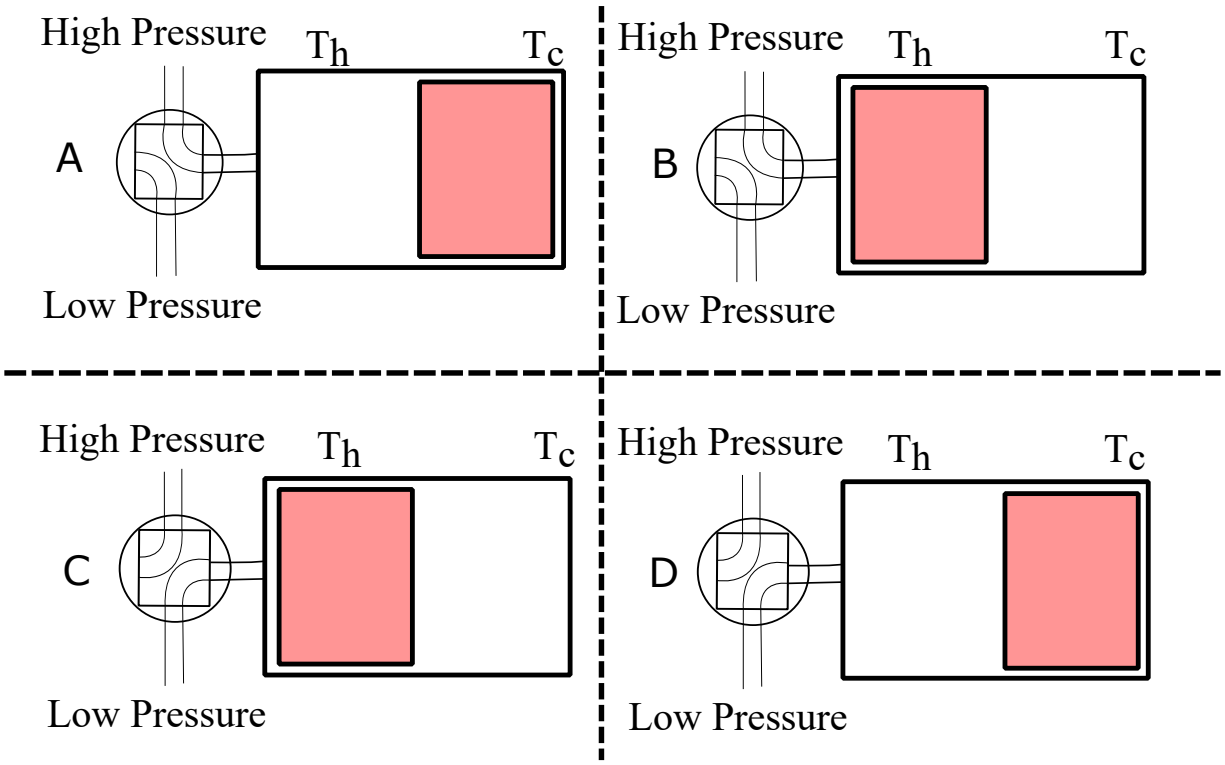

Figure A.1: Gifford-McMahon cycle.

The RDK-101D operates on this principle with some minor mechanical differences. A CAD model of the RDK-101D is shown in Fig. A.2 a).

The design goal of the cryostat was operation at <1 K for up to 24 hrs so to this end a Chase Research Cryogenics GL4 ^{4}He sorption cryocooler was chosen to achieve this temperature. A CAD model of this cryocooler is shown in Fig. A.2 b). Sorption fridges work by using an absorber to move helium gas around the cryocooler to facilitate cooling - if the absorber is cooled it will adsorb He gas but if it is heated then it will expel it. This absorber pump is one key component of the GL4 cryocooler and the other is a gas-gap heat switch. This is a component containing a further absorber and heater and a stainless steel tube. When the absorber is heated (and expels its gas), the tube will be filled with this gas and so conduct heat. If the absorber is cooled then it will adsorb all of the gas and the heat-switch will cease to conduct heat - barring some minor parasitic heat loss through the stainless steel tube. Both the pump and the heat-switch are operated by applying a DC voltage to a resistor mounted on them. Sorption cryocoolers are the choice for many scientific applications due to their simplicity and reliability [225]. The operation of the GL4 sorption fridge is described below:

- The GL4 must be pre-cooled until the coldhead is around 4 K. This is achieved with the RDK-101D. Once the head is at this base temperature the GL4 can be operated.

- The pump heater is turned on by applying a voltage. This causes the pump to warm up and

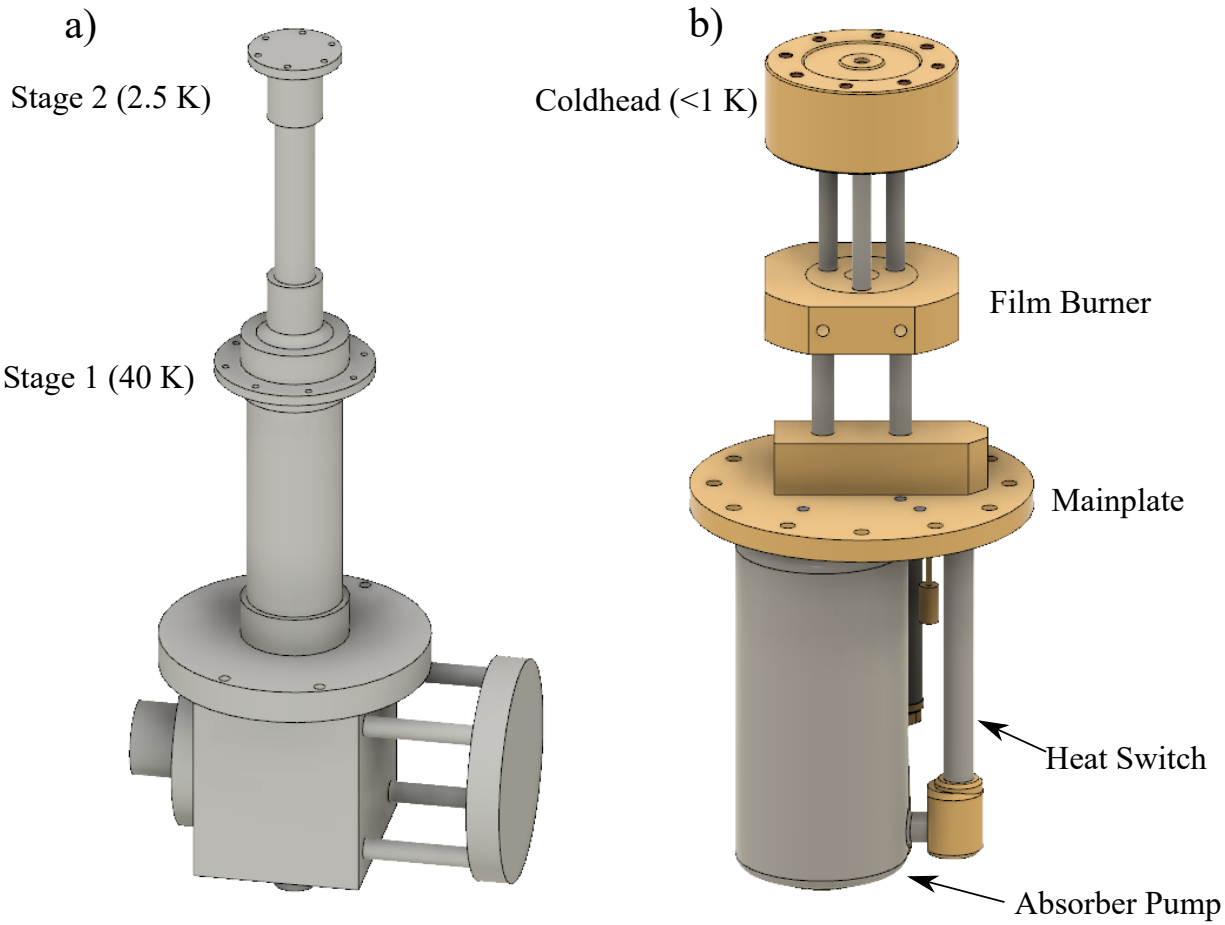

Figure A.2: a) CAD model of the RDK-101D. b) CAD model of the GL4 sorption fridge. Note that both models are not on the same scale.

expel its ^{4}He. As the pump is decoupled thermally from the rest of the GL4 (heat-switch is off) the gas is expelled but the coldhead remains cool. In this step the pump must be heated to 55 K and maintained there while the head is allowed to cool to 4 K. This ensures the ^{4}He is expelled from the pump and is liquefied in the head.

- Once the ^{4}He is liquefied in the head the pump heater is turned off and the heat-switch heater is turned on, again by applying a DC voltage. This thermally connects the pump to the GL4 mainplate and it will begin to cool. The heat-switch is heated to around 20 K and maintained there to ensure it is fully on.

- As the pump cools it begins to adsorb ^{4}He. This pumps it back up from the head and provides the required cooling. The head temperature will fall rapidly to <1 K and remain there until the ^{4}He is all evaporated from the head and adsorbed by the pump. This time varies depending on the application and load.

The film burner achieves a temperature of around 1 K during normal operation and is required as the ^{4}He turns superfluid in the head and will creep up the cryocooler due to the temperature gradient. This will degrade cryocooler performance and so it is necessary to burn it off at the film burner [226]. It also serves as a useful point to buffer parasitic loads such as cabling.

In order to interface a GM coldhead and GL4 cryocooler a variety of interfacing pieces are required. These were designed in CAD software (Solidworks to begin with and Autodesk Fusion 360 in later designs) and manufactured by an external machinist. Pieces were either manufactured in oxygen free high conductivity (OFHC) copper or aluminium. OFHC copper was chosen to maximise thermal conductivity and all copper pieces were gold plated with 1 μm of gold to avoid oxidation and degradation of the thermal contact. Fig. A.3 shows the mating of the GL4 with the RDK-101D. The dark copper coloured pieces are the new interfacing pieces. The 40 K plate is used to thermally sink cables as well as anything that does not require to be as cold as 1 K (cryo electronics etc). The 4 K plate of the RDK 101-D is connected to the GL4 mainplate with four copper affixing posts. An adapter ring, visible below the GL4 mainplate is used to affix the 4 K radiation shield. Finally an additional plate is affixed to the GL4 coldhead to allow mounting of SNSPDs. An aluminium manifold was designed to allow the input of electrical cables and optical fibres as well as the base for the outer vacuum can. Radiation shielding is required to ensure the correct operation of the cryostat as well as ensuring low-noise operation of SNSPDs. A two-layer approach is used here. On the right of Fig. A.3 the 4 K radiation shield is shown attached and the first part of a three section 40 K shield is also shown. When fully assembled the 40 K shield will fully encase the low-temperature assembly.

As the GL4 works on the basis of liquid ^{4}He sitting in the coldhead as it liquefies it is required to be operated upside down. For lab-based operations it is usual to just construct the entire

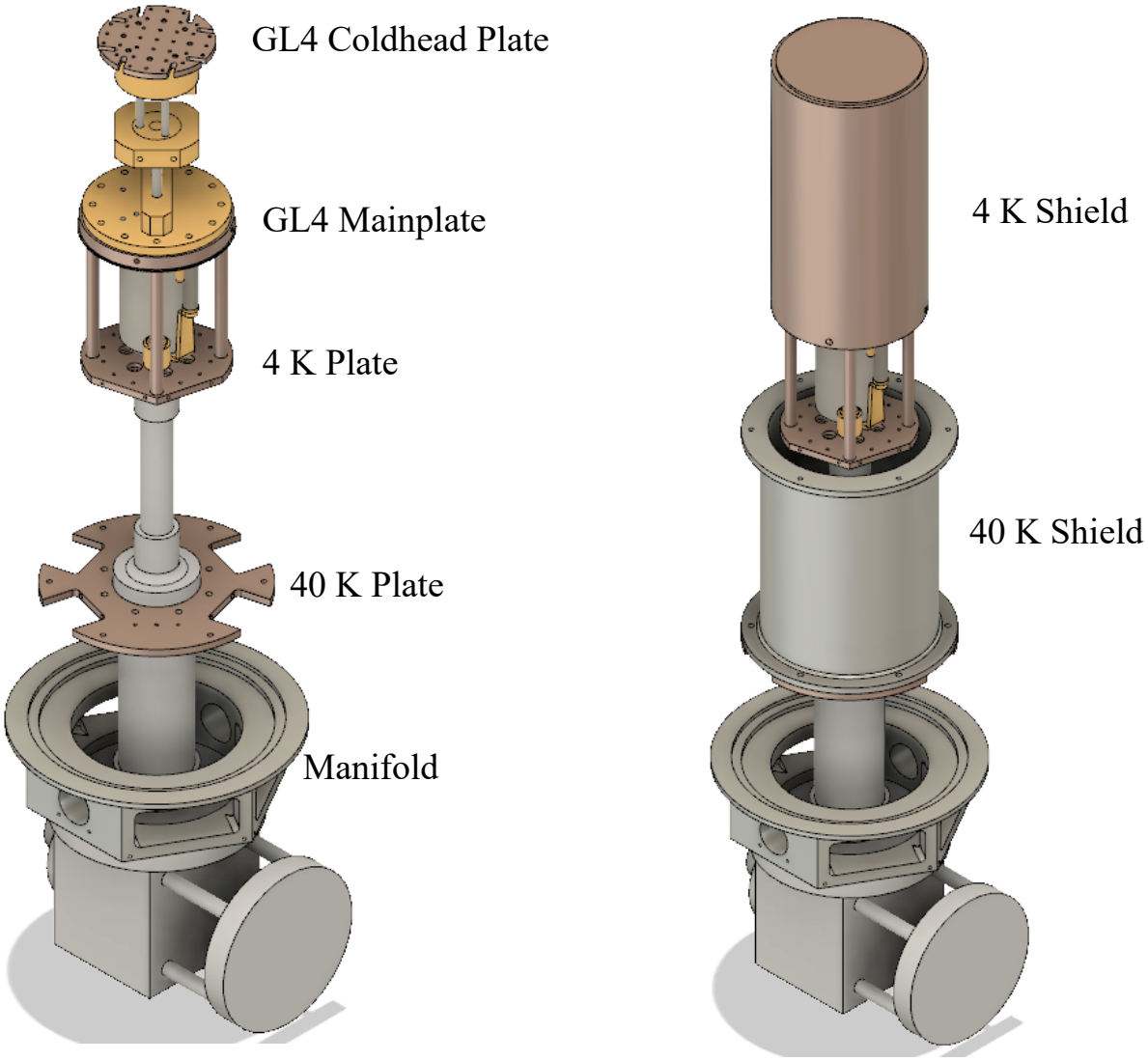

Figure A.3: Left: GL4 interfaced with an RDK 101D showing the custom copper pieces. Right: Showing the two layers of radiation shielding. The assembly is orientated pointing upwards during assembly and device loading and inverted (with the GL4 at the bottom) for operation.

cryostat in an inverted position but due to the portable design goal here a more flexible approach was implemented. An aluminium clamp was designed that securely held the entire cryostat assembly by clamping the outer vacuum can. This was then interfaced to bearings and bolted to a portable aluminium frame on wheels. In this way the fridge could be worked on and loaded with devices in the upright position and then flipped in order to be cooled. A simple brake wheel was added to fix the fridge in the 'up' or 'down' position. The pieces and assembly are shown in Fig. A.4.

A photograph of the finished cryostat in the 'up' position in its frame with the upper vacuum can and radiation shields removed is shown in Fig. A.5

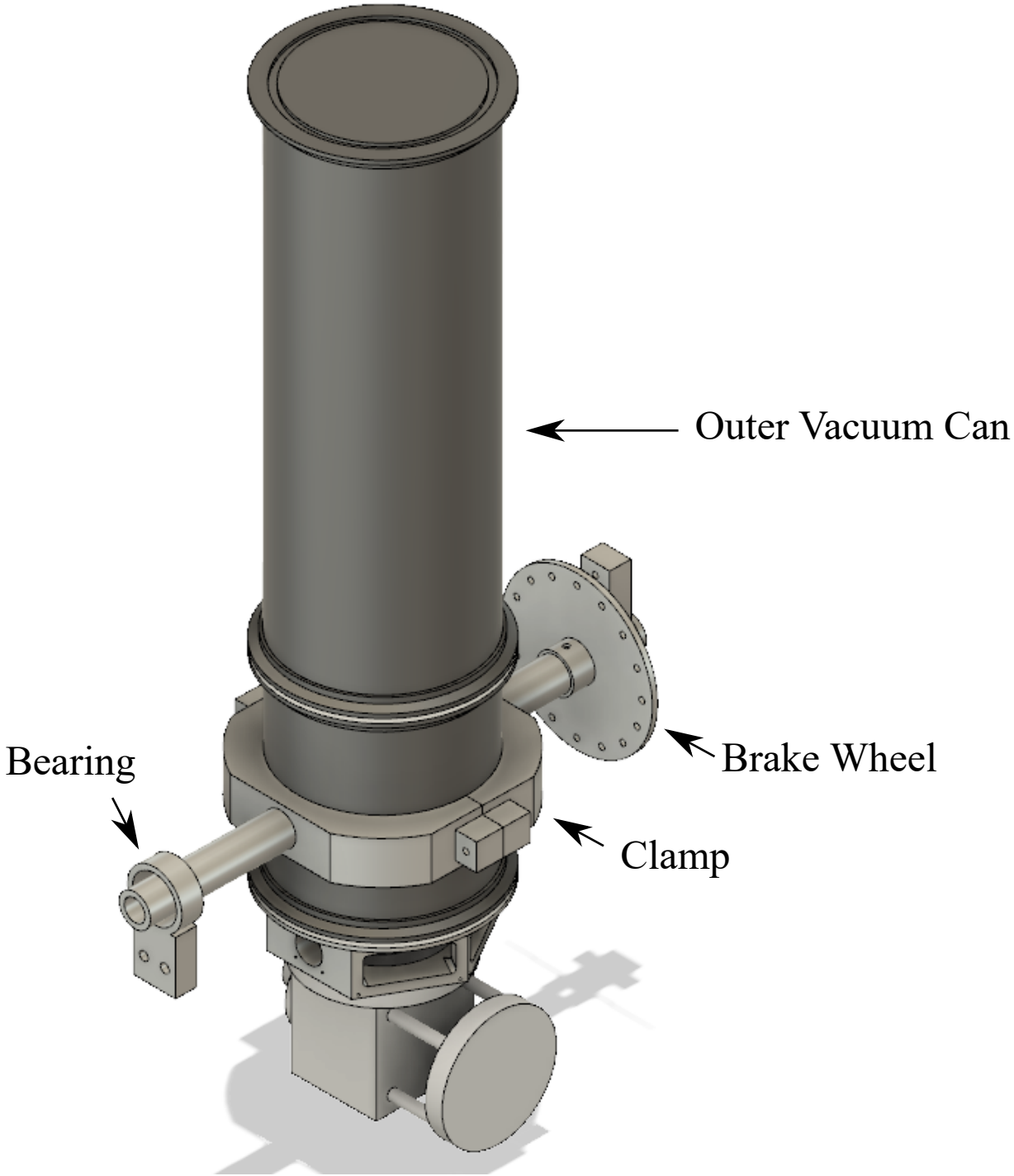

Figure A.4: Outer assembly of the cryostat showing the mechanism by which it is rotated.

Figure A.5: Photograph of completed cryostat in the upright position.

A.2 Controlling the Cooldown

Ease of use was a primary concern when considering the user interface (UI) for this cryostat. As it was designed for use in field trials, experienced operators were not always guaranteed meaning a simple and clear operating sequence was desired. In order to control when the various steps in the cooldown cycle were scheduled an accurate readout of the temperatures of various components was required. There were 4 Si diode thermometers mounted onto the GL4 mainplate, film burner, pump and heat switch. A RuO_2 calibrated resistor sensor was used for the coldhead. Readout for all of the thermometers was via Constantan twisted pairs running from the GL4 through the manifold to room temperature. The readout for the Si thermometers was performed with an SRS SIM922 temperature monitor mounted in a SIM900 mainframe. Calibration curves for each thermometer were loaded into this. The RuO_2 was read out using a SIM921 AC resistance bridge, also mounted in the SIM900 and calibrated using a manufacture provided calibration curve. The DC voltages required for the heat-switch and pump heaters was provided by a Keithley 3 channel DC supply and carried through the cryostat by copper twisted pairs.

The cooldown cycle described for the GL4 in section A.1 was controlled by a custom GUI implemented in Python and the PyQt framework. The GUI ran on a Raspberry Pi computer with a touchscreen display. Upon starting the Pi, instruments are connected and checked before the homescreen is launched. From here a simple one button click starts the cooldown and runs through the necessary voltage cycles to achieve 1 K operation. While cooling down the temperatures of the various thermometers are read out and displayed on the touch screen - logging of temperatures is also possible. The Pi can be remotely operated or cooldowns scheduled ahead of time to ensure the cryostat is cold when it needs to be. A settings page was added to tweak cooldown parameters as necessary. A full version of the cooldown Python code is available at [227].

Final additions to the cryostat were to mount the electronics for the field trial in Ch. 6, §6.2. A cryogenic bias tee was mounted onto the 40 K plate of the RDK-101D and connected to the readout electronics via flexible copper coaxial cable. From the bias tee at 40 K to the SNSPD mounted at 1 K the connection was made with semi-rigid Cupronickel (CuNi) coaxial cable, with a length of 1 m to minimise parasitic loading of the GL4 coldhead. These CuNi cables were also clamped to the GL4 main plate and film burner to further minimise loading on the coldhead.

The cryostat was tested with a differential readout tapered SNSPD as described in Ch. 6, §6.2.2. A temperature of 850 mK was achieved and held for a period of time exceeding 24 hrs. Throughout the LIDAR field trials the cryostat was utilised remotely and on a time-scheduled basis without issue. An example cooldown is shown in Fig. A.6 showing a temperature of 850 mK being achieved. The heating of the pump and subsequent turning on of the heat switch can

clearly be seen.

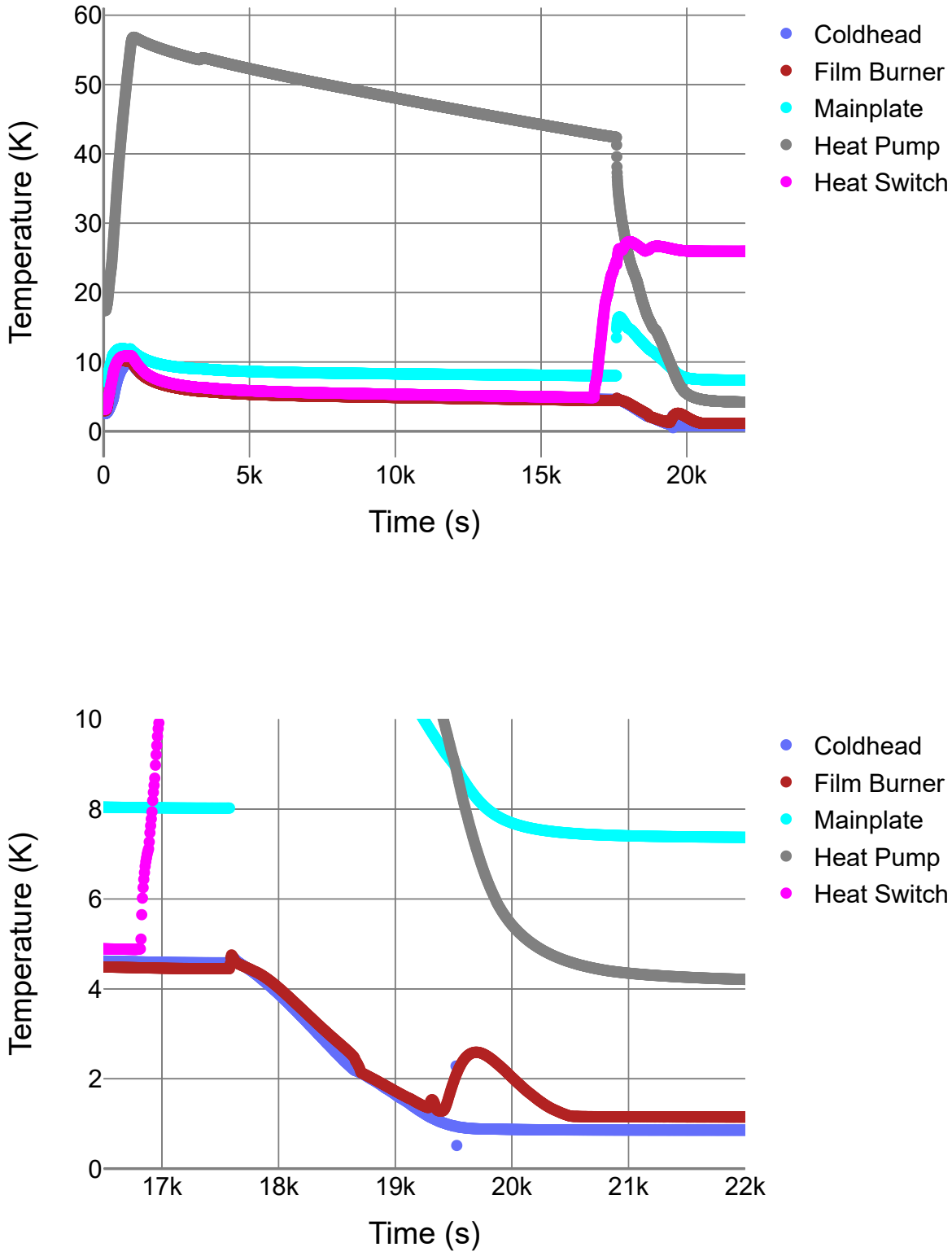

Figure A.6: Cooldown data from the completed cryostat. The bottom figure shows a zoomed view of the end of the cooldown.

Appendix B

Python Programming for Data Capture and Analysis

Python [228] is an open source general purpose programming language often used in scientific applications due to its wide variety of packages that can be used for this purpose. In this thesis I have extensively used Python to write both data gathering and data processing code that has been used to complete the experiments. In this appendix I will go over the main code that has been developed and used. All of the code is available in the references and will remain so in the future, in order that data can be reproduced if necessary and also so that it can be re-purposed by anyone who wishes to do so.

B.1 Data Gathering

Data gathering from various scientific instruments is a routine part of experimental science. Communication with instruments can be done through the GPIB interface and the standard commands for programmable instruments (SCPI) language, USB or RS232 as well as some other more obscure options. The VISA interface is used to deal with all of these. For implementation in Python the package PyVisa [229] is utilised. Typically in Glasgow an SRS SIM900 mainframe is used with the required modules - Si diode thermometer readout, voltage source, voltmeter etc - as well as a variety of other instruments such as power meters or pulse counters.

The data gathering application was designed to take data from a variety of instruments common to the characterisation and testing of devices performed in the lab at Glasgow on an almost daily basis. It is a GUI written in the TKinter interface which was chosen as it is bundled with Python and therefore required no additional packages. Upon starting the GUI the user is presented with a instrument setup page where the instruments desired must be chosen based on their addresses. Currently any SIM900 modules can be selected as well as Thorlabs powermeters, HP/Keysight optical attenuators and pulse counters. The code has been structured such that

additional instruments can be easily added as the requirement develops.

After instrument selection a list of available measurements is shown. Currently supported measurements are resistance against temperature (RT), system efficiency, photon count rate (PCR) against bias current, dark count rate (DCR) against bias current and a generic value against time measurement where data can be taken from any instrument and logged. For the DCR/PCR/Efficiency measurements the bias range and input power is required as well as the attenuation needed. An attenuation calculator is included so that attenuation values for a given number of photons per pulse can be calculated. If programmable attenuators are used then the application will automatically adjust these for the measurement - a range of attenuations can be given and performed back to back. If no programmable attenuators are present then a manual attenuation option is provided where the light input must be manually blocked/unblocked at appropriate points when prompted by the application.

Once data has been taken a basic plot page is provided to quickly visualise the data. This is designed for a quick overview rather than publication-ready plots and is implemented using the matplotlib [230] package. The data is automatically saved in the /Data folder after the measurement finishes and so is available for more in depth analysis and plotting at a later stage.

The large majority of PCR/DCR/efficiency data presented in this thesis has been obtained using this application. The full code is available at [231]

B.2 HydraHarp Control

The HydraHarp TCPSC modules from Picoquant provide a precise (ps) timing resolution option for photon-counting applications as well as a pleasant user-interface that makes them a popular choice in many applications. The bundled software is useful for taking single histograms but for building up depth images as in the 2.3 μm LIDAR experiment shown in Ch. 6, §6.1, it is not particularly well suited. Picoquant provide a DLL library for custom development and here the aim was to wrap all of these functions into Python so it was more convenient to deploy within the lab environment. The wrappings require the ctypes package which is used to call the DLLs. The library is designed to be imported into other code and used within it. Once a device (TCSPC module) is opened then the entire suite of DLL-based functions can be accessed. It is also possible to utilise it on the command line.

This library was developed for and then implemented in the data gathering code for the mid-infrared LIDAR experiment (Ch. 6, §6.1). This allowed the models to be scanned automatically within a custom environment which did not require interfacing to the Picoquant software package.

The full code is available at [232]

B.3 Becker and Hickl Processing and Control

Becker and Hickl TCSPC cards represent the cutting-edge of TCSPC hardware. They offer timing bins down to 203 fs in their high end offerings. For the ultra-fast jitter LIDAR experiments outlined in Ch. 6, §6.2, these cards provide the necessary resolution to take advantage of the detector properties. As shown in the experiment, images are taken with the Becker and Hickl software bundled with the cards and results in an output file in the .sdt format. This is a binary format specific to Becker and Hickl products. This data then needs to be processed into depth images and the application outlined here was built to achieve this aim.

Reading .sdt files is achieved easily in Python utilising the sdtfile package. This results in a 2D array of histogram data in the numPy [233] format. This data is then ready for processing into an image. The application was again designed in TKinter as it was to be deployed on a variety of different PCs in the field - using TKinter meant that all of the required packages for the GUI were already bundled with a standard Python distribution. In most cases the application was running alongside the data gathering software from Becker and Hickl so images could be quickly viewed without any transfer of data. When opened the application prompts the user for a .sdt file to process. The following options are then available:

- Gating: This is used to move the start and end point for the histogram. Typically this is used to remove unwanted back-reflections from the optical setup and home in on the peak of interest. Any large back reflections can result in poor results from the cross-correlation
- Automatically determine IRF: If no IRF file is available (or wanted) then the application can take the brightest (most counts in peak) pixel and use that as the IRF.
- Subtract back reflections: The idea of this option was that a histogram with no target could be gathered which would then contain the back reflections from the optics. This could then be subtracted from the target histograms and therefore remove the back-reflections. This option has yet to be tested.
- Fit instead of X-corr: This is useful if the cross-correlation is failing for any reason. Here instead of cross-correlation with the IRF the histograms are fit with an exponentially-modified Gaussian (EMG) to determine the peak position. This is more computationally intensive so not useful for large images.
- Correct aspect in plot: This takes the actual scene size as an input and scales the depth image accordingly.

- Largest value cut-off: If there are any artificially high returns from position-specific back reflections or such they can be removed from the image.
- Remove empty pixels: If the cross-correlation fails in a pixel it will return an empty value which results in a dip in the image. This removes these if desired.
- Bin the data: Adds an option to bin the data before the image is formed. When using small bin sizes afforded by the SPC-150NXX SNR can be gained at the expense of timing resolution by binning the data. Can use any number that can be equally divided i.e 2,4,8. If, for example 2 is chosen with 203 fs bins then it will re-bin the data into 406 fs bins.

Once the options have been chosen as desired, the 'Plot it' button will then process and output the image. The cross-correlation is performed with the 'correlate' function from the SciPy package and, if chosen, the fitting of the EMG is handled by SciPy's 'curve_fit'. The first thing that is done is the brightest pixel is selected and fitted with an EMG function. Any gating chosen is also applied to this pixel and then the plot of the fitted return histogram is shown. In this way the user can determine if the gating has been correctly chosen before commencing with the heavy processing. A prompt asks the user if they are happy to proceed. Then an instrument response function (IRF) file is asked for if it is not automatically being determined. This is also plotted and displayed to the user to check before processing begins. The IRF, however it is obtained, is then used to perform the cross-correlation of each pixel. At the end, an array of peak positions is output. If fitting rather than cross-correlation is used it results in the same output.

Results are then visualised using the Plotly package. A 2D plot of the max counts (intensity plot) is output along with a 2D and 3D depth image. The Plotly package provides high-quality, publication ready graphics with a lot of customisation options. The code for processing LIDAR images from sdt files is available at [234].

A further stream of development for the above code is leveraging the computational power of modern graphics processing units (GPUs) [235] to provide speed ups in the image processing. GPUs typically operate at lower frequencies than their CPU counterparts but have many more cores so are a benefit when performing tasks that can be done in parallel. For this work, offloading the cross-correlation of the IRF with each pixel histogram to the GPU was tested to investigate the performance gains. Interfacing with the GPU was performed with OpenCL [236] and the FFT implementations and computation framework was provided by the Reikna library [237]. For the testing presented here the CPU was a 6-core Intel i7 (2.6 GHz) and the GPU was an AMD Radeon Pro 5300M. Data was read in as usual in Python and then instead of looping over the image array and performing the cross-correlation on each pixel the data was sent to the GPU and the cross correlation was performed in parallel. As the GPU used had 4 GB of its own RAM the data was sent in batches of 64 x 64 blocks to avoid running into memory issues. Higher

performance GPUs with larger amounts of memory may not require this and would provide a further performance gain. For a test 512 x 512 pixel depth image the above process resulted in a 67 % speed up over purely using the CPU, taking 27 seconds instead of 82 seconds. This is encouraging as the code is not yet fully optimised - currently other tasks such as finding the maximum timing bin of each cross-correlated histogram are performed by the CPU and these could also be implemented fully on the GPU side, providing yet more performance improvements. Development of this will continue and will allow rapid image processing of LIDAR data in the field.

As well as the convenient histogram .sdt format the Becker and Hickl modules are also capable of saving data in time tagged formats. This is necessary for performing advanced image processing such as that shown in [138]. The time tagged data can be output at the same time as an .sdt file if required or on its own. The output is a pair of files; a .spc file containing the time tagged data and a .set file containing the setup data. For each photon that is counted an entry is saved that contains the micro time, macro time and the detector channel. Photon data is saved sequentially and is organised into per pixel sets, so that images can still be constructed. This results in a lot more information being saved - at the expense of large output files. The .set file contains parameters that pertain to the dataset such as TACRange,TACGain, ADCResolution and image size.

The goal for this library was a comprehensive set of tools for decoding and working with .spc and .set files. It is designed to be an imported library where each dataset is treated as an object where properties and functions can be accessed using the object orientated syntax. A file is first imported and a flag indicates whether a .set file will be used. If included then the user will be prompted to load the .set file. If the .set file is not available for any reason then it is possible to manually provide the parameters in the form of a list of form:

$$SetupInfoExample = [TACRange, TACGain, ADCResolution, ImageSizeX, ImageSizeY] \tag{B.1}$$

If no .set file or manual list is provided then the program will abort with an error. The create_array function can then be called to parse the data and create a numpy array. It is possible to get all of the data from each photon in one large array but in practice this will lead to memory issues for normal LIDAR experiments. Therefore other functions such as create_histo_array are provided to build histogram arrays (similar to what is saved in a .sdt file) to construct images from time tagged data. Other options include artificially shortening the integration time per pixel to see the effects of less photons in the final image.

The library is designed to be built upon depending on the specific use-case. All data is

available in convenient numpy arrays which can be saved to the .npy format or processed interactively. Additional functions can be added to the library and then specified with a 'array_type' flag as development continues. The full code for working with SPC files is available at [238].

Ongoing Work

Development is still under way towards a full suite of Python based tools for working with Becker and Hickl TCSPC cards. The main ongoing work is in wrapping the DLLs for controlling the cards without using the Becker and Hickl software which leans more towards life-science applications. At the time of writing this thesis the bulk of the library has been written and initial tests show that controlling basic functions like taking histograms works well. Once more thoroughly tested this code will be made available in the public domain. The next stage is to integrate the controlling of the TCSPC card and the controlling of the galvanometer mirrors into a unified LIDAR application with in-built image processing capability.

Appendix C

Publications and Presentations

Here is a list of the publications and presentations given during the course of this PhD.

C.1 Publications

- **Infrared single-photon sensitivity in atomic layer deposited superconducting nanowires** - Gregor G. Taylor, Dmitry V. Morozov, Ciaran T. Lennon, Peter S. Barry, Calder Sheagren, Robert H. Hadfield – Applied Physics Letters **118**(19), 191106 (2021)
  DOI:10.5525/gla.researchdata.1146

- **Two-photon Quantum Interference and Entanglement at 2.1 µm** - Shashi Prabhakar, Taylor Shields, Adetunmise Dada, Mehdi Ebrahim, Gregor G. Taylor, Dmitry Morozov, Kleanthis Erotokritou, Shigehito Miki, Masahiro Yabuno, Hirotaka Terai, Corin Gawith, Michael Kues, Lucia Caspani, Robert H. Hadfield and Matteo Clerici – Science Advances **6**(13), eaay5195 (2020)
  DOI:10.5525/gla.researchdata.882

- **Photon counting LIDAR at 2.3 µm wavelength with superconducting nanowires** - Gregor G. Taylor, Dmitry Morozov, Nathan R. Gemmell, Kleanthis Erotokritou, Shigehito Miki, Hirotaka Terai, Robert H. Hadfield - Optics Express **27**(26), 38147–38158 (2019)
  DOI:10.5525/gla.researchdata.938

- **Nano-optical photoresponse mapping of superconducting nanowires with enhanced near infrared absorption** - Kleanthis Erotokritou, Robert M. Heath, Gregor G. Taylor, Cheng Tian, Archan Banerjee, Alessandro Casaburi, Chandra M. Natarajan, Shigehito Miki, Hirotaka Terai, Robert H. Hadfield - Superconductor Science and Technology **31**(12), 125012 (2018)
  DOI:10.5525/gla.researchdata.702

C.2 Conference Presentations

- **Mid-infrared photon counting with superconducting nanowires** - Gregor G. Taylor, Dmitry Morozov, Robert H. Hadfield – , SPIE Optics + Optoelectronics Digital Forum (Invited Talk, 2021 - given online due to global pandemic)

- **Single-photon LIDAR in the Mid-Infrared with Superconducting Detectors** - Gregor G. Taylor, Dmitry Morozov, Kleanthis Erotokritou, Shigehito Miki, Hirotaka Terai, Robert H. Hadfield – , IEEE 14th Workshop on Low Temperature Electronics, Matera, Italy. (Invited Talk, 2021 - given online due to global pandemic)

- **Long-range depth imaging with 13 ps temporal resolution using a superconducting nanowire single-photon detector** - Gregor G. Taylor, Aongus McCarthy, Boris Korzh, Andrew Beyer, Dmitry Morozov, Ryan Briggs, Jason Allmaras, Bruce Bumble, Matthew Shaw, Robert H. Hadfield, Gerald Buller – Conference on Lasers and Electro-Optics (CLEO), San Jose, USA. (Oral presentation, 2020 - given online due to global pandemic)

- **Mid infrared single photon detection with superconducting nanowires** - Gregor G. Taylor, Dmitry Morozov, Kleanthis Erotokritou, Shigehito Miki, Hirotaka Terai, Robert H. Hadfield – SPIE Defense and Commercial Sensing, Advanced Photon Counting Techniques, Anaheim, USA. (Invited talk, 2020 - given online due to global pandemic)

- **Single photon LIDAR at 2.3 µm with SNSPDs** - Gregor G. Taylor, Dmitry Morozov, Kleanthis Erotokritou, Nathan R. Gemmell, Robert H. Hadfield – Single Photon Workshop, Milan, Italy. (Poster, 2019)

- **2.3 µm wavelength single photon LIDAR with superconducting nanowire detectors** - Gregor G. Taylor, Dmitry Morozov, Nathan R. Gemmell, Kleanthis Erotokritou, Robert H. Hadfield – Conference on Lasers and Electro-Optics (CLEO), San Jose, USA. (Poster, 2019)

- **Generation and Detection of Down-converted Photon Pairs at 2.080 µm** - Shashi Prabhakar, Taylor Shields, Damian Powell, Gregor G. Taylor, Dmitry Morozov, Mehdi Ebrahim, Michael Kues, Lucia Caspani, Corin Gawith, Robert H. Hadfield, Matteo Clerici – Conference on Lasers and Electro-Optics (CLEO), San Jose, USA. (Poster, 2019)

- **Mid infrared characterization of SNSPDs** - Gregor G. Taylor, Dmitry Morozov, Robert H. Hadfield - 683. WE-Heraeus-Seminar, Physics and Applications of SNSPDs, Bad Honnef, Germany. (Poster, 2018)

Bibliography

[1] "Single Quantum," https://singlequantum.com, accessed August 2021.

[2] "Quantum Opus," https://www.quantumopus.com, accessed August 2021.

[3] "Photon Spot," https://www.photonspot.com, accessed August 2021.

[4] "Scontel," https://www.scontel.ru, accessed August 2021.

[5] "ID Quantique," https://www.idquantique.com, accessed August 2021.

[6] G. G. Taylor, D. V. Morozov, C. T. Lennon, P. S. Barry, C. Sheagren, and R. H. Hadfield, "Infrared single-photon sensitivity in atomic layer deposited superconducting nanowires," Appl. Phys. Lett. **118**(19), 191106 (2021).

[7] G. G. Taylor, D. Morozov, N. R. Gemmell, K. Erotokritou, S. Miki, H. Terai, and R. H. Hadfield, "Photon counting LIDAR at 2.3 μm wavelength with superconducting nanowires," Opt. Express **27**(26), 38147–38158 (2019).

[8] M. Planck, "On the law of distribution of energy in the normal spectrum," Annalen der Physik **4**(553), 1 (1901).

[9] A. Einstein, "On a heuristic point of view about the creation and conversion of light," Annalen der Physik **17**(6), 132–148 (1905).

[10] G. N. Lewis, "The conservation of photons," Nature **118**(2981), 874 (1926).

[11] H. K. Onnes, "The discovery of superconductivity," Commun. Phys. Lab **12**, 120 (1911).

[12] W. Meissner and R. Ochsenfeld, "Ein neuer effekt bei eintritt der supraleitfähigkeit," Naturwissenschaften **21**(44), 787–788 (1933).

[13] J. Bardeen, L. N. Cooper, and J. R. Schrieffer, "Theory of superconductivity," Phys. Rev. **108**(5), 1175 (1957).

[14] T. Timusk, "The superconducting energy gap," La Physique Au Can. **67**(2), 99 (2011).

[15] F. B. Silsbee, "A note on electrical conduction in metals at low temperatures," J. Wash. Acad. Sci. **6**(17), 597–602 (1916).

[16] W. Tuyn and H. K. Onnes, "The disturbance of supra-conductivity by magnetic fields and currents. the hypothesis of silsbee," J. Frankl. Inst. **201**(4), 379–410 (1926).

[17] D. Dew-Hughes, "The critical current of superconductors: an historical review," Low Temp. Phys. **27**(9), 713–722 (2001).

[18] B. Goodman, "Type II superconductors," Rep. on Prog. Phys. **29**(2), 445 (1966).

[19] C. M. Natarajan, M. G. Tanner, and R. H. Hadfield, "Superconducting nanowire single-photon detectors: physics and applications," Supercond. Sci. Technol. **25**(6), 063001 (2012).

[20] G. Gol'tsman, O. Okunev, G. Chulkova, A. Lipatov, A. Semenov, K. Smirnov, B. Voronov, A. Dzardanov, C. Williams, and R. Sobolewski, "Picosecond superconducting single-photon optical detector," Appl. Phys. Lett. **79**(6), 705–707 (2001).

[21] A. A. Abrikosov, "The magnetic properties of superconducting alloys," J. Phys. Chem. Solids **2**(3), 199–208 (1957).

[22] L. Bulaevskii, M. Graf, C. Batista, and V. Kogan, "Vortex-induced dissipation in narrow current-biased thin-film superconducting strips," Phys. Rev. B **83**(14), 144526 (2011).

[23] A. Engel, J. Renema, K. Il'in, and A. Semenov, "Detection mechanism of superconducting nanowire single-photon detectors," Supercond. Sci. Technol. **28**(11), 114003 (2015).

[24] L. N. Bulaevskii, M. J. Graf, and V. G. Kogan, "Vortex-assisted photon counts and their magnetic field dependence in single-photon superconducting detectors," Phys. Rev. B **85**(1), 014505 (2012).

[25] A. Engel, J. Lonsky, X. Zhang, and A. Schilling, "Detection mechanism in SNSPD: numerical results of a conceptually simple, yet powerful detection model," IEEE Transactions on Appl. Supercond. **25**(3), 1–7 (2014).

[26] A. Zotova and D. Y. Vodolazov, "Photon detection by current-carrying superconducting film: A time-dependent ginzburg-landau approach," Phys. Rev. B **85**(2), 024509 (2012).

[27] F. Najafi, F. Marsili, V. B. Verma, Q. Zhao, M. D. Shaw, K. K. Berggren, and S. W. Nam, *Superconducting Nanowire Architectures for Single Photon Detection* (Springer International Publishing, Chapter in Superconducting Devices in Quantum Optics, RH Hadfield and G Johansson, 2016), pp. 3–30.

[28] D. V. Reddy, R. R. Nerem, S. W. Nam, R. P. Mirin, and V. B. Verma, "Superconducting nanowire single-photon detectors with 98% system detection efficiency at 1550 nm," Optica **7**(12), 1649–1653 (2020).

[29] F. Marsili, V. B. Verma, J. A. Stern, S. Harrington, A. E. Lita, T. Gerrits, I. Vayshenker, B. Baek, M. D. Shaw, R. P. Mirin, and S. W. Nam, "Detecting single infrared photons with 93% system efficiency," Nat. Photonics **7**(3), 210 (2013).

[30] R. Meservey and P. Tedrow, "Measurements of the kinetic inductance of superconducting linear structures," J. Appl. Phys. **40**(5), 2028–2034 (1969).

[31] A. J. Kerman, E. A. Dauler, W. E. Keicher, J. K. Yang, K. K. Berggren, G. Gol'Tsman, and B. Voronov, "Kinetic-inductance-limited reset time of superconducting nanowire photon counters," Appl. Phys. Lett. **88**(11), 111116 (2006).

[32] F. Marsili, F. Najafi, E. Dauler, R. Molnar, and K. Berggren, "Afterpulsing and instability in superconducting nanowire avalanche photodetectors," Appl. Phys. Lett. **100**(11), 112601 (2012).

[33] O. Kahl, S. Ferrari, V. Kovalyuk, G. N. Goltsman, A. Korneev, and W. H. Pernice, "Waveguide integrated superconducting single-photon detectors with high internal quantum efficiency at telecom wavelengths," Sci. Rep. **5**, 10941 (2015).

[34] H. Shibata, K. Shimizu, H. Takesue, and Y. Tokura, "Superconducting nanowire single-photon detector with ultralow dark count rate using cold optical filters," Appl. Phys. Express **6**(7), 072801 (2013).

[35] H. Shibata, K. Shimizu, H. Takesue, and Y. Tokura, "Ultimate low system dark-count rate for superconducting nanowire single-photon detector," Opt. Lett. **40**(14), 3428–3431 (2015).

[36] M. K. Akhlaghi and A. H. Majedi, "Gated mode superconducting nanowire single photon detectors," Opt. Express **20**(2), 1608–1616 (2012).

[37] A. Engel, A. Semenov, H.-W. Hübers, K. Il'in, and M. Siegel, "Fluctuation effects in superconducting nanostrips," Phys. C: Supercond. its Appl. **444**(1-2), 12–18 (2006).

[38] H. Bartolf, A. Engel, A. Schilling, K. Il'in, M. Siegel, H.-W. Hübers, and A. Semenov, "Current-assisted thermally activated flux liberation in ultrathin nanopatterned NbN] superconducting meander structures," Phys. Rev. B **81**(2), 024502 (2010).

[39] B. Korzh, Q.-Y. Zhao, J. P. Allmaras, S. Frasca, T. M. Autry, E. A. Bersin, A. D. Beyer, R. M. Briggs, B. Bumble, M. Colangelo, G. M. Crouch, A. E. Dane, T. Gerrits, A. E. Lita, F. Marsili, G. Moody, C. Pena, E. Ramirez, J. D. Rezac, N. Sinclair, M. J. Stevens, A. E.

Velasco, V. B. Verma, E. E. Wollman, S. Xie, D. Zhu, P. D. Hale, M. Spiropulu, K. L. Silverman, R. P. Mirin, S. W. Nam, A. G. Kozorezov, M. D. Shaw, and K. K. Berggren, "Demonstration of sub-3 ps temporal resolution with a superconducting nanowire single-photon detector," Nat. Photonics pp. 1–6 (2020).

[40] D. Y. Vodolazov, "Minimal timing jitter in superconducting nanowire single-photon detectors," Phys. Rev. Appl. **11**(1), 014016 (2019).

[41] N. Calandri, Q.-Y. Zhao, D. Zhu, A. Dane, and K. K. Berggren, "Superconducting nanowire detector jitter limited by detector geometry," Appl. Phys. Lett. **109**(15), 152601 (2016).

[42] A. Kozorezov, C. Lambert, F. Marsili, M. Stevens, V. Verma, J. Allmaras, M. Shaw, R. Mirin, and S. W. Nam, "Fano fluctuations in superconducting-nanowire single-photon detectors," Phys. Rev. B **96**(5), 054507 (2017).

[43] A. Barth, "Infrared spectroscopy of proteins," Biochimica et Biophys. Acta (BBA)-Bioenergetics **1767**(9), 1073–1101 (2007).

[44] P. Werle, F. Slemr, K. Maurer, R. Kormann, R. Mücke, and B. Jänker, "Near-and mid-infrared laser-optical sensors for gas analysis," Opt. Lasers Eng. **37**(2-3), 101–114 (2002).

[45] F. Marsili, F. Bellei, F. Najafi, A. E. Dane, E. A. Dauler, R. J. Molnar, and K. K. Berggren, "Efficient single photon detection from 500 nm to 5 μm wavelength," Nano Lett. **12**(9), 4799–4804 (2012).

[46] F. Marsili, V. Verma, M. Stevens, J. Stern, M. Shaw, A. Miller, D. Schwarzer, A. Wodtke, R. Mirin, and S. Nam, "Mid-infrared single-photon detection with tungsten silicide superconducting nanowires," in *CLEO: Science and Innovations,* (Optical Society of America, 2013), pp. CTu1H–1.

[47] S. Cova, M. Ghioni, A. Lotito, I. Rech, and F. Zappa, "Evolution and prospects for single-photon avalanche diodes and quenching circuits," J. Mod. Opt. **51**(9-10), 1267–1288 (2004).

[48] J. Zhang, M. A. Itzler, H. Zbinden, and J.-W. Pan, "Advances in InGaAs/InP single-photon detector systems for quantum communication," Light. Sci. & Appl. **4**(5), e286 (2015).

[49] C. Cahall, K. L. Nicolich, N. T. Islam, G. P. Lafyatis, A. J. Miller, D. J. Gauthier, and J. Kim, "Multi-photon detection using a conventional superconducting nanowire single-photon detector," Optica **4**(12), 1534–1535 (2017).

[50] X. Tao, S. Chen, Y. Chen, L. Wang, X. Li, X. Tu, X. Jia, Q. Zhao, L. Zhang, L. Kang, and P. Wu, "A high speed and high efficiency superconducting photon number resolving detector," Supercond. Sci. Technol. **32**(6), 064002 (2019).

[51] E. Schmidt, E. Reutter, M. Schwartz, H. Vural, K. Ilin, M. Jetter, P. Michler, and M. Siegel, "Characterization of a photon-number resolving SNSPD using poissonian and sub-Poissonian light," IEEE Transactions on Appl. Supercond. **29**(5), 1–5 (2019).

[52] V. Anant, A. J. Kerman, E. A. Dauler, J. K. Yang, K. M. Rosfjord, and K. K. Berggren, "Optical properties of superconducting nanowire single-photon detectors," Opt. Express **16**(14), 10750–10761 (2008).

[53] V. Anant, "Engineering the optical properties of subwavelength devices and materials," Ph.D. thesis, Massachusetts Institute of Technology (2007).

[54] Q. Guo, H. Li, L. You, W. Zhang, L. Zhang, Z. Wang, X. Xie, and M. Qi, "Single photon detector with high polarization sensitivity," Sci. Rep. **5**, 9616 (2015).

[55] F. Zheng, X. Tao, M. Yang, G. Zhu, B. Jin, L. Kang, W. Xu, J. Chen, and P. Wu, "Design of efficient superconducting nanowire single photon detectors with high polarization sensitivity for polarimetric imaging," J. Opt. Soc. Am. B **33**(11), 2256–2264 (2016).

[56] X.-Q. Sun, W.-J. Zhang, C.-J. Zhang, L.-X. You, G.-Z. Xu, J. Huang, H. Zhou, H. Li, Z. Wang, and X.-M. Xie, "Polarization resolving and imaging with a single-photon sensitive superconducting nanowire array," Opt. Express **29**(7), 11021–11036 (2021).

[57] V. B. Verma, F. Marsili, S. Harrington, A. E. Lita, R. P. Mirin, and S. W. Nam, "A three-dimensional, polarization-insensitive superconducting nanowire avalanche photodetector," Appl. Phys. Lett. **101**(25), 251114 (2012).

[58] J. Huang, W. Zhang, L. You, X. Liu, Q. Guo, Y. Wang, L. Zhang, X. Yang, H. Li, Z. Wang *et al.*, "Spiral superconducting nanowire single-photon detector with efficiency over 50% at 1550 nm wavelength," Supercond. Sci. Technol. **30**(7), 074004 (2017).

[59] X. Chi, K. Zou, C. Gu, J. Zichi, Y. Cheng, N. Hu, X. Lan, S. Chen, Z. Lin, V. Zwiller, and X. Hu, "Fractal superconducting nanowire single-photon detectors with reduced polarization sensitivity," Opt. Lett. **43**(20), 5017–5020 (2018).

[60] A. Gallivanoni, I. Rech, and M. Ghioni, "Progress in quenching circuits for single photon avalanche diodes," IEEE Transactions on Nucl. Sci. **57**(6), 3815–3826 (2010).

[61] A. Giudice, M. Ghioni, R. Biasi, F. Zappa, S. Cova, P. Maccagnani, and A. Gulinatti, "High-rate photon counting and picosecond timing with silicon-SPAD based compact detector modules," J. Mod. Opt. **54**(2-3), 225–237 (2007).

[62] M. Ghioni, A. Gulinatti, I. Rech, F. Zappa, and S. Cova, "Progress in silicon single-photon avalanche diodes," IEEE J. Sel. Top. Quantum Electron. **13**(4), 852–862 (2007).

[63] E. E. Wollman, V. B. Verma, A. E. Lita, W. H. Farr, M. D. Shaw, R. P. Mirin, and S. W. Nam, "Kilopixel array of superconducting nanowire single-photon detectors," Opt. Express **27**(24), 35279–35289 (2019).

[64] M. A. Itzler, R. Ben-Michael, C.-F. Hsu, K. Slomkowski, A. Tosi, S. Cova, F. Zappa, and R. Ispasoiu, "Single photon avalanche diodes (SPADs) for 1.5 μm photon counting applications," J. Mod. Opt. **54**(2-3), 283–304 (2007).

[65] V. Pusino, C. Xie, A. Khalid, M. J. Steer, M. Sorel, I. G. Thayne, and D. R. Cumming, "InSb photodiodes for monolithic active focal plane arrays on GaAs substrates," IEEE Transactions on Electron Devices **63**(8), 3135–3142 (2016).

[66] A. Rogalski, "HgCdTe infrared detector material: history, status and outlook," Rep. on Prog. Phys. **68**(10), 2267 (2005).

[67] X. Sun, J. B. Abshire, M. A. Krainak, W. Lu, J. D. Beck, W. W. Sullivan, P. Mitra, D. M. Rawlings, R. A. Fields, D. A. Hinkley, and B. S. Hirasuna, "HgCdTe avalanche photodiode array detectors with single photon sensitivity and integrated detector cooler assemblies for space lidar applications," Opt. Eng. **58**(6), 067103 (2019).

[68] "About PMTs: Photomultiplier tubes (PMTs)," https://www.hamamatsu.com/eu/en/product/optical-sensors/pmt/about_pmts, accessed August 2021.

[69] S. Donati and T. Tambosso, "Single-photon detectors: from traditional PMT to solid-state SPAD-based technology," IEEE J. Sel. Top. Quantum Electron. **20**(6), 204–211 (2014).

[70] R. H. Hadfield, "Single-photon detectors for optical quantum information applications," Nat. Photonics **3**(12), 696 (2009).

[71] B. S. Robinson, A. J. Kerman, E. A. Dauler, D. M. Boroson, S. A. Hamilton, J. K. Yang, V. Anant, and K. K. Berggren, "Demonstration of gigabit-per-second and higher data rates at extremely high efficiency using superconducting nanowire single photon detectors," in *Free-Space Laser Communications VII,* vol. 6709 (International Society for Optics and Photonics, 2007), p. 67090Z.

[72] X. Yang, H. Li, W. Zhang, L. You, L. Zhang, X. Liu, Z. Wang, W. Peng, X. Xie, and M. Jiang, "Superconducting nanowire single photon detector with on-chip bandpass filter," Opt. Express **22**(13), 16267–16272 (2014).

[73] V. Verma, B. Korzh, A. Walter, A. Lita, R. Briggs, M. Colangelo, Y. Zhai, E. Wollman, A. Beyer, J. Allmaras, B. Bumble, H. Vora, D. Zhu, E. Schmidt, K. Berggren, R. Mirin, S. Nam, and M. Shaw, "Single-photon detection in the mid-infrared up to 10 μ m wavelength using tungsten silicide superconducting nanowire detectors," APL Photonics **6**(5), 056101 (2021).

[74] R. Nahory, M. Pollack, W. Johnston Jr, and R. Barns, "Band gap versus composition and demonstration of vegard's law for in1- x ga x as y p1- y lattice matched to inp," Appl. Phys. Lett. **33**(7), 659–661 (1978).

[75] A. E. Lita, V. B. Verma, R. D. Horansky, J. M. Shainline, R. P. Mirin, and S. Nam, "Materials development for high efficiency superconducting nanowire single-photon detectors," MRS Online Proc. Libr. Arch. **1807**, 1–6 (2015).

[76] A. E. Lita, A. J. Miller, and S. W. Nam, "Counting near-infrared single-photons with 95% efficiency," Opt. Express **16**(5), 3032–3040 (2008).

[77] J. Gao, M. Vissers, M. Sandberg, F. Da Silva, S. Nam, D. Pappas, D. Wisbey, E. Langman, S. Meeker, B. Mazin, H. Leduc, J. Zmuidzinas, and K. Irwin, "A titanium-nitride near-infrared kinetic inductance photon-counting detector and its anomalous electrodynamics," Appl. Phys. Lett. **101**(14), 142602 (2012).

[78] M. Widarsson, M. Henriksson, P. Mutter, C. Canalias, V. Pasiskevicius, and F. Laurell, "High resolution and sensitivity up-conversion mid-infrared photon-counting LIDAR," Appl. Opt. **59**(8), 2365–2369 (2020).

[79] D. Morozov, A. Banerjee, K. Erotokritou, G. Taylor, N. R. Gemmell, D. Hemakumara, I. Thayne, and R. H. Hadfield, "Superconducting nanowire materials for mid infrared single photon detection (conference presentation)," in *Advanced Photon Counting Techniques XII,* vol. 10659 (International Society for Optics and Photonics, 2018), p. 106590G.

[80] P. Norton, "HgCdTe infrared detectors," Optoelectronics Rev. (3), 159–174 (2002).

[81] A. W. Ziarkash, S. K. Joshi, M. Stipčević, and R. Ursin, "Comparative study of afterpulsing behavior and models in single photon counting avalanche photo diode detectors," Sci. Rep. **8**(1), 1–8 (2018).

[82] X. Sun, J. B. Abshire, and J. D. Beck, "HgCdTe e-APD detector arrays with single photon sensitivity for space LIDAR applications," in *Advanced Photon Counting Techniques VIII,* vol. 9114 (International Society for Optics and Photonics, 2014), p. 91140K.

[83] G. Vojetta, F. Guellec, L. Mathieu, K. Foubert, P. Feautrier, and J. Rothman, "Linear photon-counting with HgCdTe APDs," in *Advanced Photon Counting Techniques VI,* vol. 8375 (International Society for Optics and Photonics, 2012), p. 83750Y.

[84] O. Noroozian, E. M. Barrentine, T. R. Stevenson, A. D. Brown, S. H. Moseley, E. Wollack, K. M. Pontoppidan, K. U-Yen, and V. Mikula, "Photon-Counting Kinetic Inductance Detectors (KID) for Far/Mid-Infrared Space Spectroscopy with the Origins Space Telescope (OST)," in *American Astronomical Society Meeting Abstracts #231,* vol. 231 of *American Astronomical Society Meeting Abstracts* (2018), p. 447.01.

[85] B. Cabrera, R. Clarke, P. Colling, A. Miller, S. Nam, and R. Romani, "Detection of single infrared, optical, and ultraviolet photons using superconducting transition edge sensors," Appl. Phys. Lett. **73**(6), 735–737 (1998).

[86] A. Barh, C. Pedersen, and P. Tidemand-Lichtenberg, "Ultra-broadband mid-wave-IR upconversion detection," Opt. Lett. **42**(8), 1504–1507 (2017).

[87] R. T. Thew, H. Zbinden, and N. Gisin, "Tunable upconversion photon detector," Appl. Phys. Lett. **93**(7), 071104 (2008).

[88] American Society for Testing and Materials. Committee G03 on Weathering and Durability, *Standard tables for reference solar spectral irradiances: direct normal and hemispherical on 37° tilted surface* (ASTM international, 2003).

[89] R. V. Kochanov, I. Gordon, L. Rothman, P. Wcisło, C. Hill, and J. Wilzewski, "HITRAN application programming interface (HAPI): A comprehensive approach to working with spectroscopic data," J. Quant. Spectrosc. Radiat. Transf. **177**, 15–30 (2016).

[90] H. Kaushal and G. Kaddoum, "Optical communication in space: challenges and mitigation techniques," IEEE Commun. Surv. & Tutorials **19**(1), 57–96 (2017).

[91] S.-K. Liao, W.-Q. Cai, J. Handsteiner, B. Liu, J. Yin, L. Zhang, D. Rauch, M. Fink, J.-G. Ren, W.-Y. Liu, Y. Li, Q. Shen, Y. Cao, F.-Z. Li, J.-F. Wang, Y.-M. Huang, L. Deng, T. Xi, L. Ma, T. Hu, L. Li, N.-L. Lui, F. Koidl, P. Wang, Y.-A. Chen, X.-B. Wang, M. Steindorfer, G. Kirchner, C.-Y. Lu, R. Shu, R. Ursin, T. Scheidl, C.-Z. Peng, J.-Y. Wang, A. Zeilinger, and J.-W. Pan, "Satellite-relayed intercontinental quantum network," Phys. Rev. Lett. **120**(3), 030501 (2018).

[92] P. J. Winzer, "Scaling optical fiber networks: challenges and solutions," Opt. Photonics News **26**(3), 28–35 (2015).

[93] M. N. Petrovich, F. Poletti, J. Wooler, A. Heidt, N. K. Baddela, Z. Li, D. R. Gray, R. Slavík, F. Parmigiani, N. Wheeler, J. Hayes, E. Numkam, L. Gruner-Nielson, B. Palsdottir, R. Phelan, B. Kelly, J. O'Carroll, M. Becker, N. MacSuibhne, J. Zhao, F. Garcia Gunning, A. Ellis, P. Petropoulos, S. Alam, and D. Richardson, "Demonstration of amplified data transmission at 2 μm in a low-loss wide bandwidth hollow core photonic bandgap fiber," Opt. Express **21**(23), 28559–28569 (2013).

[94] Z. Li, A. Heidt, J. Daniel, Y. Jung, S. Alam, and D. J. Richardson, "Thulium-doped fiber amplifier for optical communications at 2 μm," Opt. Express **21**(8), 9289–9297 (2013).

[95] M. Lamy, C. Finot, J. Fatome, J.-C. Weeber, G. Millot, B. Kuyken, G. Roelkens, M. Brun, P. Labeye, S. Nicolleti, A. Bogris, D. Syvridis, M. Ettabib, D. Richardson, P. Petropoulos,

and K. Hammani, "High speed optical transmission at 2 μm in subwavelength waveguides made of various materials," in *Integrated Photonics Research, Silicon and Nanophotonics,* (Optical Society of America, 2018), pp. ITu4I–6.

[96] M. Lamy, C. Finot, J. Fatome, M. Brun, P. Labeye, S. Nicolleti, A. Bogris, D. Syvridis, M. Ettabib, D. Richardson, P. Petropoulos, and K. Hammani, "Ten gigabit per second optical transmissions at 1.98 μm in centimetre-long SiGe waveguides," Electron. Lett. **53**(17), 1213–1214 (2017).

[97] N. S. Prasad and A. R. Geiger, "Remote sensing of propane and methane by means of a differential absorption LIDAR by topographic reflection," Opt. Eng. **35**(4), 1105–1112 (1996).

[98] C. R. Prasad, P. Kabro, and S. L. Mathur, "Tunable IR differential absorption LIDAR for remote sensing of chemicals," in *Application of LIDAR to Current Atmospheric Topics III,* vol. 3757 (International Society for Optics and Photonics, 1999), pp. 87–96.

[99] P. S. Kuo, "Using silica fiber coupling to extend superconducting nanowire single-photon detectors into the infrared," OSA Continuum **1**(4), 1260–1266 (2018).

[100] J. Sanghera and I. D. Aggarwal, *Infrared fiber optics* (CRC Press, 1998).

[101] B. J. Eggleton, B. Luther-Davies, and K. Richardson, "Chalcogenide photonics," Nat. Photonics **5**(3), 141 (2011).

[102] N. Kapany and R. Simms, "Recent developments in infrared fiber optics," Infrared Phys. **5**(2), 69–80 (1965).

[103] B. Bureau, C. Boussard, S. Cui, R. Chahal, M.-L. Anne, V. Nazabal, O. Sire, O. Loréal, P. Lucas, V. Monbet, J.-L. Doualan, P. Camy, H. Tariel, F. Charpentier, L. Quetel, J.-L. Adam, and J. Lucas, "Chalcogenide optical fibers for mid-infrared sensing," Opt. Eng. **53**(2), 027101 (2014).

[104] G. Tao and A. F. Abouraddy, "Advances in infrared fibers," in *Thermosense: Thermal Infrared Applications XXXVII,* vol. 9485 (International Society for Optics and Photonics, 2015), p. 94850K.

[105] A. Urich, R. R. J. Maier, F. Yu, J. C. Knight, D. P. Hand, and J. D. Shephard, "Silica hollow core microstructured fibres for mid-infrared surgical applications," J. Non-Crystalline Solids **377**, 236–239 (2013).

[106] G. Tao, H. Ebendorff-Heidepriem, A. M. Stolyarov, S. Danto, J. V. Badding, Y. Fink, J. Ballato, and A. F. Abouraddy, "Infrared fibers," Adv. Opt. Photonics **7**(2), 379–458 (2015).

[107] A. Divochiy, M. Misiaszek, Y. Vakhtomin, P. Morozov, K. Smirnov, P. Zolotov, and P. Kolenderski, "Single photon detection system for visible and infrared spectrum range," Opt. Lett. **43**(24), 6085–6088 (2018).

[108] H. Zhou, Y. Pan, L. You, H. Li, Y. Wang, Y. Tang, H. Wang, X. Liu, and Z. Wang, "Superconducting nanowire single photon detector with efficiency over 60% for 2-μm-wavelength," IEEE Photonics J. **11**(6), 1–7 (2019).

[109] S. Frasca, B. Korzh, M. Colangelo, D. Zhu, A. Lita, J. Allmaras, E. Wollman, V. Verma, A. Dane, E. Ramirez, A. Beyer, S. Nam, A. Kozorezov, M. Shaw, and K. Berggren, "Determining the depairing current in superconducting nanowire single-photon detectors," Phys. Rev. B **100**(5), 054520 (2019).

[110] J. R. Clem and K. K. Berggren, "Geometry-dependent critical currents in superconducting nanocircuits," Phys. Rev. B **84**(17), 174510 (2011).

[111] W. Zhang, Q. Jia, L. You, X. Ou, H. Huang, L. Zhang, H. Li, Z. Wang, and X. Xie, "Saturating intrinsic detection efficiency of superconducting nanowire single-photon detectors via defect engineering," Phys. Rev. Appl. **12**(4), 044040 (2019).

[112] W. Becker, A. Bergmann, C. Biskup, L. Kelbauskas, T. Zimmer, N. Klocker, and K. Benndorf, "High resolution TCSPC lifetime imaging," in *Multiphoton Microscopy in the Biomedical Sciences III,* vol. 4963 (International Society for Optics and Photonics, 2003), pp. 175–184.

[113] M. Henriksson, H. Larsson, C. Grönwall, and G. Tolt, "Continuously scanning time-correlated single-photon-counting single-pixel 3-d LIDAR," Opt. Eng. **56**(3), 031204 (2016).

[114] S. Prabhakar, T. Shields, A. C. Dada, M. Ebrahim, G. G. Taylor, D. Morozov, K. Erotokritou, S. Miki, M. Yabuno, H. Terai, C. Gawith, M. Kues, L. Caspani, R. H. Hadfield, and M. Clerici, "Two-photon quantum interference and entanglement at 2.1 μm," Sci. Adv. **6**(13), eaay5195 (2020).

[115] W. Becker, *The BH TCSPC handbook* (Becker & Hickl, 2014).

[116] "HydraHarp 400 from PicoQuant," https://www.picoquant.com/images/uploads/downloads/10-hydraharp400.pdf, accessed August 2021.

[117] "Becker and Hickl SPC-150-NXX," https://www.becker-hickl.com/wp-content/uploads/2019/04/db-spc-150nxx-v01.pdf, accessed August 2021.

[118] P. A. Hiskett, C. S. Parry, A. McCarthy, and G. S. Buller, "A photon-counting time-of-flight ranging technique developed for the avoidance of range ambiguity at gigahertz clock rates," Opt. Express **16**(18), 13685–13698 (2008).

[119] G. Kim and Y. Park, "LIDAR pulse coding for high resolution range imaging at improved refresh rate," Opt. Express **24**(21), 23810–23828 (2016).

[120] G. S. Buller and A. M. Wallace, "Ranging and three-dimensional imaging using time-correlated single-photon counting and point-by-point acquisition," IEEE J. Sel. Top. Quantum Electron. **13**(4), 1006–1015 (2007).

[121] A. McCarthy, R. J. Collins, N. J. Krichel, V. Fernández, A. M. Wallace, and G. S. Buller, "Long-range time-of-flight scanning sensor based on high-speed time-correlated single-photon counting," Appl. Opt. **48**(32), 6241–6251 (2009).

[122] J. A. Reagan, D. M. Byrne, and B. M. Herman, "Bistatic LIDAR: A tool for characterizing atmospheric particulates: Part i—the remote sensing problem," IEEE Transactions on Geosci. Remote. Sens. (3), 229–235 (1982).

[123] K. Meki, K. Yamaguchi, X. Li, Y. Saito, T. Kawahara, and A. Nomura, "Range-resolved bistatic imaging LIDAR for the measurement of the lower atmosphere," Opt. Lett. **21**(17), 1318–1320 (1996).

[124] C. V. Poulton, A. Yaacobi, D. B. Cole, M. J. Byrd, M. Raval, D. Vermeulen, and M. R. Watts, "Coherent solid-state LIDAR with silicon photonic optical phased arrays," Opt. Lett. **42**(20), 4091–4094 (2017).

[125] H. Zhou, Y. He, L. You, S. Chen, W. Zhang, J. Wu, Z. Wang, and X. Xie, "Few-photon imaging at 1550 nm using a low-timing-jitter superconducting nanowire single-photon detector," Opt. Express **23**(11), 14603–14611 (2015).

[126] R. Tobin, A. Halimi, A. McCarthy, X. Ren, K. J. McEwan, S. McLaughlin, and G. S. Buller, "Long-range depth profiling of camouflaged targets using single-photon detection," Opt. Eng. **57**(3), 031303 (2017).

[127] A. Maccarone, A. McCarthy, X. Ren, R. E. Warburton, A. M. Wallace, J. Moffat, Y. Petillot, and G. S. Buller, "Underwater depth imaging using time-correlated single-photon counting," Opt. Express **23**(26), 33911–33926 (2015).

[128] S. Pellegrini, G. S. Buller, J. M. Smith, A. M. Wallace, and S. Cova, "Laser-based distance measurement using picosecond resolution time-correlated single-photon counting," Meas. Sci. Technol. **11**(6), 712 (2000).

[129] Z.-P. Li, X. Huang, Y. Cao, B. Wang, Y.-H. Li, W. Jin, C. Yu, J. Zhang, Q. Zhang, C.-Z. Peng, F. Xu, and J.-W. Pan, "Single-photon computational 3d imaging at 45 km," arXiv preprint arXiv:1904.10341 (2019).

[130] S. Chen, D. Liu, W. Zhang, L. You, Y. He, W. Zhang, X. Yang, G. Wu, M. Ren, H. Zeng, Z. Wang, X. Xie, and M. Jiang, "Time-of-flight laser ranging and imaging at 1550 nm using low-jitter superconducting nanowire single-photon detection system," Appl. Opt. **52**(14), 3241–3245 (2013).

[131] A. McCarthy, X. Ren, A. Della Frera, N. R. Gemmell, N. J. Krichel, C. Scarcella, A. Ruggeri, A. Tosi, and G. S. Buller, "Kilometer-range depth imaging at 1550 nm wavelength using an InGaAs/InP single-photon avalanche diode detector," Opt. Express **21**(19), 22098–22113 (2013).

[132] A. McCarthy, N. J. Krichel, N. R. Gemmell, X. Ren, M. G. Tanner, S. N. Dorenbos, V. Zwiller, R. H. Hadfield, and G. S. Buller, "Kilometer-range, high resolution depth imaging via 1560 nm wavelength single-photon detection," Opt. Express **21**(7), 8904–8915 (2013).

[133] A. P. Dempster, N. M. Laird, and D. B. Rubin, "Maximum likelihood from incomplete data via the EM algorithm," J. Royal Stat. Soc. Ser. B (Methodological) **39**(1), 1–22 (1977).

[134] A. M. Wallace, R. C. W. Sung, G. S. Buller, R. D. Harkins, R. E. Warburton, and R. A. Lamb, "Detecting and characterising returns in a pulsed LADAR system," IEE Proceedings-Vision, Image Signal Process. **153**(2), 160–172 (2006).

[135] S. Hernandez-Marin, A. M. Wallace, and G. J. Gibson, "Bayesian analysis of LIDAR signals with multiple returns," IEEE Transactions on Pattern Analysis Mach. Intell. **29**(12), 2170–2180 (2007).

[136] P. J. Green, "Reversible jump markov chain monte carlo computation and bayesian model determination," Biometrika **82**(4), 711–732 (1995).

[137] Y. Altmann, X. Ren, A. McCarthy, G. S. Buller, and S. McLaughlin, "LIDAR waveform-based analysis of depth images constructed using sparse single-photon data," IEEE Transactions on Image Process. **25**(5), 1935–1946 (2016).

[138] J. Tachella, Y. Altmann, X. Ren, A. McCarthy, G. S. Buller, S. Mclaughlin, and J.-Y. Tourneret, "Bayesian 3d reconstruction of complex scenes from single-photon LIDAR data," SIAM J. on Imaging Sci. **12**(1), 521–550 (2019).

[139] A. Banerjee, R. M. Heath, D. Morozov, D. Hemakumara, U. Nasti, I. Thayne, and R. H. Hadfield, "Optical properties of refractory metal based thin films," Opt. Mater. Express **8**(8), 2072–2088 (2018).

[140] K. Il'in, D. Rall, M. Siegel, A. Engel, A. Schilling, A. Semenov, and H.-W. Huebers, "Influence of thickness, width and temperature on critical current density of Nb thin film structures," Phys. C: Supercond. **470**(19), 953–956 (2010).

[141] F. Marsili, F. Najafi, E. Dauler, F. Bellei, X. Hu, M. Csete, R. J. Molnar, and K. K. Berggren, "Single-photon detectors based on ultranarrow superconducting nanowires," Nano Lett. **11**(5), 2048–2053 (2011).

[142] Q. Zhao, A. N. McCaughan, A. E. Dane, F. Najafi, F. Bellei, D. De Fazio, K. A. Sunter, Y. Ivry, and K. K. Berggren, "Eight-fold signal amplification of a superconducting nanowire single-photon detector using a multiple-avalanche architecture," Opt. Express **22**(20), 24574–24581 (2014).

[143] Y. Korneeva, D. Y. Vodolazov, A. Semenov, I. Florya, N. Simonov, E. Baeva, A. Korneev, G. Goltsman, and T. Klapwijk, "Optical single photon detection in micron-scaled NbN bridges," arXiv preprint arXiv:1802.02881 (2018).

[144] J. Sprengers, A. Gaggero, D. Sahin, S. Jahanmirinejad, G. Frucci, F. Mattioli, R. Leoni, J. Beetz, M. Lermer, M. Kamp, S. Hofling, R. Sanjines, and A. Fiore, "Waveguide superconducting single-photon detectors for integrated quantum photonic circuits," Appl. Phys. Lett. **99**(18), 181110 (2011).

[145] M. K. Akhlaghi, E. Schelew, and J. F. Young, "Waveguide integrated superconducting single-photon detectors implemented as near-perfect absorbers of coherent radiation," Nat. Commun. **6**, 8233 (2015).

[146] X. Hu, C. W. Holzwarth, D. Masciarelli, E. A. Dauler, and K. K. Berggren, "Efficiently coupling light to superconducting nanowire single-photon detectors," IEEE Transactions on Appl. Supercond. **19**(3), 336–340 (2009).

[147] K. M. Rosfjord, J. K. Yang, E. A. Dauler, A. J. Kerman, V. Anant, B. M. Voronov, G. N. Gol'tsman, and K. K. Berggren, "Nanowire single-photon detector with an integrated optical cavity and anti-reflection coating," Opt. Express **14**(2), 527–534 (2006).

[148] S. Miki, T. Yamashita, M. Fujiwara, M. Sasaki, and Z. Wang, "Characterization of coupling efficiency and absorption coefficient for fiber-coupled SNSPD with an optical cavity," IEEE Transactions on Appl. Supercond. **21**(3), 332–335 (2011).

[149] A. Banerjee, L. J. Baker, A. Doye, M. Nord, R. M. Heath, K. Erotokritou, D. Bosworth, Z. H. Barber, I. MacLaren, and R. H. Hadfield, "Characterisation of amorphous molybdenum silicide (MoSi) superconducting thin films and nanowires," Supercond. Sci. Technol. **30**(8), 084010 (2017).

[150] A. Banerjee, "Optimisation of superconducting thin film growth for next generation superconducting detector applications," Ph.D. thesis, University of Glasgow (2017).

[151] M. Ziegler, L. Fritzsch, J. Day, S. Linzen, S. Anders, J. Toussaint, and H.-G. Meyer, "Superconducting niobium nitride thin films deposited by metal organic plasma-enhanced atomic layer deposition," Supercond. Sci. Technol. **26**(2), 025008 (2012).

[152] S. M. George, "Atomic layer deposition: an overview," Chem. Rev. **110**(1), 111–131 (2010).

[153] E. Knehr, A. Kuzmin, D. Y. Vodolazov, M. Ziegler, S. Doerner, K. Ilin, M. Siegel, R. Stolz, and H. Schmidt, "Nanowire single-photon detectors made of atomic layer-deposited niobium nitride," Supercond. Sci. Technol. **32**(12), 125007 (2019).

[154] A. Grigorescu and C. Hagen, "Resists for sub-20-nm electron beam lithography with a focus on HSQ: state of the art," Nanotechnology **20**(29), 292001 (2009).

[155] T. Chang, "Proximity effect in electron-beam lithography," J. Vac. Sci. Technol. **12**(6), 1271–1275 (1975).

[156] G. P. Watson, S. D. Berger, J. A. Liddle, and W. K. Waskiewicz, "A background dose proximity effect correction technique for scattering with angular limitation projection electron lithography implemented in hardware," J. Vac. Sci. & Technol. B: Microelectron. Nanometer Struct. Process. Meas. Phenom. **13**(6), 2504–2507 (1995).

[157] S.-Y. Lee and B. D. Cook, "Pyramid-a hierarchical, rule-based approach toward proximity effect correction. i. exposure estimation," IEEE Transactions on Semicond. Manuf. **11**(1), 108–116 (1998).

[158] K. R. Williams, K. Gupta, and M. Wasilik, "Etch rates for micromachining processing-part ii," J. Microelectromechanical Syst. **12**(6), 761–778 (2003).

[159] M. Nagao, T. Inaguchi, H. Yoshimura, T. Yamada, and M. Iwamoto, "Helium liquefaction by a Gifford-McMahon cycle cryocooler," in *Advances in Cryogenic Engineering,* (Springer, 1990), pp. 1251–1260.

[160] R. Radebaugh, "Development of the pulse tube refrigerator as an efficient and reliable cryocooler," Proc. Inst. Refrig. (London) **1999**, 00 (2000).

[161] D. Zhu, M. Colangelo, B. A. Korzh, Q.-Y. Zhao, S. Frasca, A. E. Dane, A. E. Velasco, A. D. Beyer, J. P. Allmaras, E. Ramirez, W. J. Strickland, D. F. Santavicca, M. D. Shaw, and K. K. Berggren, "Superconducting nanowire single-photon detector with integrated impedance-matching taper," Appl. Phys. Lett. **114**(4), 042601 (2019).

[162] "Chromacity Ltd," https://chromacitylasers.com/ultrafast-lasers/chromacity-opo/, accessed August 2021.

[163] P. I. Zolotov, A. V. Semenov, A. V. Divochiy, G. N. Goltsman, N. R. Romanov, and T. M. Klapwijk, "Dependence of photon detection efficiency on normal-state sheet resistance in marginally superconducting films of NbN," IEEE Transactions on Appl. Supercond. **31**(5), 1–5 (2021).

[164] D. R. Boris, V. D. Wheeler, N. Nepal, S. B. Qadri, S. G. Walton, and C. C. R. Eddy, "The role of plasma in plasma-enhanced atomic layer deposition of crystalline films," J. Vac. Sci. & Technol. A: Vacuum, Surfaces, Films **38**(4), 040801 (2020).

[165] N. E. Richey, C. de Paula, and S. F. Bent, "Understanding chemical and physical mechanisms in atomic layer deposition," The J. Chem. Phys. **152**(4), 040902 (2020).

[166] H. Kim, "Characteristics and applications of plasma enhanced-atomic layer deposition," Thin Solid Films **519**(20), 6639–6644 (2011).

[167] M. Ukibe and G. Fujii, "Superconducting characteristics of NbN films deposited by atomic layer deposition," IEEE Transactions on Appl. Supercond. **27**(4), 1–4 (2017).

[168] J. Musschoot, Q. Xie, D. Deduytsche, S. Van den Berghe, R. Van Meirhaeghe, and C. Detavernier, "Atomic layer deposition of titanium nitride from TDMAT precursor," Microelectron. Eng. **86**(1), 72–77 (2009).

[169] C. Sheagren, P. Barry, E. Shirokoff, and Q. Y. Tang, "Atomic layer deposition niobium nitride films for high-Q resonators," J. Low Temp. Phys. **199**(3), 875–882 (2020).

[170] R. Cheng, S. Wang, and H. X. Tang, "Superconducting nanowire single-photon detectors fabricated from atomic-layer-deposited NbN," Appl. Phys. Lett. **115**(24), 241101 (2019).

[171] E. Shirokoff, P. S. Barry, Q. Y. Tang, and R. Nie, "Antenna-coupled lumped-element ALD titanium nitride KIDs for CMB instruments (conference presentation)," in *Millimeter, Submillimeter, and Far-Infrared Detectors and Instrumentation for Astronomy IX,* vol. 10708 (International Society for Optics and Photonics, 2018), p. 107081M.

[172] L. A. Giannuzzi and F. A. Stevie, "A review of focused ion beam milling techniques for TEM specimen preparation," Micron **30**(3), 197–204 (1999).

[173] Q. Guo, L. You, H. Li, W. Zhang, L. Zhang, X. Liu, X. Yang, S. Chen, Z. Wang, and X. Xie, "Impact of trapezoidal cross section on polarization sensitivity of SNSPD with ultranarrow nanowire," IEEE Transactions on Appl. Supercond. **27**(4), 1–4 (2016).

[174] V. Verma, F. Marsili, B. Baek, A. Lita, T. Gerrits, J. Stern, R. Mirin, and S. W. Nam, "55% system detection efficiency with self-aligned WSi superconducting nanowire single-photon detectors," in *2012 Conference on Lasers and Electro-Optics (CLEO),* (IEEE, 2012), pp. 1–2.

[175] L. Zhang, L. You, D. Liu, W. Zhang, L. Zhang, X. Liu, J. Wu, Y. He, C. Lv, Z. Wang *et al.*, "Characterization of superconducting nanowire single-photon detector with artificial constrictions," Aip Adv. **4**(6), 067114 (2014).

[176] K. Erotokritou, R. M. Heath, G. G. Taylor, C. Tian, A. Banerjee, A. Casaburi, C. M. Natarajan, S. Miki, H. Terai, and R. H. Hadfield, "Nano-optical photoresponse mapping of superconducting nanowires with enhanced near infrared absorption," Supercond. Sci. Technol. **31**(12), 125012 (2018).

[177] A. Banerjee, R. M. Heath, D. Morozov, D. Hemakumara, U. Nasti, I. Thayne, and R. H. Hadfield, "Optical properties of refractory metal based thin films," Opt. Mater. Express **8**(8), 2072–2088 (2018).

[178] S. Steinhauer, S. Gyger, and V. Zwiller, "Progress on large-scale superconducting nanowire single-photon detectors," Appl. Phys. Lett. **118**(10), 100501 (2021).

[179] S. Miki, T. Yamashita, H. Terai, and Z. Wang, "High performance fiber-coupled NbTiN superconducting nanowire single photon detectors with Gifford-McMahon cryocooler," Opt. Express **21**(8), 10208–10214 (2013).

[180] A. M. Kowalevicz Jr and F. Bucholtz, "Beam divergence from an SMF-28 optical fiber," Tech. rep., Naval Research Lab, Washington DC (2006).

[181] S. Miki, M. Takeda, M. Fujiwara, M. Sasaki, A. Otomo, and Z. Wang, "Superconducting NbTiN nanowire single photon detectors with low kinetic inductance," Appl. Phys. Express **2**(7), 075002 (2009).

[182] X. Yang, L. You, L. Zhang, C. Lv, H. Li, X. Liu, H. Zhou, and Z. Wang, "Comparison of superconducting nanowire single-photon detectors made of NbTiN and NbN thin films," IEEE Transactions on Appl. Supercond. **28**(1), 1–6 (2017).

[183] A. Engel, K. Inderbitzin, A. Schilling, R. Lusche, A. Semenov, H.-W. Hübers, D. Henrich, M. Hofherr, K. Il'in, and M. Siegel, "Temperature-dependence of detection efficiency in NbN and TaN SNSPD," IEEE Transactions on Appl. Supercond. **23**(3), 2300505–2300505 (2013).

[184] T. Jia, C. Wan, L. Zhao, Y. Zhou, Q. Zhao, M. Gu, X. Jia, L. Zhang, B. Jin, J. Chen, and L. Kang, "Temperature dependence of niobium superconducting nanowire single-photon detectors in He-3 cryocooler," Chin. Sci. Bull. **59**(28), 3549–3553 (2014).

[185] E. E. Wollman, V. B. Verma, A. D. Beyer, R. M. Briggs, B. Korzh, J. P. Allmaras, F. Marsili, A. E. Lita, R. P. Mirin, S. W. Nam, and M. D. Shaw, "UV superconducting nanowire single-photon detectors with high efficiency, low noise, and 4 K operating temperature," Opt. Express **25**(22), 26792–26801 (2017).

[186] C. Sheppard, "Approximate calculation of the reflection coefficient from a stratified medium," Pure Appl. Opt. J. Eur. Opt. Soc. Part A **4**(5), 665 (1995).

[187] D. F. Santavicca, B. Noble, C. Kilgore, G. A. Wurtz, M. Colangelo, D. Zhu, and K. K. Berggren, "Jitter characterization of a dual-readout SNSPD," IEEE Transactions on Appl. Supercond. **29**(5), 1–4 (2019).

[188] Q.-Y. Zhao, D. Zhu, N. Calandri, A. E. Dane, A. N. McCaughan, F. Bellei, H.-Z. Wang, D. F. Santavicca, and K. K. Berggren, "Single-photon imager based on a superconducting nanowire delay line," Nat. Photonics **11**(4), 247 (2017).

[189] J. Wu, L. You, S. Chen, H. Li, Y. He, C. Lv, Z. Wang, and X. Xie, "Improving the timing jitter of a superconducting nanowire single-photon detection system," Appl. Opt. **56**(8), 2195–2200 (2017).

[190] G. Bertolini and A. Coche, *Semiconductor Detectors* (North-Holland Publishing, 1968).

[191] R. W. Klopfenstein, "A transmission line taper of improved design," Proc. IRE **44**(1), 31–35 (1956).

[192] J. A. Jacquez, J. Huss, W. McKeehan, J. M. Dimitroff, and H. F. Kuppenheim, "Spectral reflectance of human skin in the region 0.7–2.6 μm," J. Appl. Physiol. **8**(3), 297–299 (1955).

[193] G. G. Taylor, A. McCarthy, B. Korzh, A. D. Beyer, D. Morozov, R. M. Briggs, J. P. Allmaras, B. Bumble, M. D. Shaw, R. H. Hadfield, and G. S. Buller, "Long-range depth imaging with 13 ps temporal resolution using a superconducting nanowire single photon detector," in *CLEO: Science and Innovations,* (Optical Society of America, 2020), pp. SM2M–6.

[194] J. J. Liu, B. L. Stann, K. K. Klett, P. S. Cho, and P. M. Pellegrino, "Mid and long-wave infrared free-space optical communication," in *Laser Communication and Propagation through the Atmosphere and Oceans VIII,* vol. 11133 (International Society for Optics and Photonics, 2019), p. 1113302.

[195] L. Chen, D. Schwarzer, J. A. Lau, V. B. Verma, M. J. Stevens, F. Marsili, R. P. Mirin, S. W. Nam, and A. M. Wodtke, "Ultra-sensitive mid-infrared emission spectrometer with sub-ns temporal resolution," Opt. Express **26**(12), 14859–14868 (2018).

[196] L. Chen, D. Schwarzer, V. B. Verma, M. J. Stevens, F. Marsili, R. P. Mirin, S. W. Nam, and A. M. Wodtke, "Mid-infrared laser-induced fluorescence with nanosecond time resolution using a superconducting nanowire single-photon detector: New technology for molecular science," Accounts Chem. Res. **50**(6), 1400–1409 (2017).

[197] E. E. Wollman, V. B. Verma, A. B. Walter, J. Chiles, B. Korzh, J. P. Allmaras, Y. Zhai, A. E. Lita, A. N. McCaughan, E. Schmidt, S. Frasca, R. P. Mirin, S.-W. Nam, and M. D. Shaw, "Recent advances in superconducting nanowire single-photon detector technology for exoplanet transit spectroscopy in the mid-infrared," J. Astron. Telesc. Instruments, Syst. **7**(1), 011004 (2021).

[198] T. P. Greene, M. R. Line, C. Montero, J. J. Fortney, J. Lustig-Yaeger, and K. Luther, "Characterizing transiting exoplanet atmospheres with JWST," The Astrophys. J. **817**(1), 17 (2016).

[199] Y. Hochberg, I. Charaev, S.-W. Nam, V. Verma, M. Colangelo, and K. K. Berggren, "Detecting sub-GeV dark matter with superconducting nanowires," Phys. Rev. Lett. **123**(15), 151802 (2019).

[200] X. Zhao, S.-Y. Lee, J. Choi, S.-H. Lee, I.-K. Shin, and C.-U. Jeon, "Minimization of line edge roughness and critical dimension error in electron-beam lithography," J. Vac. Sci. & Technol. B, Nanotechnol. Microelectron. Materials, Process. Meas. Phenom. **32**(6), 06F505 (2014).

[201] I. Esmaeil Zadeh, J. W. Los, R. B. Gourgues, J. Chang, A. W. Elshaari, J. R. Zichi, Y. J. van Staaden, J. P. Swens, N. Kalhor, A. Guardiani, Y. Meng, K. Zou, S. Dobrovolskiy, A. W. Fognini, D. R. Schaart, D. Dalacu, P. J. Poole, M. E. Reimer, X. Hu, S. F. Pereira, V. Zwiller, and S. N. Dorenbos, "Efficient single-photon detection with 7.7 ps time resolution for photon-correlation measurements," ACS Photonics **7**(7), 1780–1787 (2020).

[202] I. Charaev, A. Dane, A. Agarwal, and K. K. Berggren, "Enhancement of optical response in nanowires by negative-tone pmma lithography," IEEE Transactions on Appl. Supercond. **29**(5), 1–5 (2019).

[203] J. J. Braat, "Extreme-UV lithography: a candidate for next-generation lithography," in *Photonics, Devices, and Systems,* vol. 4016 (International Society for Optics and Photonics, 1999), pp. 2–7.

[204] S. Owa and H. Nagasaka, "Immersion lithography: its potential performance and issues," in *Optical Microlithography XVI,* vol. 5040 (International Society for Optics and Photonics, 2003), pp. 724–733.

[205] S. Carter, M. Moore, D. Szebesta, J. Williams, D. Ranson, and P. France, "Low loss fluoride fibre by reduced pressure casting," Electron. Lett. **26**(25), 2115–2117 (1990).

[206] N. Wheeler, T. Bradley, J. Hayes, M. Gouveia, S. Liang, Y. Chen, S. Sandoghchi, S. A. Mousavi, F. Poletti, M. Petrovich, and D. Richardson, "Low-loss Kagome hollow-core fibers operating from the near-to the mid-IR," Opt. Lett. **42**(13), 2571–2574 (2017).

[207] W. Zhang, J. Huang, C. Zhang, L. You, C. Lv, L. Zhang, H. Li, Z. Wang, and X. Xie, "A 16-pixel interleaved superconducting nanowire single-photon detector array with a maximum count rate exceeding 1.5 GHz," IEEE Transactions on Appl. Supercond. **29**(5), 1–4 (2019).

[208] M. Perrenoud, M. Caloz, E. Amri, C. Autebert, C. Schönenberger, H. Zbinden, and F. Bussières, "Operation of parallel snspds at high detection rates," Supercond. Sci. Technol. **34**(2), 024002 (2021).

[209] J. P. Allmaras, E. E. Wollman, A. D. Beyer, R. M. Briggs, B. A. Korzh, B. Bumble, and M. D. Shaw, "Demonstration of a thermally coupled row-column SNSPD imaging array," Nano Lett. **20**(3), 2163–2168 (2020).

[210] M. Yabuno, S. Miyajima, S. Miki, and H. Terai, "Scalable implementation of a superconducting nanowire single-photon detector array with a superconducting digital signal processor," Opt. Express **28**(8), 12047–12057 (2020).

[211] S. Doerner, A. Kuzmin, S. Wuensch, I. Charaev, F. Boes, T. Zwick, and M. Siegel, "Frequency-multiplexed bias and readout of a 16-pixel superconducting nanowire single-photon detector array," Appl. Phys. Lett. **111**(3), 032603 (2017).

[212] A. Gaggero, F. Martini, F. Mattioli, F. Chiarello, R. Cernansky, A. Politi, and R. Leoni, "Amplitude-multiplexed readout of single photon detectors based on superconducting nanowires," Optica **6**(6), 823–828 (2019).

[213] Y. P. Korneeva, N. Manova, I. Florya, M. Y. Mikhailov, O. Dobrovolskiy, A. Korneev, and D. Y. Vodolazov, "Different single-photon response of wide and narrow superconducting Mo_xSi_{1-x} strips," Phys. Rev. Appl. **13**(2), 024011 (2020).

[214] J. Chiles, S. M. Buckley, A. Lita, V. B. Verma, J. Allmaras, B. Korzh, M. D. Shaw, J. M. Shainline, R. P. Mirin, and S. W. Nam, "Superconducting microwire detectors based on WSi with single-photon sensitivity in the near-infrared," Appl. Phys. Lett. **116**(24), 242602 (2020).

[215] I. Charaev, Y. Morimoto, A. Dane, A. Agarwal, M. Colangelo, and K. K. Berggren, "Large-area microwire MoSi single-photon detectors at 1550 nm wavelength," Appl. Phys. Lett. **116**(24), 242603 (2020).

[216] L. Thylén and L. Wosinski, "Integrated photonics in the 21st century," Photonics Res. **2**(2), 75–81 (2014).

[217] F. Najafi, J. Mower, N. C. Harris, F. Bellei, A. Dane, C. Lee, X. Hu, P. Kharel, F. Marsili, S. Assefa, K. K. Berggren, and D. Englund, "On-chip detection of non-classical light by scalable integration of single-photon detectors," Nat. Commun. **6**(1), 1–8 (2015).

[218] S. Khasminskaya, F. Pyatkov, K. Słowik, S. Ferrari, O. Kahl, V. Kovalyuk, P. Rath, A. Vetter, F. Hennrich, M. M. Kappes, G. Gol'tsman, A. Korneev, C. Rockstuhl, R. Krupke, and W. H. Pernice, "Fully integrated quantum photonic circuit with an electrically driven light source," Nat. Photonics **10**(11), 727–732 (2016).

[219] L. M. Rosenfeld, D. A. Sulway, G. F. Sinclair, V. Anant, M. G. Thompson, J. G. Rarity, and J. W. Silverstone, "Mid-infrared quantum optics in silicon," Opt. Express **28**(25), 37092–37102 (2020).

[220] D. Y. Vodolazov, Y. P. Korneeva, A. Semenov, A. Korneev, and G. Goltsman, "Vortex-assisted mechanism of photon counting in a superconducting nanowire single-photon detector revealed by external magnetic field," Phys. Rev. B **92**(10), 104503 (2015).

[221] A. Zotova and D. Y. Vodolazov, "Intrinsic detection efficiency of superconducting nanowire single photon detector in the modified hot spot model," Supercond. Sci. Technol. **27**(12), 125001 (2014).

[222] N. R. Gemmell, M. Hills, T. Bradshaw, T. Rawlings, B. Green, R. M. Heath, K. Tsimvrakidis, S. Dobrovolskiy, V. Zwiller, S. N. Dorenbos, M. Crook, and R. H. Hadfield, "A miniaturized 4 K platform for superconducting infrared photon counting detectors," Supercond. Sci. Technol. **30**(11), 11LT01 (2017).

[223] W. E. Gifford, "The Gifford-McMahon cycle," in *Advances in Cryogenic Engineering,* (Springer, 1966), pp. 152–159.

[224] R. Radebaugh, "Cryocoolers: the state of the art and recent developments," J. Physics: Condens. Matter **21**(16), 164219 (2009).

[225] L. Duband and B. Collaudin, "Sorption coolers development at CEA-SBT," Cryogenics **39**(8), 659–663 (1999).

[226] A. J. May, G. Coppi, V. Haynes, S. Melhuish, L. Piccirillo, T. Sarmento, and S. Teale, "A highly effective superfluid film breaker for high heat-lift 1 K sorption coolers," Cryogenics **102**, 45–49 (2019).

[227] "Cooldown GL4 code by G Taylor on Github," https://github.com/gregor-taylor/Cooldown_GL4, accessed August 2021.

[228] C. Sheridan, *The Python language reference manual* (Lulu Press, Inc, 2016).

[229] P. Authors, "Pyvisa: Control your instruments with python," (2016).

[230] J. D. Hunter, "Matplotlib: A 2D graphics environment," Comput. Sci. & Eng. **9**(3), 90–95 (2007).

[231] "Data gathering code by G Taylor on Github," https://github.com/gregor-taylor/DataGather-SNSPD, accessed August 2021.

[232] "Hydraharp for Python code by G Taylor on Github," https://github.com/gregor-taylor/HydraHarp-for-Python, accessed August 2021.

[233] T. E. Oliphant, *A guide to NumPy*, vol. 1 (Trelgol Publishing USA, 2006).

[234] "Becker and Hickl depth images code by G Taylor on Github," https://github.com/gregor-taylor/Becker_Hickl_SPC_Depth_Images, accessed August 2021.

[235] J. D. Owens, M. Houston, D. Luebke, S. Green, J. E. Stone, and J. C. Phillips, "GPU computing," Proc. IEEE **96**(5), 879–899 (2008).

[236] A. Munshi, "The OpenCL specification," in *2009 IEEE Hot Chips 21 Symposium (HCS),* (IEEE, 2009), pp. 1–314.

[237] "Reikna, a pure python GPGPU library," http://reikna.publicfields.net, accessed August 2021.

[238] "SPC tools code by G Taylor on Github," https://github.com/gregor-taylor/SPC-Tools, accessed August 2021.